University of Nottingham
UK | CHINA | MALAYSIA

Development of GHz Optoacoustic lenses for sub-optical resolution imaging

Thesis submitted to the University of Nottingham for the degree of **Doctor of Philosophy, 2024.**

Mengting Yao

Supervised by

Matt Clark
Richard Smith
Fernando Perez-Cota
Rafael Fuentes Dominguez

Signature _____

Date _____ / _____ / _____

Acknowledgements

I am very grateful to my supervisors, my family, lab fellows, and everyone around during my entire PhD journey.

I would like to thank Prof. Matt Clark for offering me this PhD opportunity and for his support with the funding application when I was doing my undergraduate final year project with him. From that project, I got my first taste of what research is, and from the PhD, I've learned much more from all his invaluable guidance and support. I would also like to thank all my supervisors: Dr. Richard J. Smith, Dr. Fernando Perez-Cota, and Dr. Rafael Fuentes Dominguez for their help and suggestions throughout the whole journey. I couldn't have completed this PhD without any of them.

I would like to thank my parents for everything they have made possible for me, all the effort and help. I couldn't be the person I am today without them. And my grandparents, for their care and support.

Finally, I would like to acknowledge all my colleagues who were/are part of my PhD journey from the Optics and Photonics group: Sal, Will, Don, Wenqi, Paul, Shakila, Fei, Yijie (and more). For all the times we shared, having chats about (or not about) science and engineering.

Research Outputs

Publications:

Optoacoustic Lenses for Lateral Sub-optical Resolution Elasticity Imaging. Mengting Yao, Rafael Fuentes-Domínguez, Fernando Pérez-Cota, Salvatore La Cavera III, Richard J. Smith, and Matt Clark. *Under review.*

Label-free Brillouin endo-microscopy for the quantitative 3D imaging of sub-micrometre biology. Salvatore La Cavera III, et al. *Nature Communications Biology* 7, April, 2024.

Parallel Imaging with Phonon Microscopy Using a Multi-Core Fibre Bundle Detection. Rafael Fuentes-Domínguez, Mengting Yao, William Hardiman, Salvatore La Cavera III, Kerry Setchfield, Fernando Pérez-Cota, Richard J. Smith, and Matt Clark. *Photoacoustics* 31, June, 2023.

Picosecond Ultrasonics for Elasticity-Based Imaging and Characterization of Biological Cells. Pérez-Cota, Fernando, Rafael Fuentes-Domínguez, Salvatore La Cavera, William Hardiman, Mengting Yao, Kerry Setchfield, Emilia Moradi, et al. *Journal of Applied Physics* 128, no. 16, October, 2020.

Design of a Resonant Luneburg Lens for Surface Acoustic Waves. Rafael

Fuentes-Domínguez, Mengting Yao, Andrea Colombi, Paul Dryburgh, Don Pieris, Alexander Jackson-Crisp, Daniel Colquitt, Adam Clare, Richard J. Smith, and Matt Clark. *Ultrasonics* 111, March, 2021.

Presentations:

Development of GHz optoacoustic lenses for lateral super resolution imaging. *Photonics West 2024 Photons Plus Ultrasound: Imaging and Sensing*, San Francisco, California, United States. January 2024.

GHz optoacoustic lenses for sub-optical resolution imaging. *International Congress on Ultrasonics (ICU) 2023*, Beijing, China, August 2023.

Development of Acoustic Fresnel Zone Plate lens working in GHz frequency., *Photon 2022*, Nottingham, UK, September 2022.

Ray tracing in an acoustic metamaterial., *International Congress on Ultrasonics (ICU) 2019*, Bruges, Belgium, September 2019.

Recognitions

RWB Stephens Prize, for best student papers, *International Congress on Ultrasonics (ICU)* 2023

European Adaptive Optics Summer School Scholarship, 2022.

Abstract

Brillouin light scattering (BLS) and time-resolved Brillouin scattering (TRBS) based imaging are new techniques used for imaging and characterizing cells. These methods enable the observation of elasticity-related contrast with optical resolution and label-free operation. Phonon microscopy is a process that can detect Brillouin light scattering (BLS) using laser-generated coherent phonon fields. This approach is particularly appealing for imaging because, at GHz frequencies, the phonon wavelength is sub-optical (approximately hundreds of nm). Previous research has shown that an axial resolution up to 10 times higher than that of the optical system used for the measurements can be achieved. However, the lateral resolution is still limited by the optical systems.

In this thesis, a way to improve the lateral resolution by surpassing the optical diffraction limit is proposed by using multiple designs of optoacoustic lenses to achieve GHz coherent phonon pulse focusing. These optoacoustic lenses are designed to generate a focusing sound field when a pump light illuminates them, and then the probe beam allows the sound field to be continuously monitored in time using TRBS. A numerical model based on the Fourier-Bessel angular spectrum method is used to simulate the distribution of the optoacoustically generated sound field, and the model suggests that a focused acoustic beam down to approximately 200 nm and an increased acoustic intensity are achievable.

A significant portion of this work is devoted to the design and nanoscale fabrication of these lenses, along with detailed simulations that explore their acoustic and optoacoustic properties. These lenses, which include flat Fresnel zone plates and concave structures, are engineered to potentially enhance the lateral resolution in TRBS systems beyond the constraints imposed by optical diffraction limits. The thesis also presents proof-of-concept experimental results that demonstrate the strong focusing effect of these lenses, a crucial step toward their application in high-resolution acoustic microscopy. While full-scale imaging has not yet been realized, these initial findings are promising, indicating the potential of these lenses to achieve superior lateral resolution in TRBS.

Furthermore, this research provides a foundation for future studies to integrate these lenses into TRBS systems for enhanced imaging capabilities, particularly in fields where non-invasive and high-precision observation is essential, such as in biological cell imaging. The thesis encapsulates not only the theoretical and experimental advancements in the field of acoustic microscopy but also lays the groundwork for further exploration and potential applications of these optoacoustic lenses in overcoming resolution barriers in TRBS.

Contents

Acknowledgements i

Research Outputs ii

Abstract iv

List of Tables xi

List of Figures xii

Abbreviations 1

Chapter 1 Introduction 1

1.1 Motivation 2

1.2 Thesis structure 3

1.3 Imaging beyond optical diffraction 4

1.3.1 Resolution of imaging system 5

1.3.2 Scanning electron microscope (SEM) 6

1.3.3 Scanning probe microscopy (SPM) 7

1.3.4 Super resolution optical imaging 9

1.4 Acoustic-based imaging techniques 12

1.4.1 Ultrasound 12

1.4.2 Scanning acoustic microscopy 13

1.4.3 Photoacoustics 16

1.5 Mechanical imaging of cells and tissues 18

1.5.1 Optical trapping 18

1.5.2 Atomic force microscopy 19

1.5.3 Brillouin microscopy 20

1.5.4 PLU based microscopy 22
1.6 Focusing of acoustic fields 24
1.6.1 Geometric focusing and acoustic lenses 24
1.6.2 Electronic focusing with phased array 25
1.6.3 Photoacoustic transducers for novel applications 25
1.7 Discussion and Device concept 27
Chapter 2 Background & Modelling 31
2.1 Brillouin scattering 32
2.1.1 Brillouin microscopy 32
2.2 Picosecond laser ultrasound 34
2.2.1 PLU based TRBS imaging 38
2.2.2 Optical modelling 45
2.2.3 Sound generation and propagation 49
2.2.4 Optical detection of TRBS 57
2.3 Focusing of waves 61
2.3.1 Focusing of sound 62
2.3.2 PLU based SAM 67
2.3.3 Fresnel zone plate (FZP) 70
2.3.4 Concave lenses 76
2.4 Fourier-Bessel angular spectrum method (FBASM) 79
2.4.1 Model setup 81
2.4.2 Radially symmetric propagation method 83
2.5 Nano fabrication 86
2.5.1 Electron beam lithography 89
2.5.2 Focused ion beam 90
2.6 Discussion 92
Chapter 3 Methods 93
3.1 Optoacoustic Lenses 94

3.1.1 Transducer design and simulation 95
3.1.2 FZP design 98
3.1.3 Concave lens design 101
3.1.4 NA of acoustic lenses 103
3.2 Optoacoustic lens fabrication 104
3.2.1 Transducer fabrication 105
3.2.2 Fresnel lens fabrication 106
3.2.3 Concave lens fabrication 111
3.2.4 Phase-Reversal FZP (PR-FZP) fabrication 118
3.3 Experimental set-up 119
3.3.1 Time resolved signal in GHz 120
3.3.2 ASOPS pump-probe optical system 122
3.3.3 Scanning beam sizes 125
3.3.4 Scanning method 130
3.4 Signal processing 136
3.4.1 Extract time trace 136
3.4.2 Frequency analysis - FFT 139
3.4.3 Signal amplitude modulation 140
3.4.4 Frequency analysis - wavelet 141
3.5 Discussion 143
Chapter 4 Results 145
4.1 Fresnel Zone plate lenses 146
4.1.1 Simulation 147
4.1.2 Experimental results 154
4.1.3 Discussion 158
4.2 Concave lenses 169
4.2.1 Simulation 169
4.2.2 Experimental results 173

4.2.3 Discussion . . . 182
4.3 Summary . . . 188
Chapter 5 Preliminary results and perspectives 190
5.1 Transducer optimization . . . 191
5.2 Flat Phase-reversed FZP made with nanorods . . . 192
5.2.1 Modelling of nanorods . . . 195
5.2.2 Nanorods measurements . . . 200
5.3 Optoacoustic axicon lenses . . . 203
5.4 Lens for imaging - Approaching real acoustic resolution . . . 204
5.4.1 3D micron positioner . . . 206
5.4.2 Edge detection . . . 209
5.4.3 Fibre for detection . . . 212
5.5 Transfer the lens to single mode fibre . . . 212
5.5.1 Fabrication . . . 214
5.6 Publications and my contributions . . . 216
5.6.1 Picosecond ultrasonics for elasticity-based imaging and characterization of biological cells . . . 216
5.6.2 Parallel imaging with phonon microscopy using a multi-core fibre bundle detection . . . 217
5.6.3 Label-free Brillouin endo-microscopy for the quantitative 3D imaging of sub-micrometre biology . . . 218
Chapter 6 Future work 220
6.1 Transducer optimisation . . . 220
6.2 Phonon-probe microscopy . . . 221
6.3 More about nanorods . . . 223
6.4 Summary . . . 224
Chapter 7 Conclusions 225
7.1 Summary of thesis . . . 226

7.2 Closing Remarks 229

Bibliography **230**

Appendices **255**

Appendix A White light spectroscopy **256**

Appendix B GDSII design **259**

Appendix C Water refractive index **261**

Appendix D Transforms **263**

D.1 Fourier transform 263

D.2 Hankel Transform 265

List of Tables

3.1 Major Specifications of SEM. 111

3.2 Major Specifications of FIB. 118

4.1 Positive FZP design parameters and NA. 148

4.2 Negative FZP design parameters and NA. 150

4.3 Phase reversal PR-FZP design parameters and NA. 152

4.4 Concave lens design parameters. 173

4.5 Numerical aperture (NA) of Concave lenses. 173

List of Figures

1.1 Basic schematic illustration of the sensing mechanisms used in atomic force microscopy (AFM) and scanning tunnelling microscopes (STM). 8

1.2 Enhancement of spatial resolution using STED microscopy. 10

1.3 The process of creating super-resolution images using STORM methods. 11

1.4 Scanning acoustic microscopy showing echo signals resolved in the time domain. 14

1.5 Two types of Photoacoustic microscopy systems. 17

1.6 The optical trapping mechanisms. 19

1.7 Brillouin scattering in heterogeneous biological samples. 21

1.8 Photoacoustic transmitters. 25

1.9 Photoacoustic transducers. 26

1.10 Basic device concept: multiple geomatical design over glass substrate 30

2.1 Brillouin technology generated representative data. 33

2.2 Sequence of events in picosecond laser ultrasonics. 35

2.3 Bragg's law applied to the Brillouin scattering interactions. 35

2.4 Recently reported cell images using PLU. 40

2.5 Device concept for the OAT in Phonon Microscopy. 41

2.6 Imaging capabilities of phonon microscopy. 42

2.7 Device concept, imaging and profilometry capabilities of fibre-based phonon microscopy. 44

2.8 Sequence of events in picosecond laser ultrasonics. 46

2.9 Reflection and transmission calculations in multilayer thin film structure. 47
2.10 Simulated strain pulse with gold. 53
2.11 A basic example of using the PLU model to simulate TRBS signal with a transducer and water or polystyrene (PS) as the external medium. 59
2.12 Simulated trace of a multilayer structure including a substrate, a transducer layer made of Au, a layer of water and a PMMA layer. . 60
2.13 Wavelet analysis of the simulated trace of a multilayer structure, which includes substrate, transducer layer water and PMMA layer. 60
2.14 Device concept and example scanning result for the scanning acoustic microscope (SAM). 64
2.15 Working principle and imaging capabilities of photoacoustic microscopy. 66
2.16 PLU based new scanning opto-acoustic microscope. 68
2.17 Towards lighter and more transparent lenses. 71
2.18 Front and side view of a zone plate. 73
2.19 Optical path lengths of an optical FZP. 73
2.20 Sketch showing the upper half region of a Rayleigh-Wood phase-reversal FZP from the side. 75
2.21 Sketch showing the device concept of optoacoustic PR-FZP for PLU. 76
2.22 Wave propagation path and concave spherical acoustic lens. 77
2.23 Two approaches for ultrasound transducer focusing. 79
2.24 Two approaches for ultrasound transducer focusing. 80
2.25 Scheme of the Fourier-Bessel angular spectrum propagation method. 82
2.26 Axisymmetric model plane. 83
2.27 Electron beam lithography working principle. 90
2.28 Basic principles and functions of FIB 91

3.1 Basic device concept: multiple geometrical design over glass substrate 96
3.2 transmission reflection for different metals 97
3.3 frequency amplitude for different metals 98
3.4 Schematic of FZP 99
3.5 Snapshot of a GDSII file with multiple FZPs. 100
3.6 Simulated signal intensity vs phase difference. 101
3.7 Schematic diagram of the design of a concave lens. 102
3.8 Concave lens designs with different focus and diameters. 103
3.9 Numerical Aperture (NA) of the proposed acoustic lenses. 104
3.10 Transducer characterisation 107
3.11 Process flow for submicron fabrication on of flat structure 108
3.12 Optical pictures of the design pattern of EBL made FZPs. 110
3.13 EBL made normal FZPs and FZP made with nanorods. 112
3.14 Illustration of 3D-FIB etching process. 113
3.15 Typical SEM images of concave lenses FIB-etched with different number of layers and layer thickness. 114
3.16 FIB fabrication process for 3D concave lenses. 117
3.17 Sampling clock of pump and probe - how time resolved signal is generated. 121
3.18 Schematic of the experiment used to perform pump-probe spectroscopy with NUV-NIR setup. 123
3.19 Basic diagram of the sample plane for the free-space implementation of the pump-probe system. 125
3.20 Schematic of the experiment used to perform pump-probe spectroscopy with NIR-NIR setup. 126
3.21 Basic diagram of the sample plane for the free-space implementation of a reflection pump-probe system. 127

3.22 Schematic of the experiment used to perform pump-probe spectroscopy with NUV-NIR setup . . . 128
3.23 Diagram of the optics design around the microscope body. 129
3.24 Diagram of the whole system . . . 130
3.25 Effective radius of the pump laser beam focii sizes determination by cross-correlation . . . 133
3.26 Determine the sizes of the pump and probe using the optical image. 134
3.27 A DC scanned area showing the processes to find precise positions of the lenses. . . . 135
3.28 Single point signal processing steps from the initial raw data until the extraction of the signal of interests. . . . 138
3.29 Example basic processed experimental trace, and its fast Fourier transform (FFT). . . . 139
3.30 Best match to find the TRBS signal decay rate. . . . 141
3.31 Morlet Wavelet . . . 143

4.1 Schematics and SEM pictures of postive and negative FZPs. 148
4.2 Simulation results of positive FZP with Varied Focal Depths 149
4.3 Simulation results of negative FZPs . . . 151
4.4 Simulation analysis of 2 μm focus FZP designs . . . 153
4.5 Intensity Profiles and comparisons for 2 μm focused Fresnel Zone Plates . . . 154
4.6 Time resolved Brillouin Scattering Traces and Frequency analysis of flat and positive FZP . . . 156
4.7 Experimental results showcasing the focusing capabilities of a positive FZP lens with a designed focus of 2 μm . . . 157
4.8 Schematic representation of the convolution process in image formation . . . 161

4.9 Comparative analysis of acoustic intensity and field distribution . . 162
4.10 Comparisons of simulated and experimental acoustic field distributions and their central axial profiles 163
4.11 SEM pictures of postive and negative FZPs showing the Au covered rings. 165
4.12 Fabrication issues of PR FZP 166
4.13 Simulated curved lens features using data interpolation. 167
4.14 Acoustic Intensity, acoustic field and structure of ideal PR-FZP and modified lens profile. 167
4.15 Schematic of concave lens design parameters 169
4.16 Simulated acoustic focusing of concave lenses with varied focal depths and a diameter of 4 μm 170
4.17 Simulated acoustic focusing of concave lenses with varied focal depths and a diameter of 5 μm 171
4.18 Simulated acoustic focusing of concave lenses with varied focal depths and a diameter of 6 μm 172
4.19 Time-Resolved Brillouin Scattering Traces and Frequency Analysis of flat and concave lens 175
4.20 Time-Resolved Brillouin Scattering Traces and Frequency Analysis of flat and concave lens 176
4.21 line scans across centre of D5F3 178
4.22 2D scans of a concave Lens with enhanced focusing capabilities . . . 179
4.23 Wavelet analysis of a 2d lens scan. 180
4.24 Gaussian fits of signal intensity at the designed focus across x and y axes. 181
4.25 SEM images and optical photographs of concave lenses during and after fabrication, experiments and cleaning processes. 183
4.26 Temperature vs Brillouin frequency of water 185

4.27 Temperature distribution around the transducer 186
4.28 Comparison of Brillouin frequency shifts and wavelet amplitude for different lens structures. 187

5.1 Simulation results of the performance for Au/ITO/Au cavity transducers for varying ITO thicknesses. 192
5.2 Concept of PR-FZP made with nanorods. 194
5.3 Optical response of nanorods with length equals to 130 nm. 196
5.4 Optical response of nanorods with length equals to 145 nm. 196
5.5 Optical response of nanorods with length equals to 160 nm. 197
5.6 A diagram illustrating the extensional and breathing modes of a cylindrical Rod. 198
5.7 3D cubic nanorod with sharp edges 199
5.8 Mechanical response in free vibration mod. 199
5.9 Mechanical response in fixed vibration mod. 200
5.10 COMSOL models of 3D rounded nanorods. 200
5.11 Measurements of EBL made nanorods. 201
5.12 Experimental time traces with the Michelson-like dual time delay setup. 202
5.13 SEM pictures of a positive FZP and a PR-FZP made with nanorods. 203
5.14 Simulated formation of acoustic Bessel-like beams by using concentric rings. 204
5.15 Simulated acoustic focusing of axicon lenses with varied design & focal depths and a diameter of 5 μm 205
5.16 Experimental z-approaching results from a conventional Au transducer, NIR-NIR setup with detection in transmission. 207
5.17 Experimental z-approaching results from a conventional Au transducer, NUV-NIR setup with detection in reflection. 209

5.18 Moving the glass horizontally, from no-glass to glass. 210
5.19 Moving the glass horizontally and across grating patterns. 211
5.20 Diagram showing the experimental setup for using fibre for collection. 213
5.21 Device concept of a sub-optical resolution phonon probe microscope (PPM). 214
5.22 EBL-made FZP transferred to a fiber tip using the polymer-encapsulated method. 215
5.23 Direct FIB milling lens over a fibre tip. 216

A.1 White light spectroscopy design. 257
A.2 White light spectroscopy algorithm diagram and example fitting result. 258

Chapter 1

Introduction

This thesis addresses a critical challenge in time-resolved Brillouin scattering (TRBS) techniques: the limitation in lateral resolution. The core of the research lies in the development and characterization of innovative optoacoustic lenses, designed to focus coherent phonon fields at GHz frequencies. These lenses, which include flat Fresnel zone plates and concave structures, are engineered to enhance the lateral resolution in TRBS systems beyond the constraints imposed by optical diffraction limits.

Furthermore, this research provides a foundation for future studies to integrate these lenses into TRBS systems for enhanced sub-optical imaging capabilities, particularly in fields where non-invasive and high-precision observation is essential, such as in biological cell imaging.

1.1 Motivation

In the realm of cellular biology and medical diagnostics, the visualization and characterization of live cells are imperative for progress. Yet, the process is fraught with obstacles due to the small size and sensitive nature of cells. Traditional imaging techniques, such as fluorescence microscopy, rely on fluorescent labels that can disrupt cellular function. Additionally, Electron Microscopy is incompatible with live specimens, and Atomic Force Microscopy (AFM) is invasive and restricted in application scope.

The utilization of phonons, which are quantized sound waves, offers an alternative path that circumvents the issues associated with high-energy photons. Techniques like medical ultrasound and acoustic microscopy have already demonstrated the potential of sound-based imaging at lower frequencies. The quest now is to use shorter acoustic wavelengths for non-invasive, high-resolution cellular imaging.

Opto-acoustic systems, specifically photoacoustics, have emerged as a viable solution. These systems convert light into sound, allowing for imaging without the need for invasive labels. However, photoacoustic microscopy faces limitations at the cellular level due to its dependency on the specimen's inherent photoacoustic properties.

There is a compelling need for novel methodologies to generate and detect phonons with precision. The burgeoning field of cellular biomechanics has been propelled forward by innovations in Brillouin scattering-based techniques, which offer enhanced lateral resolution and specificity. These advances have paved the way for new applications in single-cell and tissue mechanics imaging.

Despite these advancements, the resolution in conventional Brillouin microscopy is still limited by diffraction limits, restricting the potential for sub-optical reso-

lution imaging. Phonon Microscopy, using Picosecond Laser Ultrasound (PLU) to capture Time Resolved Brillouin Scattering (TRBS), offers superior axial resolution due to shorter acoustic wavelengths in the GHz frequency range. Yet, its lateral resolution remains limited by the optical system used for detection.

This thesis addresses the challenge of optical diffraction in TRBS techniques by innovating the design and implementation of nano- and micro-scale optoacoustic lenses that can work in GHz range. By refining geometric focusing mechanisms through the application of Fresnel zone plates and concave lenses, this thesis aims to enhance the resolution of coherent phonon fields generated by ultra-short laser pulses.

This work lays the foundation for sub-optical 3D mechanical imaging, which promises to significantly elevate the lateral resolution capabilities of Phonon Microscopy, providing a label-free, biocompatible imaging tool that may revolutionize our understanding of cell biology and disease pathology.

1.2 Thesis structure

A brief description of each chapter is as follows:

- Chapter 1 introduces the problem and motivation of this research and some general background knowledge.
- Chapter 2 presents a detailed background of the problem aimed to be solved in this thesis as well as more discussion of the proposed solution and objectives, and also the modelling methods that are used to obtain the optical and mechanical response of optoacoustic transducers. A Fourier-Bessel angular spectrum method is also introduced to simulate the acoustic fields. Finally,

the nano/micro fabrication techniques used in this thesis are also discussed.

- Chapter 3 shows the design and fabrication of lenses, the experimental setup, the signal processing methods.
- Chapter 4 describes the main results of this work. This includes simulation and experimental results for both Fresnel Zone plate and concave lenses with different focus.
- Chapter 5 discusses preliminary results have been achieved in different directions using the lenses and also presents the projects I have participated and published.
- Chapter 6 discusses potential areas for future research.
- Chapter 7 summarises the work which has been presented in this thesis.

1.3 Imaging beyond optical diffraction

This section is dedicated to the study of imaging techniques that can perform imaging ability beyond optical diffraction. The aim is to simply present existing imaging techniques relying on different physical mechanisms that can break the natural diffraction limit.

Firstly, resolution of an imaging system are discussed, then few most common super resolution techniques, such as scanning electron microscopy (SEM), scanning transmission microscopy (STM) and atomic force microscopy (AFM) are presented, flowing which are optical super-resolution microscopy based on fluorescence microscopy, with special interests in their bio-comparability.

1.3.1 Resolution of imaging system

In 1873, Ernst Abbe, discovered that optical resolution is inherently constrained by light diffraction. This principle dictates that the resolving ability of optical instruments like microscopes is bound by the wavelength of light (λ) and the numerical aperture (NA) of the optics, limiting the minimum distinguishable distance between two points to $\lambda/2NA$.

This is then modified by Rayleigh adding a factor of 1.22 from the definition of Bessel function of 1st kind, given the Rayleigh criterion defined lateral resolution (the minimum distance between two separable source point):

$$d_x = 0.61\frac{\lambda}{NA} \tag{1.1}$$

For the case of depth, the resolution is given by:

$$d_y = 2\frac{\lambda}{NA^2} \tag{1.2}$$

For the depth resolution, NA^2 comes from the wavefront convergence effect, the focusing ability in the axial direction depends on how much the wavefronts converge. This convergence causes the axial resolution to scale with NA^2 because the depth of focus decreases quadratically as NA increases. Shorter wavelengths means better resolution. Practically, objective lenses can have a maximum NA of ~ 1.4 (in oil). For white light centred at 500 nm, a microscope can reach a theoretical best resolution of ~ 250 nm and 500 nm for the lateral and axial resolutions, respectively.

Though viewed as unbreakable barriers, recent advancements in imaging technol-

ogy have now made it possible to circumvent this diffraction limit under specific conditions, by using different physical mechanisms. In the following sections, techniques utilising electron (SEM), scanning probe (STM and AFM) will be presented, and few optical super-resolution techniques (STED and STORM), working for live cell imaging, will also be introduced.

1.3.2 Scanning electron microscope (SEM)

Electron microscopy uses accelerated electron beams to scan the surface of samples. Ernst Ruska's "Nobel lecture" [1] provides an inspiring account of how the electron microscope was invented, driven by the desire to surpass the resolution of light microscopes. In fact, electron acceleration enables the achievement of significantly shorter wavelengths, below the nm scale, when typical light wavelengths range from UV to NIR [200 - 1000] nm. Several characteristics of a sample surface, such as its geometry or topography (the size and form of the materials making up the surface) and other attributes (crystallographic orientations or physical/chemical qualities), can be accessed using a scanning electron microscope (SEM) [2].

The electron source is the initial component of a SEM. Electrostatic and electromagnetic lenses are used to regulate the electrons' energy and beam diameter in order to generate a controlled electron beam. Due to low beam current, low electron beam diameters (nm radius) result in low contrast but great spatial resolution. Better contrast imaging is made possible by increased beam currents, however this also results in an increase in beam size. Thus, a trade-off between contrast and spatial (lateral) resolution needs to be made.

One of the primary limitations of SEM is the requirement for extreme vacuum to be maintained throughout the apparatus, from the electron beam source to the sample chamber, in order to prevent electron collisions with non-sample elements.

The material to be investigated is exposed to the electron beam, and for the interaction between the electrons and the material to occur, the substance must be conductive (have an additional conductive layer).

The above constraints make SEM not suitable for biological related imaging but still serve good perpose for the imaging of the micro/nano optoacoustic lenses fabricated in this thesis, more about the use of SEM to check the fabrication quality of lenses will be discussed in the Chapter 3.

1.3.3 Scanning probe microscopy (SPM)

Under the umbrella phrase "scanning probe microscopy", a series of standard techniques are reorganised to assess the structural, mechanical, optical, electrical, and magnetic properties of a material's surface. The first one uses scanning tunnelling microscopy (STM) [3], which works by creating a tunnelling effect between a conductive material's surface and a sharp metallic point known as the probe Figure 1.1 (a). The conducting material's surface is approached close to (a few angstrom above) the atomic-scale tip, and a very localised tunnelling effect may happen if a voltage is created between the tip and the surface. The tip/sample surface distance is closely correlated with the likelihood of electrons tunnelling over the potential barrier between the tip and the surface. Next, a scan (raster scan) can be performed, which allows the sample surface to be mapped as precisely as possible by measuring the current flowing through the tip at various points (but a set height). In the most exact configurations, the size of the tip at the apex — which can be as small as one atom — controls the lateral resolution.

Following the initial tunnelling effect tests, the atomic force microscope (AFM) was created, which operates on the same concept but with a different interaction between the tip and the sample. The AFM measures the atomic forces between the

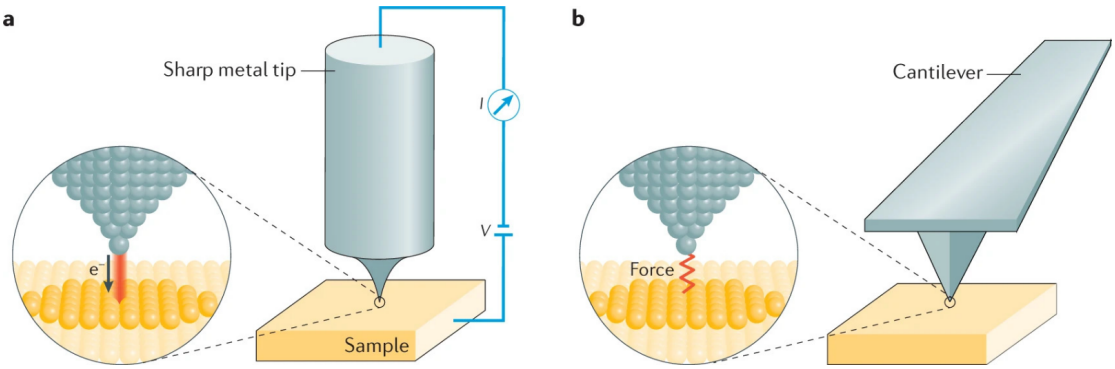

Figure 1.1: Basic schematic illustration of the sensing mechanisms used in atomic force microscopy (AFM) and scanning tunnelling microscopes (STM): (a) The surface of a conducting material is probed using a sharp metallic tip in the STM configuration by measuring the tunnelling current that is created between the probe's tip and the surface of the sample. (b) In the AFM scenario, the cantilever with the sharp tip mounted on it is used to measure the atomic forces through the cantilever's deflections. In both situations, raster scanning is used to image the sample surface and acquire nm lateral resolutions. Image reproduced from [4].

tip and the surface of the sample in place of the tunnelling current. A cantilever has its tip at its free end, and the force applied to the cantilever fixes its deflection, which alters the tip-surface distance. Using the AFM for raster scanning involves measuring the cantilever's deflections (displacements along the tip-surface axis) as a result of the atomic forces detected at the tip's apex Figure 1.1 (b). Laser sensing is typically used to measure the small-scale displacements of the cantilever. Scanning atomic forces has an advantage over tunnelling in that measurements can be made in less constrained environments and even with non-conducting materials.

AFM is also a commonly used method for high-resolution mechanical measurements. More details will be discussed in following mechanical imaging Section 1.5.

1.3.4 Super resolution optical imaging

One important tool for cell imaging is fluorescence microscopy. The fundamental mechanism of fluorescence is the absorption of light energy (a photon) by an indicator, which is followed by the emission of some of this light energy (as another photon) a few nanoseconds later. The released photon has less energy than the absorbed photon since some energy is lost throughout this process. Compared to light with a long wavelength (towards the red), light with a short wavelength (towards the blue) has more energy. As a result, the wavelength of light emitted from an indicator is typically longer than the wavelength of light absorbed (excitation) [5]. This effect is employed in fluorescence microscopy to observe particular molecules or locations within a given cell. Labels or fluorescence stain are used to achieve this.

However, diffraction still limits the spatial resolution of a fluorescence microscope, and the use of fluorescent labels has sparked questions regarding their potential toxicity and the possible effects this could have on biological sample health [6].

Radiation of short wavelength can achieve greater resolution than the optical microscope (see equation (1.1)). Imaging techniques discussed in the previous sections has revealed cell sub-structures of fixed (dead) specimens with great detail. However, if the sample is no longer live and functioning, its difficult to understand how these sub-structures' function.

However, Fluorescence microscopy based super-resolution techniques, with its ability to do live cell imaging (though with potential toxic labels), provides new potential for super-resolution live cell imaging. This kind of resolution can be obtained by using nonlinear techniques, such as confining light emission to regions smaller than a depth of focus or diffraction spot. Several methods, including stochastic

optical reconstruction microscopy (STORM)[7] and stimulated emission depletion (STED) [8], have been used to achieve super-resolution.

Stimulated Emission Depletion Microscopy (STED)

STED uses two lasers to overcome the light diffraction limit as shown in Figure 1.2. Two synchronised pulsed lasers excite and deplete the fluorescence. Since the depleting laser is focused into a ring shape, the central area of the excitation laser can thus remains unaffected. The area from which the fluorescence is emitted is a little change in the laser's illumination, and it is practically less than the excitation laser's diffraction limit.

Figure 1.2: Enhancement of spatial resolution using STED microscopy. It depicts two wire-like entities marked with fluorophores represented by gray circles. The application of STED introduces a doughnut-shaped light pattern that intersects with the focal area's excitation spot. This interaction causes a depletion on most of the fluorophores within the doughnut area, denoted by yellow circles, effectively silencing their fluorescence. Consequently, only the central fluorophores within the doughnut emit fluorescence, indicated by a green glow, resulting in increased imaging resolution.

This technique has been used to image living cells with a lateral resolution of up to 30 nm [8]. This method's primary drawback is the high flux of laser light (per pixel), which causes significant photo-bleaching (fluorescence loss) and may harm the specimen.

Stochastic Optical Reconstruction Microscopy (STORM)

By using multiple colours and three dimensions, Stochastic Optical Reconstruction Microscopy (STORM) combines the high-accuracy localization information of individual fluorophores to reconstruct a super-resolution image. All of the fluorophores in a sample are fluorescent under a typical microscope, providing a smooth image. But in the case of STORM, only a small number of fluorophores are stochastically switched on at any given moment. After a while, these fluorophores become bleached and enter the "dark state". After that, a second group of fluorophores randomly turns on.

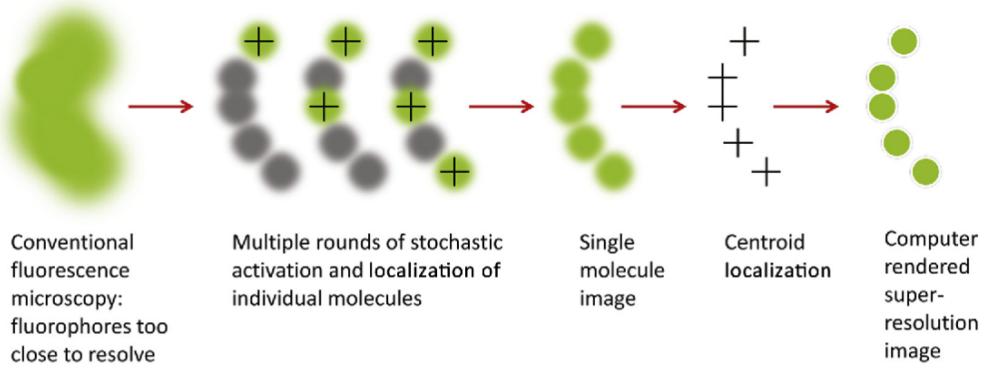

Figure 1.3: The process of creating super-resolution images using STORM methods. Reconstructing super-resolution photographs can be accomplished by repeatedly identifying the centroids of individual random fluorophores. Figure reproduced from [9].

As seen in Figure 1.3, different fluorophores shift between light and dark states, and only a small fraction is detected in each snapshot of an image. The ultimate super-resolution picture is produced by plotting several of these snapshots of various fluorophores.

1.4 Acoustic-based imaging techniques

As early as the sixth century BC, when Pythagoras talked about the mathematical features of instrument strings, people became interested in acoustics.

Ultrasound imaging is nowadays commonly used in many domains including medical/biological imaging [10] and non-destructive testing of industrial components for its non-invasive nature. To get acoustic images, ultrasound pulses are sent into the thing being studied, like a patient or a wall made of concrete. A transducer is used to send and record the pulses. Pulses are mirrored by the different interfaces in the sample as they move through it. This could be the tissues and organs of a patient or cracks and holes in concrete. By keeping track of the amplitude of the pulses that are returned and/or the time between pulse echoes, you can learn about the structure below the surface of the probe.

1.4.1 Ultrasound

Ultrasound imaging is a well-known clinical imaging method that gives real-time, quantitative information about a patient's anatomy and physiology. It is one of the most common types of clinical imaging and is becoming more and more useful for guiding interventional clinical treatments. This is because it doesn't use ionising radiation and is relatively affordable to purchase as well as maintain.

A sound wave travels through liquids as a longitudinal wave, which means that the particles in the medium move in a way that is parallel to the sound wave's propagation direction. The sound waves transmit their energy physically by changing the pressure variations on the particles.

The principles of acoustic physics (reflection, refraction, absorption, and scatter-

ing) are used to create ultrasound images. The ultrasound that is used to identify and describe various tissue types is attenuated as a result of these characteristics. The attenuation coefficient describes how much ultrasound is attenuated. A tissue's acoustic impedance refers to how much resistance it provides to impede the passage of an ultrasonic beam. The ratios of reflected and transmitted sound waves are determined by the differences in the acoustic impedance of the two media.

Snell's law controls the angle of the reflected, or transmitted sound waves. Depending on the kind of material the transmitted wave passes through, its velocity may be greater or lower than the incident wave. The wavelength shifts while the frequency stays the same during the velocity change. The density and compressibility (or stiffness) of the material have an impact on the ultrasonic wave's velocity. Because the frequency stays constant as the wavelength increases, the greater the ultrasonic velocity, the lower the compressibility (or higher the stiffness), and/or the lower the density.

1.4.2 Scanning acoustic microscopy

High frequency acoustic waves can be used in acoustic microscopy, offering high resolution for subsurface inspection and making the technique a strong contender to find hidden flaws in biological and elastic samples as well as opaque hard materials.

Sokolov introduced the use of acoustic microscopy in 1949, and high-resolution imaging for examining the internal structure of non-transparent substances saw a breakthrough in the early 1970s [11]. When compared to electron microscopy, scanning acoustic microscopy (SAM) has the advantages of being quicker and requiring less sample pretreatment [12].

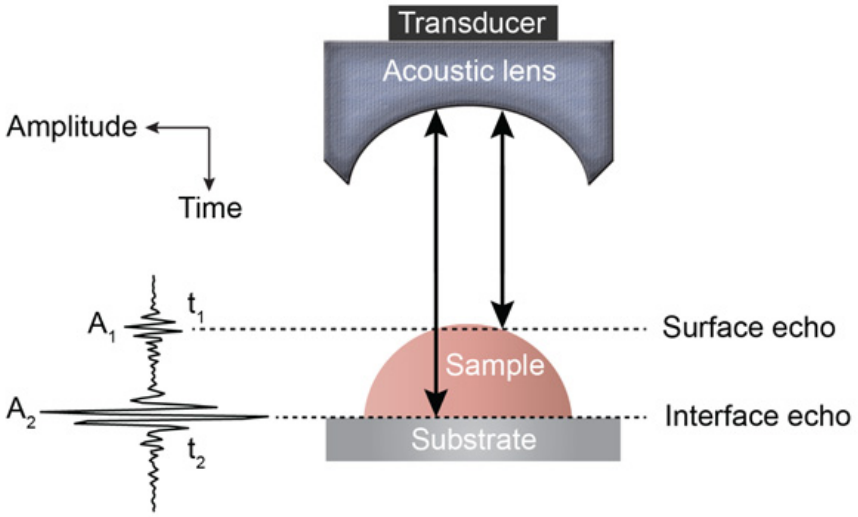

Figure 1.4: Schematic of a SAM, showing echo signals resolved in the time domain. The echo signal from the surface of the sample is received at time point t_1 and has an amplitude of A_1, while the echo signal reflected from the sample-substrate interface is received at time point t_2 and has an amplitude of A_2. It is possible to determine the specimen's mechanical and elastic properties by calculating the arrival time of each maximum and its corresponding amplitude. Image reproduced from [13].

The echo signal from the surface of the sample is received at time point t_1 and has an amplitude of A_1, while the echo signal reflected from the sample-substrate interface is received at time point t_2 and has an amplitude of A_2. It is possible to determine the specimen's mechanical and elastic properties by calculating the arrival time of each maximum and its corresponding amplitude.

A conventional SAM is made up of an ultrasonic emitting transducer, a mechanical scanner and an image processor. As shown in Figure 1.4, the transducer plays an important role as a lens with energy transfer function that delivers and focuses the acoustic wave generated by the piezoelectric array and as a detector that also accepts the echo reflected from the sample [13, 14]. When sound hits an object, it can be transmitted (scattered at 0°), absorbed, reflected, or scattered (scattered at 180°). The scattered pulses travelling in a specific direction can be detected. A detected pulse alerts one to the existence of an object or boundary. The duration required for an acoustic source to generate the pulse, for it to be scattered by an

object, and for the detector to receive it, usually at the same time as the source, is known as the pulse's "time of flight". Knowing the speed through the medium, one can use the time of flight to calculate the inhomogeneity's distance from the source.

The location under investigation is allocated a value based on the measurement. A small movement of the transducer (or object) is followed by another insonification. Until the entire area of interest has been examined, this process is repeated in a methodical manner. Frequently, an image of the object is created by assembling the values for each point. The geometry or material composition of the object determines the contrast that can be perceived in the picture. The physical scanning resolution or the beam width (which is based on sound frequency, typically between 1 and 1000 MHz) are the two factors that limit the image's resolution.

Transducers utilized in standard ultrasound applications and Scanning Acoustic Microscopy (SAM) typically emit pulses in the MHz range, with corresponding acoustic oscillation wavelengths on the scale of centimeters and micrometers. Most of these transducers are based on electro-acoustic principles. However, the resonance frequency generated by these piezoelectric transducers is inversely proportional to the thickness of the piezoelectric element. As a result, the higher the frequency, the more challenging and sensitive the fabrication and operation of these transducers become. More details on how researchers pursue higher resolution (higher frequency & the coupling fluid used for sound transmission) will be discussed in 2.3.1. High frequency acoustic pulses (opto-acoustic) of the GHz range can be produced using laser pulses in order to get over this limit, and thus pave the way to optical or even sub-optical resolution imaging.

1.4.3 Photoacoustics

Thanks to "The Photophone" developed by A. G. Bell with assistance from S. Tainter, the idea of an interaction between light, an electromagnetic wave, and sound, an elastic wave, was first demonstrated experimentally at the end of the 19th century [15]. Bell first described the light-sound interaction known as the photoacoustic phenomenon in a letter that was published in Nature in the 1880s. Bell stated that "when a vibratory beam of light falls upon these substances (different metals being studied) they emit sounds." But it wasn't until the early 1960s, when T. H. Maiman invented the laser (Light Amplification by Stimulated Emission of Radiation), that the photoacoustic effect made a significant advancement [16]. In under three years, R. M. White used lasers to demonstrate the development of elastic waves in materials, giving rise to the field of laser ultrasonics [17].

The photoacoustic effect, also known as the optoacoustic effect, is the process by which laser light is absorbed by a material and transforms into acoustic (elastic) waves. Since the acoustic wave can alter the material's optical characteristics locally, it is also possible to track the wave's propagation using a laser light once it has been introduced into the sample through the optoacoustic effect. This acousto-optic interaction can thus be combined with the optoacoustic generation to create multiple non-contact techniques for various applications, such as characterising materials and non-invasive imaging, at scales typically unreachable for conventional ultrasound techniques (using transducers).

For a photoacoustic microscopy (PAM) system, optical excitation and acoustic detection are the basic configurations. The PA signals, i.e. the acoustic waves, are generated by optical absorption of the target. Both the optical excitation and ultrasonic detection are focused down to a small region of a sample. There

two types of PAM systems: optical-resolution (OR-PAM) or acoustic-resolution (AR-PAM), depending on whether the optical signal or ultrasonic signal is more tightly focused as shown in Figure 1.5.

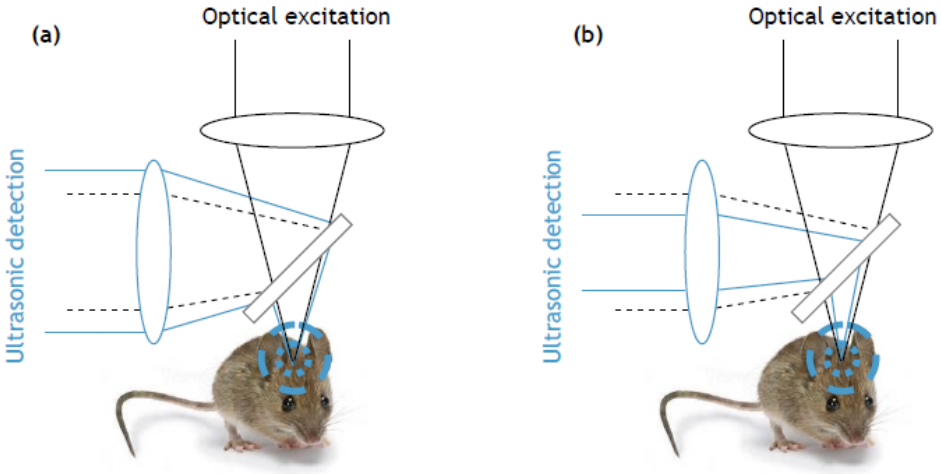

Figure 1.5: Two types of Photoacoustic microscopy systems. (a) Optical-resolution photoacoustic microscopy (OR-PAM), (b) Acoustic-resolution photoacoustic microscopy (AR-PAM). Image reproduced from [18].

The lateral resolution is determined by the overlap of the dual foci from both the optics and ultrasound, and the axial resolution depends on the photoacoustic wave wavelength. Typical PAM is capable to achieve a lateral resolution of tens of μm and an axial resolution of hundreds of μm. These resolutions are capable to get an imaging depth up to 1 mm, which is the maximum achievable depth due to the optical diffusion limit [18].

The dual foci's overlap determines the lateral resolution, and the photoacoustic wave bandwidth determines the axial resolution. Achieving an axial resolution within hundreds of μm and a lateral resolution within tens of μm is the norm. The optical diffusion limit allows for an imaging depth of up to 1 mm, which is the maximum depth at which these resolutions can be achieved.

1.5 Mechanical imaging of cells and tissues

Mechanical imaging and characterization present compelling alternatives to optical imaging. The correlation of cells' elastic properties—such as elasticity, speed of sound, and strain—with essential cellular processes, including mitosis and migration, remains largely unexplored at the sub-cellular level. Consequently, there is a growing interest of research focused on characterizing these properties through standard mechanical testing and developing imaging techniques based on mechanical contrast. For example, the test of detaching or deforming a cell have been measured using techniques such as optical trapping [19] and atomic force microscopy (AFM). Meanwhile, AFM [20], together with Brillouin microscopy [21], also provide ways to perform mechanical imaging of cells.

1.5.1 Optical trapping

Optical Trapping, also known as Optical Tweezers (OT), based on a concept outlined by Arthur Ashkin in 1986 that later earned him the Nobel Prize in Physics [22, 23], is a technique that uses light to hold a particle or an object in place.

The shape of the target can cause the laser beam to scatter when it is aimed at a particle, cell, or other microscopic object. This scattering reflects a shift in the light's momentum, which causes an object to experience force (Newton's third law of motion). The target is trapped in the beam's focal point by this force, giving the microscopist exceptional precision over the target's x, y, and z positions. Figure 1.6 illustrates this idea. Using several beams and adjusting their focus locations allows precise three-dimensional object movement control.

Measuring the mechanical properties of cells through optical trapping is of great interest due to its non-contact nature and capability to adjust force by varying

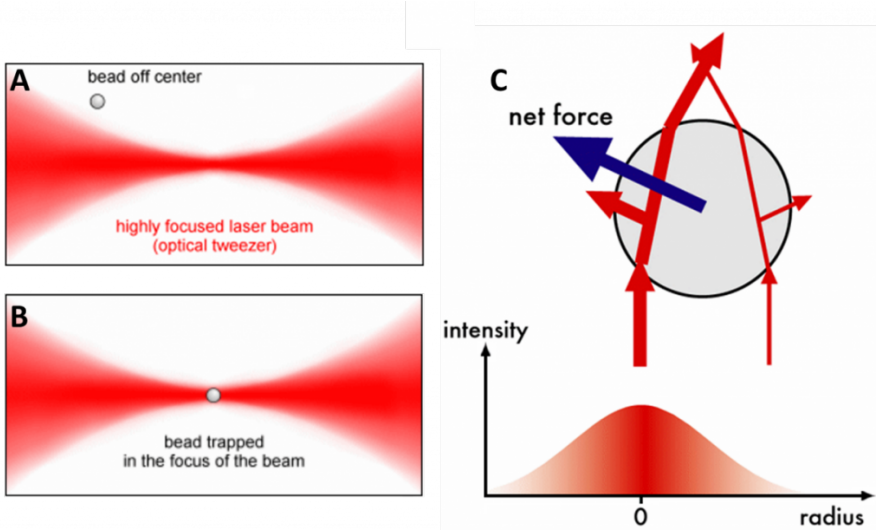

Figure 1.6: The optical trapping mechanisms. (A) A tiny spherical bead in close proximity to a laser with high focus. The bead moves towards the highly focused area of the beam due to the net scattering of light from this laser, as shown in (B, C). The two light rays scattering through the sphere and their motion (red arrows). The bead moves towards the direction of the brightest light when it scatters because of the stronger change in momentum brought about by the brighter light (intensity shown by the chart below). Image reproduced from [24].

laser power. This allows for defined study into the biomechanics of complex yet regular shapes such as cell membrane surfaces.

1.5.2 Atomic force microscopy

Nanoscale imaging is the main application of the AFM microscope, however it can also be used to probe the stiffness of surfaces. The basic working principle has already been discussed in the previous Section 1.3.3: The cantilever has a laser pointed at its rear, which is then detected using the knife-edge method. The cantilever then moves up and down in response to the scanning surface as the tip is scanned. Topology or stiffness can be measured by calculating the optical intensity detected, which is proportionate to the cantilever detection [25].

Elasticity in formation can then be estimated by measuring the forces applied in

all axes to the surface, causing deformations. Employing this approach, it has been discovered that the elastic properties at specific points within cells vary distinctly between healthy and cancerous cells [26]. The pressure exerted by the AFM probe can be invasive to cells, potentially leading to alterations in their morphology or function. Thus to perform imaing of cells using AFM requires special treatments to the sample. For instance, by using a fixing method, researchers managed to image various type of cells including kidney cells, cardiomyocytes and broblasts [27]. However, though with a high resolution, the AFM is still constrained to the vicinities of the surface.

1.5.3 Brillouin microscopy

It's around 100 years anniversary since the discovery by L. Brillouin and L. I. Mandelstam of the scattering of light by an elastic (acoustic) disturbance [28, 29]. Brillouin light scattering (BLS) is the result of an inelastic interaction of light and inhomogeneities (e.g. density fluctuations) within a material. The inhomogeneities giving rise to the scattering are fluctuations in the dielectric or magnetic properties of a material that have the same effective wavelength as the optical wave.

An inelastic scattering event gives rise to either a Stokes shift, where the photon loses momentum to a phonon, or an anti-Stokes shift, where the photon gains momentum from a phonon. Both Brillouin Stokes and anti-Stokes shifts can be measured as Brillouin frequency shifts using a spectrometer or a fast CCD (Figure 1.7). The frequency shift of the scattered photon is related to the mechanical properties (such as sound velocity) and optical properties (such as refractive index) of the sample. One way to understand this process is to consider the sound wave in the material as producing a periodic modulation of the refractive index, which scatters light. Since this modulation propagates at the speed of sound, the

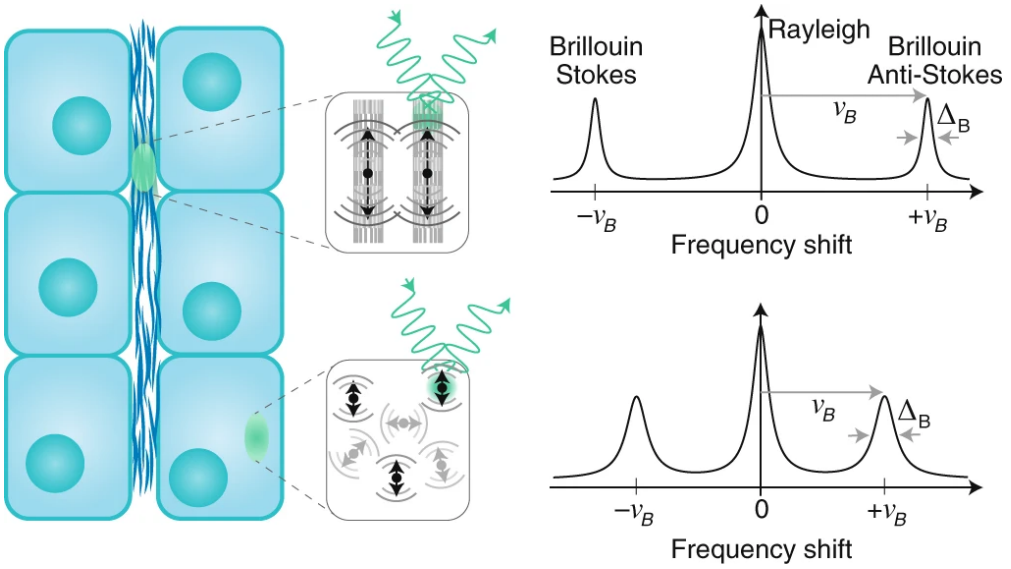

Figure 1.7: Brillouin scattering in heterogeneous biological samples: Acoustic waves propagating in the longitudinal (axial) axes are inelastically scattered from monochromatic laser light. In general, there is a high Brillouin frequency shift when light is scattered off solid materials (like collagen fibres; top). By comparison, the spectrum originating from the liquid-like cytosol (bottom) has a bigger linewidth, indicating a more viscous medium, and a lower shift, suggesting a less rigid material. Image reproduced from [21].

scattered light undergoes a Doppler shift in frequency. Brillouin light scattering measures these GHz fluctuations over a length scale defined axially by the optical wavelength and transversely by the illumination and collection geometries, in conjunction with the phonon propagation length in the medium. The resulting measurement, known as the Brillouin frequency, serves as an indicator of the speed of sound to refractive index ratio in the medium. More simply, it can be interpreted as analogous to an elastic stiffness, where stiffer materials exhibit higher Brillouin frequencies, as shown in Figure 1.7.

This technique provides a non invasive way to measure and image sub-surface mechanical properties of cells with high resolutions. More background will be discussed in the following background chapter (section 2.1.1) with more details.

1.5.4 PLU based microscopy

PLU based microscopy, by using Picosecond laser ultrasound (PLU) based time-resolved Brillouin scattering, offers imaging of opto-acoustic properties with optically limited lateral resolution and axial resolution limited by acoustic wavelength. It uses an ultrashort pulsed laser to generate a coherent strain pulse (coherent phonons) from a thin metal transducer (usually a Ti layer over 100 nm for biological samples), followed by a second laser pulse to detect the strain as it propagates through the sample, which is transparent to the probe laser wavelength. Generating of coherent phonons significantly enhances the scattering efficiency compared to spontaneous Brillouin scattering [30, 31, 32, 33, 34, 35].

The method known as picosecond laser ultrasound (PLU) has long been used to observe ultra-fast acoustic events. PLU is also capable of accessing Brillouin Light Scattering (BLS) by temporally resolving the propagation of a coherent phonon field generated by a laser. Time-Resolved Brillouin Scattering is the term used to describe this process (TRBS). The Doppler shift can typically be neglected in TRBS because the speed of acoustic phonons is too small relative to the speed of light for the Doppler effect to produce significant measurable shifts in the optical signal, allowing it to be safely ignored in time-resolved Brillouin scattering experiments.

Researchers also use picosecond acoustic interferometry and time-domain Brillouin scattering to refer this process. The wavelength of the TRBS signals is less than that of visible light, and they are usually in the GHz frequency range. This offers a chance to image with contrast related to elasticity, with the assumption that for a biological sample in which refractive index and photoelastic coefficient are considered not to vary much between different part of a cell, maybe leading to sub-optical acoustic resolution imaging.

Phonon microscopy

With special designed thin film transducer and experimental configurations, Phonon microscopy - one of the PLU based microscopy - has been proven to produce 3D images of biological cells in culture medium with sub-micron resolution, with phonon resolution in the axial direction [36, 37, 38]. The lateral resolution is currently constrained by the optical system used to perform the measurements. This limitation forms the basis of this thesis, which aims to enhance the lateral resolution of existing Phonon microscopy techniques. More detailed background and theory of Phonon microscopy will be discussed in following background Section 2.2.1.

PLU based microscopy powered new insights into cell biology

A range of time resolved Brillouin scattering (TRBS) based technologies, including Phonon microscopy, provide the ability to measure and image subcellular mechanical properties inside both plants and animal cells that were previously not accessible with conventional methods, and provide new approaches to answer more challenging cell biology questions. 3D imaging of single cell or subcellular structures of bovine aortic endothelial cells, fat cells and 3T3 fibroblast cells have been reported [32, 39] with both single-layer metallic transducer design and Fabry-Perot cavity transducer design. Also, a study [40] looking at a mitotic macrophage-like cell demonstrated that combined measurement of both the hypersound propagation inside a cell, and of the hypersound reflection at the metal/cell adhesion interface, give access to the Brillouin frequency, cell thickness, interfacial stiffness and cell mass density for multiple imaging in a single run of experiment [40].

1.6 Focusing of acoustic fields

Focusing the acoustic energy produced by piezoelectric transducers (PTs) or optoacoustic transducers into a particular region is crucial for both industry and medical research. Research on acoustic focusing has led to various applications such as non-destructive testing techniques and many medical related therapeutic techniques [41]. Ultrasound waves excited by curved PTs are capable of transmitting and focusing energy inside a body for medical purposes such as diagnostic sonography. Meanwhile, optoacoustic transducers also have great application in field like photoacoustics, allowing higher imaging resolution. Apart from single element transducers, focusing of acoustic fields can also be achieved by using a electrical array, thus with more precise control of the source field and also achieve more complicated focusing effect, such as multi foci.

1.6.1 Geometric focusing and acoustic lenses

Using an acoustic lens or focusing geometrically using a concave transducer are the two most basic ways to create focus. When the transducer is powered for geometric focusing, the transducer surface is configured so that each point on the surface is the same distance from a desired focal point. This produces substantial constructive interference at that location (Figure 1.8 (a) [42]). For a lens, a flat transducer surface is attached to a shaped profile that has a sound speed that varies from the coupled medium. A single point of focus for the sound is achieved by varying the thickness of the lens throughout the surface (Figure 1.8 (b) [43]). The benefit of both approaches is that just one driving signal is required. However, it is not feasible to generalize to multiple foci or random fields due to the fixed focal position.

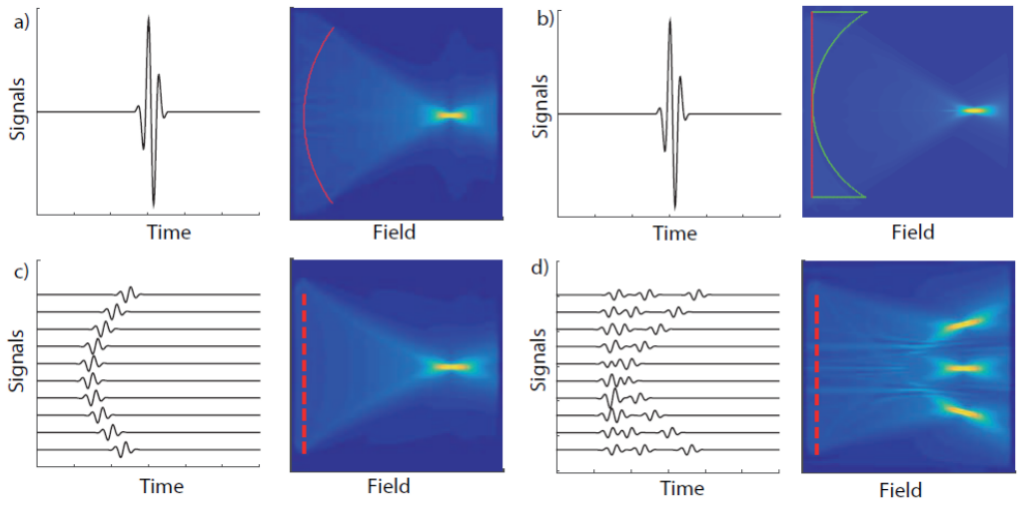

Figure 1.8: Illustrations of different types of focusing: (a) Geometric focusing, (b) By using an acoustic lens, (c) Electronic focusing, and (d) Electronic focusing for multiple foci. For the acoustic lens (b), the green line indicates the physical structure of the lens. Image reproduced from [42, 43, 44].

1.6.2 Electronic focusing with phased array

Using a transducer array and electrical focussing is a more flexible method. This is comparable to geometric focusing, with the exception that the driving signal to each array element is delayed such that the signals they produce arrive at a target focused point simultaneously, rather than physically shaping the source or using a lens. As a result, a focus is created and constructive interference is produced (Figure 1.8 (c)) [44]. One benefit of electronic focusing is the ability to flexibly steer the focal position axially and laterally by adjusting the electrical delays. By adding the driving signals for each focus, it is also possible to generalise it to the simultaneous creation of many foci (Figure 1.8 (d)).

1.6.3 Photoacoustic transducers for novel applications

Photoacoustic films are used to make multiple types of transducers depending on applications (Figure 1.9). The most common type of transmitters are planar

ones, which are made of a transparent glass substrate with a thin layer of photoacoustic coating on top (see Figure 1.9 (a)), because of the ease of fabrication. Focusing transmitters made of a photoacoustic film coated on a transparent concave substrate can generate high-amplitude photoacoustic pulses (Figure 1.9 (b)) [45, 46, 47]. The working frequency for [45] shows a lens with designed frequency of 15 MHz and a lens profile diameter of 6 mm. Compared to planar transducers, produced photoacoustic pulses from the concave surface in these focused transducers are concentrated on the focus, or the radius-of-curvature of the concave surface, and have very high pressure amplitudes [48].

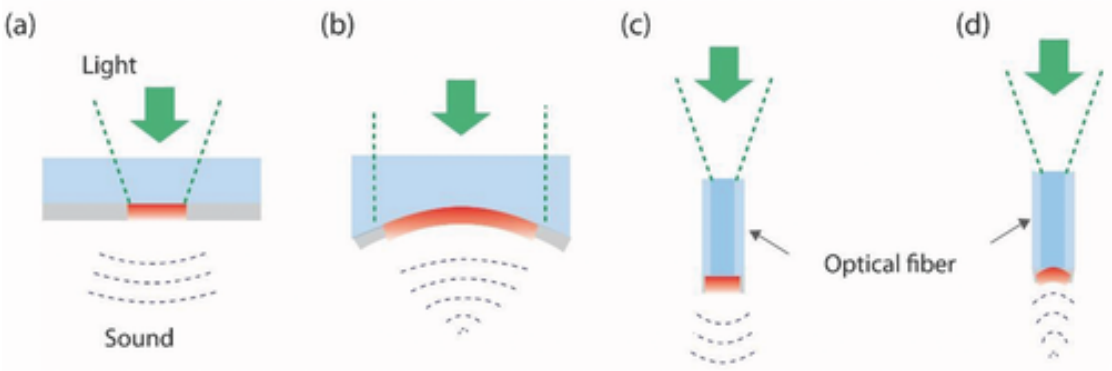

Figure 1.9: Photoacoustic transducers. (a) A planar transducers consisting of a thin photoacoustic layer on top of a transparent substrate. (b) Focused transducers composed of a thin photoacoustic layer coated on a transparent concave substrate. (c) Planar fibre-optic photoacoustic transducers with a photoacoustic coating on the tip of an optical fibre. (d) Focused fibre-optic photoacoustic transducers having a photoacoustic layer coated on the curved transparent surface attached to the tip of an optical fibre. Image reproduced from [48].

One can realise a highly miniaturised flexible photoacoustic transmitter thanks to recently developed nanocomposites' efficient photoacoustic generation. This is because high-amplitude photoacoustic signals can be obtained with a small area of photoacoustic composites, such as a composite on an optical fibre (diameters smaller than 1 mm) (Figure 1.9 (c)). Such miniaturized photoacoustic transducer is desirable for imaging and therapeutic applications, e.g., minimally invasive sensing applications or endoscope applications. One can integrate optical fibre-based

transmitters with a focusing scheme (Figure 1.9 (d)) [48].

Given the success of optoacoustic lenses operating in the MHz range, it is a natural progression to investigate whether these structures can function effectively at GHz frequencies. However, at such high frequencies, Photoacoustic (PA) signals attenuate rapidly, necessitating the use of alternative techniques. Picosecond Laser Ultrasound (PLU) operates within this GHz range.

To generate GHz $\sim$ THz, ultrafast laser pulses are used. Multiple microscopic mechanisms are involved in the photo-generation processes of GHz to THz CAPs. Deformation potential (DP) mechanism, the thermoelasticity (TE), the inverse piezoelectric effect (PE) and the electrostriction all contributed in the photo-generation process of sound [49]. The thermoelasticity generation is of the great interests in this thesis, more details will be discussed in the following background section 2.2.3. If GHz optoacoustic lenses can be effectively implemented, they have the potential to enhance the lateral resolution of PLU systems, which are currently limited by the capabilities of the optical system.

1.7 Discussion and Device concept

Even though acoustics has been used for a long time to see and find things millimetres or larger, it has a lot of potential for very high resolution imaging at the microscopic or even nanoscopic level. In most common materials, from metals to soft biological tissue, the speed of sound is five orders of magnitude slower than the speed of light. This means that sound waves carry a lot less energy. When short wavelengths are needed for high resolution imaging, this is especially important. In optics, this problem causes the well-known effects of biological phototoxicity, especially for wavelengths in the near ultraviolet (NUV) or shorter part of the

electromagnetic spectrum. It has also led to a wave of fluorescent label-based super resolution imaging techniques, which we talked about in the introduction. In acoustics, on the other hand, it has been very hard to make and find sound waves with wavelengths (and therefore resolution) that are the same as NUV photons. A lot of different piezoelectric and photoacoustic techniques have been created over the years that easily show how acoustic focusing works, even though they only work at frequencies of a few megahertz, which means that the spatial resolution is only $\sim$ 1 mm.

Sound waves and high frequency piezoelectric transducers were used in scanning acoustic microscopy (SAM), which made it possible to take pictures with a high level of detail and showed that the method worked on different types of cells. There were, however, some problems with this collection of techniques. First, acoustic wavelengths can be shortened to $\sim$ 100 nm by using piezoelectric transducers with higher frequencies, such as those in the GHz range. Wavelength and resolution decrease as frequency (f) increases, but attenuation of waves in watery tissue increase with f^2, which means that there are too many losses and the acoustic path lengths are too short. To get around this, lower frequency transducers (e.g., $\sim$ 100 MHz) can be used if the sample's sound velocity is slowed down. This can be done by freezing the specimen, which limits the technique's use in biology (more details about sound focusing in SAM will be discussed in the Background chapter 2.3.1).

New developments in optically-driven acoustic methods, like photoacoustics and laser ultrasound, have helped solve some of SAM's earlier problems. Photoacoustic generation of sound waves makes it much easier to design and build transducers because photoacoustic transmitters don't need to be connected to electricity and are more resistant to optical excitation than their fragile piezoelectric counterparts. These improvements have sparked new interest in making acoustics with

wavelengths below a micron. However, this method had problems with mechanical instability and a low signal-to-noise ratio. This was partly because the acoustic field attenuates as it moves towards and away from the object being imaged, resulting in a low amplitude.

Time resolved Brillouin scattering (TRBS) is a method that uses inelastic light scattering to beat the attenuation of SAM-based methods by a factor of two. In TRBS, an acoustic field that moves directly through the material causes a change in the refractive index, which scatters light in the form of a probe laser beam. This means that GHz frequency phonons can be detected without touching anything and without the need for long path length pulse-echo setup. This helps to lessen the effects of acoustic attenuation in some ways and opens the possibility of 3D imaging. In microscopy, TRBS has been used to show label-free high contrast mechanical imaging over a variety of biological and solid-state samples.

The research presented in the thesis focuses on addressing the critical challenge of optical diffraction in time-resolved Brillouin scattering (TRBS) techniques by innovating the design and implementation of nano- and micro-scale optoacoustic lenses. These lenses, as shown in Figure 1.10), including flat Fresnel zone plates and concave structures, are engineered to enhance the lateral resolution by focusing the coherent phonon fields generated by ultra-short laser pulses in TRBS systems beyond the constraints imposed by optical diffraction limits.

This work lays the foundation for sub-optical 3D mechanical imaging, which promises to significantly elevate the lateral resolution capabilities of Phonon Microscopy, providing a label-free, biocompatible imaging tool that may revolutionize our understanding of cell biology and disease pathology.

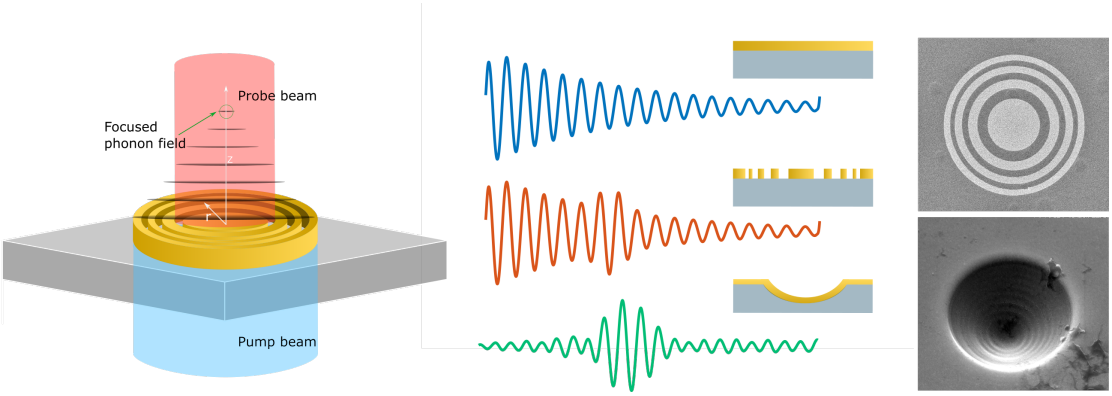

Figure 1.10: Basic device concept: multiple geomatical design over glass substrate, including transducer with flat, Fresnel zone plate design and concave structures.

Chapter 2

Background & Modelling

The initial sections delve into Brillouin scattering, laying the groundwork for its theory and practical use in microscopy. The narrative then transitions to the convergence of acoustics and optics through picosecond laser ultrasound, covering aspects such as optical modelling, sound generation and propagation, and the optical detection of Time-Resolved Brillouin Scattering (TRBS). Moreover, the chapter discusses enhancing TRBS imaging with picosecond laser ultrasound techniques.

Subsequent sections focus on the mechanisms of light and sound focusing, detailing the use of Fresnel zone plates and concave lenses for directing waves. The challenges associated with other acoustic-based imaging techniques are thoroughly examined. Further analysis introduces the Fourier-Bessel angular spectrum method (FBASM), showcasing the model setup and techniques for radial propagation.

The chapter also delves into nano-fabrication techniques pivotal to these explorations, highlighting electron beam lithography and focused ion beam methods as critical for crafting structures that enable sophisticated control of sound waves.

2.1 Brillouin scattering

Brillouin light scattering (BLS) is the result of an inelastic interaction of light and inhomogeneities (e.g. density fluctuations, thermally excited ultrasonic waves) within a material. The first experimental observations were published by Leon Brillouin in 1922 [28] and Leonid Mandelstam in 1926 [29].

As mentioned in Section 1.5.3, Brillouin scattering occurs when the propagating is scattered in a translucent solid or liquid media. The scattered light beam experiences a frequency shift due to the movements of scattering element (e.g. thermally excited ultrasonic waves - thermal phonons).

Two ways are commonly used to measure the Brillouin shift: spectrometry (Section 1.5.3) or time resolved PLU measurements (Section 2.2). The scattered light beam interferes with the reference beam in the PLU method. Brillouin oscillations, a term used to describe the intensity modulation produced by this interference, are resolved in time. And the Brillouin frequency f_B can be calculated using Fourier transform.

2.1.1 Brillouin microscopy

The advent of non-scanning high-resolution optical spectrometers has facilitated the establishment of the field of Brillouin microscopy and imaging about 20 years ago [50]. The need for label-free, contact-free techniques to assess the mechanical characteristics of biomaterials at the cellular and subcellular levels is driving advancements in Brillouin microscopy. Figuring out the local biomechanics of cells and tissues makes it possible to guess what will happen to cells and how tissues will get sick.

Brillouin microscopy relies on a process of inelastic scattering in which light interacts with GHz acoustic waves at the frequency f_B - named as the Brillouin light scattering (BLS). The measured shift is dependent on the speed of sound and the materials' refractive index n (see equation 2.7).

Since the Brillouin scattering can only be observed on a transparent material, which makes it very useful for studying polymers [51], semiconductors [52], and biological tissue. This method has been used to gauge the sound speed of bone [53], muscle [54], and eye tissue [55]. Among other things, it has been utilised to image ex vivo biological cells [56] and the eye in vivo [57].

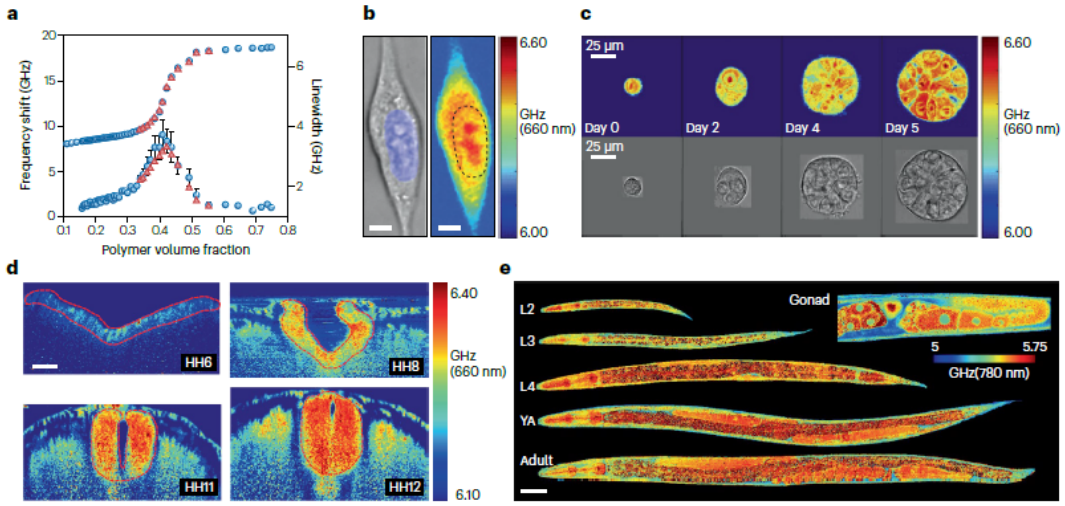

Figure 2.1: Brillouin technology generated representative data: (a) f_B and its linewidth of gelatine versus polymer volume fraction. The theoretical values obtained from the viscoelastic fit are represented by red triangles. (b) A live 3T3 cell Brillouin microscopy image. The cellular nucleus is indicated by a dashed line and a blue shadow, scale bar is 5 mum. (c), Brillouin images of a single cell and three spheroids at different stages of growth (human breast cancer line MCF10CA1h), scale bar is 25 μm. (d) Cranial neural tube tissue of four embryos at different culturing stages. The neural plate region is delineated by a red dashed line, scale bar is 50 μm. (e) live nematodes at three larval stages (L2–L4) and two adult stages, scale bar is 50 μm. The gonad is shown in magnified detail in the insert, scale bar is 25 μm. Image taken from [50]

More recently, more to cell imaging as shown in Figure 2.1 (b), faster and better SNR enables the "real-time" checking of samples, as shown in (c) - (e): (c) shows

one cell and three spheroids at different stages of growth, (c) shows the frontal neural tube tissue of four embryos at different stages of growth, (d) are Brillouin pictures of live worms at three stages of development (L2–L4) and two stages of development (A and B) [50].

2.2 Picosecond laser ultrasound

Any innovative method that can yield more information is highly desirable given the interest in cell research. Non-invasive imaging techniques are more pertinent since they enable the study of cells in a living environment. Some drawbacks from both the acoustic and Brillouin microscopy can be addressed by a technique named time resolved Brillouin scattering (TRBS) based on picosecond laser ultrasound (PLU) and Brillouin scattering. This is an all optical method that uses the pump-probe technique [58] to generate GHz ultrasound and detect using Brillouin scattering. The scattering efficiency is significantly increased, usually four to six orders of magnitude greater than that of Brillouin microscopy, by producing a coherent acoustic pulse. Brillouin oscillations can also be resolved in-depth with acoustic wavelength because PLU is a time-resolved technique. But at this point, optical diffraction still limits the lateral resolution, necessitating the use of transducers. This thesis aims to address this issue.

Picosecond/femtosecond light pulses' absorption by a medium has the ability to create acoustic waves (coherent phonon field) in the gigahertz to terahertz range. These propagation waves can be tracked using appropriately synchronized light pulses. This technique, referred to as picosecond laser ultrasonics, offers a viable tool for investigating the physical attributes of structures at the micron, or even nanoscale.

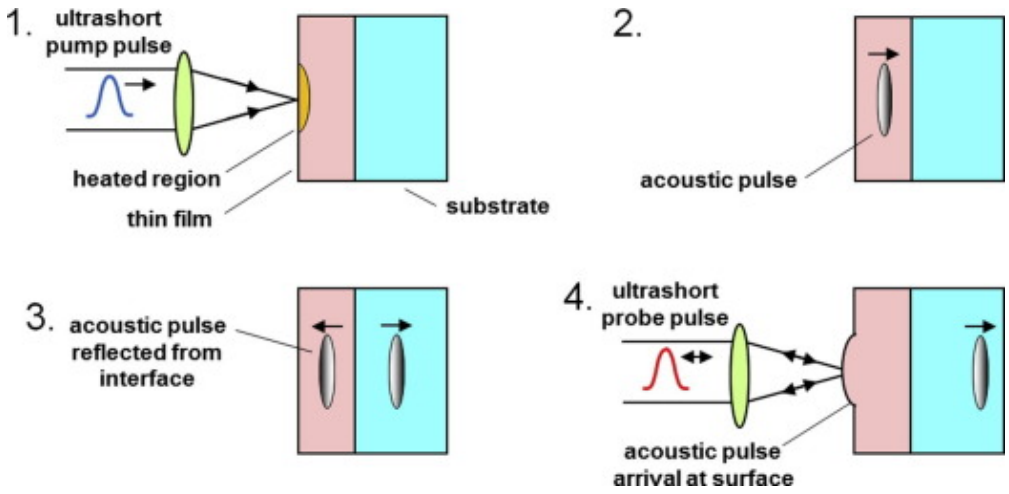

Figure 2.2: Sequence of events in picosecond laser ultrasonics. Image taken from [59]

Photoacoustics and laser ultrasound share the same basic excitation mechanism for a given material: (1) optical absorption, (2) heat generation, (3) thermal expansion and contraction, (4) which launches acoustic waves into the surrounding environment. At depths of typically nm to μm, subsurface structures or inhomogeneous regions beneath the surface have the ability to reflect back the acoustic pulse to the surface. Figure 2.2 provides a schematic representation of this using an opaque thin-film on a substrate as an example.

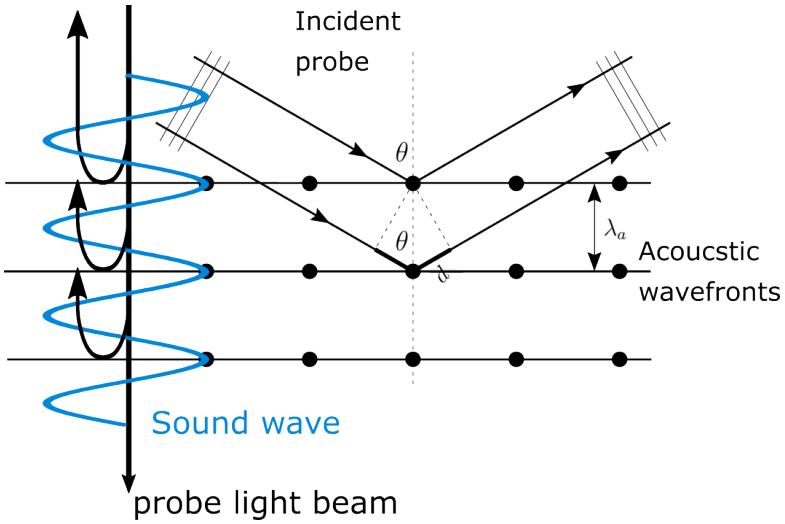

Figure 2.3: Bragg's law applied to the Brillouin scattering interactions.

In the strain regions with wavelength λ_a, the acousto-optic effect of an acoustic

wave produces a grating, the optical field will scatter at successive positions of the acoustic wavefront (see Figure 2.3). Therefore, just as with diffraction gratings, the relationship between the acoustic phase and the optical phase will determine whether the scattered optical wavefronts either constructively or destructively interfere. In order for constructive interference to occur, a photon that scatters from the first acoustic wavefront must have an $N2\pi$ (integer value N) phase difference with a photon that scatters from the second acoustic wavefront. Consequently photon 2 travels an additional distance L (2d) compared with photon 1, which is related to the acoustic wavelength λ_a by:

$$L = 2\lambda_a \cos\theta \tag{2.1}$$

This requires that photon 2 acquires an additional phase that is an integer multiple of 2π:

$$\Delta\phi = nkL = [nk2\lambda_a \cos\theta = N2\pi] \tag{2.2}$$

where k is optical wave factor and θ is the angle of incidence of the optical field with respect to the acoustic field. It is an expression of Bragg's law, which was originally derived for predicting X-ray diffraction patterns. By simplifying the terms in the brackets in Equation 2.2 with the following probe light wave equation:

$$k = \frac{2\pi}{\lambda_{\text{probe}}} \tag{2.3}$$

Bragg's law can be alternatively expressed as:

$$\lambda_a = \frac{\lambda_{\text{probe}}}{2n\cos\theta} \tag{2.4}$$

where λ_{probe} is the optical probing wavelength and for the case of the fundamental diffraction order (N = 1). Also by knowing the relationship between the Brillouin frequency, acoustic wave travelling with velocity v and the acoustic wavelength:

$$\lambda_a = \frac{v}{f_B} \tag{2.5}$$

the phase matching condition for Brillouin scattering between the optical and acoustic fields can be written:

$$f_B = \frac{2nv}{\lambda_{\text{probe}}}\cos\theta \tag{2.6}$$

For the special case of normal incidence, the expression reduces to:

$$f_B = \frac{2nv}{\lambda_{\text{probe}}} \tag{2.7}$$

which relates the optical frequency shift to the optical wavelength and the material properties refractive index and sound velocity. Given a coherent monochromatic light source in the NUV-NIR range, and a typical biological material (e.g. $n \approx 1.33$ and $v \approx 1500$ m/s), the Brillouin shift and associated acoustic waves will be in the GHz frequency range. Equation 2.6 serves as the central design equation for any optical system that seeks to measure Brillouin scattering. It shows that by choosing the optical probe wavelength, the incidence angle of the probe beam, and a material with properties $[n, v]$, that the system will be able to measure inelastic

photons that have shifted by f_B.

2.2.1 PLU based TRBS imaging

The scattering efficiency in Brillouin microscopy is very low, in about the range of $\sim 10^{-9} - 10^{-12}$. This is because only a few of the spontaneously generated vibrations have the appropriate direction and frequency to be able to scatter with a particular probing wavelength into the detector [25]. This means that when a higher SNR is needed for imaging, large average power and long integration times must be used. However, if a coherent acoustic field with the appropriate direction and frequency is generated instead of depending on spontaneously generated vibrations, it will result in an increase in the amount of scattered light. This is made possible by PLU and the pump-probe laser configuration. When the pump pulse hits a metal film, it makes a strain pulse that moves across the film in a way that is not parallel to the visual axis but perpendicular to the metal layer's plane. Part of the probe pulse is scattered from the coherent sound field when it gets there. The rest of the beam is reflected in the transducer and interferes with the light that has been scattered so that Brillouin oscillations can be seen.

When the material's refractive index n is known, using PLU to measure the speed of sound in translucent samples can be done directly. Similarly, if the density is known, the elastic modulus can be determined. If the refractive index and Brillouin frequency are examined concurrently, there is a significant opportunity for quantitative measurements. Previously measurements have been reported over polymer shells [60], semiconductors [61], dielectrics [62] and fixed biological cells.

In the early 2000s, sub-cellular scale single-point TRBS measurements were carried out for the first time [63]. This was accomplished by placing onion cells on top of a bulk titanium substrate that served as an optoacoustic transducer [64].

The pump and probe pulses were directed through the top of the cell using a high NA objective lens, which produced a $\sim 1\ \mu m$ diameter spot for the thermoelastic generation process and high spatial resolution. Since the probe field will experience maximum modulation where the strain amplitude per unit volume is maximised, the degree of overlap between the pump and probe spots overlap is critical [65]. The microscope's axial spatial resolution was adequate for measuring TRBS in subcellular elements like the nucleus and vacuole. The first 1D scanning of Brillouin frequency across onion cells was motivated by these preliminary experiments, which suggested that TRBS could measure properties of biological media related to viscoelastic behaviour [64].

As instrumentation continued to improve, the first images of cells using PLU soon followed [31, 32]. The first most widespread transducer design is a single metal-layer typically fabricated of Ti and with thickness > 100 nm [30]. The transducer is usually fabricated onto a sapphire substrate, which along with the transducer thickness, is meant to optimise thermal conduction following the pump-induced heat rise. The pump beam is illuminated from the beneath the substrate/transducer and the specimen sit on top as shown in Figure 2.4 (a). Due to the thickness of the transducer, the pump is absorbed within the first ten's of nanometres of the layer and generates a broadband phonon field with frequencies up to ~ 100 GHz. This broadband packet then travels from the bottom of the transducer to the top interface with the cell where it reflects and transmits into the specimen. In this case, the probe is delivered from the top, made it go through the specimen first.

Imaging is performed by measuring the TRBS signal at a single position in the cell, which is then scanned in x and y. Elasticity-related properties such as the Brillouin frequency are attained by Fourier transforming the time-domain signal into the frequency domain - then plotting all the pixels creating a 2D Brillouin frequency map. Figure 2.4 (c)-(e) are some examples showing the imaging capa-

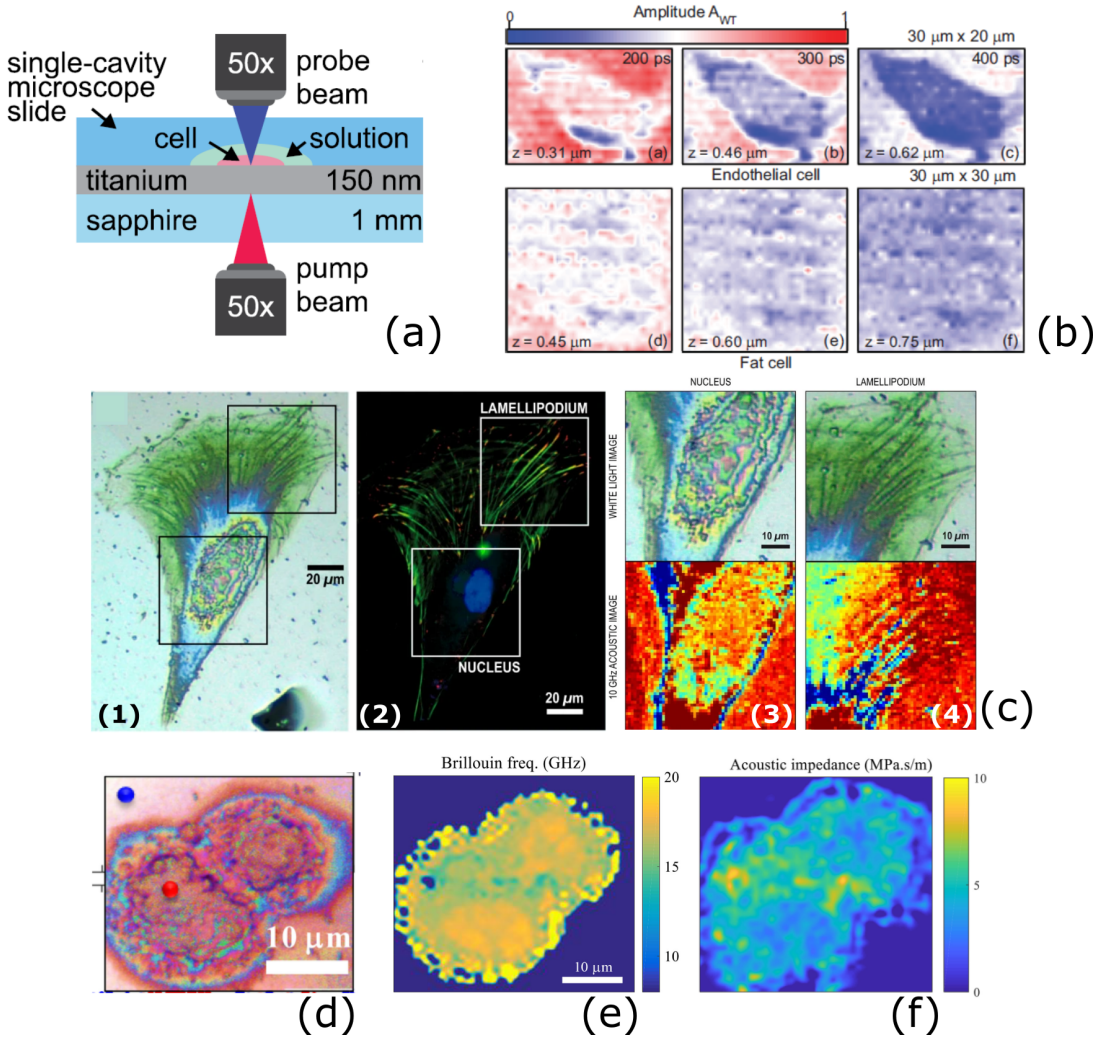

Figure 2.4: Recently reported cell images using PLU. (a) One popular PLU configuration. (b) Amplitude of the Brillouin oscillation signal on two different cells Image reproduced from [32]. (c) (1) white-light image of a hMSC.(2) Fluorescent image displaying the nucleus (blue), actin (green), and vinculin (red). Squares represent areas that have been scanned using iPOM, scale bar is 20 μm (3) Optical (top) and the acoustic (bottom) image of the nuclear region. (4) Optical (top) and the acoustic (bottom) image of the lamellipodium. The acoustic images were taken at 10 GHz, and the scale bar is 10 μm. Image reproduced from [31]. (d) The optical image shows a typical early telophase orlate anaphase nuclear morphology of bi-lobed structure, a single nucleus dividing into two daughter cells of approximately 15 μm in diameter. (e) Map of Brillouin frequency. (f) The acoustic impedance map at the Brillouin frequencies. Image reproduced from [40]

bilities of TRBS based techniques. These results, which display the contrast of the cell's internal features, have promising potential imaging capabilities of PLU-based TRBS imaging.

Phonon microscopy

State of the art transducer design for PLU-based imaging was limited to single (quasi-bulk) layers of metal until the emergence of new design of transducer which focuses on TRBS imaging and enables imaging of live cells, the technique, is named as Phonon Microscopy.

Phonon Microscopy uses a transducer design consists of three thin film layers, which are Au, ITO (indium tin oxide) and Au as shown in Figure 2.5 [66]. The three layers form a Fabry-Perot cavity which can be designed to have a particular optical transmittance and reflectance that depends on the cavity size (dielectric thickness H_{ITO} and metal thickness H_{Au}) and the optical wavelength [25]. From the optical transmission model described in Section 2.2.2, the transmission and reflection versus ITO thickness (H_{ITO}) for fixed Au layer thicknesses and wavelength can be calculated as shown in Figure 2.5 (b) and (c).

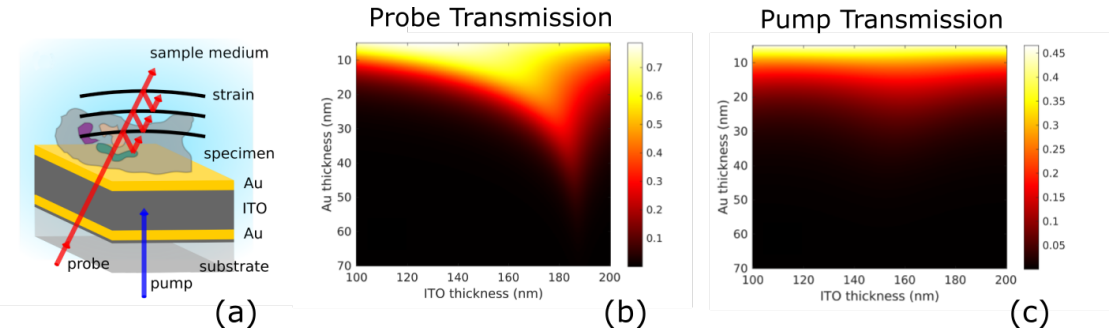

Figure 2.5: Device concept for the OAT in Phonon Microscopy. (a) The OAT geometry is a nanometric Fabry Perot cavity consisting of two gold partial mirrors spaced by the transparent material ITO. Both the pump and probe wavelengths are incident from beneath the transducer. (b) Transmission spectra for pump (NUV light). (c) Transmission spectra for probe (NIR light). Due to the partial transparency of the cavity the probe beam is capable of performing TRBS and is collected for detection above the specimen in this case. Image reproduced from [67].

By carefully designing the thicknesses of the Au and ITO layers, the degree of optical interference within the cavity can be controlled, this results in specific

wavelengths resonating in the cavity leading to strong transmission and reflection characteristics. Then we can achieve different design purpose for better cell imaging capabilities, such as: maximise transmission of the NIR probe wavelength, minimise the transmission of the phototoxic NUV pump to protect cell structure and ensure high amplitude strain pulses generated.

Phonon microscopy was among the first techniques to report the successful imaging of biological cells (3T3 fibroblasts) using PLU [36]. Compared with competing TRBS-imaging techniques, the cavity produces heat at a much lower rate than single Ti-layer transducers where NUV is delivered through the cell, and similar heating characteristics to techniques where only NIR is delivered through cell. It is also the first TRBS transducer technology to image living cells. Besides, it was shown that the instantaneous Brillouin frequency along the signal time-of-flight could be used to z-section the specimen with using sub-optical wavelength phonons.

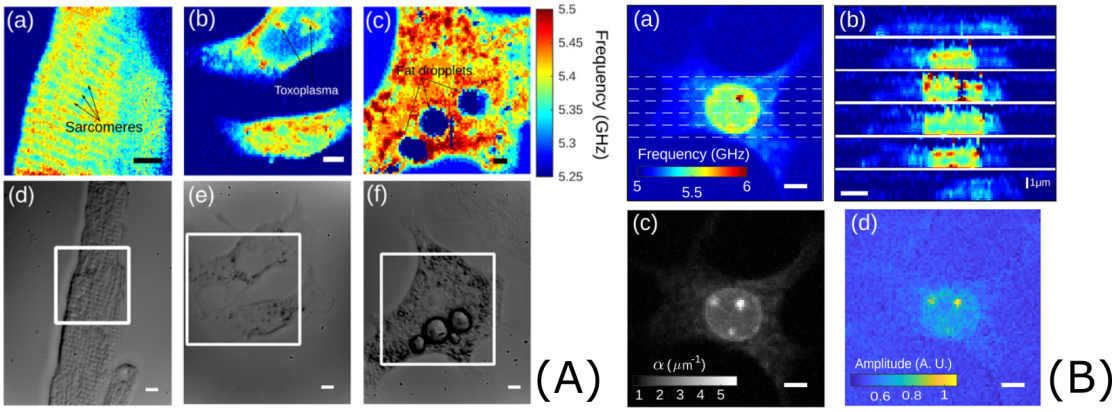

Figure 2.6: (A) Phonon microscopy applied to cardiac muscle cells (a,d), Toxoplasma gondii cellular infection (b,e), and stem cell differentiation into adipos cells (c,f). (B) Reconstruction of time-resolved data of a 3T3 fibroblast cell using Phonon microscopy. (a) is the averaged f_B map. (b) Wavelet analysis in the time domain was used to obtain the XZ cross sections extracted from (a), which are shown by the dashed white lines. (c) Sound attenuation coefficient map. (d) Sound amplitude map at t=0, scale bar is 5 μm. Image reproduced from [68].

Though PLU-based TRBS imaging techniques are relatively young with the earli-

est proof of concept being first demonstrated in 2015, applications of the technology to many different types of cells have been done, including human mesenchymal stem [31], osteoblastic, osteosarcoma, cardiac, 3T3 fibroblast [36], adipose [37], Toxoplasma-infected cells, HeLa, Acanthamoeba castellani [69], and PC12 (neuron-like) [34]. Some of the result figures are shown in Figure 2.6. By only extracting the Brillouin frequency signal, three key cell types with great applications in healthcare and biology are shown in set (A), though the interpretation of the data is still challenging. Clearly imaging of sarcomeres is shown in (a) and (d), a structure of fibres that muscle cell contains, gives measurement of elastic behaviour, and thus might provide useful insights into both heart normophysiology and heart disease. (b) and (e) show a cell infected with Toxoplasma gondii: a cell-infecting parasite. (c) and (f) show a stem cell differentiating into an adipose cell. Many of these experiments have quantified novel elastic signatures of the nuclear mechanical network [70] or the process of encystation [69].

More worth noting here is that phonon imaging can also be achieved in 3D using a fibre probe as shown in Figure 2.7. The fundamental working principle is similar to Phonon microscopy, however, instead of the specimen sitting on a transducer, a phonon probe is used to inject coherent acoustic phonons (CAPs) into a sample and, using the optical Brillouin scattering effect, to measure the specimen's vibrational response, with all these procedures done using a 125 μm single mode fibre with a 5 μm core with an optoacoustic transducer sputtered on the tip.

One of the main challenges that faces PLU-based cell imaging is increasing the acquisition speed of the instrumentation to allow real-time operation. Besides, despite the true acoustic resolution resolved in time, the lateral resolution still remain limited by the optics used to take the measurements, which is also the main challenge this thesis trying to accomplish.

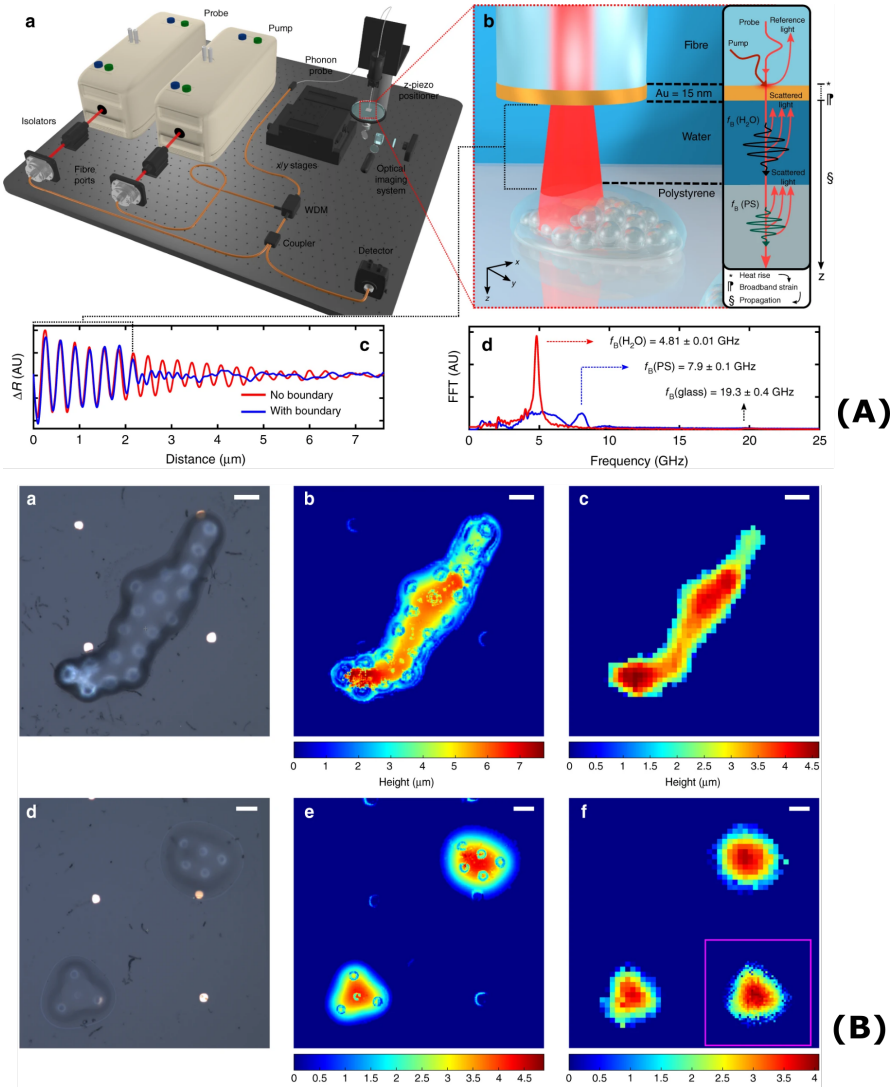

Figure 2.7: Device concept, imaging and profilometry capabilities of fibre based phonon microscopy. (A) Device concept. (a) & (b) show the experimental layout of the phonon probe system. (c), (d) are measured TRBS signals and their FFT, the transition in materials is observed. (B) (a) & (d) Optical bright-field images of the scanned sample - Polystyrene microstructures. (b) & (e) Complete height of the microstructures can be seen via optical profilometry, although there are artefacts because of the objects' optical inhomogeneity. (c) & (f) 3D reconstruction of height for picosecond ultrasonic profilometry using the phonon probe. Image reproduced from [71].

To address this challenge, this thesis proposes making nano/micron-scale optoacoustic lenses to focus coherent phonon fields and thus overcome the lateral resolution limitation. To fabricate these nano/micron-scale structures, multiple nanofabrication techniques, including two-photon polymerization (TPP), nanoimprint

lithography (NIL), electron beam lithography (EBL), and focused ion beam (FIB), are reviewed and selected for fabrication purposes based on this thesis in the following Section 2.5.

2.2.2 Optical modelling

This section aims to find a solution for the electric field in an arbitrary transducer-structure surrounded by arbitrary media at every point in one-dimensional. The generation of elastic waves can be determined by modelling the transducer's optical absorption (Section 2.2.3), which can be done once the system's fields have been established. Additionally, the optical detection system can be propagated through the system in time by solving for the electric fields throughout space. The elastic behaviour of the material will be transduced into the optical detection system as this probe beam encounters modulations to the optical properties of the structures (Section 2.2.4). These principles will specify how the device (conventional flat optoacoustic transducers) this thesis suggests works, enabling simulation and optimisation of its performance discussed in Section 3.1.1.

With complex exponential with amplitude E_0 that oscillates in space (e.g. z) and time (t), monochromatic plane electromagnetic waves of frequency ω can be written in complex notation in the following form:

$$\mathbf{E} = \mathbf{E}_0 e^{i(kz \pm \omega t)} \tag{2.8}$$

As an incident optical wave (E_i) encounters a change in dielectric (non-magnetic) material (from material 1 to 2) as shown in Figure 2.8, part of the field will reflect (E_r) and part will transmit (E_t). According to the Fresnel equations [72, 73], when an incident field is polarised tangentially (s-polarized) to the plane of incidence and

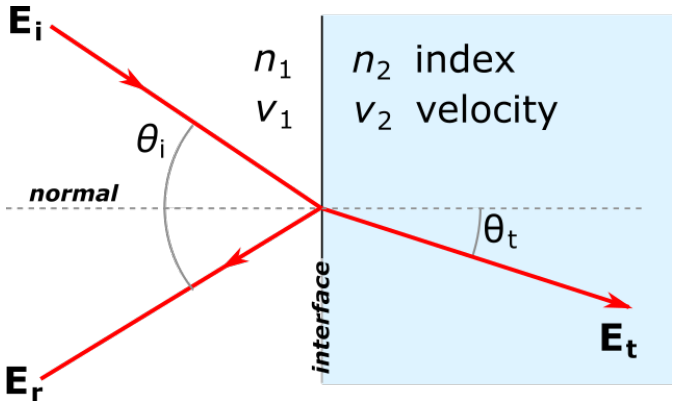

Figure 2.8: Reflection and transmission of an electromagnetic wave at an interface of two materials with different refractive index.

encounters a boundary, the ratios of the amplitude of the reflected and transmitted wave with respect to the incident one are given as:

$$r_s = \frac{\mathbf{E}_{0r}}{\mathbf{E}_{0i}} = \frac{n_1 \cos\theta_i - n_2 \cos\theta_t}{n_1 \cos\theta_i + n_2 \cos\theta_t} \tag{2.9}$$

$$t_s = \frac{\mathbf{E}_{0t}}{\mathbf{E}_{0i}} = \frac{2n_1 \cos\theta_i}{n_1 \cos\theta_i + n_2 \cos\theta_t} \tag{2.10}$$

Similarly, the ratios for fields that are polarised in parallel with the plane of incidence (p-polarization) are given as:

$$r_p = \frac{\mathbf{E}_{0r}}{\mathbf{E}_{0i}} = \frac{n_2 \cos\theta_i - n_1 \cos\theta_t}{n_1 \cos\theta_t + n_2 \cos\theta_i} \tag{2.11}$$

$$t_p = \frac{\mathbf{E}_{0t}}{\mathbf{E}_{0i}} = \frac{2n_1 \cos\theta_i}{n_1 \cos\theta_t + n_2 \cos\theta_i} \tag{2.12}$$

For the purpose of solving a one dimensional problem, with $\cos\theta_i = \cos\theta_t = 1$, the ratios of the incident and reflected/transmitted field amplitudes can be found

as:

$$r_s = \frac{\mathbf{E}_{0r}}{\mathbf{E}_{0i}} = \frac{n_1 - n_2}{n_1 + n_2} \tag{2.13}$$

$$r_t = \frac{\mathbf{E}_{0t}}{\mathbf{E}_{0i}} = \frac{2n_1}{n_1 + n_2} \tag{2.14}$$

$$r_p = \frac{\mathbf{E}_{0r}}{\mathbf{E}_{0i}} = \frac{n_2 - n_1}{n_1 + n_2} \tag{2.15}$$

$$r_p = \frac{\mathbf{E}_{0t}}{\mathbf{E}_{0i}} = \frac{2n_1}{n_1 + n_2} \tag{2.16}$$

Then using the transfer matrix method (TMM) as shown in Figure 2.9 and the knowing Fresnel coefficients, we can now construct a way to solve the transmittance and reflection of a multiple layer structure.

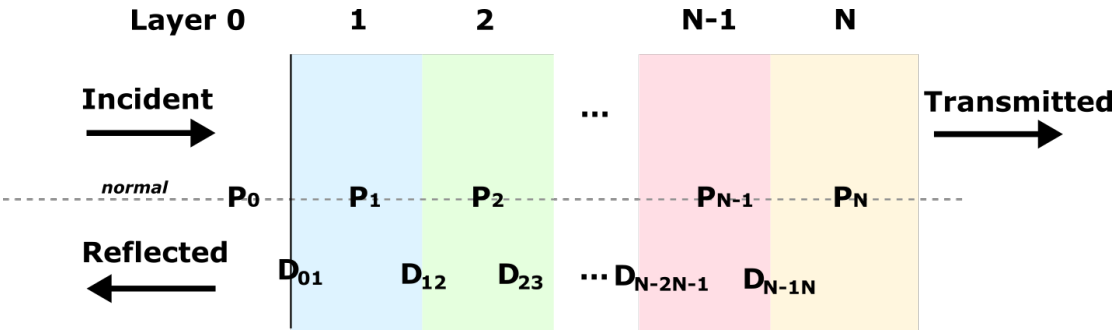

Figure 2.9: Reflection and transmission calculations in multilayer thin film structure using Transfer Matrix Method (TMM).

One transmission matrix $\mathbf{D}$ is used to describe the effect of an interface related to the complex Fresnel coefficients for both parallel and perpendicular polarizations t_s, r_s, t_p, r_p, for simplicity, only r and t will be use in the following calculations. Consider from layer 0 to 1, $\mathbf{D}_{01}$ is given as [74]:

$$\mathbf{D}_{01} = \frac{1}{t_{01}} \begin{bmatrix} 1 & r_{01} \\ r_{01} & 1 \end{bmatrix} \tag{2.17}$$

Another matrix - propagation matrix $\mathbf{P}$ - was used to include the propagation to follow the optical path ($\delta = ln$, where n is the refractive index and l is the path length) induced to the beam on each layer($\delta_0..\delta_N$). Consider the propagation in layer 0, $\mathbf{P}_0$ is given as :

$$\mathbf{P}_0 = \begin{bmatrix} e^{i\delta_0} & 0 \\ 0 & e^{-i\delta_0} \end{bmatrix} \tag{2.18}$$

By using TMM, the transfer matrix $\mathbf{M}$ is then defined as:

$$\mathbf{M} = \begin{bmatrix} m_{11} & m_{12} \\ m_{21} & m_{22} \end{bmatrix} = \mathbf{D}_{01}\mathbf{P}_0 \ldots \mathbf{D}_{N-1N}\mathbf{P}_N \tag{2.19}$$

Following this and the definitions for total reflectance $\mathbf{R}$ and transmittance $\mathbf{T}$ [59, 65, 74], we get:

$$\mathbf{R} = \frac{m_{21}}{m_{11}} \tag{2.20}$$

$$\mathbf{T} = \frac{1}{m_{11}} \tag{2.21}$$

The subsequent sections show the outcomes of these computations, and they are used to choose the material and thickness of the transducer layer, by modelling the absorption of the pump beam, and the reflection of the probe beam (while

using the reflection detection mode).

2.2.3 Sound generation and propagation

When the pump laser pulse is focused and absorbed by a pump-light-absorbing material (opaque materials - primarily metals), the light energy is converted into heat. This process generates an acoustic strain pulse, known as CAP (Coherent Acoustic Phonons), encompassing a broad frequency range of phonons. Depending on the power density of the pump laser light, two distinct CAP generation regimes are observed: ablation and thermoelastic.

In the ablation regime, if the power density is sufficiently high, part of the illuminated surface undergoes vaporization, resulting in forces normal to the surface. However, this process can damage the material being studied. On the other hand, when the power density of the laser is below the ablation threshold, the sample is heated without causing damage. In this lower-power regime, thermal stresses become the source of strain, leading to the generation of CAP.

In this context, we focus on the thermoelastic regime. In this regime, the sample is heated, and the resulting thermoelastic stresses are responsible for the generation of the acoustic strain pulse (CAP), commonly known as ultrasound.

The generation of ultrasound using short light pulses allows to maintain low average powers while achieving high peak powers to produce distinct sound pulses. Shorter pulses result in a higher concentration of energy in the form of higher frequencies.

In order to generate high-frequency ultrasonic pulses, extremely fast optical pulses are necessary. Directly measuring the energy contained in each pulse is challenging. However, the total energy of a pulse, denoted as Q, can be determined based on

the average power:

$$Q = \frac{P_{avg}}{f_p} \tag{2.22}$$

where f_p is the repetition rate of optical pulses (pulses per second) and P_{avg} is the average power. The following relation can also be used to calculate the peak power:

$$P_{\text{peak}} = \frac{Q}{\tau} \tag{2.23}$$

where τ is the duration time of the pulse. The energy density, which is the amount of energy radiated over a given area, is another helpful measurement:

$$\mu_p = \frac{P}{a} \tag{2.24}$$

where P can either be the peak or average power and a is the irradiated area of a laser spot, with a radius r, and $a = \pi r^2$.

The transformation of optical energy into heat is thought to occur instantaneously, and is controlled by a delta function ($\delta(t)$) that is centred on the moment the pump arrives at the film's surface. Furthermore, it is considered that the heat is contained within a spatial region (below the film's free surface) equivalent to the pump laser's optical penetration depth, or absorption length, ζ. The penetration depth in metallic films is typically tens of nm.

To find the shape of the CAP pulse produced by thermal elasticity, we need to first guess how the pump light absorption will change the thermal field distribution

ΔT.

Complex refractive index is defined as the complex sum of the refractive index (n) and extinction coefficient (κ):

$$\tilde{n}_1 = n - i\kappa \tag{2.25}$$

where κ stands for the absorption coefficient of the light in material and related to the attenuation coefficient α as:

$$\alpha = \frac{4\pi\kappa}{\lambda_{pump}} \tag{2.26}$$

which produces an absorption length (or skin depth) of:

$$\zeta = \frac{1}{\alpha} = \frac{\lambda_{pump}}{4\pi\kappa} \tag{2.27}$$

Note that the expression of the optical penetration depth stands for both the pump and probe laser light. Taking into account these assumptions, the total energy $Q_{absorbed}$ absorbed by the film, along the depth axis of the film (z-axis, with $z = 0$ the free surface and $+z$ directed inside the film), is:

$$Q_{absorbed} = \frac{(1-R)Q}{a\zeta} e^{-z/\zeta} \tag{2.28}$$

with R the optical intensity reflection coefficient. This absorption of energy produces an instantaneous temperature rise $\Delta T(z)$ given by:

$$\Delta T(z) = \frac{Q_{absorbed}}{C} \tag{2.29}$$

where C is the specific heat per unit volume of the material (heat capacity). By replacing the $Q_{absorbed}$ in the above equation, we get the expression for $\Delta T(z)$:

$$\Delta T(z) = \frac{(1-R)Q}{a\zeta C} e^{-z/\zeta} \tag{2.30}$$

The temperature elevation inside the film, causes the heated part of the sample to expand with a characteristic linear (isotropic film) thermal expansion coefficient β, by only consider the displacement in z-direction, the stress-strain relation in the presence of a thermal stress is given by [59]:

$$\sigma_z = \rho_0 v^2 \eta_z - 3B\beta\Delta T(z) \tag{2.31}$$

where v is the sound velocity, ρ_0 the material density B the bulk modulus. Giving the displacement u_z along the z direction (with $\eta_z = \partial u_z/\partial z$), leads to the strain propagation equation for u_z:

$$\frac{\partial^2 u_z}{\partial t^2} = v^2 \frac{\partial^2 u_z}{\partial z^2} + \frac{v^2 \eta_0}{\zeta} e^{-z/\zeta} \tag{2.32}$$

with η_0 from the boundary condition of z=0, t=0, η_z= 0:

$$\eta_0 = \frac{3B\beta\Delta T_0}{\rho_0 v^2} \tag{2.33}$$

where the initial temperature rise is:

$$\Delta T_0 = \frac{(1-R)Q}{a\zeta C} \tag{2.34}$$

thus the initial strain becomes:

$$\eta_0 = \frac{3B\beta(1-R)Q}{aC\zeta v^2} = \frac{\gamma(1-R)Q}{a\zeta v^2} \tag{2.35}$$

with $\gamma = 3B\beta(1-R)Q/C$ the Gruneisen parameter. Finally, solving all these equations, the solution for the strain is given as [75, 59]:

$$\eta(z,t) = \eta_0 e^{-z/\zeta} - \frac{\eta_0}{2}\left[e^{-\frac{z+vt}{\zeta}} + e^{\frac{|z-vt|}{t}\zeta}\,\mathrm{sign}\,(z-vt)\right] \tag{2.36}$$

where sign correspond to the sign (or *signum*) function.

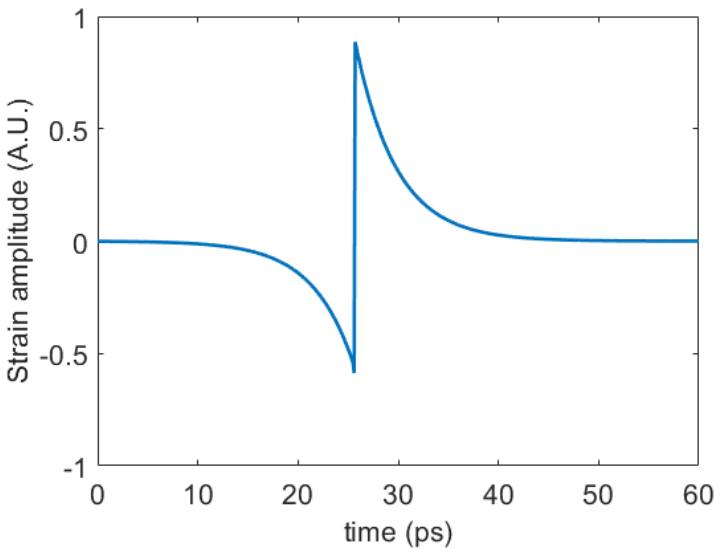

Figure 2.10: Simulated strain pulse with gold. The geometry for this example is a 150 nm gold layer preceded by a glass substrate and followed by water. The unipolar strain pulse reflects at the glass/gold interface producing the bipolar strain pulse over the first 60 ps.

These calculations allow the evaluation of the strain distribution and temperature

rise caused by the energy absorption from a short laser pulse in a material. Figure 2.10 is an example of simulated strain generated by a pump pulse with a $\lambda_{pump} =$ 415 nm from a 150 nm gold thin film deposited over glass and followed by water. The strain profile obtained with Eq. (2.36) highlights two properties: a progressive decay, and a bipolar pulse. These strain pulse from thin metallic films come with frequencies of GHz, and they serve good purpose for photoacoustic generation in Brillouin region in this thesis.

The propagation of sound waves is governed by the wave equation [76]:

$$\left(\frac{\partial^2 p}{\partial x^2} + \frac{\partial^2 p}{\partial y^2} + \frac{\partial^2 p}{\partial z^2}\right) = \frac{1}{v^2}\frac{\partial^2 p}{\partial t^2} \tag{2.37}$$

with p the sound pressure, and ν the speed of sound related to the B bulk modulus (measure of material stiffness) and ρ the density:

$$v = \sqrt{\frac{B}{\rho}} \tag{2.38}$$

Consider the simplest case of 1D propagation of plane wave along z-axis, the wave equation Eq. (2.37) can be rewritten as:

$$\frac{\partial^2 p}{\partial z^2} = \frac{1}{v^2}\frac{\partial^2 p}{\partial t^2} \tag{2.39}$$

The general solution of the above equation is:

$$p(z,t) = f(z - vt) + g(z + vt) \tag{2.40}$$

where f and g denote arbitrary functions with existing second derivatives, f describes a pressure disturbance propagating at a speed v toward $+z$, and g describes a pressure disturbance propagating at a speed v toward $-z$. If consider a harmonic function, plane waves traveling in the $+z$ direction can be written as:

$$p(x,t) = p_0 \mathrm{e}^{i(\omega t - kz)} \tag{2.41}$$

where p_0 is the pressure amplitude, ω is the angular frequency, and the wave number is $k = \frac{\omega}{v} = \frac{2\pi}{\lambda}$.

According to definition, the particle velocity $\mathbf{v}$ is:

$$\mathbf{v} = \frac{kp_0}{\omega\rho}\mathrm{e}^{i(\omega t - kz)} = \frac{p_0}{v\rho}\mathrm{e}^{i(\omega t - kz)} \tag{2.42}$$

Then introduce the acoustic impedance Z which is the ratio of the acoustic pressure P and the particle velocity $\mathbf{v}$ as follow based on equation (2.41) and (2.42):

$$Z_0 = \frac{p}{\mathbf{v}} = \rho v = \sqrt{K\rho} \tag{2.43}$$

For plane waves, the value of impedance Z depends only on the material constants: density ρ and sound velocity v. This parameter plays an important role in reflection and refraction at the boundaries of different media.

Sound waves transport the energy contained in the medium through which they propagate. The energy content per unit volume is called the energy density. The energy flow is characterized by the sound intensity I, which is defined as the energy passing per second through an imaginary window of unit area perpendicular to

the direction in which the sound waves propagate:

$$I = \overline{p\mathbf{v}} = \frac{p_0^2}{2Z} \tag{2.44}$$

where the overbar denotes a time average.

Acoustic impedance provides a measure of the acoustic transmittance T_{sound} and reflection R_{sound} of waves travelling normally through an interface as:

$$T_{sound} = \frac{4Z_1Z_2}{(Z_1 + Z_2)^2} \tag{2.45}$$

and

$$R_{sound} = \left(\frac{Z_1 - Z_2}{Z_1 + Z_2}\right)^2 \tag{2.46}$$

The greater the difference between the acoustic impedances of the two materials at a boundary in the body the greater the amount of reflection. No reflection of sound waves occurs when two media have the same characteristic acoustic impedance.

Similar to the optical case, sound also gets attenuated as it propagates through media and it is important to include it in the model since the sound attenuation in a fluid is very high for ultrasound. This loss of intensity is expressed as:

$$I_{loss}(x) = I_0 e^{-\alpha_{loss} z} \tag{2.47}$$

where z is the propagation distance and α_{loss} is the attenuation coefficient which is a material property that strongly depends on the frequency of the sound prop-

agating through. Knowing the attenuation coefficient from experimental traces then feed back to the simulation can help adjust the model to produce better fitting simulation results.

2.2.4 Optical detection of TRBS

The generation of a coherent phonons or say acoustic pulse (CAP), by the absorption of the ultrashort pump light pulse, has been discussed in Section 2.2.3. The experiment employed in this thesis is a pump-probe technique, relying on a second time delayed probe laser pulse to monitor the propagation of CAP. To be more specific, the time-resolved Brillouin scattering (TRBS) method is used for detection. This technique permits the measurement of phonon travel through medium both above and underneath the optoacoustic transducer layer.

The coherent acoustic phonons are photo-detected temporally by monitoring the ultrafast transient changes of the detected optical reflectivity or transmissivity $\frac{\Delta R}{R}$, $\frac{\Delta T}{T}$. The pump can be considered as a trigger inducing only the conversion process of the optical energy of the pump beam to mechanical energy [77]. Only the transmitted or reflected intensity changes of the probe laser are collected by a photodiode are considered for detection [68].

As the optical properties of the substrate are modified under the strain with a depth penetration ζ, the interfered original and strain scattered probe beam allows to get the phase ϕ and the amplitude A of the acoustic signal (through photo-elastic coupling). Material strain causes perturbations in the electric field permittivity [78], and thus modulate the reflection and transmission of the probe beam. These modulations are recorded by using a photodetector and an oscilloscope with trigger from the asynchronous laser systems.

The interaction between the probe light and strain results in transient changes in the electric field reflectivity:

$$\frac{dr(t)}{r} = -iC \int_0^\infty \eta(t,z) e^{i2kz} dz \tag{2.48}$$

where C is a sample dependent complex constant proportional to the acousto-optic (photo-elastic) interaction [75, 79, 33]. $\eta(t,z)$ is the strain field along the z direction already discussed in the previous Section 2.2.3. Equation (2.48) indicates that transient changes in reflectance reveal the time-evolution of the strain pulse. The interaction between light and strain pulse is quasi-static, with the strain pulse evolving significantly slower than the interaction duration.

There exist several interpretations of Equation (2.48) that may provide a deeper knowledge of the physical aspects of particular experimental realisations. Detailed derivations are already deeply studied and published on several review/tutoring papers from Gusev et al. [33, 80] and Matsuda et al. [59].

Based on the paper by Matsuda et al. [59], a MATLAB model was written to simulate 1D time resolved Brillouin signal for multi layer structures. Figure 2.11 demonstrates using the PLU model to simulate TRBS. A single gold thin-film is working as the optoacoustic transducer to produce strain which travels into the surrounding medium. The simulated Brillouin frequency is determined by the refractive index and sound velocity in the medium (water or polystyrene, for example). Signal filtering is applied to better show the components of interests, which are water or polystyrene (PS).

In order to better simulate the final detected signal, it is necessary to introduce signal attenuation, which can also be used to explore the behaviour of the generated phonons in the multilayer medium, an example of which is shown in Figure 2.12,

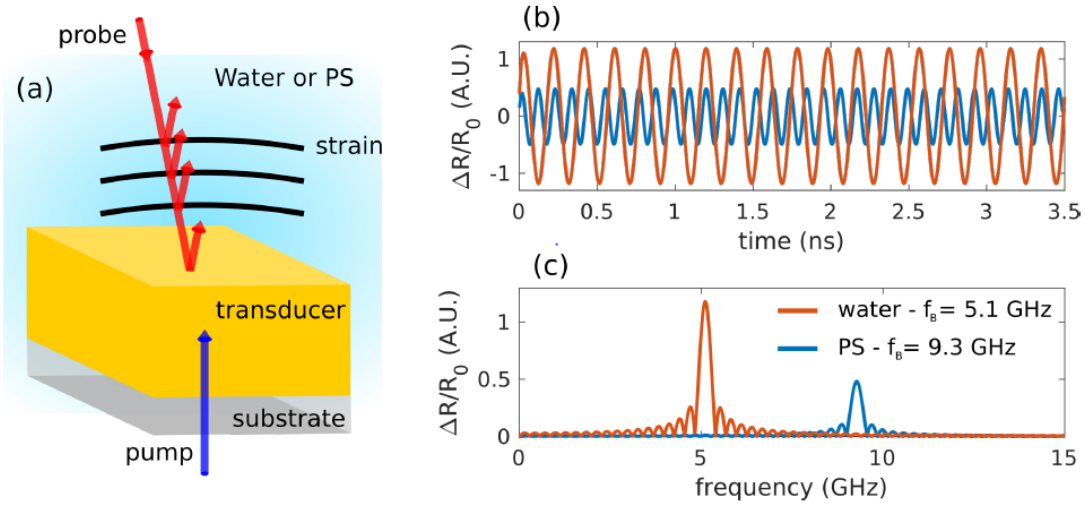

Figure 2.11: A basic example of using the PLU model to simulate TRBS signal with a transducer and water or polystyrene (PS) as the external medium. (a) The simulation's assumed geometry is as follows: the optical probe wavelength is set to probe = 780 nm, and the pump beam enters the system from the substrate side and the probe beam from the medium side. The modulation depth depicted in (b) results from the optical beating between the elastic and inelastic photons. (c) The time resolved signals in (b) are cast into the frequency domain using FFT. The measured Brillouin frequency (frequency location of the peaks) will differ because of the variations in the refractive index and sound velocities between PS and water. Image reproduced from [67].

first a 2 μm layer of water and then a 1 μm layer of PMMA. The corresponding TRBS signal is shown in the top of Figure 2.12, and the bottom sub-figure shows the frequency spectra (FFT) for different layers. Figure 2.13 includes a wavelet transform of the simulated time trace to better illustrate the simulation ability of the model. FFT and wavelet details are discussed in the following methods chapter (section 3.4.2 and section 3.4.4).

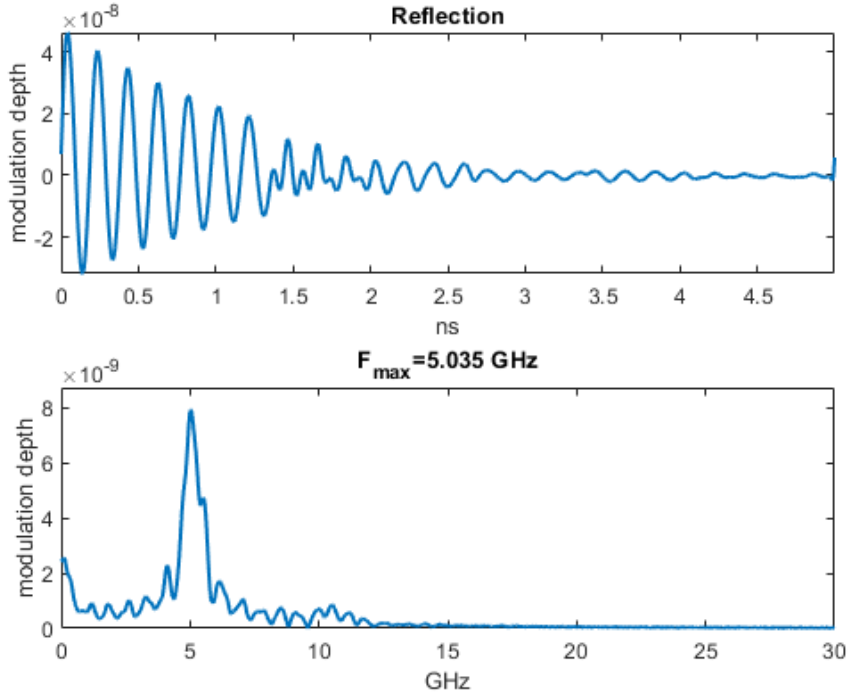

Figure 2.12: Simulated trace of a multilayer structure including a substrate, a transducer layer made of Au, a layer of water and a PMMA layer.

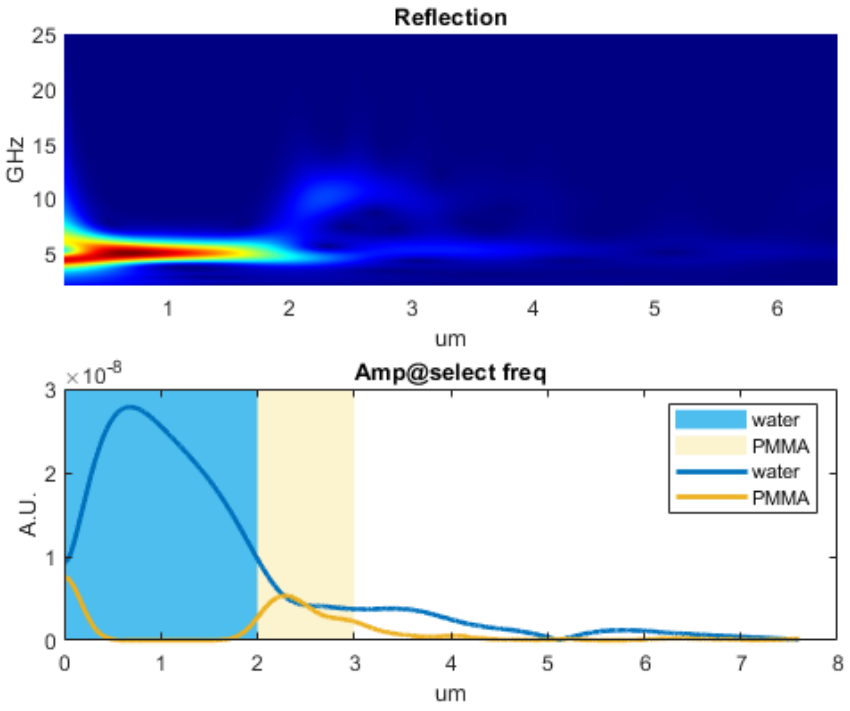

Figure 2.13: Wavelet analysis of the simulated trace of a multilayer structure, which includes substrate, transducer layer water and PMMA layer.

2.3 Focusing of waves

The phenomenon of wave focusing is a cornerstone in the advancement of numerous optical and acoustic applications. The most important bit of this process lies the ability of lenses to converge or diverge waves, thereby concentrating energy. In the context of optical waves, light focusing through lenses harnesses refraction principles, fundamentally described by Snell's law, to direct light paths towards a focal point [72]. Similarly, the focusing of acoustic waves relies on the precise curvature of surfaces to guide sound into concentrated regions, with applications ranging from medical imaging to industrial non-destructive testing.

Since both mechanical and electromagnetic waves can be focused using the same underlying theory, acoustic lenses (and also optoacoustic lenses) can concentrate sound in the same manner that optical lenses can focus light. Acoustic waves can be studied and treated with the same equipment as electromagnetic waves. The generation and propagation of the sound field are simplified to a single-frequency problem, thus easing the design process for the purpose of proof of concept. In this thesis, all optoacoustic lenses are designed for a single sound frequency of 5 GHz, as the typical Brillouin frequency (f_B) measured in cell imaging by Phonon microscopy falls within the range of 5 to 6 GHz for a probe wavelength (λ_{probe}) of 780 nm. Although the strain pulse generated by the pump pulse is broadband within the GHz range, the detection can be considered as single-frequency due to the selective nature of Brillouin scattering. Only photons with a fixed probe wavelength (λ_{probe}) and phonons that meet the Bragg condition are detectable. Therefore, the single sound frequency (λ_{phonon}) model becomes valid.

2.3.1 Focusing of sound

Sound focusing is one of the most significant issues in the study of acoustics because of its many uses. Acoustic lenses, devices that can focus acoustic energy in a particular area, are the source of this focalization phenomenon. Applications for acoustic lenses are numerous and diverse. They include non-destructive testing, industrial syntheses and processes, drug and gene delivery, medicinal applications for the detection and/or treatment of medical diseases, and more [81, 82, 83]. Acoustic lenses have a wide range of uses, making them a hot topic in the scientific world. Sound can either be focused using diffraction or refraction processes [84, 85], with a a huge spectrum of advanced applications with acoustic metasurfaces [86, 87, 88, 89], holographic structures [90] and phononic crystals [91].

The aim of this thesis is to demonstrate the focusing of high-frequency sound ($\sim$ 5 GHz) in water using optoacoustic lenses and Picosecond Laser Ultrasonics (PLU), thereby paving the way for non-destructive acoustic imaging with sub-optical resolution. The main challenge of any acoustic related microscope is that the resolving power (resolution & signal intensity) is set primarily by the frequency of sound travelling within the system and the energy efficiency, including such as sound attenuation, sound coupling in different medium and detection sensitivity. Two technologies have made great push in focusing of acoustic waves in high frequency for imaging: Scanning acoustic microscopy (SAM) and photoacoustics.

Scanning acoustic microscopy (SAM)

SAM made use of concave acoustic lenses and high frequency piezoelectric transducers, which offered a path for acoustics towards high resolution imaging and demonstrated proof of concept on a range of biological cells, both fixed [92, 93]

and living cells [94]. Figure 2.14 shows an example using SAM to perform living cell imaging, (a) show the device concept of SAM, a thin-film piezoelectric transducer at one end of a sapphire crystal is excited by a radio-frequency electrical pulse. An acoustic plane wave then produced by the transducer travels via the sapphire crystal to a concave lens with a wide opening angle. The acoustic beam is focused to a diffraction-limited spot in the liquid because of the concave interface. The object reflects some of the acoustic energy. The lens gathers the reflected acoustic waves, and the transducer transforms them back into an electrical signal. The brightness of an image element in the acoustic micrograph is determined by the detected acoustic power. The object is mechanically scanned in a raster pattern, creating the object's reconstructed picture point-by-point. (b) is an example living cell image taken using SAM. A resolution of 0.72 μm is claimed and the scale bar is 20 μm for this chicken heart fibroblast cell. Higher resolution has been achieved for imaging is $\sim 200nm$ by utilising higher frequency piezoelectric transducers ($\sim$ 4.4 GHz) with an acoustic lens with a radius of 13 μm [95].

However, this collection of techniques suffered from a series of challenges. Firstly, as the wavelength and resolution scale inversely with frequency (f), the attenuation of the waves in aqueous tissue scales with f^2 leading to great losses and short acoustic path lengths. To achieve shorter wavelengths and resolution without increasing f a lot, researchers found that they can use coupling fluids with lower acoustic attenuation and/or lower velocity than water, such as cryogenic liquids and high pressure inert gases. Among all the liquids, helium performs the best for high resolution application at cryogenic temperature [97]. Yet, this leads to another problem: very low temperatures contradict the conduct of non-destructive imaging purpose for cells, as the ultra-low temperature helium used for higher resolution would freeze and kill the cells, thus limiting the applicability of the technique to biology.

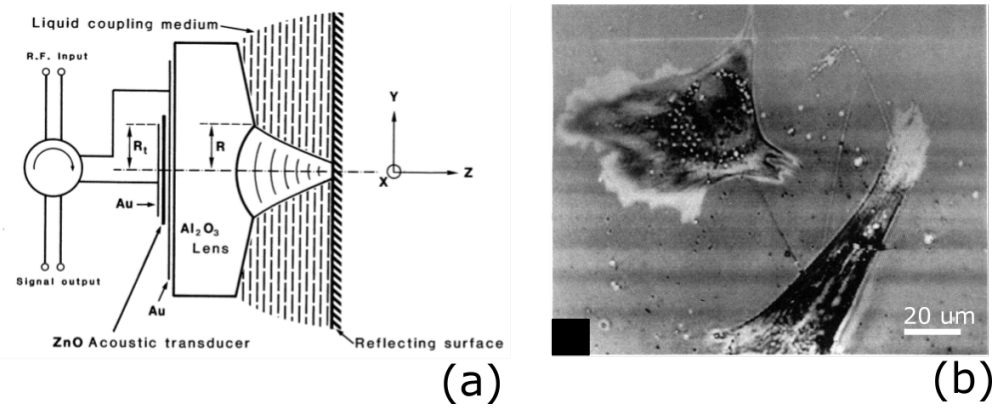

Figure 2.14: Device concept and example scanning result for the scanning acoustic microscope (SAM). (a) Schematic of the reflection acoustic microscope. A concave acoustic lens is attached to a high frequency piezoelectric transducer and constructed from an acoustically transmissive material, such as sapphire. In addition to transmitting sound waves into the coupling medium or sample, the transducer also serves as a receiver for sound waves that bounce off the specimen's acoustic impedance boundaries when it is in a quiescent state. Image reproduced from [96]. (b) Acoustic micrograph of chicken heart fibroblast cells on a sapphire substrate, showing its ability to resolve sub-cellular features of living cells. A resolution of 0.72 μm is claimed and the scale bar is 20 μm. Image reproduced from [94].

Besides, the performance of piezoelectric transducers at higher frequencies is poor because they become more difficult to fabricate and drive properly, as the resonance frequency inversely scales with the thickness of the piezoelectric element. For instance, ZnO (zinc oxide) - a widely used piezoelectric material, carries a great risk that the acoustic resonance may be too low for proper functioning [98]. Additionally, if inhomogeneity or stress is introduced to the thin-film piezoelectric element, there is a high risk of cracking under electrical excitation [99]. Finally, further complexity arises due to the requirement for a minimised yet functional mini electrical control system.

To overcome all these challenges and facilitate an easier approach for non-invasive, acoustic-based imaging techniques, opto-acoustic systems were proposed in the mid-1980s as a viable alternative to electro-acoustic ones. This not only simplifies the electrical barriers to acoustic microscopy but also opens up the possibility of achieving resolutions comparable to those of optical microscopy systems in

acoustic-based imaging.

Photoacoustics microscopy

The Photoacoustic Section 1.4.3 in the Introduction Chapter already gave a short history of the early exploration of Photoacoustic technique. Here just quick recap and direct jump to the modern art of Photoacoustic imaging techniques, and its advantages & disadvantages. By using focused lasers and ultrasonic transducers as receivers, photoacoustic microscopy is able to produce non-invasive images of cells and tissue with sub-micron resolution [100]. Figure 2.15 (a) is a common set up modern Photoacoustic microscopy system. When a laser pulse hits the interested region of the specimen, it absorb the laser energy and then it experiences thermal expansion (also contraction with cooling after), then sound waves are generated and propagate through. Finally, a conventional piezoelectric transducer is used for detection. One requirement for the specimens are that they need to be strong optical absorbing materials. Though many biological tissue tend to have a low optical absorption, endogenous chromophores (such as haemoglobin, DNA, RNA and melanin), in reverse, have great optical absorptions [101].

Some advantages of Photoacoustic microscopy are: The photoacoustic generation of acoustic waves greatly simplifies transducer design and fabrication, since photoacoustic transmitters do not require electrical connectivity and are more robust to excitation (optical) than their fragile piezoelectric counterparts. It has the potential for optical resolution, when the focused light is smaller than the focused spot of the detection transducer[101]; Photoacoustic also provides a way to reduce the acoustic attenuation by reducing the acoustic path. Unlike the SAM, no need for the reflection of sound to travel double the path from the region of interests to the transducer. Meanwhile, Photoacoustic microscopy is able to function in

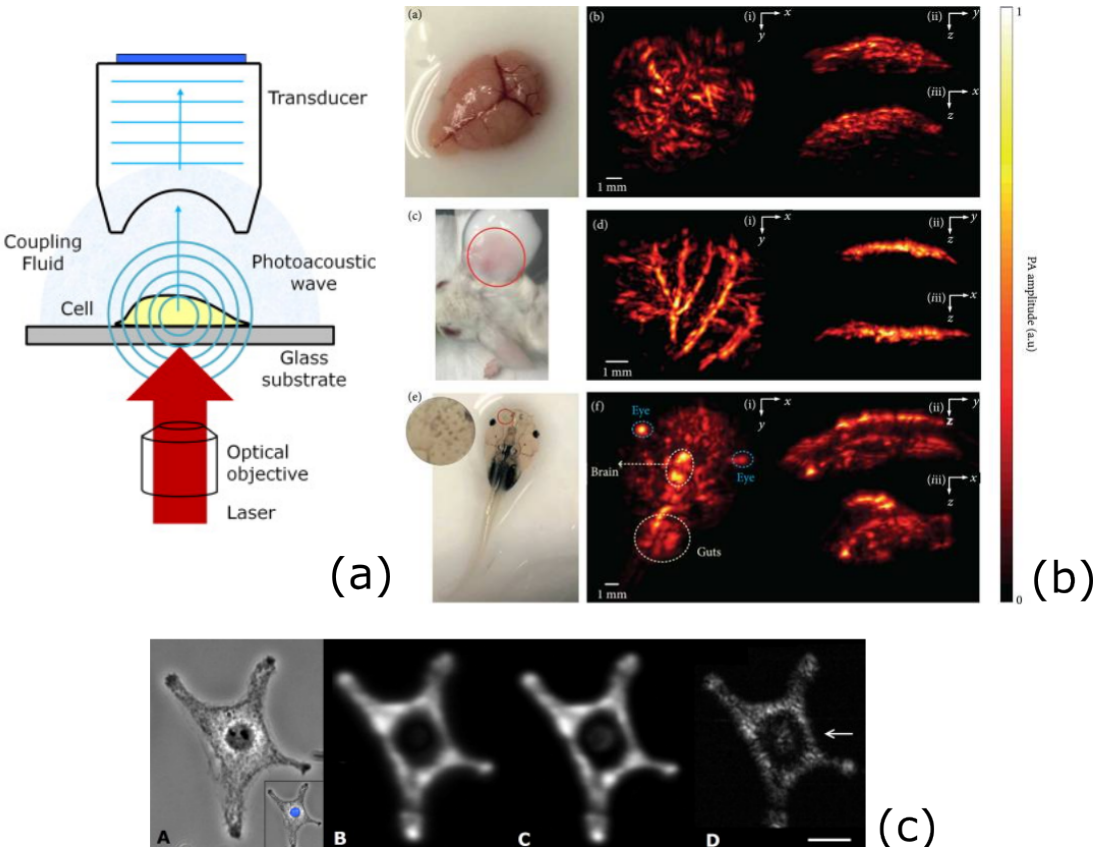

Figure 2.15: Working principle and imaging capabilities of photoacoustic microscopy. (a) Schematic of a conventional photoacoustic microscopy. A piezoelectric receiver detects the acoustic waves produced by optical absorption in the specimen when a pulsed laser is used to illuminate it. Image reproduced from [102]. (b) 3D Photoacoustic Computed Tomography (3D-PACT) of ex vivo brain and in vivo mouse ear and tadpole. Image reproduced from [103] (c) Photoacoustic imaging of a melanoma cell. A is the brightfield optical image, B–D are photoacoustic images measures of the same cell with different transducers: B-200 MHz, C-375 MHz and D-1200 MHz. The ability to resolve the nanoparticles inside the cells increase as the transducer frequencies increases. Image reproduced from [102].

broadband sound frequency, since the size of the object, the sound velocity, the optical penetration depth of the absorbing material, and the pulse width of the generating laser will all affect the system's frequency response [104, 105]. Finally, a longer acoustic penetration depth can be reach when different frequencies are evolving in the imaging. For example, Figure 2.15 (b) shows a set of imaging with larger tissue sizes, with a working frequency of ∼23 MHz, the system can provide lateral and axial resolutions of $\sim 114\ \mu m$ and $\sim 57\ \mu m$, with a penetration depth

around few mm[103]. However for lower frequency, like 5 MHz, the penetration depth will then be $\sim$ few cm.

However, as mentioned above, for biomedical material with a low light absorbing, Photoacoustic microscopy can function well. Meanwhile, the capacity to focus the laser to a small area, which is directly connected to the optical lens's numerical aperture (NA), limits the lateral resolution. Though Photoacoustic pictures of both cells and tissue in vitro or in vivo can be produced using a variety of contrast agents, including dyes and nanoparticles[106, 107]. They method then again conflict with one of the driven purpose doing acoustic based microscopy - bio compatibility.

Recent advances in optically-driven acoustic techniques, such as laser ultrasound and picosecond laser ultrasound, have offered solutions to some of the previous challenges of SAM and Photoacoustic microscopy, and also open the door towards sub-micron wavelength acoustics imaging. For instance, next section will introduce a PLU based SAM method trying to achieve this goal.

2.3.2 PLU based SAM

Researchers have already attempted to achieve PLU focusing in Scanning Acoustic Microscopy (SAM) [108] by using a femtosecond laser pulse to generate a brief acoustic pulse, which is then focused onto the sample using a specially designed and micro-fabricated acoustic lens with a radius of a few μm. Through a thin layer of water, the sound is transmitted to the sample. The lens gathers the sound that the sample reflects, and it then goes through an optical resonant cavity that is monolithically integrated. A time-delayed probing light pulse is used to detect the caused change in this cavity's characteristics.

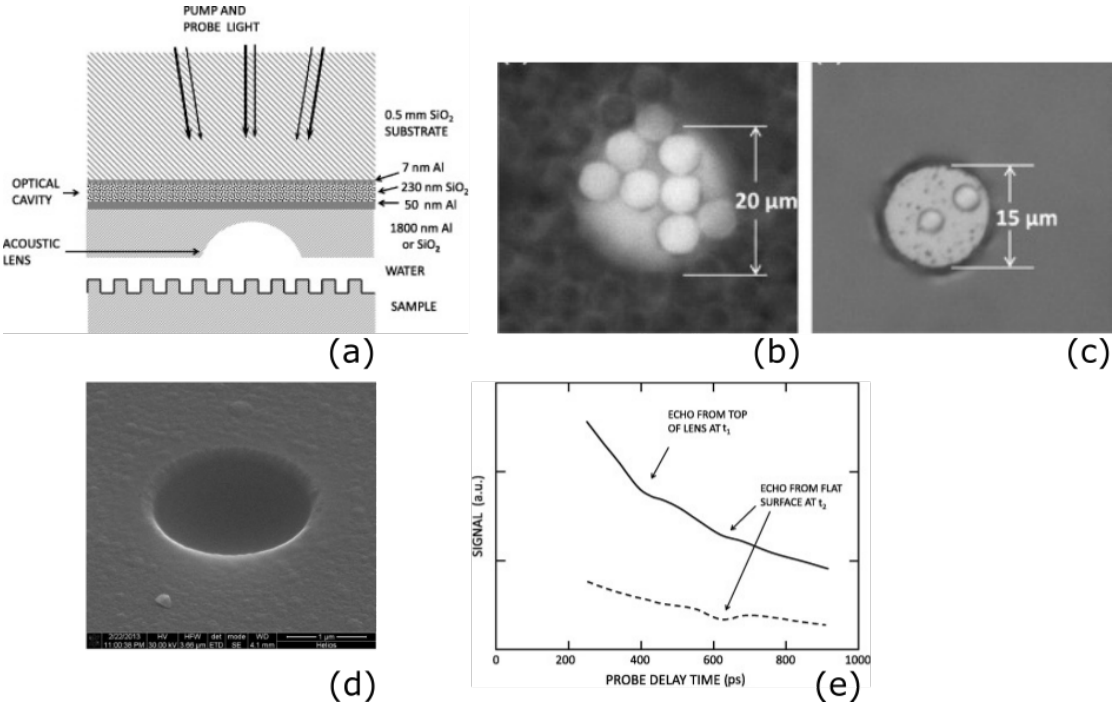

Figure 2.16: PLU based new scanning opto-acoustic microscope: (a) Schematic diagram of the proposed scanning opto-acoustic microscope. (b) Optical image of a 5 μm silica spheres on a 20 μm diameter aluminum island. (c) Optical image of two acoustic lenses formed after indentation and removal of silica spheres on a 15 μm diameter island. (d) Scanning electron microscope image of a SiO_2 lens of radius 1.5 μm. (e) Pump-probe data used to locate the acoustic lens. The dashed curve was obtained with the pump and probe beams at a position such that the sound is not incident on the acoustic lens. Figure reproduced from [108].

Figure 2.16 (a) shows the design of the SAM. The acoustic lens is fabricated within a 1.8 μm Al or SiO_2 film deposited below the optical cavity, designed to improve the signal-to-noise ratio. An optical set-up that can focus the laser spot to about 3 μm diameter on the cavity. A lens fabrication method based on nanoindentation of aluminum was used: Pressing the flat nanoindenter tip with silica spheres attached directly into a metal film. Figure 2.16 (b). (c) are some examples of fabricated samples, with spheres patterned to round islands with different sizes. Figure 2.16 (d) shows an SEM image of a SiO_2 lens of radius 1.5 μm. The result of the pump-probe measurement is shown as the dashed curve in Figure 2.16 (e). The data in this plot have been treated to exclude the influence of sound waves reverberating through the glass substrate, or Brillouin oscillations.

It comes at around $t_1 = 620ps$. At this point, the probe's time delay is fixed, and the lens structure is scanned in both x and y directions. The amplitude of the echo from the flat and free surface reduces when the pump and probe beams are exactly above the lens, but it still remains since the area they illuminate goes somewhat beyond the lens's surface. The solid curve in Figure 2.16 (e) shows that at time t_2, a new and earlier echo that originates from sound reflected from the top of the lens occurs at the same point. However, suffered from inadequate stability of the mechanical stage and poor signal to noise ratio, this work hasn't reach the fundamental limits for the performance of this type of instrument, as the numerical simulations' suggestion of a 50 nm resolution.

However, this technique suffered from mechanical instabilities and low signal-to-noise ratio, due in part to the low acoustic amplitude since the acoustic field attenuates as it propagates both to and from the imaging object. In this thesis, instead of using the device concept from SAM, a time resolved Brillouin scattering (TRBS) detection technique introduced in the previous Section 2.2 was utilized to achieve both the phonon focusing (via optoacoustic lenses) and saving of acoustic path - no need for sound to travel in reflection and thus get rid of huge attenuations. I expect that the optoacoustic nature of picosecond ultrasound offers more possibilities regarding acoustic lenses design and detection.

When designing these lenses, geometry and efficiency play a critical role in determining how well it functions in different applications. An optimal design would be one in which the lens had a flat or simple geometry for the ease of fabrication and great energy efficiency. In this sense, lenses based on Fresnel Zone Plate (FZP) and concave structures are of greater interests. Concave lenses are the ones that come to mind first, as many optical lenses are of this structure, but they are highly challenging to manufacture. Fresnel Zone Plates (FZPs) are easier for fabrication. Traditional FZPs can be implemented either alternating with absorbing regions

and transparent regions, or phase-reversal FZPs with reversed phase regions. To make phase-reversal FZPs, two methods, one using FIB and one utilizing gold nanorods, and special experimental setups will be introduced with more details to generate and detect the signals in the preliminary results and perspectives Section 5.2.

2.3.3 Fresnel zone plate (FZP)

The concept of diffraction and interference leads to the implementation of Fresnel zone plates, which utilize zones of constructive and destructive interference to focus waves without the need for traditional lens materials. As a flat lens, it derives from the Fresnel zones concept and has found applications across various electromagnetic spectrums, including optics [109], X-rays [110, 111], microwaves [112], and sound [113, 114, 115, 116, 117]

Fresnel zone plates as ideal lens

The concept of FZP come from wavelength in X-ray range, the refractive index of materials is slightly smaller than unity in the X-ray frequencies, requiring inverse lens profiles and the phase shift of materials is comparable to their absorption term. The latter leads to severe absorption losses for all but the lightest materials and inherently limits the effective aperture size.

Fortunately, the problem of thick lens material was already solved two hundred years ago in the optical range. Lighthouses were essential navigational guides in the early 19^{th} century. Improving their brightness and fuel effciency required the better utilization of their emitted light. Traditional bulk glass lenses with the required large apertures and short focal lengths were very large and extremely

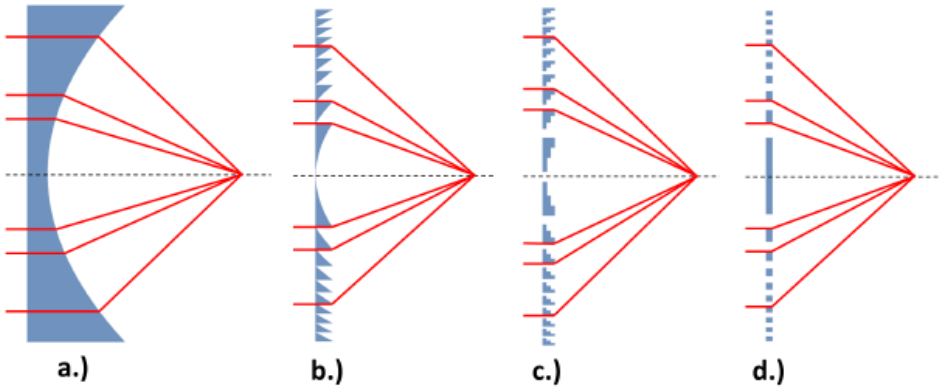

Figure 2.17: Towards lighter and more transparent lenses. By leaving out the bulk of the lens material while retaining the curvature the resultant Fresnel lens (b) will retain the optical properties of the ideal lens (a) using only a fraction of the lens material. Yet, since the blazed profile of the Fresnel lens is hard to produce with nanoscale structures, it can be approximated with a discrete number of steps (c) with the binary zone plate being the most basic approximation (d).

heavy. Augustin-Jean Fresnel realized that only the curvature of the lens participates in the focusing. This allowed him to separate the lens into several thin segments, while leaving out the bulk of the lens material to reduce its weight [118] (see Figure 2.17).

The same scheme can be adopted to X-rays and sound, as the ϕ phase of the electromagnetic radiation is not an absolute value, but is redundant according to 2π. The above described phase shift profile $\Delta\phi(r)$ of an ideal lens can be wrapped modulo 2π without any changes to the focusing properties:

$$\Delta\phi(r) = \frac{2\pi}{\lambda}\left(\sqrt{f^2 + r^2} - f\right) \bmod \pi \tag{2.49}$$

As seen on Figure 2.17(c), this results in a sawtooth like phaseshift function between 0 and 2π phase shift, eliminating absorption losses within the bulk lens material. The phaseshift of the lens jumps to zero, when it becomes a multiple of 2π. Therefore the outer radius r_n of the n^{th} zone always corresponds to:

$$\Delta\phi(r) = \frac{2\pi}{\lambda}\left(\sqrt{f^2 + r_n^2} - f\right) = 2n\pi \tag{2.50}$$

This equation can be easily rewritten into the zone plate equation:

$$r_n^2 = n\lambda f + \frac{n^2\lambda^2}{4} \tag{2.51}$$

This equation is the principal construction rule of Fresnel zone plates, determining the outer radius of the nth ring of a zone plate with f focal length and λ photon energy. A more detailed go through from discrete zones to the zone plate equation will also be introduced in the following section.

FZP basis

The zone plate is made up of a periodic structure of opaque and transparent circular zones. As the radius gets bigger, the period of the structure gets shorter. A diagram of a zone plate can be seen in Figure 2.18. The radius that marks the nth boundary between an opaque and a transparent zone is labelled as r_n. The integer n ranges from 1 for the innermost zone to N for the outermost zone. dr_n stands for the width of a certain area between r_n and r_{n-1}.

Here is a hands-on explanation of how to get to the expression for the zone placement. As shown in Figure 2.19, which is an optical path diagram. Let S stand for a point source that sends out radiation with a wavelength of λ. The source should be seen at point P by a zone plate put between points S and P at O. The zone plate is in the middle of the optical axis SP and its perpendicular. The geometry is radially symmetric.

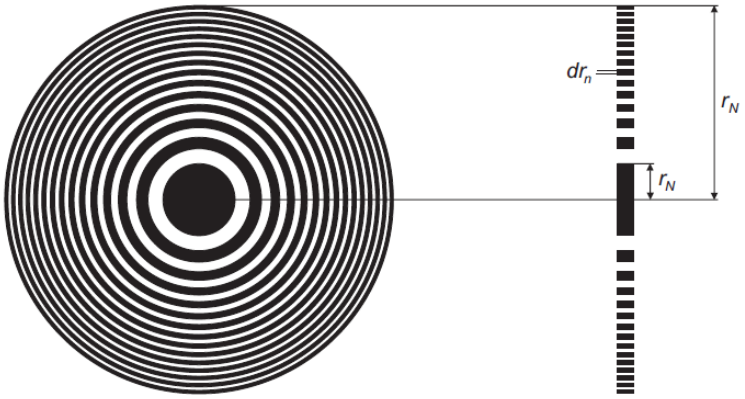

Figure 2.18: Front and side view of a zone plate. The radius for the innermost zone r_1, outermost radius r_N and zone width dr_n for the n'th zone are shown. Image reproduced from [119].

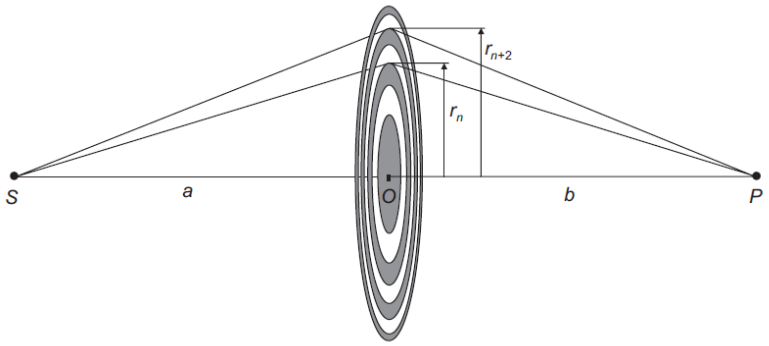

Figure 2.19: Optical path lengths between the source point S and image point P via a zone boundary pair at radii r_n and r_{n-2}. Image reproduced from [119].

Imagine a wave coming from S. It will interact with the zone plate at some point a radius r. Each of these points can be thought of as a Huygens-Fresnel secondary-wavelet source that adds to the amplitude at P. When the wavelets get to P, they will have different phase and amplitude depending on how long the optical path is from S to P. You can find the total amplitude at P by integrating over all the optical paths that have the right amounts of amplitude and phase. In the event that the radius r is much smaller than either a or b, the amplitude can be left alone and only the differences in phase need to be thought about.

The optical paths shown in Figure 2.19 make it clear that as the radius gets

bigger, the phase at P will change from 0 to 2π, which will cause both positive and negative interference. Only contributions that add positively at P will be sent through because the contributions with, say, phases between 0 and π will be blocked with opaque zones. To do this, each new zone needs to have an optical path length that is $n\lambda/2$ longer than the optical path length at the optical axis. The Pythagorean theorem can now be used to find the zone radii:

$$\sqrt{a^2 + r_n^2} + \sqrt{b^2 + r_n^2} = a + b + \frac{n\lambda}{2} \tag{2.52}$$

Solving for r_n we get

$$r_n^2 = \frac{n\lambda(a+b)ab + \frac{1}{4}n^2\lambda^2\left(3ab + a^2 + b^2\right) + \frac{1}{8}n^3\lambda^3(a+b) + \frac{1}{64}n^4\lambda^4}{\left(a + b + \frac{1}{2}n\lambda\right)^2} \tag{2.53}$$

If a is much smaller than b, and introducing the focal length of the zone plate as $1/a + 1/b = 1/f$, Eq. (2.53) can be simplified to:

$$r_n^2 = n\lambda f + \frac{n^2\lambda^2}{4} \tag{2.54}$$

and now we have the design equation of r_n for FZP with specified frequency λ and focus f:

$$r_n = \sqrt{n\lambda f + \frac{n^2\lambda^2}{4}} \tag{2.55}$$

Phase-reversal Fresnel zone plate

Conventional FZP suffers a low focusing intensity because part of the energy is blocked or not generated in the proposed device in this thesis. Phase-Reversal FZP (PR-FZP) is one of the new techniques put forward. In PR-FZPs, blocking regions are switched out for phase reversal regions. These regions fix the phase of the pressure contributions (in acoustics) by adding a phase shift π that can create a constructive interference at the designed focal distance. Unlike FZPs, all parts of the PR-FZP contribute to the focal region in a good way. This should make the lens more efficient and increase the focal intensity.

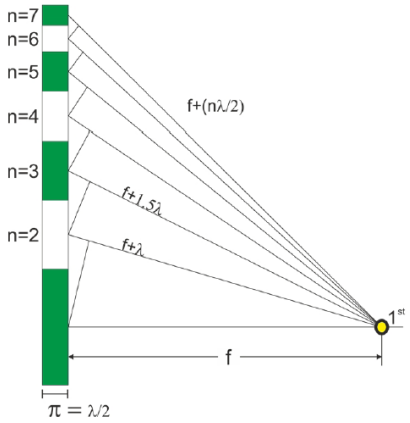

Figure 2.20: Sketch showing the upper half region of a Rayleigh-Wood phase-reversal FZP from the side. Opaque zones are replaced by phase-reversal ones and contribute to the intensity at the focus. For simplicity, only the 1st order focus is depicted. Both zone plates are illuminated from the left side.

Normal implication of PR-FZP is made by replacing the opaque Fresnel zones with transmissive phase-reversal ones, where the phase reversal zones induce a $\lambda/2$ phase shift relative to open zones. The phase-reversal zones would absorb some of the radiation depending on the incoming waves and the material of the phase-reversal zones. This brilliant suggestion was brought up the first time by Lord Rayleigh in his article on wave theory in 1888 [120] and was demonstrated for the first time by R.W. Wood in 1898 [121]. This specific type of FZP is called

as Rayleigh-Wood phase reversal zone plate. Figure 2.20 shows an illustration of the upper half part of a Rayleigh-Wood phase reversal zone plate.

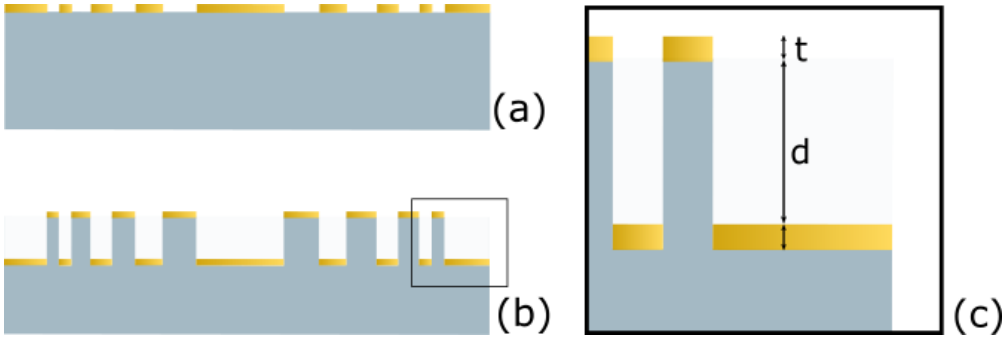

Figure 2.21: Sketch showing the device concept of optoacoustic PR-FZP for PLU. (a) is conventional FZP device proposed in this thesis. (b) is the PR-FZP with thin transducer layer and π phase difference. (c) zooms in the square area in (b) showing the thickness difference of the transducer layer and geometrical phase difference layer.

However, for the optoacoustic PR-FZP design proposed in this thesis, which is specific to PLU applications, the π phase difference can be implemented simply by creating a geometrical path difference for the phonons generated in the two sets of zones as shown in Figure 2.21. The depth required to create the path difference d is related to λ_{phonon}, which is around 390 nm, and the thickness of the optoacoustic layer is varying between 20 nm to 30 nm.

2.3.4 Concave lenses

Geometrical acoustics

The most common configuration for acoustic lenses is a curved surface and a coaxial plane. A focusing effect will result from the concave lens because the acoustic lens material's sound velocity is frequently higher than the propagation medium's.

The acoustic lens transducer functions in water and is made up of an acoustic lens

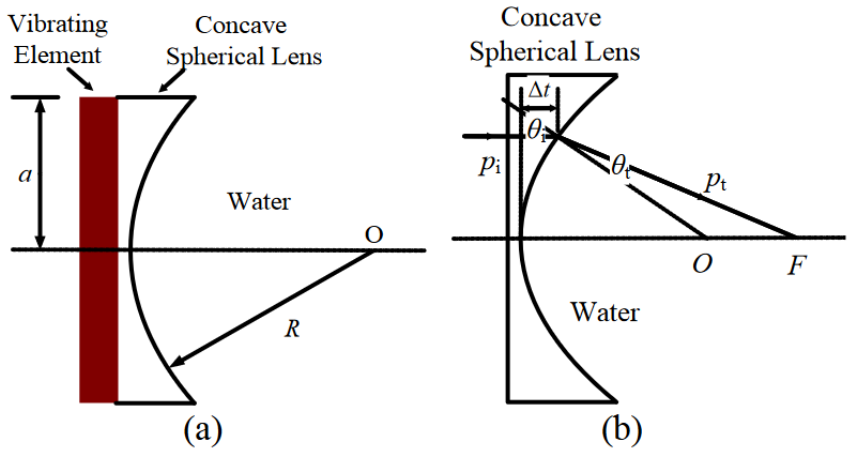

Figure 2.22: Wave propagation path and concave spherical acoustic lens. Image taken from [122].

and a vibrating element, as Figure 2.22 (a) illustrates. A circular plane makes up the vibrating element's surface. The acoustic lens is a plane-concave structure with a concave sphere on one side and a circular plane on the other. The acoustic lens's plane is where the vibrating element is attached. The vibrating element's radius is indicated by the sign a. The concave spherical surface's curvature radius is represented by the sign R. The concave spherical centre is denoted by O.

Figure 2.22 (b) illustrates the propagation process generated by the theory of optical ray imaging, which assumes that sound waves propagate as rays. The normal direction of the sound wave produced by the vibrating element enters the acoustic lens from the plane side. The wave then refracts into water on the acoustic lens's concave sphere surface, intersecting the transducer's centre axis at the focal point, or F. The focal length is the separation between the F point and the concave sphere's centre point [122].

Snell's law states that the refractive index of a lens medium that enters water can be calculated as follows:

$$n = \frac{\sin\theta_{\mathrm{i}}}{\sin\theta_{\mathrm{t}}} = \frac{c_1}{c_2} \tag{2.56}$$

where c_1 is the longitudinal wave velocity in a lens, θ_i is the incidence angle, θ_t is the refraction angle, and c_2 is the sound velocity in water. This formula demonstrates the relationship between the sound velocity values in the two media and the sound wave refraction angle value at the interface between them. The incident angles of an acoustic wave change with the incident positions on the concave sphere surface of the acoustic lens because the refraction angle increases as the sound velocity increases in the refractive medium. With reference to the Eq. (2.56) and the geometric relationship shown in Fig. 2.22 (b), the expression for the intersection point length of the refraction wave and the central axis of the acoustic lens transducer can be ascertained as follows [122]:

$$F = R\left(1 + \frac{1}{\sqrt{n^2 - \sin^2\theta_{\mathrm{i}}} - \sqrt{1 - \sin^2\theta_{\mathrm{i}}}}\right) \tag{2.57}$$

when θ_i or a is small, it becomes:

$$F \approx R\left(1 + \frac{1}{n-1}\right) \tag{2.58}$$

However, consider the challenges in nano-fabrication process, a easier spherical lens (similar as SAM) is chosen to use for the proof of concept purpose of this project.

Normal incidence

For the purpose of GHz acoustic focusing presented in this thesis, the active optoacoustic element is geometrically curved rather than using the material property differences between the lens and the propagation material. Thus, an assumption of normal incidence of sound waves is made here to simplify the design of concave lenses. Since different travelling path lengths of an acoustic lens can result in uneven losses of ultrasound energy, it is generally believed that a transducer with a curved active layer performs better [123, 124].

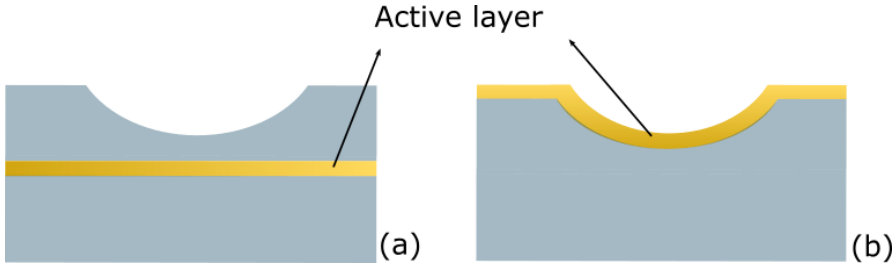

Figure 2.23: Two approaches for ultrasound transducer focusing: (a) incorporating a focused lens and (b) curving the active optoacoustic transducer layer.

The structure proposed in 2.23 (b) proposed here also has the advantage of not losing energy in the lens medium, sounds are launched directly to the medium of interests.

2.4 Fourier-Bessel angular spectrum method (FBASM)

The modelling of optical and sound propagation through nonlinear systems is often an extremely demanding computational task. However, considering the single-frequency femtosecond laser used (not exactly a single frequency, it is simplified here as a single frequency given its ultra-short pulse duration in time) and the Brillouin scattering-selected single sound frequency, the propagation of both light and sound waves may be simplified by assuming a radially symmetric beam profile.

Also, the Bragg condition for beams propagating in the same direction defines the optical probing wavelength, which controls the sound wavelength: For λ_{probe} [37], $\lambda_{sound} = \lambda_{probe}/2n$, where n is the refractive index in the medium. The main advantage of using an FBASM over commercially available finite element method (FEM) software (such as COMSOL) is that FBASM requires significantly fewer computational resources. However, its implementation demands greater effort in programming all the physical aspects of the simulation.

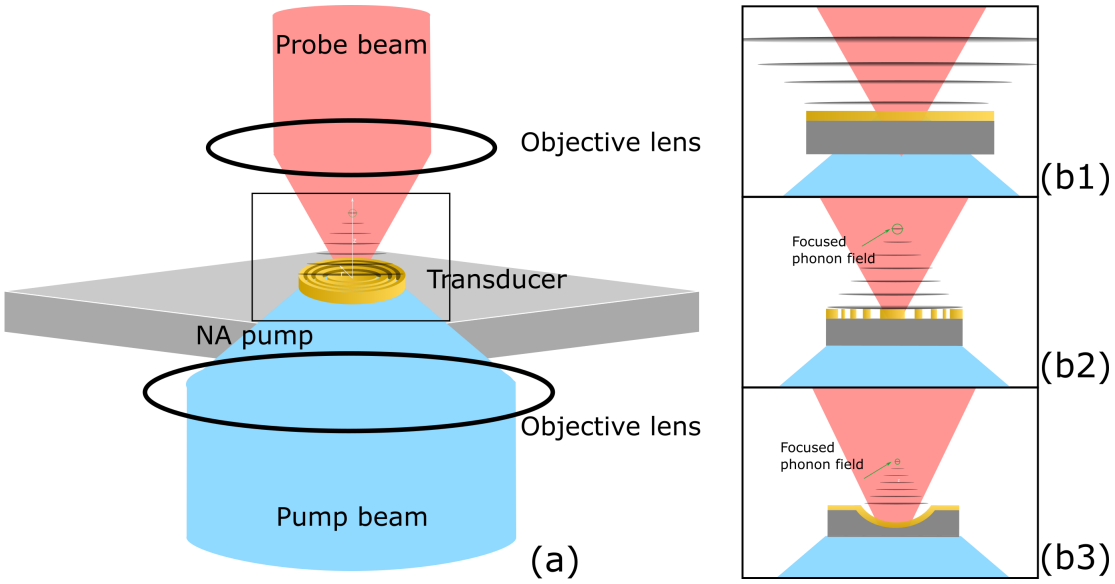

Figure 2.24: Schematic of the modelling setup. (a) The spatial distribution of the picosecond ultrasound source at the thin-film transducer layer at z_0 is defined by the computed pump beam PSF. The pump PSF was assumed to be an Airy disk and the initial sound field is assumed proportional to the pump PSF (the initial sound field can be modified by changing the initial phase to include the design of optoacoustic lenses) which is propagated into the medium using Fourier-Bessel angular spectrum propagation (FBASP). (b1-b3) Zoom in of the transducer and the estimated phonon fields from different structures.

Figure 2.24 (a) shows the concept of the modelling of pump laser generated sound field. The spatial distribution of the picosecond ultrasound source at the thin-film transducer layer z_0 is defined by the computed pump beam PSF (assumed to be an Airy disk). The initial sound field transmitted into the medium is proportional to the pump PSF for a conventional flat transducer. However, when a lens structure was introduced (FZP and concave structures), the preset acoustic phase

at z_0 was modified using the lens profile. Figure 2.24 (b1-b3) are illustrations zoom in the black square in (a), showing all three types of transducer, FZPs and concave structures are expected to create a focused phonon field. Then, the modified $u_{sound}(r, z_0)$ can be propagated to the entire preset field using Fourier-Bessel angular spectrum propagation (FBASP).

2.4.1 Model setup

This model requires input of the from the pump-probe system set up, especially the objectives related parameters, such as NA of the objective that deliver the pump. Once the NA of the lens has been determined, point spread function (PSF) for the λ_{pump} were calculated using an Airy disk assumption as shown below (Amplitude A and Intensity I):

$$\mathrm{A}(r) = \frac{2 \times \mathrm{J}_1(k \times NA \times r)}{k \times NA \times r} \tag{2.59}$$

$$\mathrm{I}(r) = |\,\mathrm{A}(r)|^2 \tag{2.60}$$

where J_1 is the first order Bessel function of the first kind.

The initial wavefront of the sound field generated at the transducer layer is flat (for a flat transducer) and is proportional to the PSF of the pump beam focused on the transducer. However, the wavelength of the optical probing, which is determined by the Bragg condition for beams propagating in the same direction, is controlled by the equation: $\lambda_{sound} = \lambda_{probe}/2n$, where n is the refractive index in the medium for λ_{sound}. In the model, the initial wavefront of the sound field generated at a lens structure is not flat. Instead, based on the geometrical designs (see Sections

3.1.2 and 3.1.3), the preset acoustic phase at z_0 was modified using the lens profile. This pre-calculated phase change of the sound field to $u_{sound}(r, z_0)$ is illustrated in the flowchart in Figure 2.25. The following process of FBASM is used: Hankel transform, propagation and the Inverse Hankel transform shown in the flowchart are detailed in the following sections.

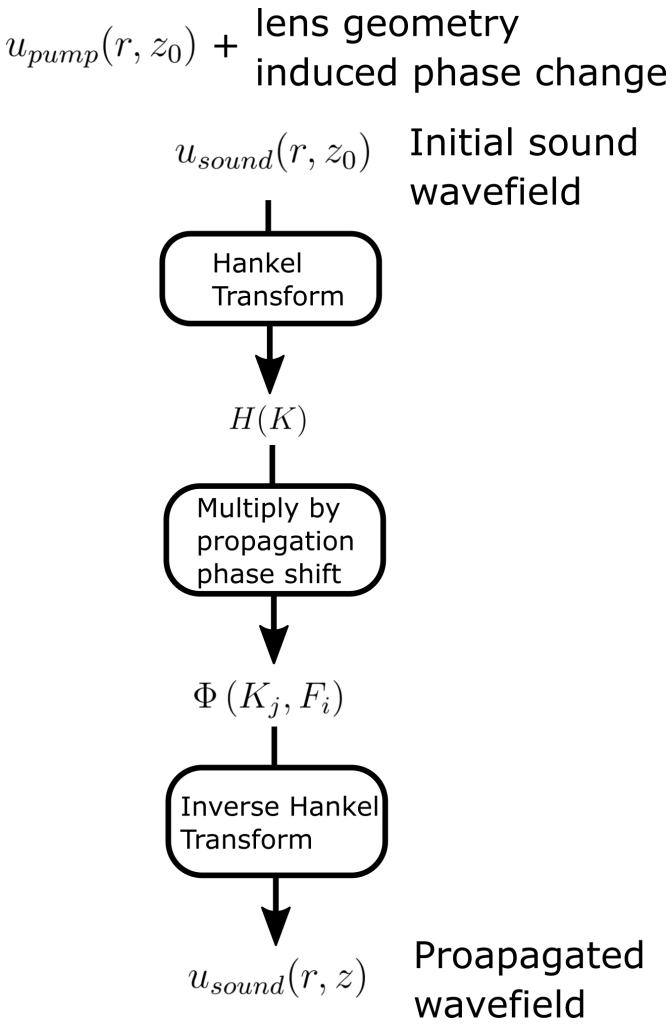

Figure 2.25: Scheme of the Fourier-Bessel angular spectrum propagation method for a circularly symmetric optical wavefield $u_{sound}(r, z_0)$, the initial wavefield's angular spectrum $H(K)$ is calculated using Hankel transform. Then, the the sound propagation is done by multiplying the phase-shift in the angular spectrum. Finally, the propagated sound field result is transfer back as $u_{sound}(r, z)$ by using inverse Hankel transform.

2.4.2 Radially symmetric propagation method

Then the modified sound initial field is ready for propagation, to perform propagation in the angular spectrum, angular spectrum of the disturbance $u_{sound}(r, z_0)$ is its two-dimensional Fourier transform according to definition. Meanwhile, for computation efficiency considerations, here a radially symmetric plane was chosen to perform the simulation. As illustrated in Figure 2.26, the simulation grid is marked by the red dashed area. For enhanced visualization, the simulation results within the light blue plane are reconstructed using axis symmetry.

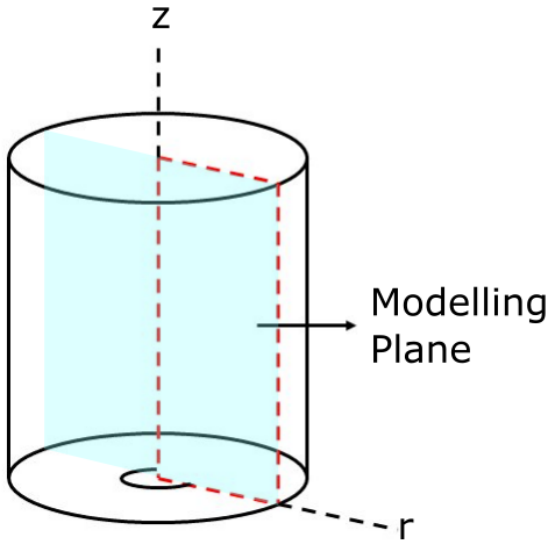

Figure 2.26: Axisymmetric model plane.

The field in cylindrical co-ordinates may be specified as:

$$u(r, \theta, z) \tag{2.61}$$

where

$$x = r\cos\theta, \qquad k_x = k_r \cos\phi \tag{2.62}$$

$$y = r\sin\theta, \quad k_y = k_r \sin\phi \tag{2.63}$$

$$r^2 = x^2 + y^2, \qquad k_r^2 = k_x^2 + k_y^2 \tag{2.64}$$

One dimensional Hankel transform can be used in place of the two dimensional Fourier transform. Also known as the Fourier-Bessel transform, the Hankel transform (of order zero) is an integral transform that is comparable to a two-dimensional Fourier transform with a radially symmetric integral kernel, more details are discussed in Appendix D.2. Although the Fast Fourier Transform (FFT) is known for its efficiency, reducing the sample points by assuming radial symmetry enables the use of the 1D Hankel transform technique. While less efficient than FFT, this approach still leads to savings in computing power. In order to apply this propagation technique a Hankel-based radial propagation method is developed. This unified approach offers a standardized way to calculate the propagated fields of both the sound and optics field. For the purpose of this thesis, only the phonon field $u_{sound}(r, z)$ is of interest.

After knowing the initial phonon field, $u_{sound}(r, z_0)$, in the model, r is defined as $r_j = j \cdot px$, where px is the pixel size and $j = 0, 1, ..., L-1$. This discretizes the radial domain over which the field is defined. The spatial frequencies in the angular spectrum is then defined as $K_j = \frac{j}{L} \cdot \frac{2\pi}{2px}$, reflecting the conversion from spatial positions to frequencies.

Hankel transform (HT)

The Hankel transform of the input field $u_{sound}(r, z_0)$ is computed over discretized radial positions and spatial frequencies. The discrete approximation of the Hankel transform is:

$$H(K) = \sum_{j=0}^{L-1} u_{sound}(r_j, z_0) J_0 \left(K_j r_j\right) r_j \Delta r \tag{2.65}$$

where J_0 is the Bessel function of the first kind of order 0, and Δr is the spacing between radial positions, implicitly assumed to be captured in the computation since $r_j = j \cdot px$.

Propagation phase shift

For each propagation distance F_i, the phase shift due to propagation is calculated for each spatial frequency:

$$\Phi\left(K_j, F_i\right) = 2\pi \frac{F_i}{w} \sqrt{1 - \left(\frac{w K_j}{2\pi}\right)^2} \tag{2.66}$$

This phase shift is applied to the frequency-domain representation of the field. A mask is also applied to taper the higher spatial frequencies to reduce artifacts from the abrupt cutoff.

Inverse Hankel transform (IHT)

The field is then transformed back into the spatial domain using the inverse Hankel transform, which, in its discretized form for propagation, can be represented as:

$$U_f\left(r_j, F_i\right) = \sum_{k=0}^{n-1} P\left(K_k\right) J_0\left(K_k r_j\right) K_k \Delta K \tag{2.67}$$

where $P\left(K_k\right)$ is the phase-shifted and masked field in the frequency domain, and ΔK is the spacing between spatial frequencies, implicitly included in the computation.

The FBASM approach allows for efficient simulation of optically generated phonon field propagation, incorporating considerations for numerical accuracy and computational efficiency. Optoacoustic lenses design will be introduced in the following methods chapter (Section 3.1.2 and 3.1.3). Simulation results using FBASM will be presented in the results chapter (Section 4.1.1 and 4.2.1).

2.5 Nano fabrication

A major challenge in the proposed project is the fabrication of optoacoustic lenses, with smallest feature of $\sim 100nm$. Building these 2D and 3D micron, nanostructure requires different fabrication technology. Advanced nanotechnology research for 2D and 3D fabrication has been rapidly expanding in recent years. In 2D fabrication approaches, various lithography techniques, such as UV-lithography, electron beam lithography (EBL), X–ray lithography have been employed to create a variety of 2D patterns [125].

UV lithography employs UV light to transfer patterns from a mask to a surface, providing a resolution $\sim 100nm$. Its cost-effectiveness is a primary advantage, but it is constrained by the UV wavelength and the pre-requirement of masks, any new designs requiring new masks can increase the total cost and make the whole fabrication period longer. X-ray lithography, offering a finer resolution of

$\sim 15nm$, is lauded for its accuracy, efficiency, and speed; however, it is costly, and the masks used are delicate [126, 127]. Electron Beam Lithography (EBL) achieves resolutions below 10 nm by scanning a substrate with an electron beam to pattern a thin resist layer, followed by selective resist development. EBL stands out for its high precision and ability to handle complex and varied materials, though it is hampered by significant costs, intricate maintenance requirements, and slower patterning speeds due to the beam's serial nature [128, 129, 130]. But for prototyping and research interests, with the access to a nano-fabrication centre in the university, EBL became the best choice for the fabrication of flat structures designed in this thesis.

By using layer by layer strategies [131, 132, 133, 134], some 3D structures can be made based on those 2D fabrication techniques. However, such 3D fabrication techniques provided limited 3D fabrication capabilities because of a time-consuming layer-by-layer strategy, high cost of using expensive facilities multiple time, and limited ability for fabrication of designs with increased complexity and arbitrary designs [135].

Thus, a 3D fabrication technique that can perform direct making of 3D structures at a high resolution and also cost-effective process is highly desirable. Among all the new techniques, two-photon polymerization (TPP), nanoimprint lithography (NIL) and focused ion beam have the potential to make the required 3D structures for this thesis.

3D printing via two-photon polymerization (TPP) enables patterning within a photosensitive material using a focused laser beam, achieving resolutions of $\sim 50nm$. This technology, also known as direct laser writing (DLW), exposes a photo-reactive resin locally in three dimensions using pulsed, high-energy femtosecond laser beams [136]. This method eliminates the need for masks, simplifying the

creation and printing of complex 3D structures, yet it is constrained by the size of the working field, time efficiency, throughput, and associated costs [137, 138, 139].

Nanoimprint lithography (NIL) involves using a mold to shape a resist at the nanoscale, subsequently solidified by heat or UV light, capable of achieving resolutions of $\sim 10nm$. Its principal advantage lies in its suitability for mass production, but it is restricted by the optical and mechanical properties of the organic polymer resist used, such as its transparency and thermal stability [140, 141, 142].

Focused ion beam (FIB) milling utilizes a concentrated ion beam, typically gallium (Ga+), to perform precise sputtering or milling on targeted locations, with resolutions also below $\sim 10nm$. FIB milling is noted for its high precision and versatility in applications ranging from imaging to transmission electron microscopy (TEM) sample preparation. However, the introduction of Ga+ ions can result in additional contamination, radiation damage, and alterations to the structure of the material being processed [125, 143, 144, 145].

Among the methods discussed, Focused Ion Beam (FIB) milling is the chosen technique due to its superior flexibility in making various designs directly onto substrates like glass or sapphire substrate. This direct approach is particularly beneficial for transducer fabrication (more details about the transducers will be discussed in Chapter 3), as it avoids the potential damage or melting of polymers, a risk inherent to TPP when subsequent sputtering or evaporation processes are applied for metal thin-film deposition. Moreover, the availability of FIB milling machine within the university's nano centre facilitates convenient access, which, coupled with its capability to achieve high-resolution patterning, ensures the creation of lens profiles with the required quality for precise optoacoustic lenses.

2.5.1 Electron beam lithography

The concept of "lithography" traces back to Alois Senefelder's 1796 invention for efficient replication of texts and images via a limestone master template [146]. Today's nanofabrication largely relies on lithographic methods, involving the transfer of predefined patterns onto substrate surfaces. Driven by the electronics industry's continuous push for smaller feature sizes, a wide range of modern lithographic techniques have emerged for micro- and nano-scale patterning, catering to the needs of both industrial and academic sectors [147].

Electron beam lithography is a widely-used technique for creating structures ranging from multiple microns to sub 10 nm. It uses a finely focused electron beam to create latent images in resist layers. This exposure process alters the solubility of the photoresists: making it more soluble in positive photoresists or less soluble in negative photoresists. The resulting pattern is then developed, transferred via etching or by depositing other materials. Figure 2.27 shows the working principle of EBL. Complex structures at very small length scales can be fabricated by iterating a number of steps of this method [148]. Controlled by a computer, this method eliminates the need for a physical mask, making it more convenient for photomask patterning in the electronics industry. However, the use of a single writing beam in most electron beam machines results in a serial, and thus slower, patterning process. Consequently, its application is primarily confined to academic research, process development, rapid prototyping, and small-scale production, with mass production remaining beyond its scope.

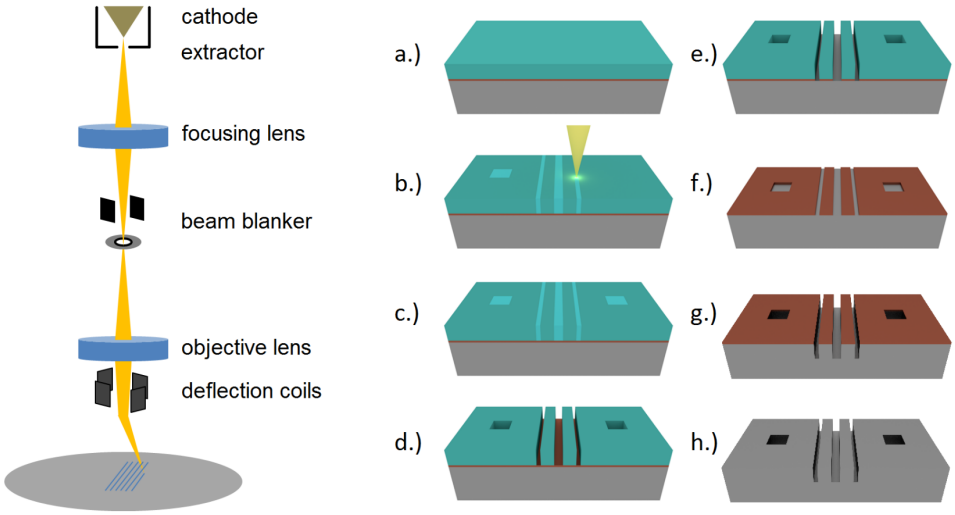

Figure 2.27: Electron beam lithography working principle. Left: Fundamental components of an electron beam lithography tool include a collimated electron source, beam blanking unit, focusing lens, and deflection system. Right: The patterning process typically begins with (a) a resist-coated substrate, followed by (b) electron beam exposure to define patterns in the resist. The process continues with (c) developing the exposed resist, leading to (d) selective dissolution. Subsequently, (e) the pattern in the resist is transferred to a hard mask. The (f) patterned mask is then (g) etched onto the substrate, and finally, (h) any remaining hard mask material is removed. Figure reproduced from [149]

2.5.2 Focused ion beam

Focused Ion Beam (FIB) micromachining is a sophisticated fabrication method for micro- and nanoscale structuring, enabling precision ion milling. FIB employs a focused ion beam for sample surface scanning and miling. Over recent decades, FIB has been of greater importance in the semiconductor industry, aiding in circuit modification [150, 151], repair [152, 153], and failure analysis [154, 155], as well as in materials science for Transmission Electron Microscopy (TEM) sample preparation [156, 157]. Modern FIB machines, typically dual-beam systems, combine ion and electron beams to facilitate simultaneous imaging and milling. As a mask-less, direct-write technique, FIB is widely utilized for the rapid development of various photonic and phononic [158] micro- and nanostructures across multiple applications.

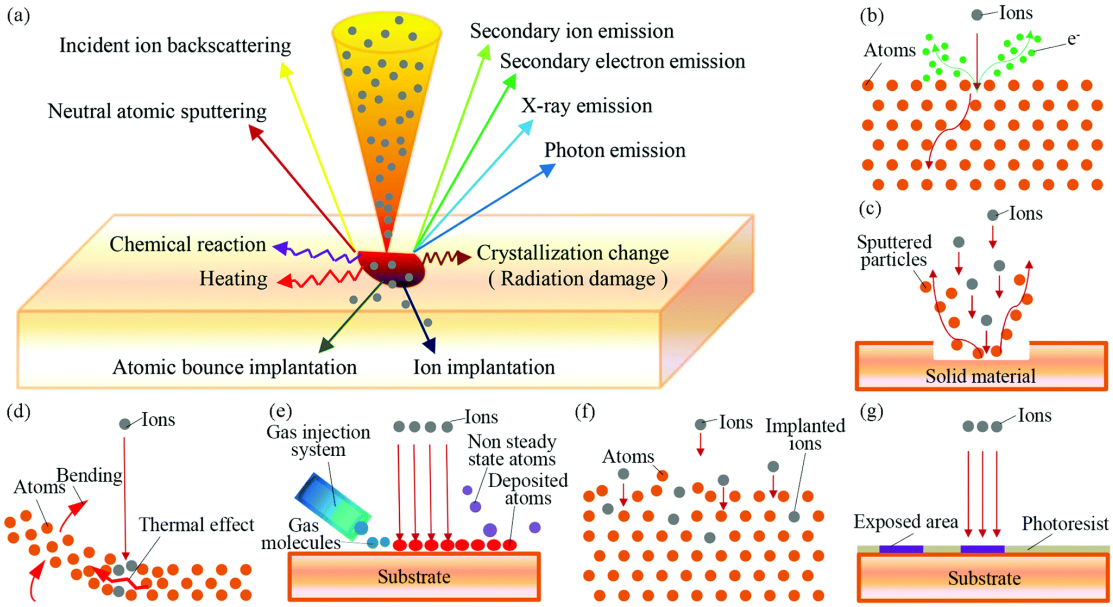

Figure 2.28: Basic principles and functions of FIB. (a) The basic interaction mechanism between the ion beam and solid material. (b)–(f) Schematic diagrams of the microscopic interaction mechanism between ions and atoms or molecules in (b) imaging, (c) etching, (d) irradiation, (e) deposition, (f) implantation and (g) lithography. Figure reproduced from [159]

FIB operates based on the physical phenomenon that collision cascade initiated when an accelerated ion strikes a surface. Sputtered target ions (i.e., nanomachining) are a common result of interactions, in targeted locations as well as additional side effects, such as beam heating, chemical reaction, crystallization change and implantation of atomic bounce and ions as shown in Figure 2.28 [158, 160, 161].

Similar to electron beam lithography, FIB has a slower writing process but achieves high resolution. Unlike the former, it does not depend on resist development, lift-off, and etching, and can often operate as a single-step procedure. By using a specific beam-steering protocol, the FIB system can precisely deposits energy at targeted locations, enabling the creation of 3D structure prototyping and combinatorial arrays with variable sizes, pitches, and aspect ratios in the milled structures.

2.6 Discussion

In conclusion, this chapter explores the evolving synergy between theoretical insights and experimental advancements in Brillouin scattering and picosecond laser ultrasound, and also the imaging techniques based on these techniques. It delves into the topic of wave focusing, ranging from fundamental principles of light and sound behaviour to advanced fabrication techniques that drive today's innovations. Additionally, the chapter provides a detailed discussion on non-invasive techniques related to acoustics. It also integrates the theoretical framework of Fresnel zone plates with practical uses of concave lenses, offering a comprehensive view of wave manipulation. Methods such as the Fourier-Bessel angular spectrum method (FBASM) and radially symmetric propagation are discussed, highlighting their significance in lens profiling and system setup. Lastly, the chapter underscores the importance of nano-fabrication techniques, like electron beam lithography and focused ion beam, as crucial for creating sophisticated wave-controlling devices.

Based on the theory and models developed in this chapter, more device design, fabrication and experimental methods will be discussed in the following methods chapter.

Chapter 3

Methods

In this chapter, the design and fabrication processes for optoacoustic lenses - including flat transducers, concave lenses, and flat zone plate lenses - are detailed. Various nano/micron fabrication techniques are employed to construct these structures. This is followed by an outline of the experimental set-up, detailing how the Asynchronous optical sampling system (ASOPS) is used to obtain time-resolved signals and the various configurations tailored to specific lens and experiment needs. The chapter also covers signal processing techniques, which encompass basic procedures to eliminate thermal background, digital filtering, and frequency domain analyses using FFT and wavelet. These methodologies are essential for understanding the experiments presented in Chapter 4. The foundational concepts and procedures discussed here pave the way for the experimental results that follow.

3.1 Optoacoustic Lenses

In this section, the focus is on introducing various designs of optoacoustic lenses specifically crafted for the generation and precise focusing of gigahertz (GHz) acoustic waves. The chapter provides an extensive examination of these optoacoustic lens designs, emphasizing their innovative features and highlighting their pivotal role in advancing scientific research and imaging technology.

Section 3.1.1 introduces a flat optoacoustic transducer design. It covers the optimization of this transducer for signal quality and thermal performance. This optimization process involves examining various design parameters to ensure that the transducer can produce clear and strong signals while remaining thermally stable, even in demanding operational conditions. This section provides valuable insights into the design and functionality of optoacoustic transducers, which are crucial components for later lenses design with more complicated geometrical structures.

In Section 3.1.2, various lens designs will be showcased, each with its distinctive features and potential applications. The discussion will extend to examining simulated outcomes using the models introduced in Section 2.4. Through the analysis of simulation results, we can evaluate the efficacy of these lenses in theory.

The section 3.1.3 will focus on discussing the theoretical performance of various designs, addressing practical fabrication challenges, and analysing the trade-off between these two aspects. The ultimate goal is to make informed choices in design compromises that enable the achievement of the best possible results.

The last section 3.1.4 will go through the NA of acoustic lenses, detailed definition and calculation will be introduced.

3.1.1 Transducer design and simulation

As discussed in the previous background section, an optoacoustic transduction component that converts optical photons into acoustic phonons is required. This conversion is achieved thermo-elastically, meaning a metallic thin-film is used to absorb ultra-short femtosecond (fs) pump pulses, generating picosecond strain pulses as a result. Therefore, the performance of this metallic transducer depends on its optical and thermal properties. Phonon microscopy has shown that a metallic-dielectric zero-order Fabry-Perot interferometer can be designed to achieve required cell imaging goals. This interferometer creates a cavity that resonates both optically and mechanically, while also protecting the specimen from transducer-induced heating [162, 163]. However, for this study's proof of concept, a single metallic layer will be used.

The basic design idea is to presuppose that the acoustic wave is launched perpendicular to a sufficiently small meta-structure, with the main consideration being the focusing effect that the particular lens geometry will have on the GHz acoustic wave of interest (determined by the probe laser and the medium in which the acoustic wave is delivered). Figure 3.1 shows optoacoutic transducer designs with different geometries, from flat to lenses with different geometric designs, including Fresnel Zone Plate (FZP), Phase-Reversed Fresnel Zone Plate (PR-FZP) and concave lenses.

The overall design concept can be effectively divided into two distinct components. First, there's the optimization of the flat transducer's performance. This entails fine-tuning various parameters and characteristics to ensure that the transducer functions at its best, delivering optimal results in terms of generating and transmitting/reflecting acoustic signals.

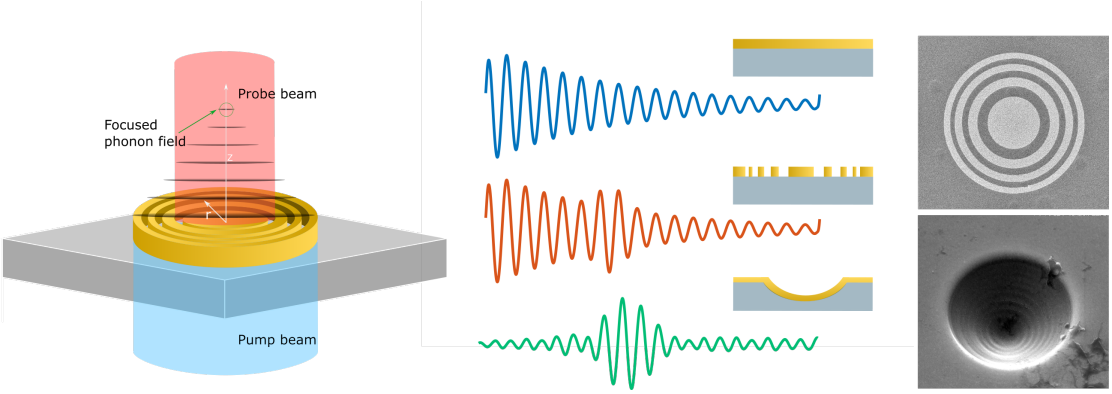

Figure 3.1: Basic device concept: multiple geometrical design over glass substrate

Secondly, there's the geometrical design aspect, which involves crafting the specific shapes and configurations of different lenses. These lenses are engineered with a particular goal in mind: to achieve desired focusing effect of the sound waves at specific frequency - Brillouin frequency.

Layer material and thickness choice

As introduced in Section 2.2, an analytical model based on TMM was introduced to calculate the transmission and reflection coefficient of light through multi layer thin film structure, PLU was also introduced to simulate the TRBS signal intensity.

A comparison has been made between the performance of gold and other materials that can be coated using a sputter coater, as well as often mentioned materials in the literature (gold (Au), silver (Ag), copper (Cu), chromium (Cr), aluminium (Al), and titanium (Ti)) [25] in Figure 3.2 and 3.3. The amplitude of the frequency peak of water is used as a measure of the signal amplitude that the transducer is capable of producing.

Though the simulation results indicate that copper (Cu) provides the best potential for higher TRBS signal amplitude, gold (Au) ranks as the second-best. However, considering ease of fabrication (Au sputtering is directly accessible within

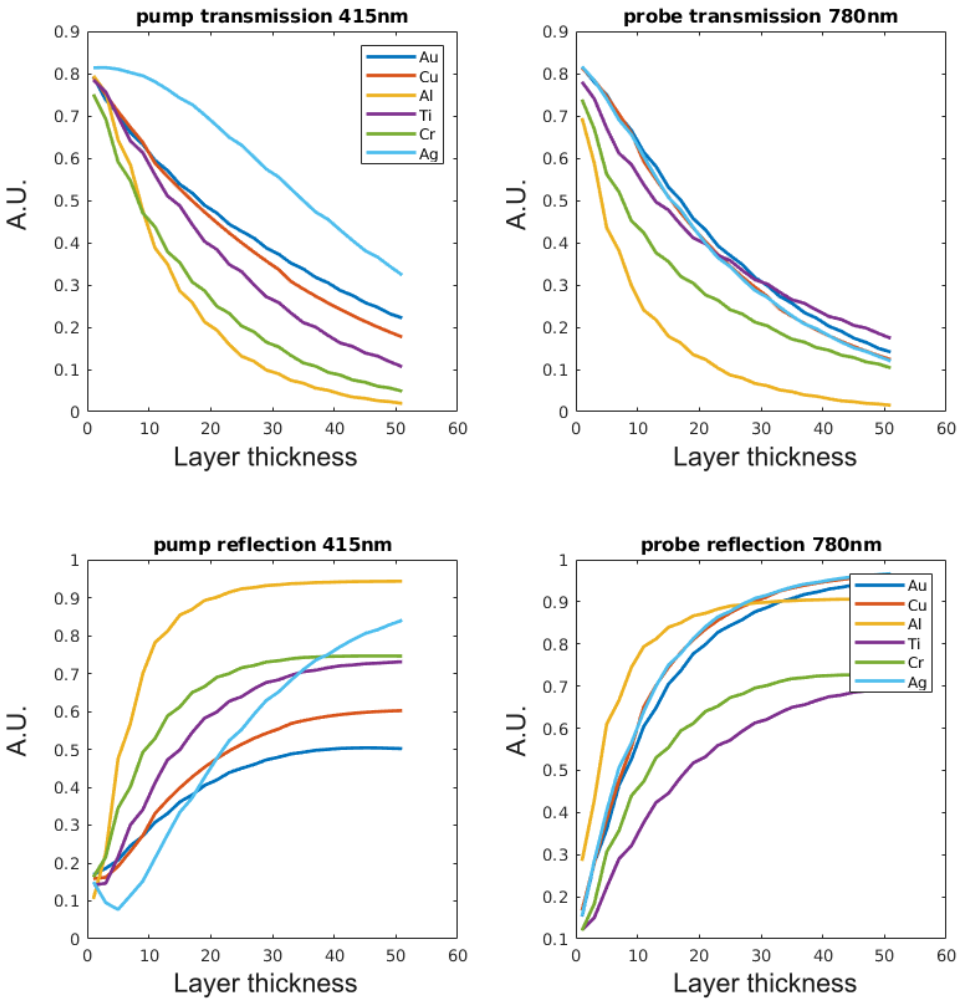

Figure 3.2: Compare different metals' transmission (top) and reflection (bottom) for pump (left) and probe (right). For each subplot, x-axis is the thicknness of the corresponding metal and the y-axis are normalised transmission or reflection value.

the lab) and good reflection for $\lambda_{probe} = 780nm$, as shown in Figure 3.2, Au was chosen. Furthermore, the Au trace in Figure 3.2 suggests that a maximum signal amplitude might be achieved with an Au layer of approximately 25nm thick. Meanwhile, within the range of the simulation, an increase in the thickness of the Au layer does not significantly change the signal amplitude. Thus, for device thermal performance considerations, such as better insulation from the near-ultraviolet (NUV) radiation of the pump, an Au layer of approximately 30nm thick is selected

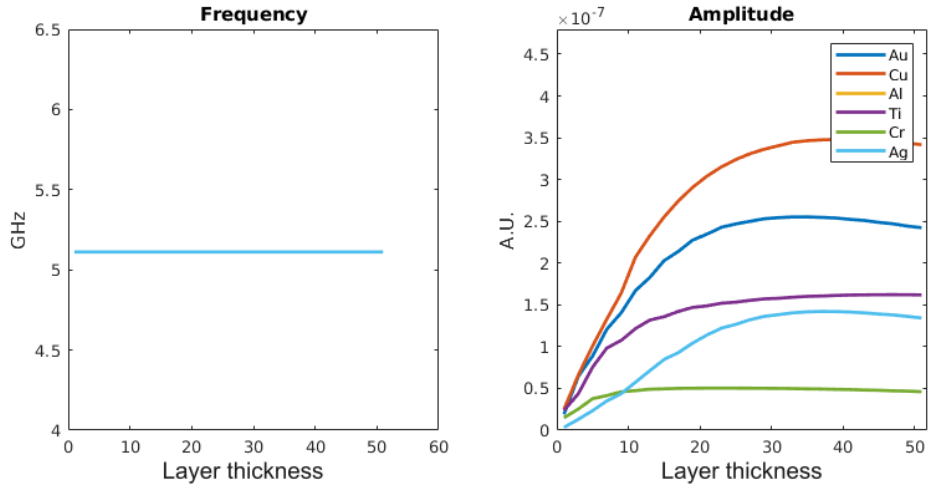

Figure 3.3: Compare different metals' Brillouin frequency and amplitude vs metal layer thickness. Left is the dominant water Brillouin frequency. Right is the signal amplitude of different metal materials, x-axis is the thickness of the corresponding metal.

for later fabrication.

3.1.2 FZP design

Binary FZP

Similar to how a conventional optical lens works, Fresnel zone plates can be used to focus waves by creating a wave with a greater amplitude at the focus. According to some earlier research, Fresnel zone plates have the ability to amplify sound waves in specific directions [164]. The radius and width of each ring is calculated for the sound wave to have path lengths that will constructively interfere at the focus as discussed in the background section 2.3.3. The difference between positive (centre being filled) and negative (centre being empty) Fresnel zone plates will be demonstrated in the design. As mentioned before, due to the Bragg condition, we can get the wavelength of the phonon of interested:

$$\lambda_{\text{phonon}} = \frac{\lambda_{\text{probe}}}{2n} \tag{3.1}$$

Figure 3.4 shows a recap of the device concept of FZPs proposed in the background chapter (Section 2.3.3). The FZP ring radius r_n is given by:

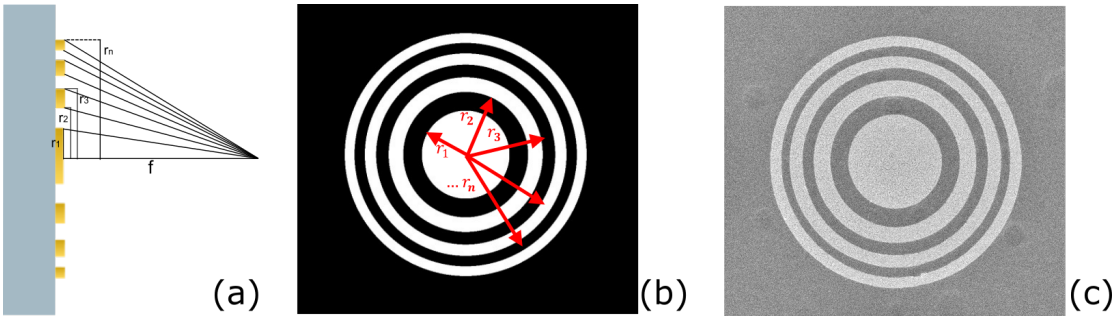

Figure 3.4: (a, b) Focusing principle of FZP. (c) SEM picture of an EBL made FZP.

$$r_n = \sqrt{n\lambda_{\text{phonon}}\, f + \frac{(n\lambda_{\text{phonon}})^2}{4}} \tag{3.2}$$

where f is the designed focal length; n is the number of rings.

From this equation, the radius r_n can be calculated based on a specific focal length and number of rings. Meanwhile, for each set of r_n, all even, or all odd, plates can have a constructive effect, effectively making up negative or positive FZP, respectably. Figure 4.1 shows an example of a pair of positive and negative FZPs. Finally, based on the calculated FZP parameters, a GDSII file can be generated using MATLAB for EBL fabrication as shown in Figure 3.5, a viewing/editing software Klayout was used to capture this snapshot. More details about GDSII file can be found in Appendix B.

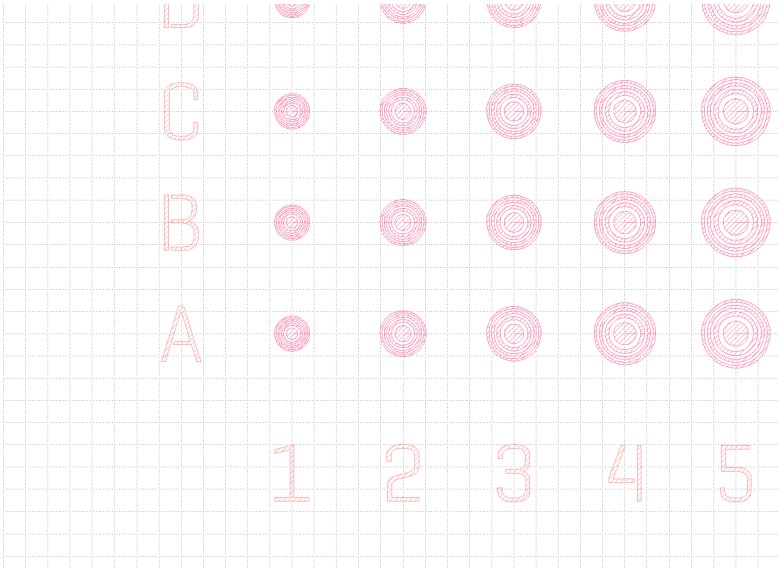

Figure 3.5: Snapshot of a GDSII file with multiple FZPs.

Phased reverse FZP

FZP mainly includes two types: normal FZP and phase reversal FZP. The none OAT transducer region won't absorb the pump energy and generate no coherent phonon field. Since almost half of the incident laser energy is wasted by the empty regions, the normal FZP has a low focusing ability. PR-FZP replace empty regions with phase reversal regions that correct the phase of the pressure contributions by adding a π phase change that generates constructive interference at the focal distance [165, 166]. The focusing ability of PR-FZP is usually higher than that of normal FZP, so it has a better application prospect [167].

The transmission and phase reversal regions are typically included in the concentric circle structure in a PR-FZP. In this case, we have two layer of transducer plane with a depth difference as shown in Figure 3.6 (a). Both regions contribute to the focusing of acoustic energy.

Phase-Reversal lenses, unlike traditional FZPs, take advantage of all the incident energy by adding phase compensation regions instead of binary energy blocking

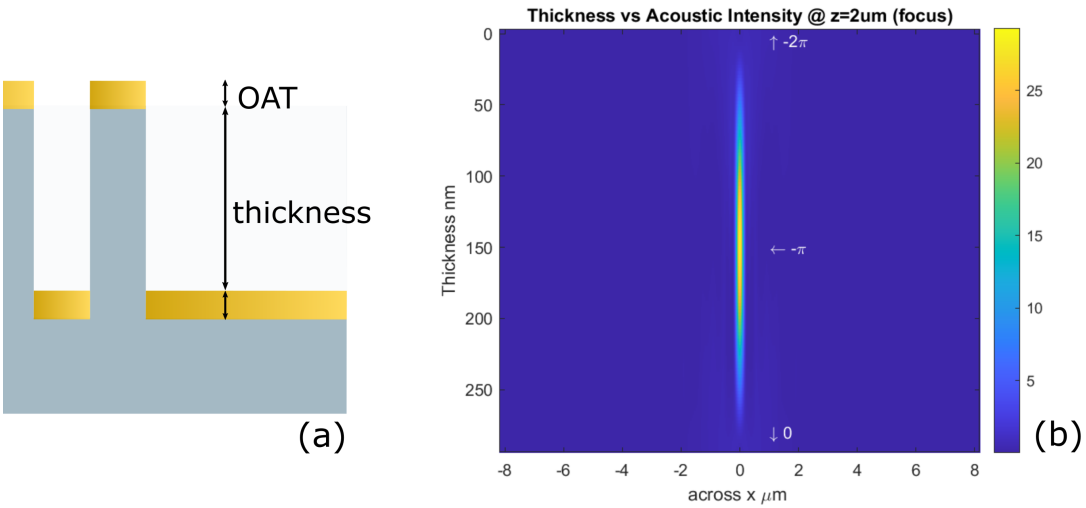

Figure 3.6: Simulated signal intensity vs phase difference.

regions. By using the FBASM model introduced in Section 2.4, as shown in Figure 3.6 (b), the maximum signal vs thickness of two layers were found around π phase difference (around 150 nm).

3.1.3 Concave lens design

Concave acoustic lenses represent a straightforward approach to focusing acoustic waves, leveraging their three-dimensional structures to manipulate the direction and concentration of energy. Unlike the Fresnel Zone Plates discussed earlier, which are planar diffractive structures, concave lenses are inherently three-dimensional and thus present unique challenges in nanofabrication. The complexity of their shape necessitates the use of specialized fabrication techniques such as Focused Ion Beam (FIB) milling, which allows for precise sculpting of the lens profile directly into the substrate material.

Despite the complexities in their fabrication, concave lenses offer significant advantages in terms of energy efficiency. Their curved surfaces are inherently adept at capturing and redirecting the entirety of the incident pump laser energy, ensuring

minimal loss and maximum transfer of energy to the focused acoustic field.

Moreover, the durability and reusability of these concave structures add to their appeal. Fabricated by milling into robust materials like glass substrates, they can withstand repeated use. After conducting experiments, the lenses can be easily regenerated through a process of acid cleaning followed by re-sputtering of the functional layers. This ability to recycle the lenses for multiple tests without degradation in performance is an economical and practical advantage, allowing for extended research use and consistent experimental conditions.

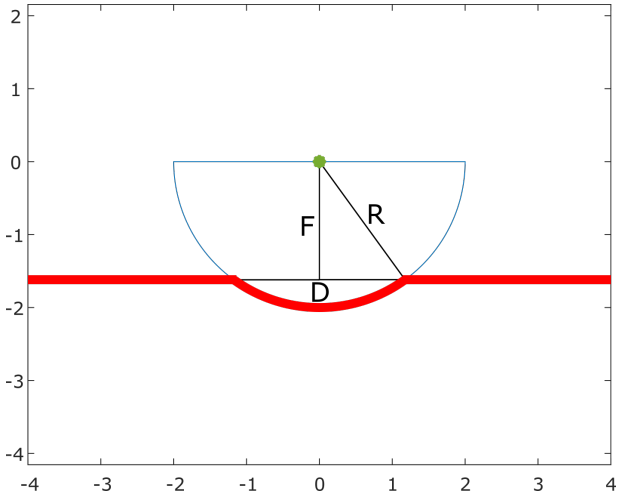

Figure 3.7: Schematic diagram of the design of a concave lens.

Figure 3.7 depicts the design of a single concave optoacoustic lens intended for GHz sound focusing applications. A half circle shape represented by a blue line that forms a U-shaped curve, this curve suggests the design of the lens which focuses acoustic waves towards the focal point at the centre of the half circle (The small green circle.). Red line indicates the optoacoustic transducer layer, the curvature is proposed to be made using FIB (more details around fabrication will be introduced in the following fabrication Section 3.2.3).

A series of nine concave lenses designs are arranged in a 3×3 grid as shown in Figure 3.8. From left to right, the columns indicate increasing focal lengths of

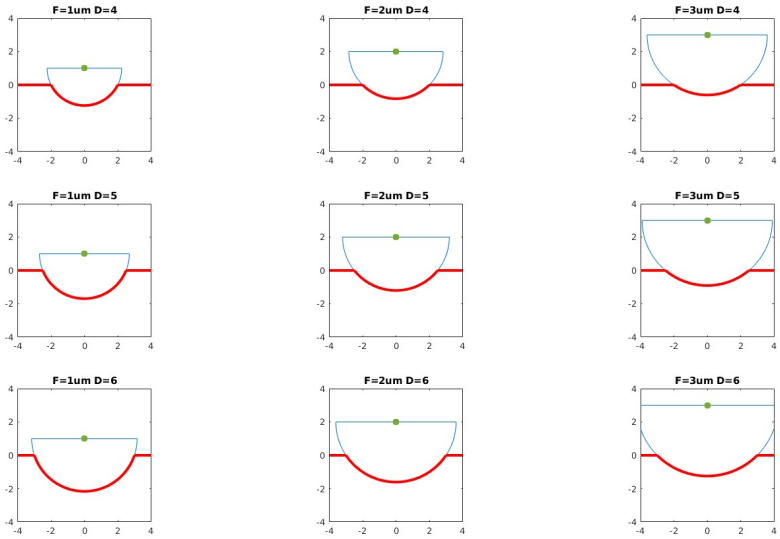

Figure 3.8: Concave lens designs with different focus and diameters.

the lenses: F=1, F=2 and F=3 μm. From top to bottom, the rows correspond to increasing diameters of the lens at the ground surface: D=4, D=5, and D=6 μm.

3.1.4 NA of acoustic lenses

The "Numerical Aperture" (NA) is the most important number associated with the light/sound gathering ability of an optical or acoustic lens. It is directly related to the angle of the cone which is formed between a point on the specimen and the front lens for either light or sound [168, 169], determined by the equation:

$$\mathrm{NA} = n \sin \alpha \tag{3.3}$$

At room temperature, water's optical refractive index n is $n = 1.333$ (though it varies slightly with temperature). In terms of acoustics, it is the sound velocity divided by the sound velocity of a reference material, most commonly water; hence, water has an acoustic refractive index of 1. Since this thesis trying to achieve

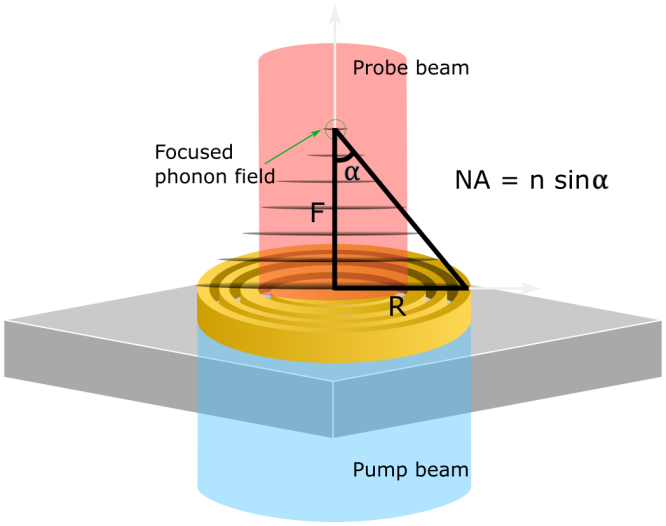

Figure 3.9: Numerical Aperture (NA) of the proposed acoustic lenses.

acoustic focusing in water as shown in Fig. 3.9, thus here $n = 1$ is used for the calculation results in chapter 4. Knowing the radius R and focus F, NA can be calculated as:

$$\mathrm{NA} = \frac{R}{\sqrt{R^2 + F^2}} \tag{3.4}$$

3.2 Optoacoustic lens fabrication

In order to fabricate all the designs of different optoacoustic lenses discussed above, multiple nano/micron-scale fabrication techniques, including Electron Beam Lithography (EBL), Focused Ion Beam (FIB), and thin-film deposition techniques such as sputtering and thermal diffusion, will be used and discussed in this fabrication section.

3.2.1 Transducer fabrication

In order to form thin-films of the materials discussed above in Section 3.1.1, the physical vapour deposition technique - sputtering will be used. Prior to fabrication, a substrate cleaning process is involved for better fabrication quality, following that is the thin film deposition process, finally a thin-film transducer characterisation process is performed to check the fabrication quality.

Substrate cleaning process: Before beginning the deposition process, the substrates underwent cleaning, which involved four steps. In each step, the substrates were placed in a glass beaker filled with one solvent, and the beaker is then placed in an ultrasonic bath machine. The solvents used were ethyl-lactate, acetone, methanol, and isopropanol (IPA), applied in that sequence, with each step lasting for 10 minutes. Before moving to the next step, the substrates were rinsed with the subsequent solvent. Once the final cycle (IPA) was completed, the substrates were dried using nitrogen gas [25].

Thin film layer deposition: Au and ITO depositions were performed with a sputter coater (HHV BT300). First mounting the samples to the removable rotating stage using conductive tapes. Then the machine is pumped down to a vacuum of approximately 1×10^{-4} mbar. Once the required vacuum is achieved, argon gas (used as a sputtering catalyst) is introduced into the chamber. The thickness of the deposited material is determined by a combination of the plasma current (applied to the magnetron) and the duration of the deposition process. To establish a calibration for the sputtering deposition process, it's important to characterize this deposited thickness.

Transducer layer characterisation

Having accurate knowledge of the device dimensions is crucial for effectively comparing theoretical and experimental performance. Here a convenient and low-cost white light spectroscopy method was used to measure the film thickness based on the transmission spectra of the device. A Matlab script was written in order to determine the film thickness from the experimental transmission spectrum, which was normalised by the transmission spectrum of only the glass substrate. Details of the white light spectroscopy and the analysing script can be found in Appendix A.

Using the assumption that the material identity of the film is known (e.g. gold), the optical properties of that material can be used to simulate theoretical transmission spectra (using the aforementioned Fresnel coefficient model) over a range of potential thicknesses (blue curves in Figure 3.10 (a)). The best matched theoretical spectrum is located and assigned as the thickness measurement (fit quality in Figure 3.10 (b)).

3.2.2 Fresnel lens fabrication

Fresnel Zone Plates (FZPs) are flat lenses that can focus energy beams without relying on the more challenging-to-manufacture concave or convex geometries.

Flat FZP made with Electron Beam Lithography (EBL)

The fabrication process of the Fresnel Zone Plate (FZP) samples involved a sequence of steps integrating Electron Beam Lithography (EBL) and thermal evaporation deposition techniques. The following section details each essential step in

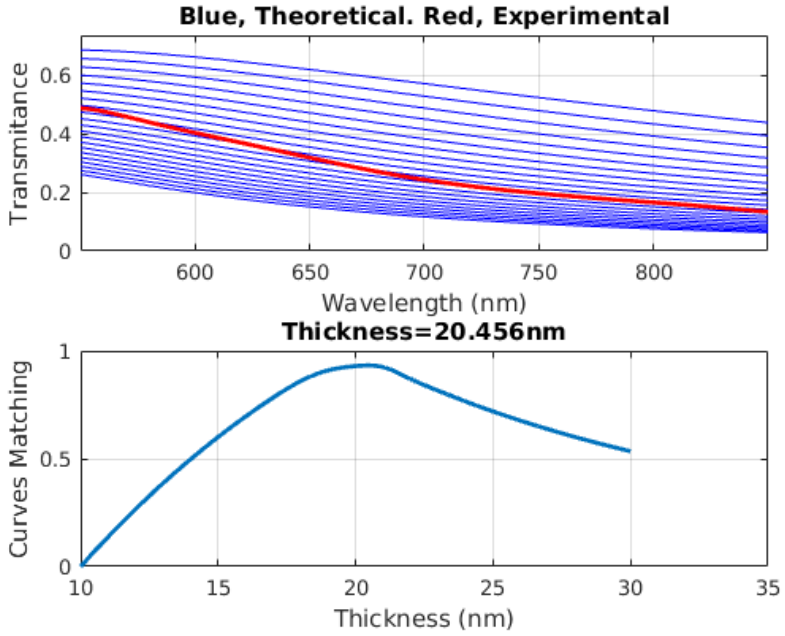

Figure 3.10: Example shows the results of a script used to measure the thickness of a gold layer. On the top, blue lines represent model curves and the red lines shows the experimental data. Below, the curves are compared. If the model and theory perfectly match, the curve's value is one. In this case, the thickness of the ITO layer for the device being measured can be found at the peak of the matching curve.

the fabrication process and a process flow is shown in Figure 3.11:

1. **Substrate preparation and resist layer application**

   The fabrication process began with the selection of a glass coverslip as the substrate. Before proceeding, the coverslip underwent thorough cleaning to ensure a clean surface free from contaminants. Subsequently, an electron beam resist layer (AR-P 6200) was uniformly coated onto the cleaned glass coverslip. This resist layer served as the primary pattern for the subsequent lithographic steps.

2. **Introducing the conductive protective layer**

   During electron beam exposure, it was important to mitigate charge build-up effects that could degrade the quality of the fabricated FZP pattern. To

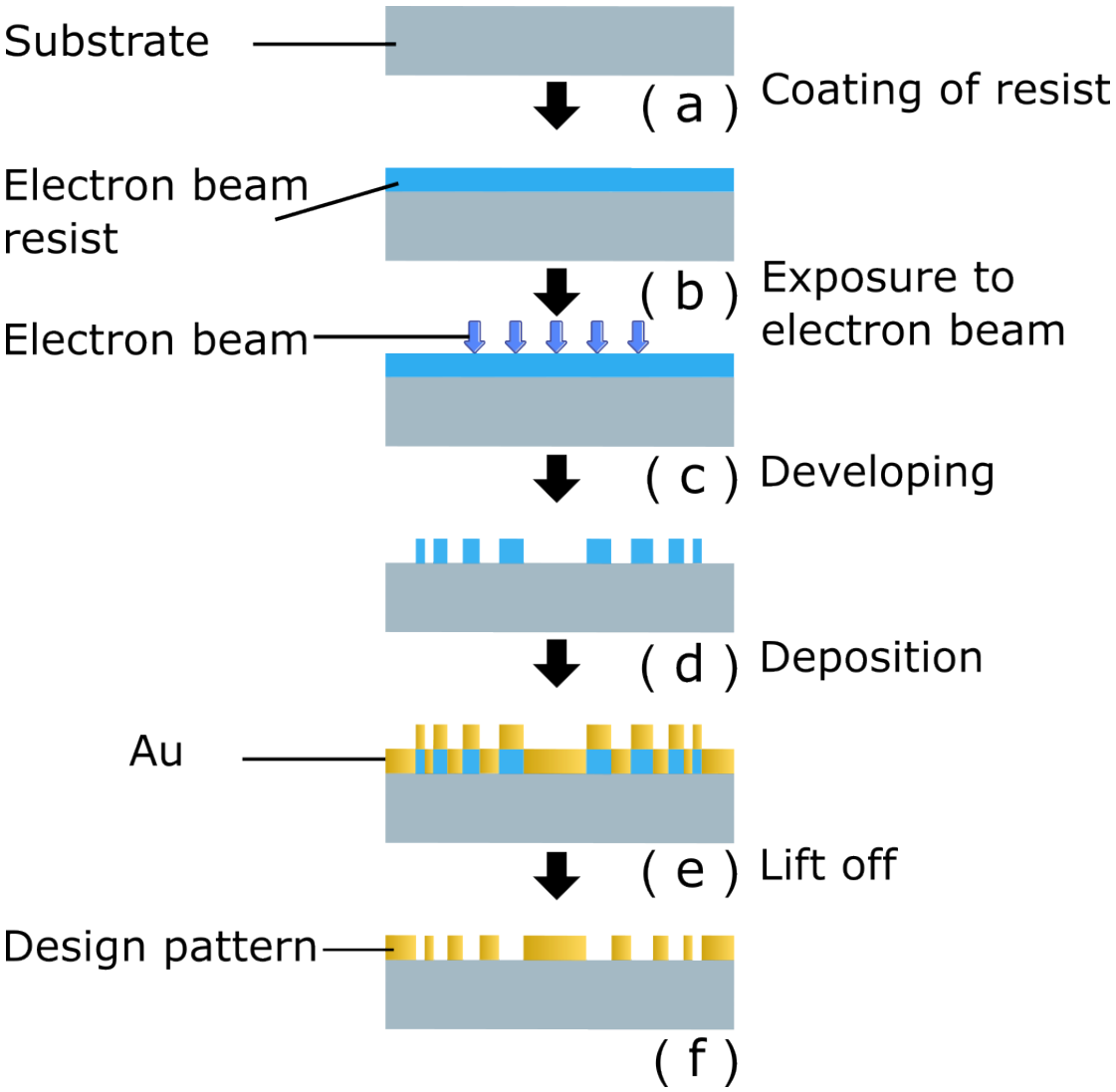

Figure 3.11: Process flow for submicron fabrication on flat structure: (a)-(b) Photolithography resist is deposited on a cleaned substrate using spin coating method. (c) E-beam applys a predefined mask (programmed with GDSII). (d) After developing, only the reverse mask of resists remained. (e) Then deposit Au over the top of the whole sample. (f) Perform lift-off to get the final design.

address this, an extra protective and conductive layer (AR-PC 5090) was carefully applied on top of AR-P 6200. This conductive layer was designed to dissipate the charges efficiently during electron exposure, preserving the fidelity of the pattern. Special attention was given to selecting an appropriate conductive material and optimizing its thickness to achieve optimal charge dissipation without compromising other performance aspects.

3. **Soft baking and electron beam exposure**

   To stabilize the resist layers and improve their adhesion to the substrate, a soft baking procedure was conducted. The soft baking conditions were optimized to achieve the desired mechanical properties of the resist layers. Following soft baking, the coverslip underwent electron beam exposure utilizing a Nanobeam nB5 device with custom GDS designs. The electron beam exposure was crucial in defining the intricate patterns required for the FZP sample.

4. **Removal of the conductive protective layer**

   After successful electron beam exposure, the conductive protective layer was no longer required. A washing process involving deionized water was carried out to gently remove the conductive layer without causing any damage to the underlying pattern.

5. **Deposition of Indium Tin Oxide (ITO) and gold (Au) layers**

   To enhance the functionality of the FZP samples, a 5 nm layer of indium tin oxide (ITO) was carefully deposited on the exposed pattern. The ITO layer contributed to improved adhesion of the next Au layer to the substrate and provided additional protection to the FZP structure. A 20 nm layer of gold (Au) was applied using a n-type thermal evaporator. The choice of gold thickness was specifically tailored to allow the passage of probe light, essential for the intended optical functionality of the FZP sample.

6. **Lift-off procedure**

   The final step in the fabrication process involved the lift-off procedure using AR 600-546. This step aimed to remove any excess materials, leaving only the well-defined pattern of the FZP sample on the glass coverslip. The lift-off procedure was performed with precision to ensure the final FZP structure's accuracy and integrity.

Due to the small size of a single FZP, only a few µm, it is difficult to locate its exact position in experiments. Furthermore, due to a certain loss rate in the EBL production process, each fabrication run produces an entire array of FZPs simultaneously, with different designs (and multiple repetitions of each design) being formed into a large design pattern. As shown in the Figure 3.12 (a), this is a design pattern including both positive and negative FZPs. Each region is designed for better positioning and to avoid large unusable areas caused by EBL production or sample transportation. The horizontal numbers and uppercase letters serve similar purposes. Figure 3.12 (b) then zooms in on a 10×10 lens array, where lens focal lengths range from 1 µm to 10 µm, corresponding to the design's focal lengths, and letters A to J repeat in the same row. The distance between each lens is 10 µm, allowing multiple FZPs to be scanned in a single experiment without the need for repeated calibration of laser focusing, signal intensity, etc.

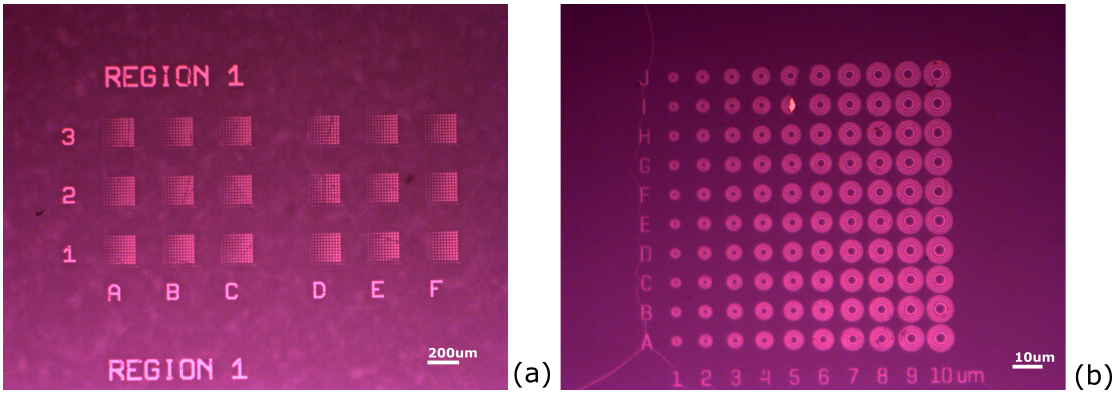

Figure 3.12: Optical pictures of the design pattern of EBL made FZPs. (a) Big letters of Region and labelling of FZPs with different designs. (b) Zoom in of a area of negative FZPs.

The fabricated Fresnel Zone Plates (FZPs) on a glass substrate are checked using a Scanning Electron Microscope (SEM) to characterize their properties and assess fabrication quality. To perform SEM on these samples, they must be conductive. This can be achieved through either a permanent ITO coating above the substrate or a washable chemical conductive layer applied after the FZPs' fabrication. The SEM facilities available at the Nanoscale and Microscale Research Center (NMRC)

at the University of Nottingham include the JEOL 7000F FEG-SEM and JEOL 7100F FEG-SEM. Some characteristics of these instruments are described below in table 3.1. The two machines listed share very similar capabilities, as they are very similar models. Both are used due to their availability at the NMRC:

SEM Specification	
Model	JEOL 7X00F FEG-SEM
Electron Source	Schottky Field Emission Gun
Accelerating Voltage	0.5 to 30 kV
Resolution	1.2nm (30kV), 3.0 nm (1kV)
Probe Current	1 pA to 200 nA
Magnification	10× to 500,000×

Table 3.1: Major Specifications of SEM.

Figure 3.13 showcases example SEM pictures of the EBL-made lenses: 3.13 (a) and (b) are SEM images of EBL-made FZPs, while 3.13 (c) is an SEM image of a FZP made with nanorods. All were created using the process introduced in this section, featuring a 20nm Au layer and mounted on a glass substrate. Experimental results of conventional FZPs will be discussed in detail in the following results chapter 4, and more on the device concept and preliminary discoveries of FZPs made with nanorods will be covered in the Phase-Reverse FZP Section 3.2.4 and preliminary results and perspectives Section 5.2.

3.2.3 Concave lens fabrication

Focused ion beam (FIB) milling is a popular technique in the semiconductor industry, materials science research, and for prototyping nano/micron devices with both 2D and 3D structures due to its precision and ability to produce small features. In this section, the design and fabrication process of concave lenses over glass substrate is described in details.

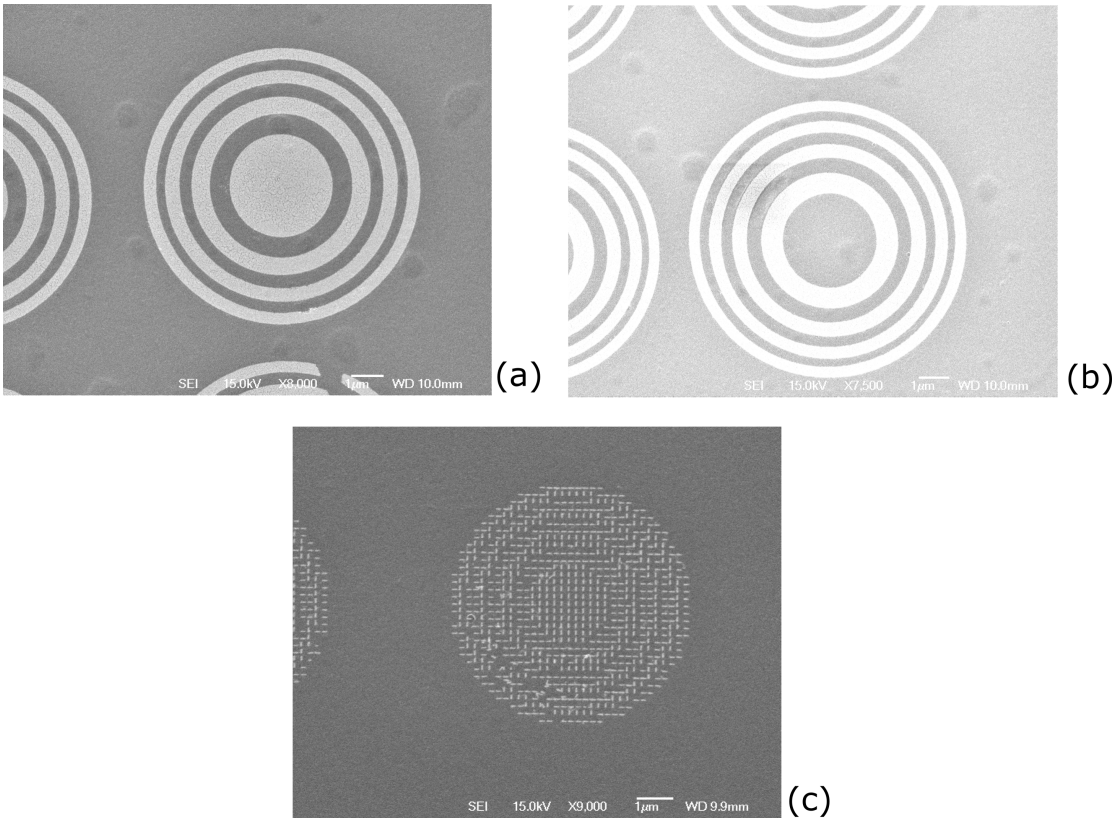

Figure 3.13: (a) and (b) are SEM snapshot of two different FZP lenses. (c) Fresnel Zone Plate made up of nanorods, in this case, the rods are 160nm×40nm and they are in two perpendicular orientations.

Fabrication process

3D-FIB processing is performed as follows (Figure 3.14). Figure 3.14 (a) illustrates the desired final dish-like structure. We have a concave surface with a depth (U_0) and a diameter (D_0). The angle θ_0 represents the inclination angle of the dish's edge with respect to the horizontal plane. The relationship between D_0, θ_0 and the designed focus F are defined using below functions:

$$U_0 = D_0 \left(1 - \cos\theta_0\right) / 2 \sin\theta_0 \tag{3.5}$$

$$F = D_0 / 2 \sin\theta_0 - U_0; \tag{3.6}$$

Figure 3.14 (b) showcases the sequential FIB milling process. The FIB is directed to mill the material layer-by-layer, with a single layer milling height of h_0. The milling begins from the top, gradually removing material to create a concave structure. The layers represented by the horizontal lines indicate the progressive removal of material from the substrate. Fig. 3.14 (c) showcases the intermediate stages of the FIB milling process. Each "No." represents a progressive milling step.

$$U_0 = L \cdot h_0 \tag{3.7}$$

Figure 3.14 (d) represents the final result of the FIB milling process.

In summary, the provided figures illustrate a FIB-based method to fabricate a dish-like structure. The method starts with the desired design, followed by sequential layer-by-layer milling using a FIB, until the final desired depth and shape are achieved.

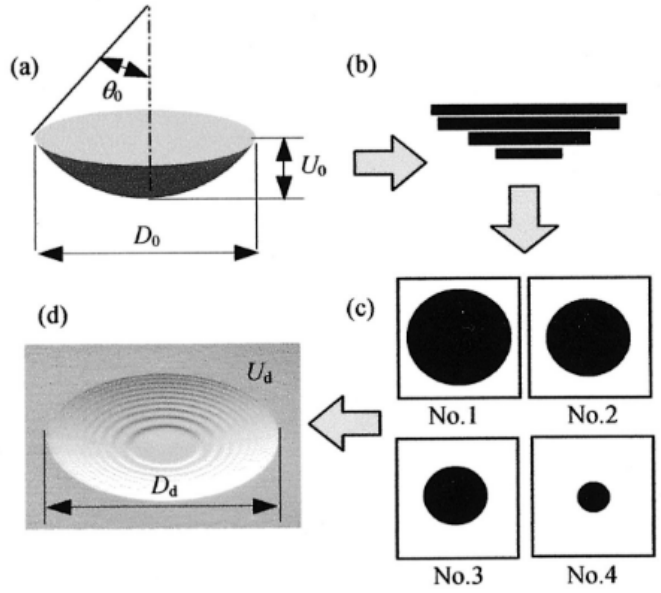

Figure 3.14: Illustration of 3D-FIB etching process. Image (a) and (c) reproduced from [170].

FIB layer choice An important consideration in the fabrication process is the selection of the number of layers. In microfabrication, the precision and uniformity of the resultant structure often depend on the granularity of the layers being milled. For a structure aiming for a depth of 2-3 μm, a minimum of 15 layers is recommended. This is based on multiple fabrication experiences and ensures that each layer is milled to a thickness of approximately 150-200 nm.

Such granularity allows for more controlled and uniform milling, reducing the risk of defects and ensuring consistent structural properties across the entire dish. Furthermore, using multiple thinner layers as opposed to fewer thicker ones can result in smoother surfaces, as shown in Figure 3.15 (b), minimizing post-processing needs. Figure 3.15 (a) shows the result of fabrication using an insufficient number of layers. The outcome is quite rough, and the individual layers are clearly distinguishable.

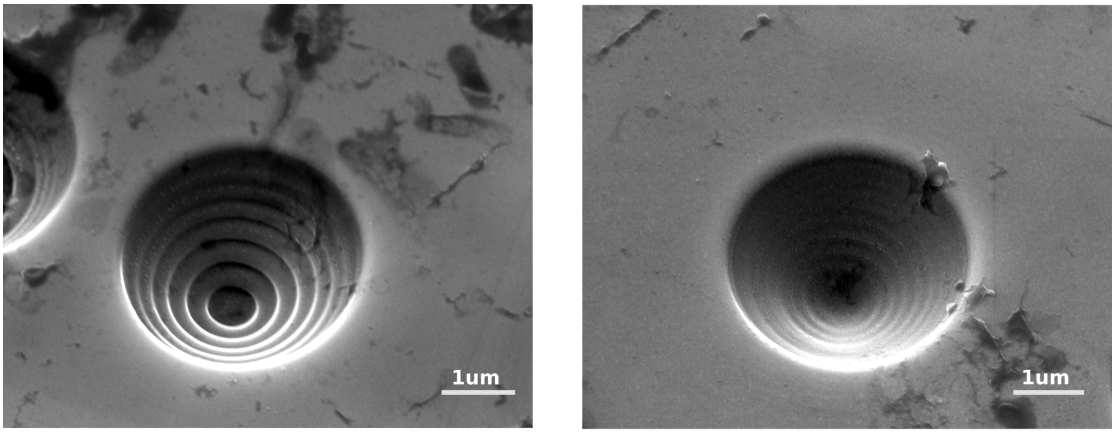

Figure 3.15: Typical SEM images of concave lenses FIB-etched with different number of layers (L) and thickness of each layer (h_0), (a) is with 8 layers and (b) is with 15 layers.

3D lens made with Focused Ion Beam (FIB)

The fabrication process of the 3D concave lenses involved a sequence of steps integrating Focused Ion Beam (FIB) and metal sputtering techniques. The following section details each essential step in the fabrication process and a process flow is shown in Figure 3.16:

1. **Substrate preparation and adhesion layer application**

   In the initial phase of the Focused Ion Beam (FIB) fabrication, the substrate was prepared and an adhesion layer was applied. The substrate underwent thorough cleaning to remove contaminants, ensuring an ideal surface for the layers that followed. In a manner similar to the prior fabrication of the EBL-made FZP lens, a thin indium tin oxide (ITO) layer was applied to improve adhesion and serve as an intermediary surface, especially for bonding with gold (Au).

2. **Loading pre-designed design files**

   The pre-designed files from the earlier design section were loaded to define patterns. Patterns could be directly drawn using the default FIB software, which allowed for a series of concentric circles with consistent thickness but varying radii, or they could be imported as BMP files.

3. **Milling and SEM check**

   The subsequent step involved milling while simultaneously performing Scanning Electron Microscopy (SEM) checks. FIB settings played a crucial role in determining milling precision. The choice between imaging and milling impacts real-time adjustments. The primary process parameters that had effects included acceleration voltage, ion beam current, dwell time, volume per dose, and milling time. A more detailed selection of these parameters will be discussed in the subsequent FIB process parameters section.

4. **Transducer layer sputtering**

   Similar to the fabrication of flat transducers, the deposition of ITO and Au was performed using a sputter coater (HHV BT300). The same thin film layer characterization was also conducted. A 5nm ITO and a 30nm Au layer were deposited onto the concave glass structures to create a functional curved 3D optoacoustic lens.

Meanwhile, although FIB may lack the advantage in batch producing lenses, it offers the benefit of enabling sample recycling, thus allowing for reuse in multiple rounds when the transducer layer is damaged or contaminated with bacteria or other dirt.

FIB process parameters

The FIB facility available and used at the Nanoscale and Microscale Research Center (NMRC) at the University of Nottingham is FEI Quanta 200 3D Dual Beam FIB-SEM system. Some characteristics of this machine are described below in table 3.2.:

Dish recycling

Sputter coated transducer layer can be stripped using a mixed acid solution so the FIBed dishes over glass substrate can be re-coated and used for different purposes: such as dirts blocking the lens or different transducer layer required for different experimental purpose. A standard solvent cleaning process as the one described in Section 3.2.1 was also required after the acid cleaning process. All chemicals were used within a fume hood at all times for health and safety purpose.

A substrate recycling solution was made by mixing 2ml Nitric acid (68%) with 1ml

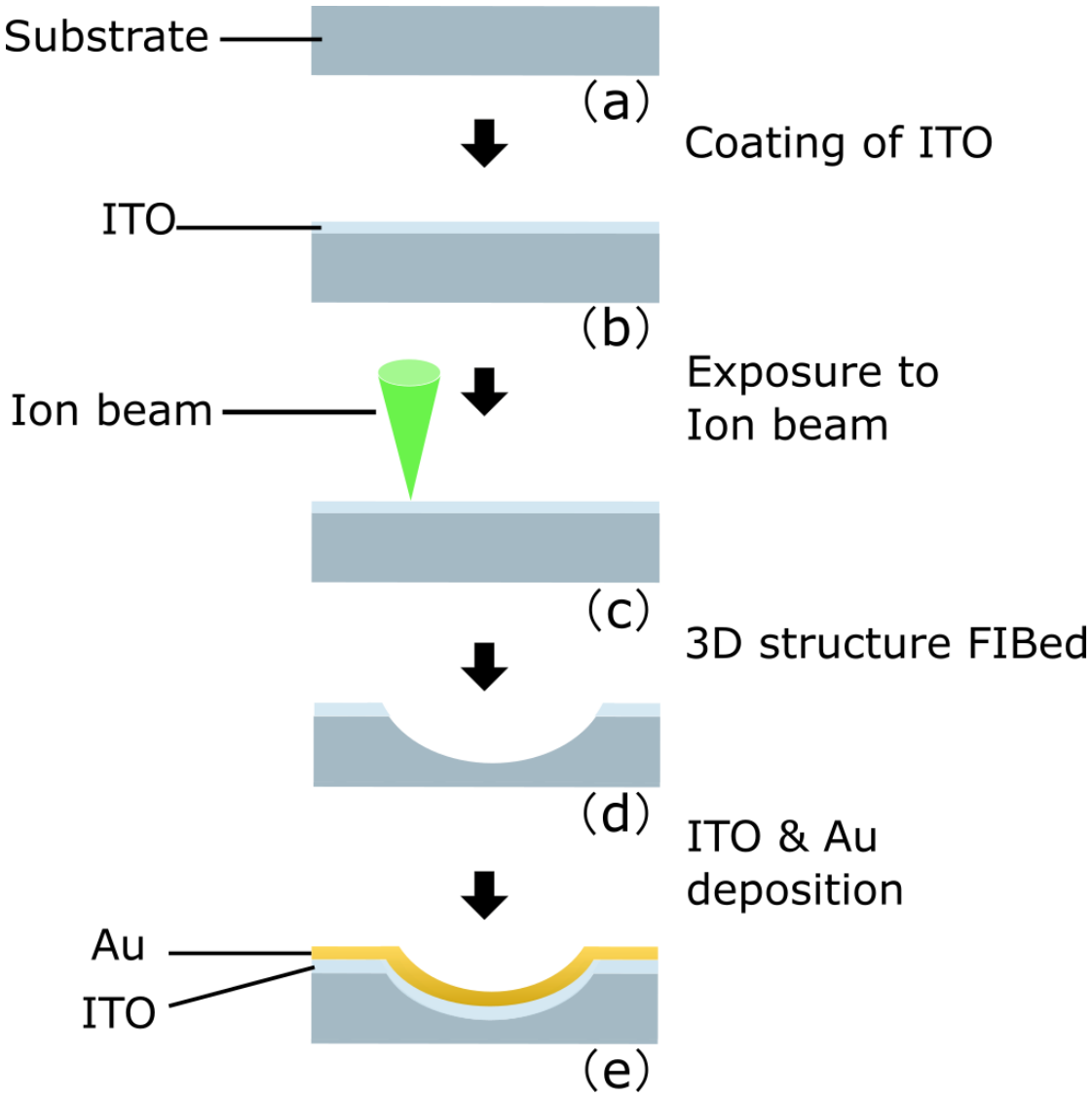

Figure 3.16: FIB fabrication process used to make 3D concave lenses. (a)-(b) Conduction layer is formed on the target region by coating of ITO. (c) Surroundings of the target region are roughly milled with Ga ion beam to prepare a section (thickness: a few μm or less). (d) FIB milling finished and 3D structure made. (e) Adhesion layer ITO and Au metal layer is deposited to functionalize the optoacoustic transducer.

Hydrochloric acid in a glass beaker, and the glass substrate with transducer layer on was placed in to this immediately. Then the beaker was covered and left in ultrasonic bath for 2mins to remove any remaining material inside the micron size concave lenses. The waste was then neutralised with sodium bicarbonate before disposal. The cleaned sample was then washed using solvent and finally dried with

FIB Specification	
Model	FEI Quanta 200 3D Dual Beam FIB-SEM
Accelerating voltage for electron beam	200V to 30 kV
Accelerating voltage for ion beam	5 to 30kV
Electron beam resolution	1.2nm (30 kV) at high vacuum mode
Ion beam resolution	10 nm (30 kV) at 1pA
SEM Magnification	30× to 1.28M×
FIB Magnification	40× to 1.28M×

Table 3.2: Major Specifications of FIB.

nitrogen.

3.2.4 Phase-Reversal FZP (PR-FZP) fabrication

Phase-Reversal lenses, unlike traditional FZPs, take advantage of all the incident energy by adding phase compensation regions instead of binary energy blocking regions [171]. PR-FZP can be either fabricated using FIB or EBL (though requiring special experimental set up), the thickness of the FIB layer was determined in the PR-FZP design Section 3.1.2. More details about FIB made PR-FZP will be discussed in the results Section 4.1.3 and more EBL made PR-FZP will be discussed in the preliminary results and perspectives Section 5.2.

In conclusion, two different nano/micron fabrication techniques were presented for the fabrication of diverse 2D and 3D structures, EBL for flat 2D structures and FIB for 3D structure. In conclusion, EBL is capable to mass fabrication in a single run with super high resolution and FIB is an advanced technique that can be used for rapid prototyping of novel 3D micron/nano structures [172].

3.3 Experimental set-up

The fundamental working principle of PLU and pump-probe spectroscopy in general is that the pump pulse is absorbed in a periodic manner that repeats at the pulsed laser system's repetition rate. One probe detection pulse, which measures the transducer/specimen's reflectivity or transmissivity at a discrete time location as the wave propagates, is produced for every pump excitation pulse. These generation-detection events gradually stagger in time until a certain time window of the acoustic wave has been sampled and recorded because of the aperiodicity between the timings of the pump and probe pulses. Based on this fundamental understanding, the following sections are centred around four key topics:

1. The concept of measuring the time resolved signal of a high-frequency acoustic wave.
2. The equipment required to carry out this operation.
3. The special optics choice made to achieve experimental requirements.
4. The scanning methods used to running scans, from finding the region of interests to taking experimental data.

In the field of PLU, and more generally in pump-probe spectroscopy, the absorption of a pump pulse happens repeatedly at the same interval as the pulsed laser system. For every activation of the pump pulse, a corresponding probe detection pulse samples the reflectivity or transmissivity of the transducer or specimen at a specific moment as the wave travels through.

What's intriguing here is the intentional mismatch in timing between the pump and probe pulses. This aperiodicity leads to the generation and detection events

being gradually offset in time, allowing for a thorough examination of a certain time window of the acoustic wave.

The latter part of this section delves into the typical techniques to achieve this staggered timing, as well as the additional optical/electronic components that support this measurement process.

3.3.1 Time resolved signal in GHz

Sampling

To accurately capture a GHz frequency acoustic waveform, careful synchronization between pump and probe pulses is essential. For instance, when studying an acoustic wave in water with a central frequency of $f = 5GHz$ (like the Brillouin frequency of water in the near-infrared region), each wavefront's period is approximately 200 ps.

To ensure proper frequency capture of the wave, the Nyquist principle dictates that each wave cycle should have at least two discrete samples. This means that the largest time interval between successive positions of the probe pulse should be $\Delta t_{\max} = 100ps$ (in practice, the sampling rate is often considerably much higher than this).

In order to increase the precision of the time resolved signal, or the resolution with which two frequencies can be distinguished, the number of sampling within each cycle should be much higher, which requires that these $\sim ps$ sampling intervals taken place over the whole physical phenomenon of few nanoseconds.

Asynchronous optical sampling (ASOPS) system

ASOPS offers a way to achieve super high time resolution by utilising two lasers with slightly different repetition rates. For example as shown in Figure 4.13, if a master laser (pump) is set to $80MHz$, and the slave laser (probe) set to $80.01MHz$ (a delay rate of $\Delta f = 10kHz$), the slave laser will cumulatively step away from the master at a rate of $1.5ps$ per pulse. Using this technique, the entire $12.5ns$ time-of-flight between pump pulses $(1/f)$ can be reconstructed in 100 μs, the beat period of the master/slave.

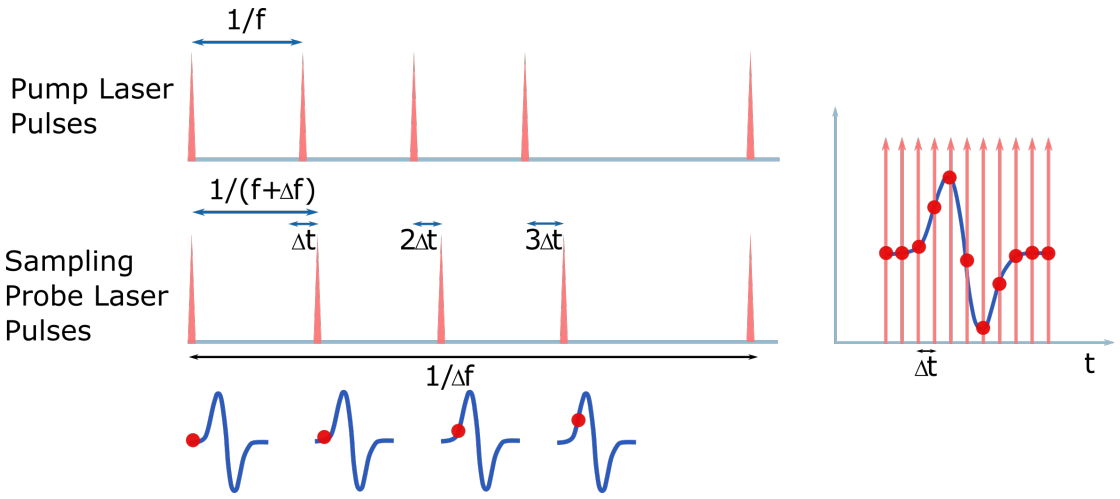

Figure 3.17: Sampling clock of pump and probe - how time resolved signal is generated.

The following section outlines pump-probe experiments utilizing the ASOPS laser system, which is renowned for its exceptional time resolving capabilities. To conduct ultrafast acoustic measurements, the necessary optics and electronics will be introduced. These components will be discussed in the context of demonstrating the focusing effect of the optoacoustic lenses presented in previous Section 3.2.3.

3.3.2 ASOPS pump-probe optical system

Ultrafast pulsed laser sources

In this study, lasers from the Tsunami Series by Spectra Physics were utilized. Specifically, the Millennia eV 532 nm pump laser activated the titanium: sapphire gain medium inside the Tsunami's cavity. This configuration provided a wavelength variability of about 200 nm within the Near Infrared (NIR) spectrum, which spanned from 700 nm to 900 nm, and generated 100 fs ultrashort pulses.

Two Tsunami cavities were employed for the pump and probe laser pulse trains. In the ASOPS configuration, the relative repetition rates of these cavities were electronically controlled using a function generator (as detailed in Section 4.2.1). This approach ensured synchronization with the primary 80 MHz oscillator (associated with the pump laser). Once the wavelengths were tuned and mode-locking was achieved, the Gaussian beams emitted from the laser cavities reached average powers typically between $1 \sim 2W$.

The NIR output of one beam, typically the pump beam, can be frequency doubled using a second harmonic generation crystal when NUV wavelengths were desired to enhance optoacoustic energy transfer efficiency. Such a NUV-NIR configuration was common for applications like phonon microscopy and ultrafast spectroscopy of metallic nanoparticles. A typical NUV-NIR configuration of the experiment is shown in Figure 3.18.

Optical design

A high-power mirror directs the beams from the tuning cavities' output aperture to the next set of optics further down the line. A half wave-plate and a polarising

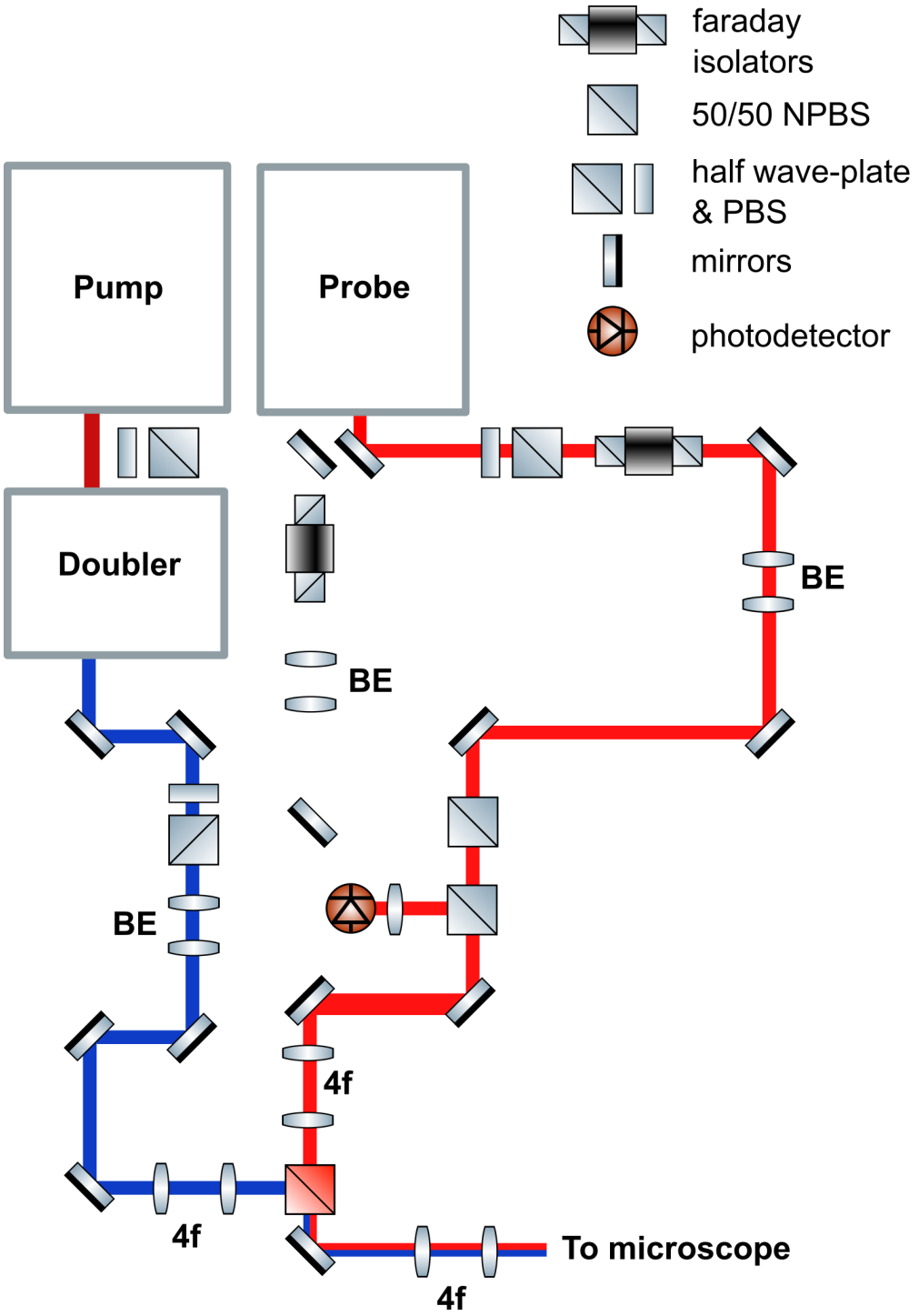

Figure 3.18: Schematic of the experiment used to perform pump-probe spectroscopy with NUV-NIR setup.

beam-splitter are used together to lower the average power from high $\sim W$ to low $\sim mW$ range. The power is decreased based on the position of the wave-plate. Faraday isolators stop back reflections from going back into the Tsunami cavities

and making the cavity modes more stable. Newport Broadband Faraday Optical Isolators are used in the system, which allow $\sim$ 90% of transmission and high isolation in the NIR path.

The rest optical components in the system are built specifically to carry out standard pump-probe measurements in free-space. Each pump/probe path contains a beam-expander, which allows the expanded beam to fill the whole back aperture of the focusing objective and for better collimation adjusting. The expanded and collimated beams then pass through a final turning mirror (which can be used to adjust the overlapping between the pump and probe spots) before entering a 4f imaging system. By using 4f systems, turning mirror adjustments can be imaged onto the back focal plane of the objective lenses without causing the objective aperture to be clipped. Following the first 4f, NUV and NIR are combined with a dichroic beam-splitter which is followed by a fast scanning mirror. This allows simultaneous raster scanning of both pump and probe spots if desired. Additional 4f systems are used because the beams are periscoped up to the sample, which is placed on the microscope body and objectives lenses (see Figure 3.19).

As shown in Figure 3.20, the optical system can be changed to an NIR-NIR setup (with an NIR pump wavelength) by adding a magnetically detachable mirror between the pump cavity and its doubler. Using this kind of setup could be better if there are worries about NUV phototoxicity or if a certain nanostructure has an NIR range optical resonance. The basic optical elements in this different NIR configuration are the same. A 50/50 non-polarizing beam-splitter (NPBS) joins this pump with the NIR probe-labeled beam in the system. Notably, the two NIR beams can switch between being a pump and a probe as needed in real life.

The probe light can also be delivered from the top objective, allowing for detection in reflection during experiments with specific beam size and overlapping require-

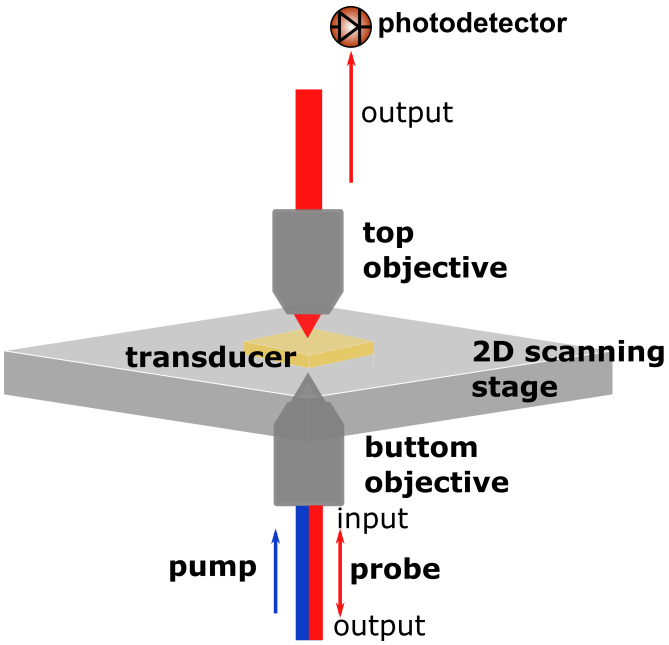

Figure 3.19: Basic diagram of the sample plane for the free-space implementation of the pump-probe system. Either a NUV-NIR or NIR-NIR pump-probe combination is directed through a series of 4f systems such that the beams can be translated in space while still being accepted into the back aperture of a microscope objective lens (bottom objective). After interacting with the transducer and sample, the probe light can be detected in two configurations: the signal light that is transmitted through the sample, and signal light that reflects from the transducer/sample and travels back through the optical systems in Figures 3.18 and 3.20. A mechanical stage can be used to control the x/y position of the pump-probe spots with respect to the sample for scanning and imaging.

ments. Figure 3.21 displays a basic diagram of this configuration. A more detailed optics design will be introduced in the subsequent section discussing the control of beam sizes.

3.3.3 Scanning beam sizes

Different objectives were chosen in order to produce different sized pump and probe beams; a 5x objective was chosen at the bottom for a sufficiently large pump beam to obtain a large enough NUV spot and thus can cover the whole opto-acoustic transducer (OAT) lens; a relatively small probe beam was chosen

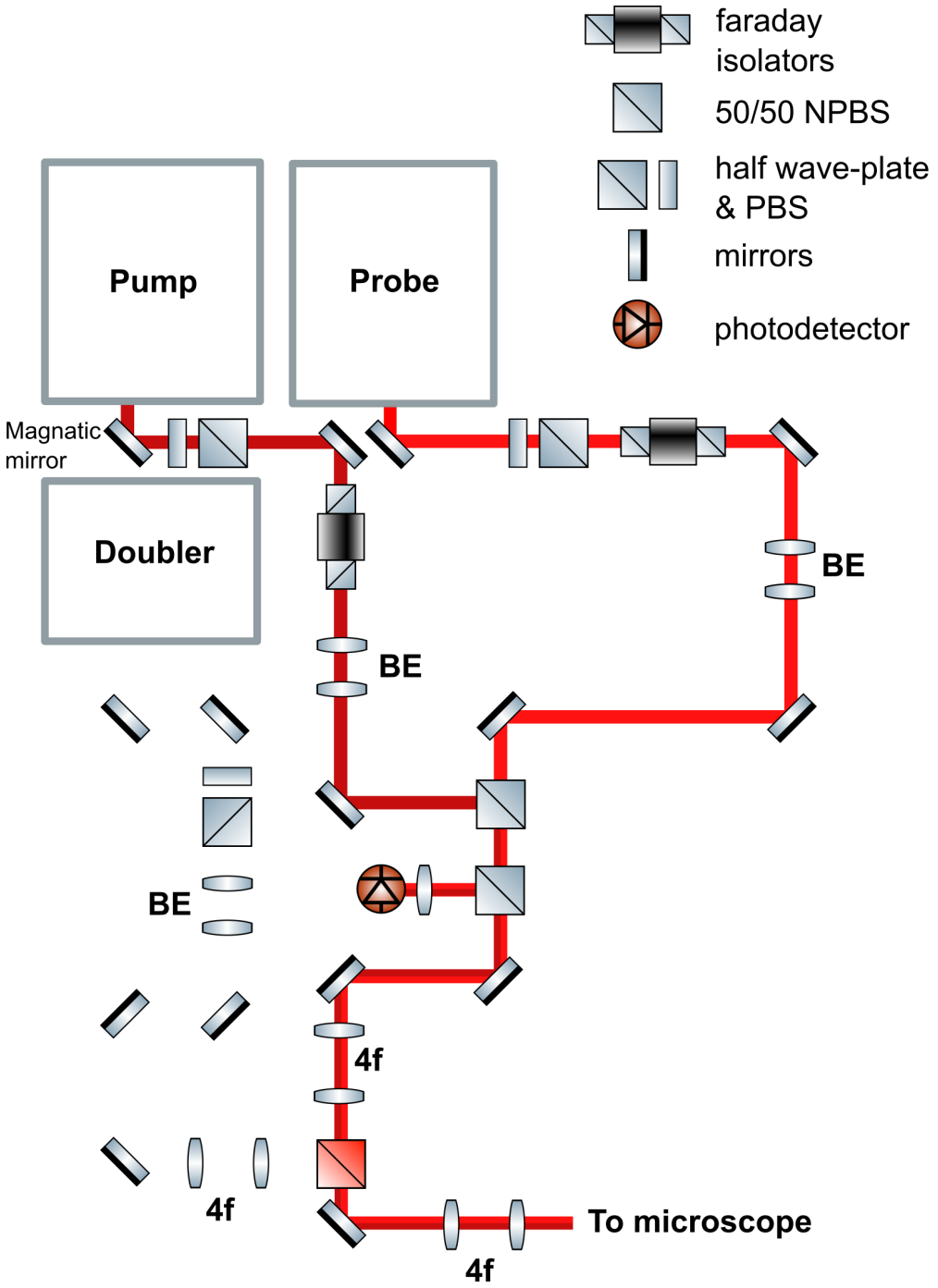

Figure 3.20: Schematic of the experiment used to perform pump-probe spectroscopy with NIR-NIR setup.

to allow for more room for future real acoustic PSF experiments and to in order to have a relatively small probe beam, as well as to allow more space for future real acoustic PSF experiments and to address the possibility of defocusing due to liquid evaporation, a 10x dipping objective was chosen for the top. A more

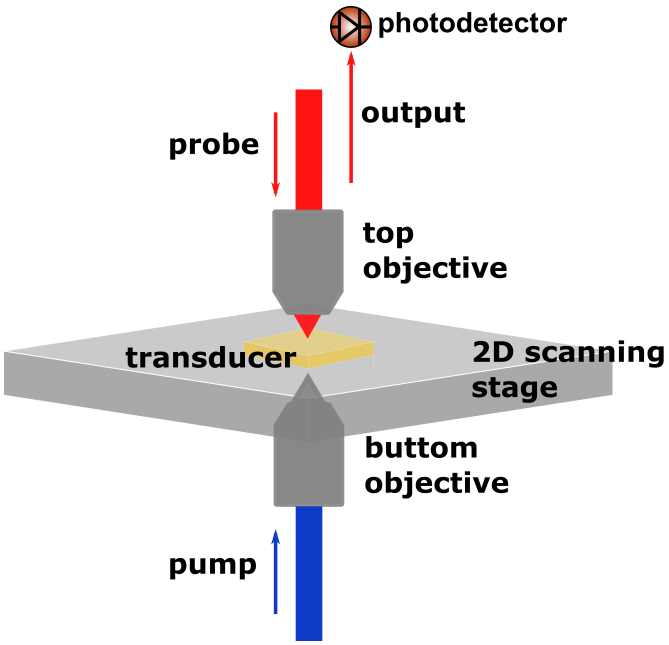

Figure 3.21: Basic diagram of the sample plane in the free-space implementation of the pump-probe system, where the probe beam is delivered from the top and detection occurs in reflection.

detailed beams size discussion is in the following Section 3.3.4.

To deliver the probe light from the top and separate it from the pump beam path, a single mode optical patch cable was used to divert the probe beam to the top of the microscopy body as shown in Figure 3.22 and 3.23. Two fibre ports were used to convert free space beams to fibre and then back to free space. A set of quarter-wave plate, polarised beam spliter and a half-wave plate was used to achieve detection in reflection.

Detection

The Thorlabs Si Switchable Gain Detector (PDA36A) is used in our experiments. It works within a wavelength spectrum of $350 - 1000nm$, our 780nm probe choice sit in this range. Depending on the requirements, we select a gain of either $20dB$ or $10dB$, accompanied by a detection bandwidth of either $1MHz$ or $5.5MHz$. The

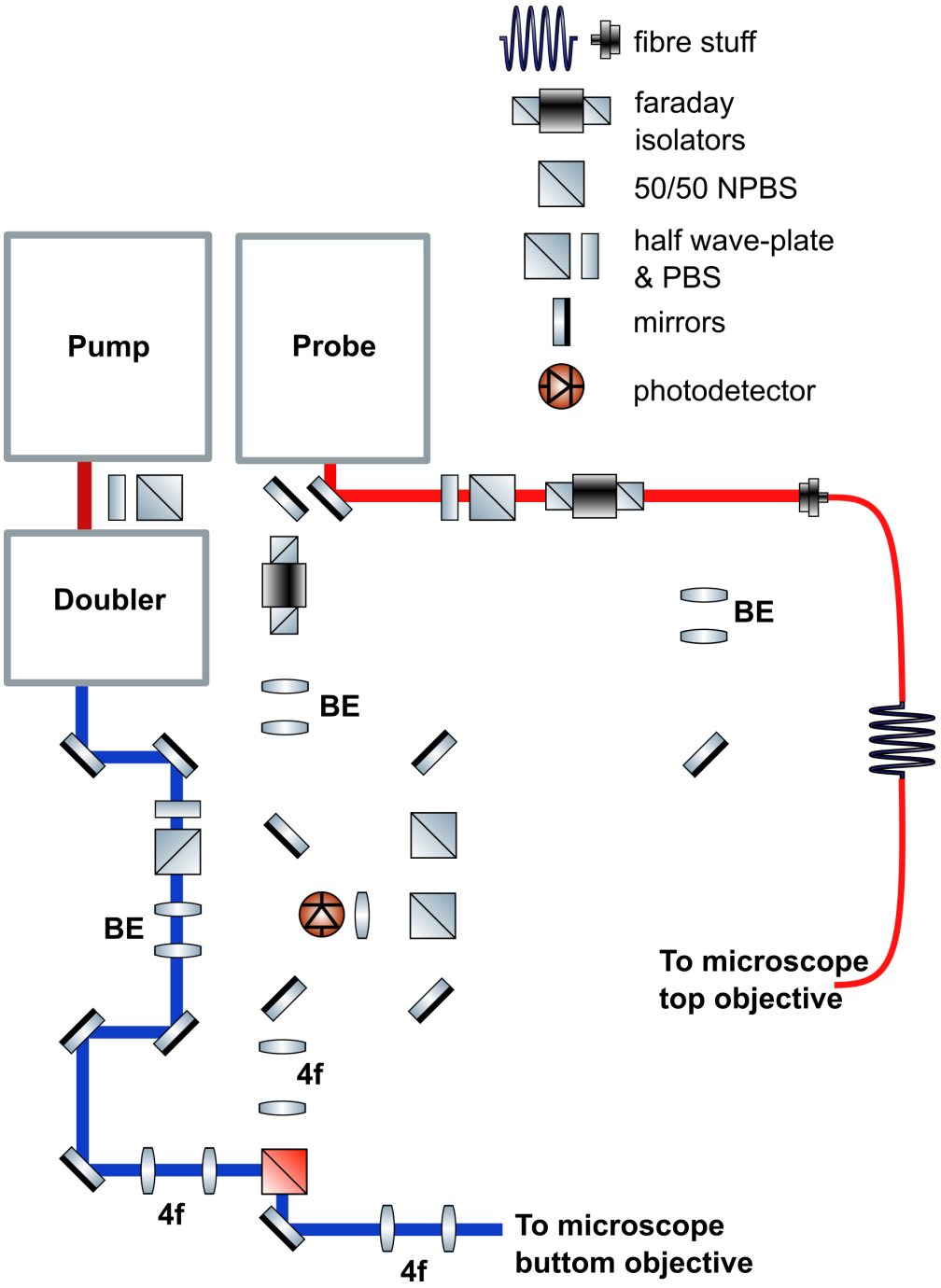

Figure 3.22: Schematic of the experiment used to perform pump-probe spectroscopy with NUV-NIR setup, probe is delivered via a single mode fibre and is focused on the sample plane from the to objective and then reflect back to the photodiode on the top.

disparity between the $100\mu s$ acquisition timeframe (indicated by $\Delta f = 10kHz$) and the $12.5ns$ signal duration (represented by $f = 80MHz$) also causes acoustic frequencies to be decreased by a multiplier of 8000 in the observed signal. As a

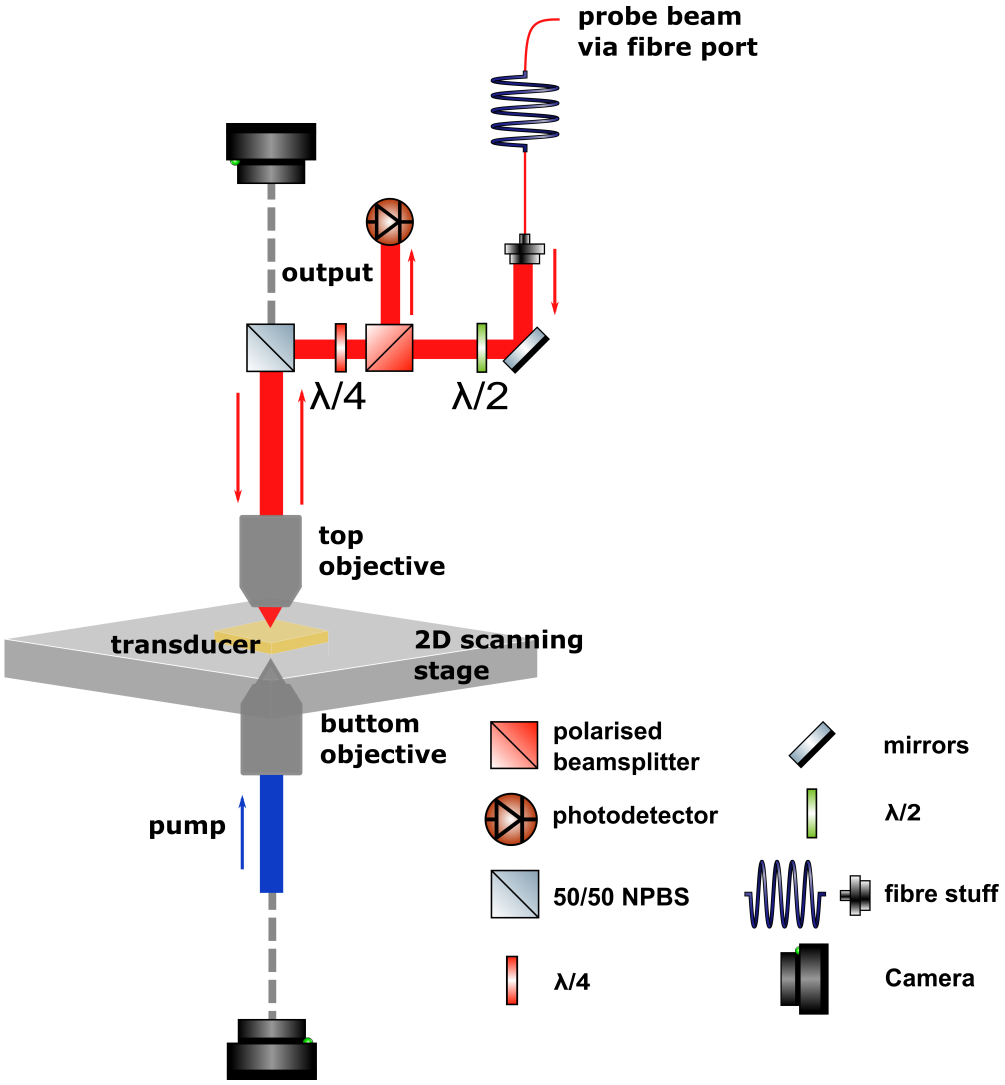

Figure 3.23: Diagram of the optics design around the microscope body. Either a NUV-NIR or NIR-NIR pump-probe combination can be achieved by sending either NUV or NIR pump beam via the bottom objective. Probe is sent through a single mode patch cable and through the top objective, thus achieve reflection detection and has the ability to separate the beam size control for pump and probe delivering path.

result, a detection bandwidth of $1MHz$ corresponds to an approximate frequency of $8GHz$ in the signal area, whereas a bandwidth of $5.5MHz$ corresponds to nearly $50GHz$. Given that the TRBS's target frequency spectrum in liquids and biological samples ranges from 1 to $20GHz$, the system's bandwidth of around $50GHz$ or $8GHz$ is big enough for the majority of tasks.

After a signal is collected at the detector, it is transmitted through a coaxial

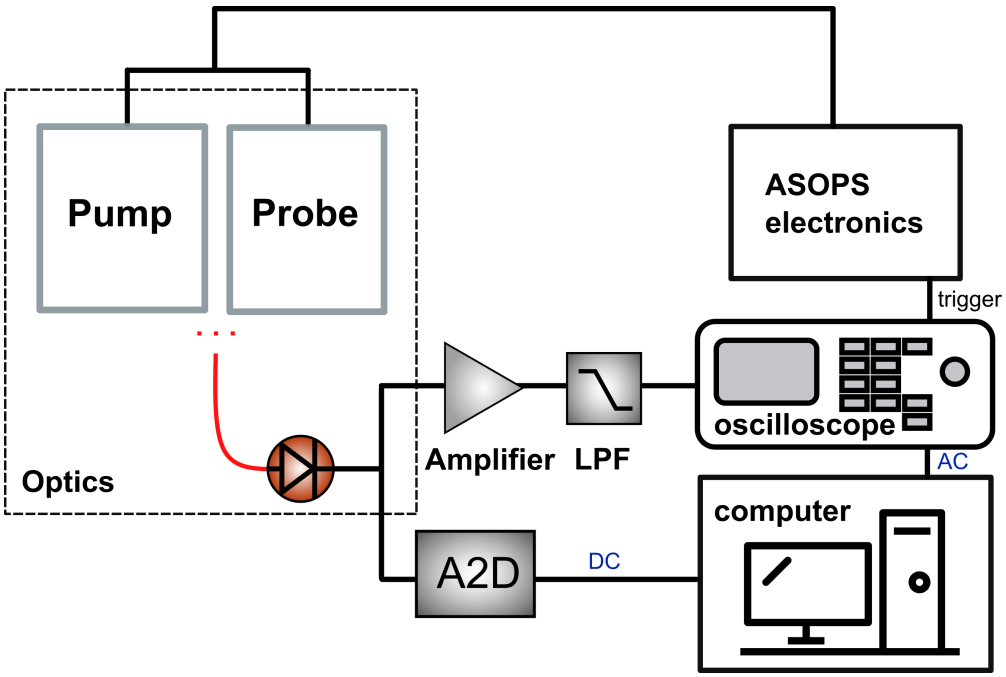

Figure 3.24: Diagram of the whole system.

cable to: (1) a Mini-Circuits RF amplifier (ZFL-500LN-BNC) and (2) a BNC-2110 analogue-to-digital converter. The latter digitizes the signal's DC light level photovoltage, which is then used in subsequent signal processing. The amplifier's output goes through a low-pass filter before being sent to a digital oscilloscope (LeCroy HRO66Zi). The frequency waveform generated by the function generator (for instance, $\Delta f = 10kHz$) is designated as the external or input trigger for the oscilloscope. While the oscilloscope's sampling rate can reach up to $2GS/s$, to prevent over-sampling, a rate close to $100MS/s$ is typically selected, aligning with the ASOPS system's $80MS/s$ discretization (at $\Delta f = 10kHz$).

3.3.4 Scanning method

In this section, the step-by-step experiment procedures using the ASOPS system described above is presented. The experimental procedures is divided in three main steps, applied to most results presented in the results chapter 4.

1. **Align the pump and probe**

   Due to the optical system design, the pump beam offers greater flexibility and can be precisely adjusted using the scanning mirror. First, ensure that both the pump and probe beams are visible in the camera view, and slightly adjust the probe delivery for coarse alignment. Then, using both the camera and the co-peak signal from the scope to closely monitor the beams, adjust the pump beam's position with the scanning mirror to achieve the maximum signal. This may also involve adjusting both objectives to focus or defocus the beam, depending on the desired overlap characteristics. To check the overlap, once the maximum signal has been manually identified, a quick scan using the scanning mirror with a fixed probe and moving pump can be conducted to find the position of maximum overlap. Figure 3.25 (b) is an example result.

2. **Find the area of interests**

   The nano/micron structures are visible in the camera. However, each individual lens is similar to, or even smaller than, the size of the laser beams. This makes it challenging to precisely determine the position of the lens and to identify the center of the lenses. In this context, a quick DC scan proves to be very useful. An OAT with a unique surface geometric characteristic will yield a distinctly recognizable optical (DC) scan result as shown in Figure 3.27 (b).

3. **Do the scan**

   Two types of scans are utilized for the mirror. The first is the traditional scan, where only the sample is moved while both the pump and probe beams remain fixed. The second is the relative probe scan. In this method, each time the sample is moved, the pump beam is also adjusted (based on calibration calculations for the scanning mirror movement) to achieve a scanning

probe with the pump beam and sample position held constant.

Before conducting an experiment, users must create an executable "con-file". This file contains scan instructions, such as mechanical stage movements, the number of measurements at each point, and other related directives. This con-file is then fed into the data acquisition software known as D-scan.

As the experiment progresses and even after its completion, D-scan records the experimental data across various files and formats:

1. A "dat-file": This holds the raw output from the oscilloscope (AC).
2. An "m-file": This encompasses meta-data for the scan, including naming conventions for file bases and parameters related to the oscilloscope.
3. A "d-file": This captures the average photovoltage levels (DC).

Both the pump and probe beams are focused using different objective lenses: a $5\times$ microscope objective lens for the pump beam and a $10\times$ water dipping objective for the probe beam, typically onto the surface of the OAT. The electric field intensity distribution of both lasers at the focal spot can be expressed using the Airy disk equations (2.59) and (2.60). For simplicity, if we ignore the minor interfering ripples around the edges, the focused laser beams can also be approximated quite well by a Gaussian function. The distribution of the pump laser pulse using Gaussian approximation is given by:

$$I(x,y) = I_0 \times \exp\left(-2\frac{x^2+y^2}{a_{pump}^2}\right) \tag{3.8}$$

with I_0 the peak intensity (at the center of the beam), x and y the spatial coordinates. a_{pump} is the radius of the electric field amplitude distribution at the $1/e^2$

(or about 13.5%) level. Figure 3.25 (a) is a simulated pump - probe correlation estimation.

To find out the pump laser beam's effective radius in the experiment, a cross correlation map of the pump and probe laser beams by moving the pump laser beam around the fixed probe laser beam (Figure 3.25 (b)) was measured.

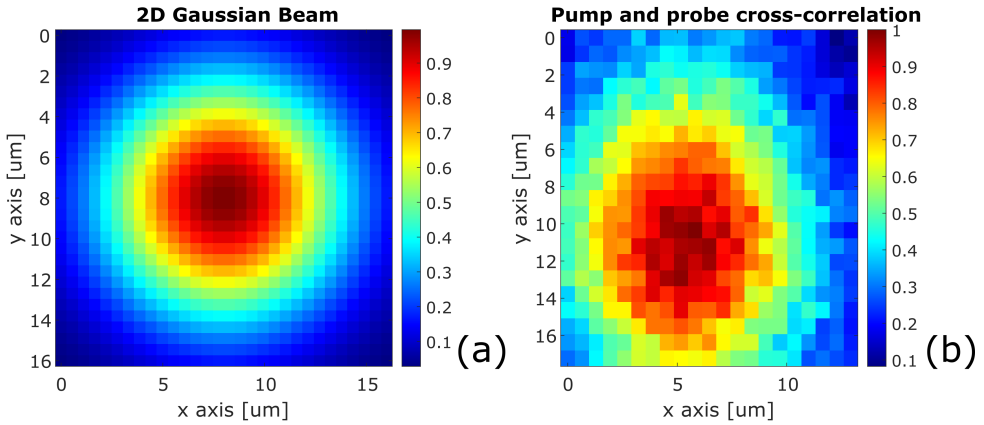

Figure 3.25: Effective radius of the pump laser beam focii sizes determination by cross-correlation, obtained by a raster scan of the (fixed) probe beam by the (moving) pump beam on the surface of a flat Au OAT deposited on a glass substrate. (a) Simulated beam size using Gaussian assumption. (b) Experimentally obtained pump-probe cross correlation.

The scan has been made on a 13×17 μm^2 area with a step size of 0.65 μm in x axis and 0.85 μm in y axis, centred on the pump spot, on a 30nm gold(Au) transducer deposited on a glass substrate.

Another method to measure the size of laser beams is using camera approximation. Utilising the integrated camera for alignment within the microscope body, optical images were captured. In order to prevent camera saturation and damage, neutral density filters were inserted into the optical path to lower the laser power that reached the camera. The EBL sample is overlapped by fits-sized laser beam spots. Calibration of the camera view size was done using the GDSII design for the EBL. There is a black box that zooms in area of interests, the FZP where laser beams are placed has a design focus of 2 μm and the has a diameter of 4.46 μm. The

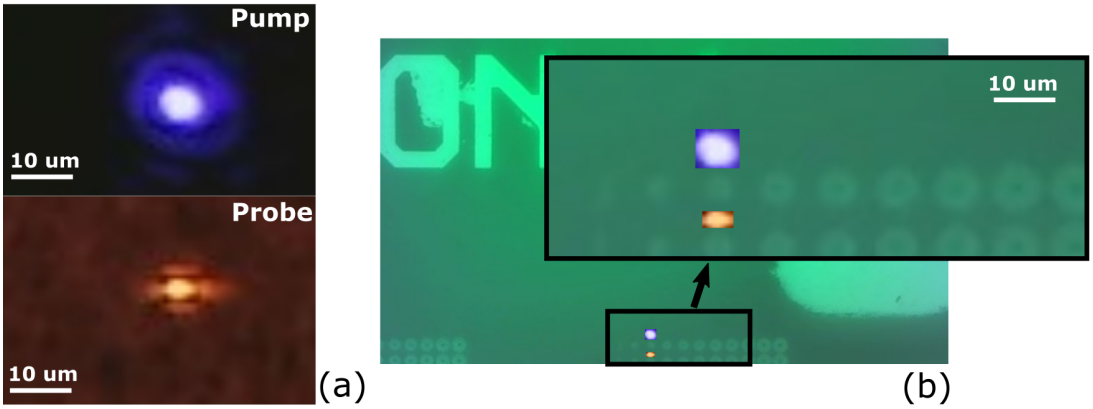

Figure 3.26: Determine the sizes of the pump and probe using the optical image. (a) Optical images were taken using the built-in camera for alignment in the microscope body. Neutral density filters were placed in the optical path to reduce the laser power reaching the camera, thereby avoiding camera saturation and damage. (b) Laser beam spots, sized to fit, overlap the EBL sample. Camera view size calibration was conducted based on the GDSII design for the EBL. A black box zooms in on the area of interest; the pump has a measured FWHM of approximately 5 μm. The probe's distribution is uneven, with a wider FWHM of approximately 3.5 μm along the x-axis and a narrower FWHM of approximately 2.5 μm along the y-axis.

pump's FWHM is about 5 μm. The probe is spread out unevenly, with a wider FWHM of about 3.5 μm on the x-axis and a narrower FWHM of about 2.5 μm on the y-axis. To illuminate the entire lens, the pump beam needs to be large enough to cover it completely. Although a sufficiently large pump beam is achieved here to illuminate the entire $F = 2$ μm lens, the challenge lies in practical experiments - aligning the pump and probe beams together and also finding the centre of the lenses, since the pump beam size is comparable to the lens size.

To find both the EBL made and FIB made lenses, the first step is to find all the structures using the build in optical microscopy (Figure 3.27 (a) shows an example how the finding process is done of a FIB made sample with 9 concave lenses). Then, using a raster scan with larger scan steps, for example, an area of $100 \times 80 \mu m^2$ was scanned with a scan step of 1 μm. Since the probe is placed on

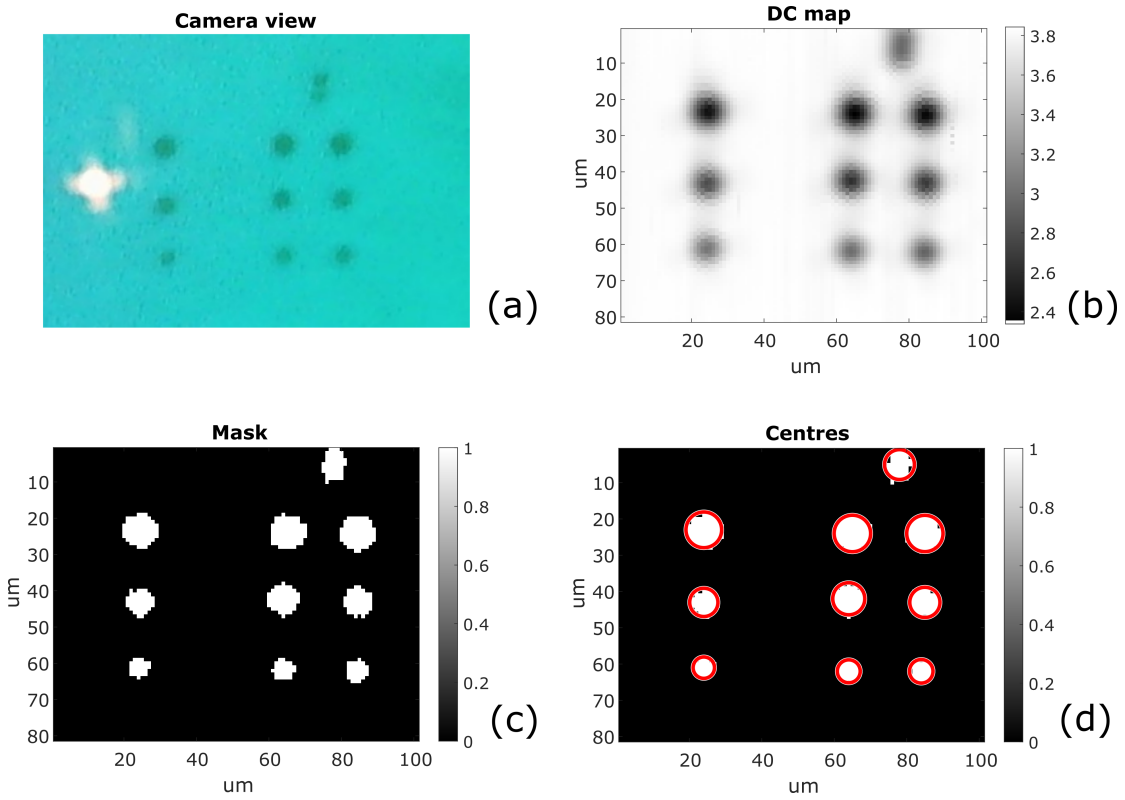

Figure 3.27: A DC scanned area showing the processes to find precise positions of the lenses. (a) Camera view of the region of interests. (b) DC map of the scan area, $100 \times 80 \mu m^2$ was scanned with a scan step of 1 μm. (c) Masked DC map, lens pixels are filtered and labelled white here. (d) The calculated centroid and radius, labelled in red circles.

top and the detection is done in reflection mode, thus, when the probe approaches the dish, compared to a flat surface, less probe light travels back to the detector, resulting in a blacker region in the DC scan as shown in Figure 3.27 (b). Then, by applying a mask with a custom threshold to the DC scan (Figure 3.27 (c)), the lens area can now be found by calculating the centroid position and radius size for each single lens, as shown by the red circles around the mask-filtered lens areas in Figure 3.27 (d). Meanwhile, the calculated centroid position can later be loaded to perform fine scan over each single lens to perform PLU measurements.

3.4 Signal processing

In this section, the procedure for processing the TRBS experimental signal is outlined. Matlab serves as the primary tool, assisting in organizing, manipulating, and presenting the data. The waveform captured by the oscilloscope requires refinement to eliminate any unwanted components. Only after this refinement can the time-of-flight of the acoustic phenomena, as detected by the ASOPS pump-probe system, be accurately determined.

By transitioning the time-domain signal into the frequency domain, Brillouin spectroscopy becomes feasible. This process is essential for determining the viscoelastic characteristics of the material where the phonon probe resides. The discussion will then shift to the evaluation of signal frequency in relation to time, known as time-frequency analysis. This evaluation is crucial for leveraging the phonon probe as a three-dimensional imaging device for microscopic entities.

3.4.1 Extract time trace

A custom MATLAB script is used for basic signal processing. This script is specifically designed to parse and process the raw data, a methodology for which will be detailed subsequently.

A light pulse that is absorbed causes the sample's temperature to rise. The refractive index changes as a result of this temperature shift, which has an impact on a material's local reflection and transmission. This causes the light level to vary gradually, as shown in laser ultrasound investigations. This phenomenon is known as thermal background. They will overlap in time because the thermal background's length is longer than our acoustic signals' period. The raw trace is trimmed and fitted to a polynomial curve to separate them. Next, a graph is

created by superimposing the fitted curve quality over the source trace (Figure 3.28 (c)). The fitted curve is deducted from the source curve after it has been confirmed that the fitting accurately follows the source trace (Figure 3.28 (d)).

A light pulse that is absorbed causes the sample's temperature to rise. The refractive index changes as a result of this temperature change, which has an impact on a material's local reflection and transmission. This causes the light level to change gradually, as seen in laser ultrasound experiments. This phenomenon is known as thermal background [25]. They will overlap in time because the thermal background's duration is longer than our acoustic signals' period. The raw trace is cropped and fitted to a polynomial curve to separate them. Next, a graph is created by superimposing the fitted curve quality over the source trace (Figure 3.28 (c)). The fitted curve is deducted from the source curve after it has been confirmed that the fitting accurately follows the source trace (Figure 3.28 (d)).

The experimental case study used for this discussion of signal processing, is a 20 nm gold transducer on a planar glass slide, sitting in a Petri-dish filled with water. The experimental set-up was that of the NUV-NIR free-space configuration shown in Figure 3.22, where the signal has been detected in reflection (reflected output in Figure 3.23).

For the experiments in Chapter 4, time traces were taken either individually or as an array. Each time trace exhibits a rapid change in signal level, known as the "co-incidence peak", attributed to short-lived electronic effects. Additionally, there's a thermal background signal due to temperature changes. On top of this, the signal of interest emerges: the time flight of Brillouin scattering signal(Figure 5.13).

The signal process method introduced is used to process all the traces gathered form experiments, following the steps shown in Figure 3.28, which will be discussed

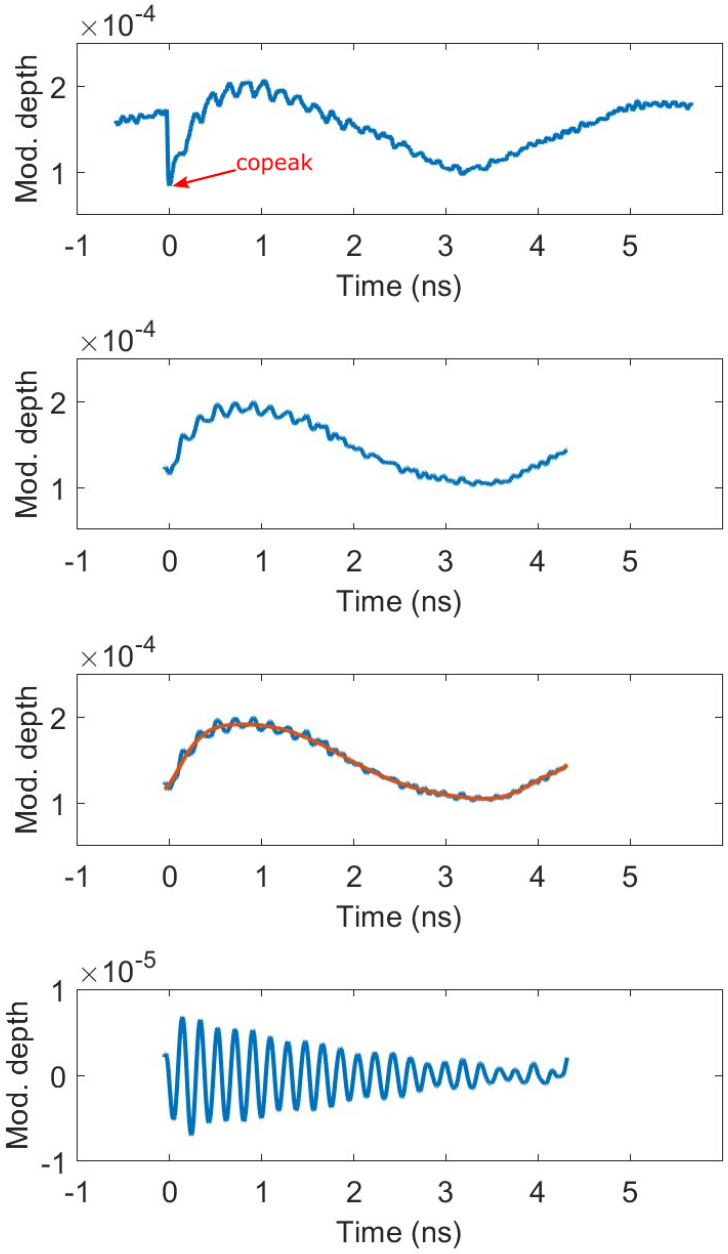

Figure 3.28: Single point signal processing steps from the initial raw data until the extraction of the signal of interests. (a) Raw but averaged AC/DC signal as output from the scope.(b) Location of the coincidence peak found when the pump and probe are synchronised and a user-defined offset is applied to indicate the start of the region of interest. (c) The slow thermal decay following the coincidence peak is fitted to a polynomial expression and will be subtracted in the next step. (d) Final modulation depth of the time domain acoustic signal.

below. The trace is truncated at the end time of the time window of interest, starting from time 0 (at the coincidence peak) and continuing until the oscillatory signal decays. Subsequently, the thermal background is eliminated by subtracting a fitted polynomial function. After that, a fast Fourier transform FFT is then performed, to get evaluation of the peak frequencies.

3.4.2 Frequency analysis - FFT

By calculating the FFT of a processed trace and by looking at the peaks of the signal, one can precisely determine the quantity of the Brillouin frequency of interests: f_B. However, creating a picture (point by point scan) by repeating the process numerous times takes time and increases the risk of human error. More details about Fourier transformand Fast Fourier transform realization can be found in appendix D.

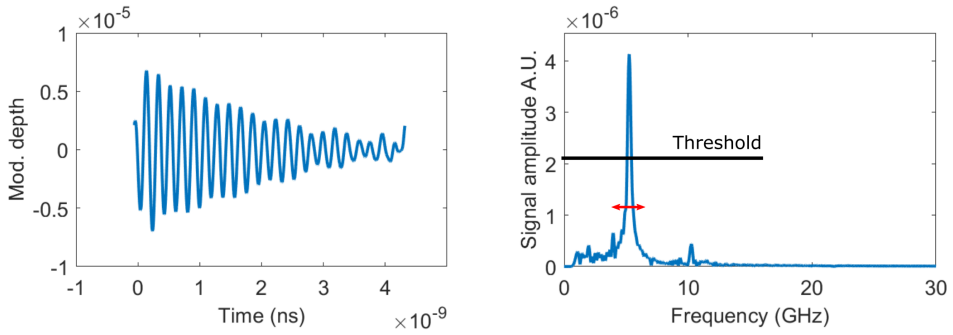

Figure 3.29: Example basic processed experimental trace, and its fast Fourier transform (FFT).

A threshold on the amplitude and a range of expected frequency values are set in order to automatically determine the frequency of a peak from a trace. Because there are multiple signals produced by a measurement during transmission, this range avoids evaluating the incorrect peak. Similarly, the threshold makes it impossible to determine a noise peak's frequency. Next, the highest value within the intended range is identified and associated with its frequency position. (b)

displays the Fourier transform of the trace displayed in Figure 3.29 (a). There, the black line denotes the threshold, and the red portion of the trace shows the range where the maximum is looked for. The detected frequency is eliminated and the point is regarded as lost data if the peak's amplitude is less than the threshold's (black line) value.

3.4.3 Signal amplitude modulation

The time domain can be utilised to extract more information about the rate of signal decay once the dominant signal frequency (f_B) has been determined. As was recently shown, there are two ways that signals can be attenuated in opto-acoustics: optical and acoustical. As such, care must be taken in determining the source of the attenuation effect. Nonetheless, acoustics will be the primary factor in signal attenuation in the case of low NA supplied by the optical fibre [173]. Either way, an iterative minimum-value search procedure can be used to determine the rate of general signal attenuation. The objective is to empirically create an equation for the TRBS signal, which is thought to be a sinusoid with exponential decay:

$$S(t) = A + B\sin\left(2\pi f_B t + \phi\right) e^{-\alpha v t} \tag{3.9}$$

where A is a vertical offset, B the sinusoid amplitude, α is the attenuation rate, and v is the sound velocity in the medium. In order to numerically determine the parameters in Equation (3.9), few assumptions are made [67]: (1) experimental signal frequency ($f_B \approx 5$GHz in water), (2) amplitude (B = amplitude of modulation depth), (3) offset ($A = 0$), (4) phase offset of the sinusoid ($\phi = \pi$). Then by trying a series of numbers of the decay rate α, a starting reference number from

literature for α is $\sim 0.5\mu m^{-1}$ [174], then the best match can be found as shown in Figure

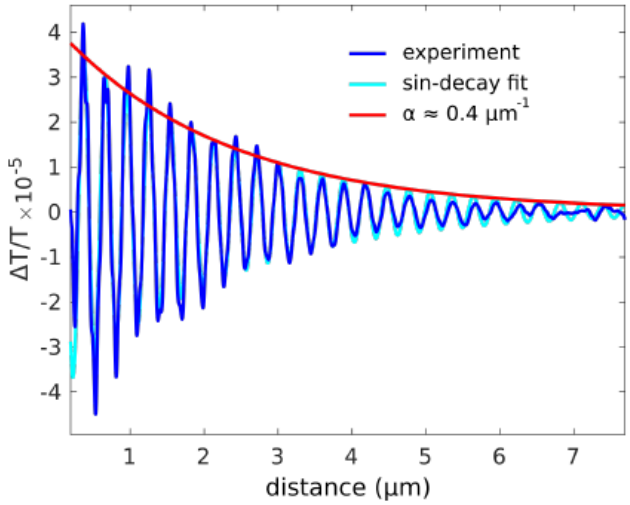

Figure 3.30: Best match to find the TRBS signal decay rate. By quantitatively developing an expression for a decaying sinusoid that matches the properties of the experimental signal, the attenuation of the TRBS signal can be found. Image reproduced from [67].

Figure 3.30 shows the result of this process for the an example experimental trace in 3.29 (blue for the experimental trace, cyan for the fitted trace). The attenuation rate α is found $\sim 0.4\mu m^{-1}$. This attenuation can also be feed back to both the picosecond laser ultrasound (PLU) model and the Fourier-Bessel angular spectrum method (FBASM) model discussed in Section 2.2 and 2.4 for better simulation outputs.

3.4.4 Frequency analysis - wavelet

There will be a change in Brillouin frequency f_B if the measurement volume of phonon microscopy and, by extension, the phonon probe has a change in the local sound velocity and/or refractive index. If f_B changes, it could be because of a change in the material or the state of a single material. Taking the Fourier transform of the whole time-length of the TRBS signal will show multiple frequency

peaks that can be used to confirm the existence of this effect.

For every time trace (or pixel on the image) at every time position, wavelet transforms are calculated, and the corresponding centre frequency (f_B of water) of the wavelet number with the largest amplitude is recorded. An x, y, t matrix of f_B is the end result of this. Many conversions are possible from this matrix: $f_B = 2n\nu/\lambda_o$ can convert the refractive index to sound velocity if it is known, and $z = \nu * t$ can convert the temporal axis to spatial [175]. The wavelet transform is defined as [176, 177]:

$$W_\psi(a,b) = \frac{1}{\sqrt{a}} \int_{-\infty}^{\infty} f(t)\psi\left(\frac{t-b}{a}\right) dt \tag{3.10}$$

where $\psi(\tau)$ is the mother wavelet, a function of dimensionless time τ. a denotes the wavelet dilation and b is the time shift of the wavelet. The wavelet transform of a one dimensional signal such as a time series is a two dimensional map of the amplitude, W_ψ, at a given frequency (or dilation a) as a function of the signal time (or shift b). From this, the frequency with maximum amplitude is extracted for each time in the trace.

The mother wavelet used here is the Morlet which is a complex exponential multiplied by a Gaussian window:

$$\psi(\tau) = (\pi B)^{-1/2} e^{2i\pi\omega_0\tau} e^{-\tau^2/B} \tag{3.11}$$

where ψ is the value of the wavelet at non-dimensional time τ with angular frequency ω_0 and bandwidth B. Figure 3.31 shows the wavelet with bandwidths $B = [1, 3, 5]$.

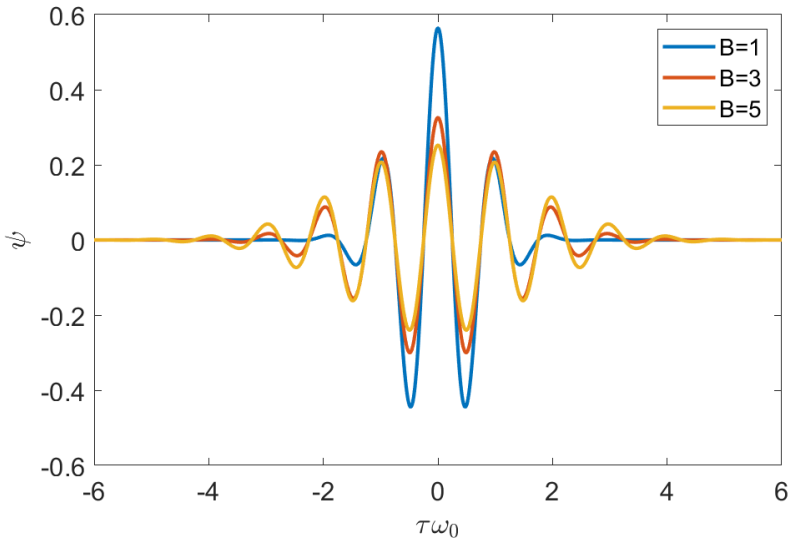

Figure 3.31: Morlet Wavelet for $B = [1, 3, 5]$

The resolution of the axial reconstruction is dependent on the bandwidth of the wavelet used. A higher bandwidth means there are more cycles before the wavelet has decayed - this essentially performs temporal averaging of the signal. The result is better frequency precision, but worse axial resolution.

An example using the wavelet method described here was shown in Section 2.2.4, Figure 2.13: a wavelet analysis of the simulated trace of a multilayer structure, which includes substrate, transducer layer water and PMMA layer.

3.5 Discussion

In the Methods chapter, the design and fabrication of optoacoustic lenses are introduced. These lenses, including Fresnel zone plates and concave lenses, are produced using advanced nano/micron techniques such as electron beam lithography and focused ion beam etching. To ensure precise acoustic focusing, simulation optimization methods are also introduced to optimize the lens structures, followed by experimental methods using time-resolved Brillouin scattering (TRBS).

The TRBS setup employs an Asynchronous Optical Sampling System (ASOPS), allowing for precise GHz-range signal detection. Finally, signal processing techniques, including FFT and wavelet analysis, are discussed as methods to reduce noise and improve data clarity.

Following the methods introduced in this chapter, simulation and experimental results, along with discussions, will be presented in the subsequent results chapter.

Chapter 4

Results

This chapter delves into the simulation and experimental results that build upon the foundational theory and design of optoacoustic transducers for the detection of Brillouin oscillations. The previously discussed theoretical frameworks and methodologies pave the way for a comprehensive examination of various optoacoustic lenses, including multiple Fresnel Zone Plates and concave structures, engineered for the focusing of coherent phonon fields. The simulation, fabrication, and experimental methods established in the preceding chapters are now brought to fruition through a series of experiments that underscore these methods.

In this chapter, by integrating the approach of generating focused coherent acoustic waves using all types of structures with a time-domain resolved Brillouin scattering (TRBS) technique, continuous optical monitoring of focused GHz acoustic fields in water will be demonstrated in both simulations and experimental results. Detailed simulations and measurements of acoustic focusing achieved by both Fresnel Zone Plate and concave structures are presented.

Moreover, this chapter discusses the current limitations inherent in the existing systems, providing a critical assessment of the challenges faced. Through an ex-

ploration of preliminary simulation and experimental results, strategies for solving these challenges are explored. This analysis not only identifies potential solutions but also lays the groundwork for the next steps in the evolution of phonon microscopy, ultimately guiding future research efforts toward the realization of true acoustic resolution.

4.1 Tracking focused picosecond coherent phonon fields with FZP lenses

Fresnel Zone Plates (FZPs) are diffractive structures that focus waves by exploiting the principles of diffraction and interference. As discussed in Section 2.3.3, they consist of concentric rings where each zone alternately generates coherent phonon fields. Depending on the construction of these zones, FZPs can be classified into positive, negative, or phase-reversal types.

Fresnel Zone Plates offer an efficient way for concentrating acoustic waves. This design uses constructive interference at specific focal points, effectively focusing energy without the use of a curved surface. The intrinsic flatness of FZPs simplify the production process, making easier fabrication through standard lithographic techniques becomes possible.

To demonstrate the acoustic focusing effect of nano-fabricated Fresnel zone plates, both numerical simulations and experimental measurements have been carried out.

4.1.1 Simulation

Numerical simulations were conducted using the single-frequency Fourier-Bessel angular spectrum method (FBASM) in Section 2.4 to model the equivalent acoustic field for various designs. Simulations were executed on an axisymmetric plane with 8192 steps (step size = 1×10^{-9} m, yielding a simulation radius of 8.192 μm) and 320 layers along the z axis. Logarithmic spacing was employed to reduce computation time while maintaining fine sampling in the near field, with a maximum simulation depth of 6 μm.

The model suggests that a $\sim$ 5 GHz acoustic beam is focused to a spot of approximately 200 nm in diameter, achieving a sub-optical focused acoustic beam size compared to the pump beam (λ_{pump} = 415 nm) used to generate the corresponding coherent phonon field. This result verifies the proposed design of using optoacoustic lenses for sound focusing.

Positive FZPs

A positive FZP has alternating on and off rings as discussed in Section 3.1.2. The on zones are coated with Au and thus allow the generation of coherent phonons, while the off zones are blank (Figure 4.1). The zones are designed such that the wavefronts from the opaque (Au) zones constructively interfere at the focus, which enhances the wave intensity at that point. Figure 4.1 (a) is a schematic of a positive FZP and (c) is a SEM image of a positive FZP with a designed focus of 3 μm.

NA of proposed positive FZP lenses are shown in table 4.1, R is calculated using the FZP design equation (3.2), knowing the focus F, NA of the proposed lenses can then be calculated using the acoustic NA equation (3.4).

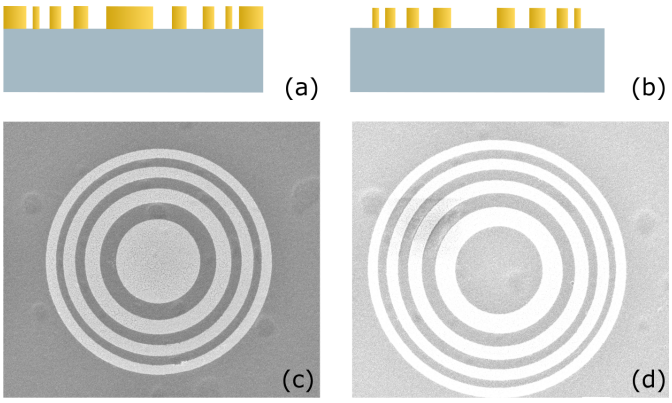

Figure 4.1: Schematics and SEM pictures of postive and negative FZPs. (a) is the illustration of a postive FZP and (c) is a SEM picture. (b) is the illustration of a negative FZP and (d) is a SEM picture.

Positive FZP	$F = 1\,\mu m$	$F = 2\,\mu m$	$F = 3\,\mu m$	$F = 4\,\mu m$
R	$R = 1.586\,\mu m$	$R = 2.065\,\mu m$	$R = 2.453\,\mu m$	$R = 2.787\,\mu m$
NA	0.846	0.718	0.633	0.572

Table 4.1: Positive FZP design parameters and NA.

Figure 4.2 displays simulation results for positive FZPs tailored for multiple focal lengths. The series of images delineates both the acoustic field (left) and intensity (right) profiles of Positive FZPs with focal depths of 1 μm to 4 μm. The field simulations showcase the FZPs' ability to diffract and interfere acoustic waves constructively, forming precise focal points. The intensity maps concurrently exhibit the concentration of acoustic energy, with the areas of highest brightness marking the sharpest focus. The gradual increase in focal depth from 1 μm to 4 μm (NA getting bigger as well as the radius of FZPs stay the same) leads to a corresponding expansion in the intensity profiles, demonstrating the FZPs' adjustable focusing capability. These findings highlight the potential of Positive FZPs in customizing the focal spot size, crucial for versatile resolution requirements in applications ranging from detailed biological tissue imaging to material characterization at variable depths.

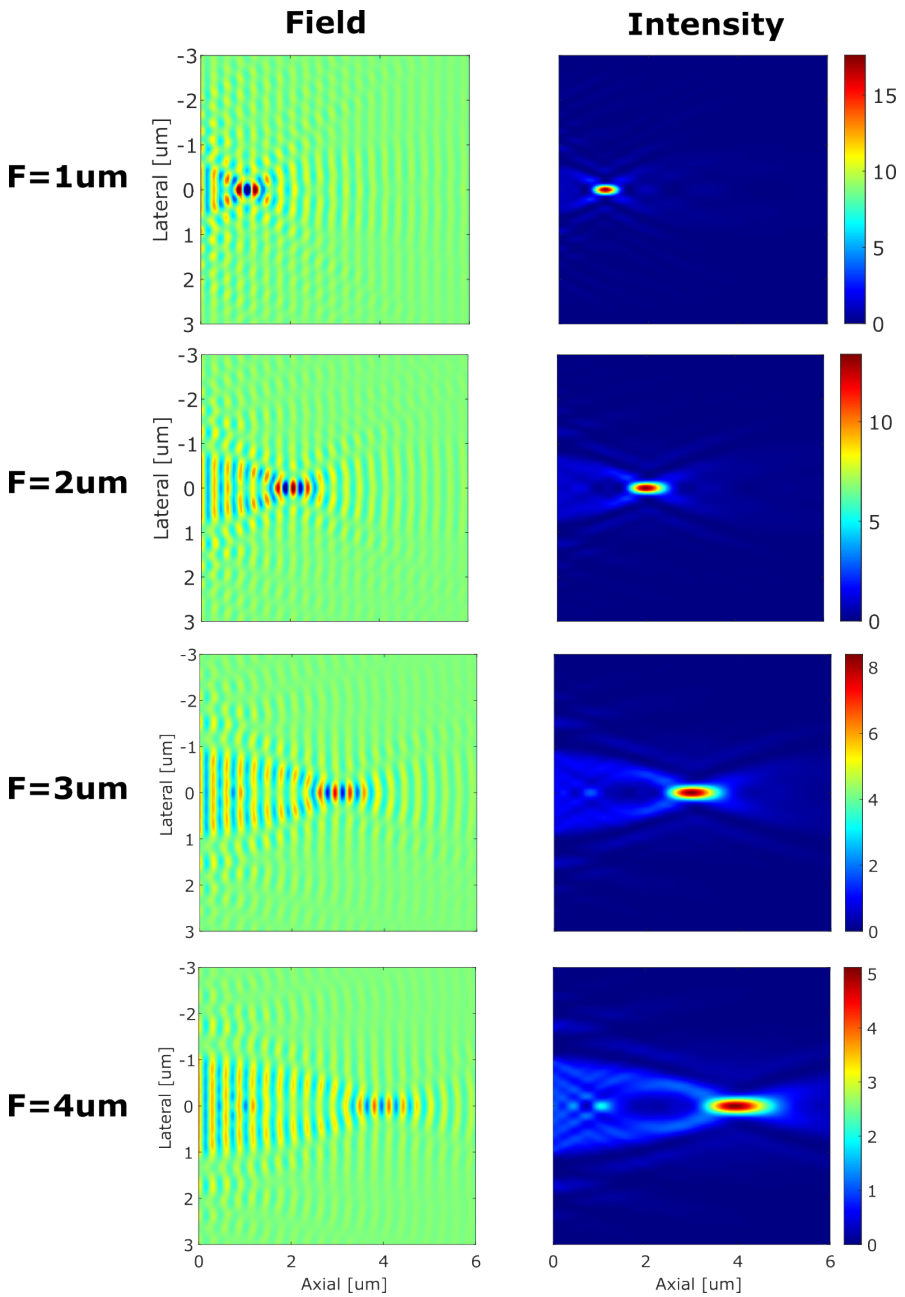

Figure 4.2: Simulation results of positive FZP with varied focal depths: acoustic field and intensity profiles for positive FZPs designed for three different focal depths. From top to bottom, the simulations correspond to focal depths of 1 μm, 2 μm, 3 μm, and 4 μm. (Left) The field simulations illustrate the wavefront manipulation achieved by the FZP design across the lateral dimension. (Right) The associated intensity maps display the acoustic energy focusing at each respective focal depth, indicated by the peak brightness.

Negative FZPs

In contrast, a negative FZP has its on and off zones reversed relative to a positive FZP. Here, the zones that were coated with gold in the positive FZP are now blank, and vice versa. NA of proposed negative FZP lenses are shown in table 4.2.

Positive FZP	$F = 1\,\mu m$	$F = 2\,\mu m$	$F = 3\,\mu m$	$F = 4\,\mu m$
R	$R = 1.732\,\mu m$	$R = 2.236\,\mu m$	$R = 2.646\,\mu m$	$R = 3.000\,\mu m$
NA	0.866	0.745	0.661	0.600

Table 4.2: Negative FZP design parameters and NA.

The negative FZP also focuses waves, but it generally results in a weaker focal spot compared to the positive FZP because the constructive interference is less efficient due to the reversal of zones. Figure 4.1 (b) is a schematic of a negative FZP and (d) is a SEM image of a negative FZP with a designed focus of 3 μm.

Figure 4.3 depicts a series of simulations conducted on negative Fresnel Zone Plates (FZPs), each calibrated for focal depths of 1 μm to 4 μm. The left column provides a visual representation of the acoustic field distribution, indicating the effectiveness of the negative FZP structure in steering the acoustic wavefronts. The right column offers insight into the acoustic energy intensities achieved at these focal points, with the colour gradients reflecting the spatial distribution of the focused energy. Notably, as the designated focal depth increases, the intensity maps reveal a corresponding spread of the focal region, illustrating the adjustable nature of the FZP's focusing capacity, similar as the results for the positive FZPs.

Phase Reverse FZPs

A PR-FZP is a more complex variant where each neighbour zone induces a phase shift (usually half a wavelength, or π radians), reversing the phase of the generated

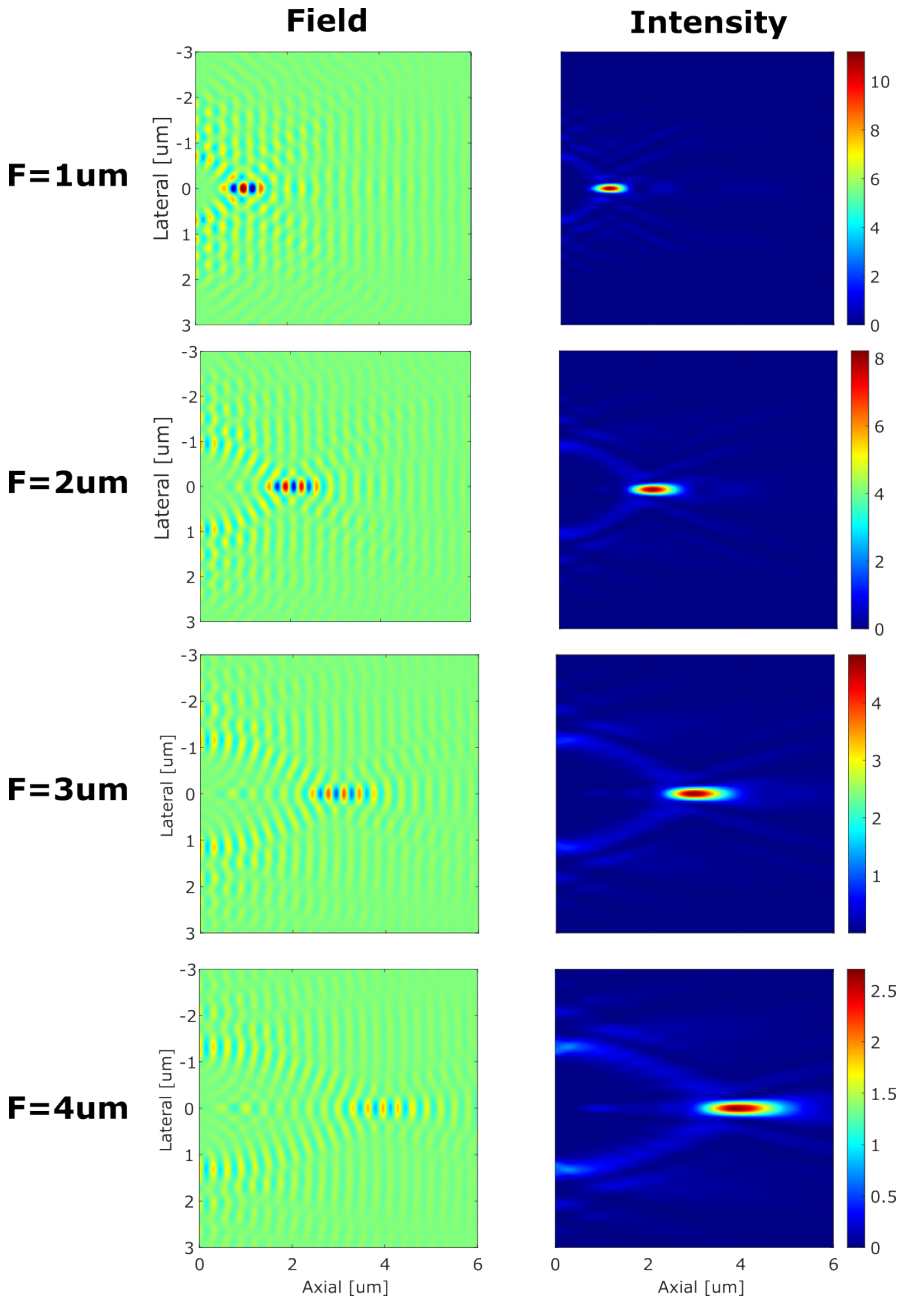

Figure 4.3: Simulation results of negative FZPs with different focal depths: Acoustic field and intensity profiles for negative FZPs designed for focal depths of 1 μm, 2 μm, 3 μm, and 4 μm. (Left) Simulated field distributions demonstrating wave manipulation across the lateral dimension. (Right) Corresponding intensity maps indicating the distribution and concentration of acoustic energy at each focal depth.

acoustic wave.

This phase shift causes the wavefronts from successive zones to still constructively

interfere at the focus, but it can allow for more efficient use of the pump light, as there are always zones coated with Au to generate coherent phonon fields. NA of proposed PR-FZP lenses are the same for the negative FZPs, detailed values are shown in table 4.3.

PR-FZP	$F = 1\,\mu m$	$F = 2\,\mu m$	$F = 3\,\mu m$	$F = 4\,\mu m$
R	$R = 1.732\,\mu m$	$R = 2.236\,\mu m$	$R = 2.646\,\mu m$	$R = 3.000\,\mu m$
NA	0.866	0.745	0.661	0.600

Table 4.3: Phase reversal PR-FZP design parameters and NA.

Figure 4.4 provides a detailed comparative simulation of three Fresnel Zone Plate (FZP) designs—Positive, Negative, and Phase Reversal (PR)—all designed for the same focal depth of 2 μm. The leftmost column (a, d, g) reveal the structural intricacies of each FZP variant, essential for their specific diffractive action. The middle column (b, e, h) captures the phase manipulation prowess of each design, as it showcases the engineered wavefronts converging at the 2 μm mark. The intensity maps (c, f, i) on the rightmost column vividly visualize the energy focusing ability of the FZPs, with the color intensity indicating the efficacy of wave concentration at the intended focal depth. Within the scope of this thesis, these simulations are pivotal for demonstrating how the strategic modification of FZP designs can significantly enhance acoustic wave focusing.

Figure 4.5 illustrates the focal plane intensity distributions for three different Fresnel Zone Plate designs, all aimed at a 2 μm focus depth. Panels (a), (b), and (c) display the intensity profiles for Positive, Negative, and PR FZPs, respectively. Each panel shows a distinct pattern of energy concentration, with the PR FZP exhibiting a notably intense focal point. The dashed lines across the intensity maps denote the targeted 2 μm focal depth, allowing for a direct visual comparison of the focusing efficiency among the FZP designs. Panel (d) further elucidates these differences through a cross-sectional intensity plot along the central axis, where

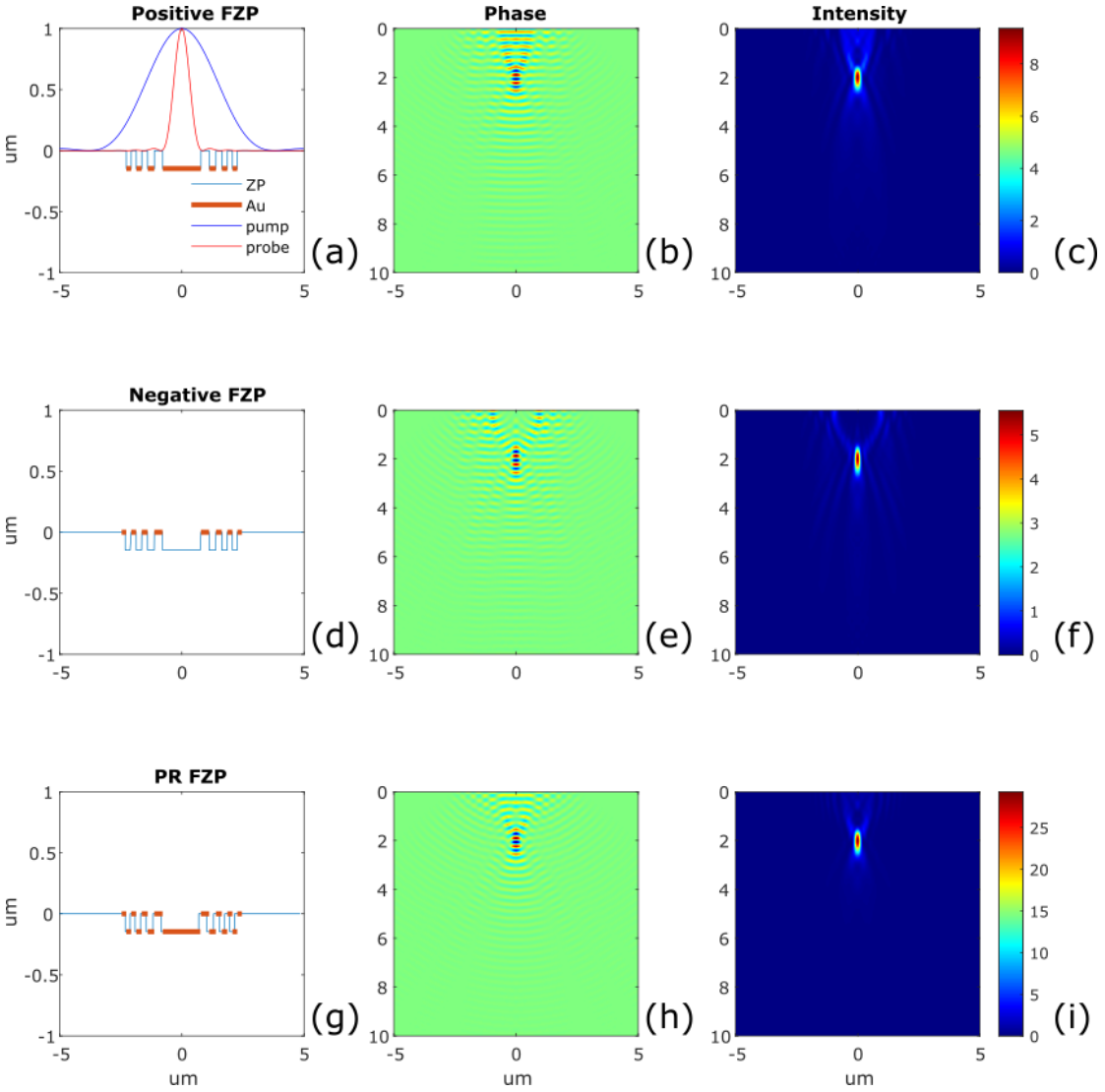

Figure 4.4: Simulation analysis of 2 μm focus FZP Designs: (a, d, g) depict the structural profiles for Positive, Negative, and PR FZPs, respectively, each engineered for a 2 μm focal depth. (b, e, h) are phase distribution simulations, showing the precise control of wavefronts each FZP design exerts. (c, f, i) display the corresponding acoustic intensity maps at the 2 μm focal point, illustrating the concentration and distribution of energy. The x-axis indicates the axial position while the y-axis represents the lateral position, with the lens located on the left.

the peak intensities clearly delineate the superior focus achieved by the PR FZP. Black arrows pinpoint the FWHM measurements: 224 nm for Positive FZP, 192 nm for Negative FZP, and 210 nm for PR FZP. These FWHM values collectively imply that the phonon field can be refined to a narrow focus in the vicinity of 200 nm. Such precision, indicated by the FWHM values, is instrumental in the

pursuit of sub-micron resolution in phonon microscopy, as it directly influences the system's capability to resolve fine details, crucial in applications such as live-cell imaging and material characterization within the realm of TRBS methodologies.

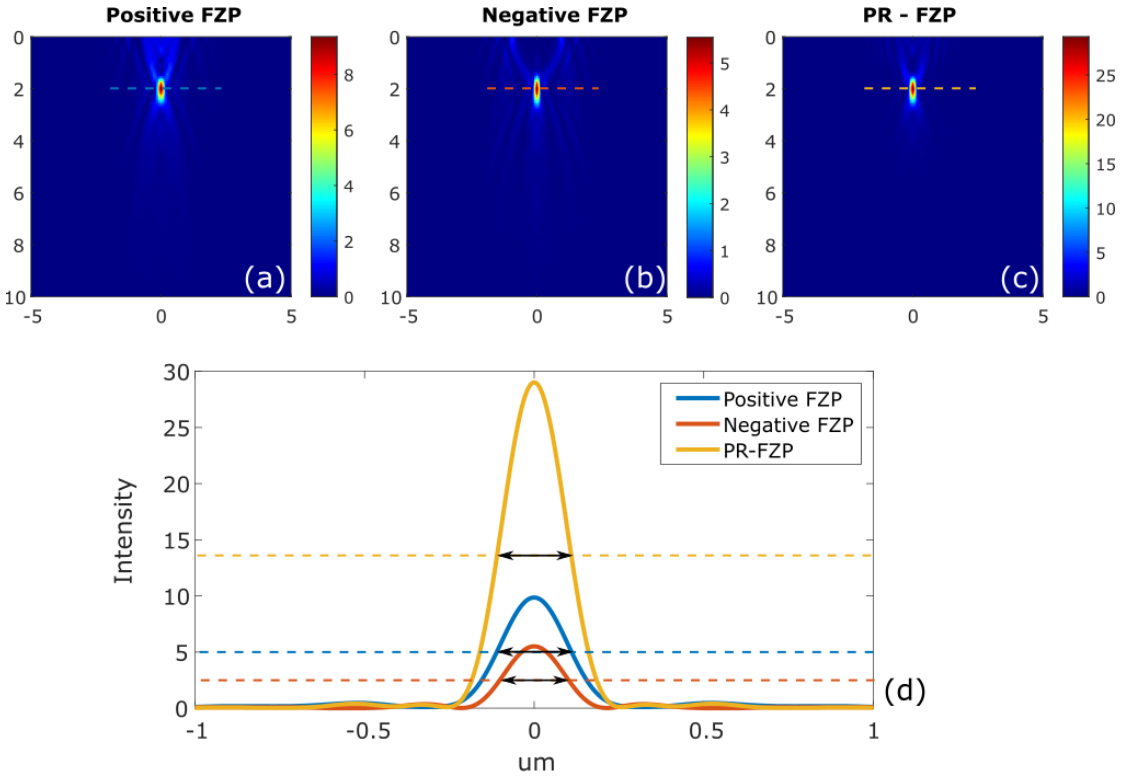

Figure 4.5: Intensity profiles and comparisons for 2 μm focused FZPs: (a) Positive FZP, (b) negative FZP, and (c) Phase Reversal (PR) FZP intensity distributions at the focal plane, with the dashed line indicating the 2 μm focus depth. (d) Cross-sectional intensity comparison along the central axis for all three FZP types, demonstrating their relative focusing capabilities at the 2 μm mark.

4.1.2 Experimental results

Experimental measurements of a positive FZP with a focus of 2 μm are presented, including both centre traces and line scans, to demonstrate the focusing capabilities of FZPs.

In a TRBS measurement, the sound propagates from the generation transducer along the z-axis. Thus, it has the ability to scatter light from different spatial

position in the medium. Though the measurement is in time domain. If the refractive index is known, then the time trace can be converted from the temporal axis into a spatial axis. The speed of sound v can be calculated using the following equation:

$$\nu = \frac{\lambda_{\text{probe}}\, f_B}{2n} \tag{4.1}$$

which allows the conversion from the time axis to spatial axis as:

$$z = t\nu \tag{4.2}$$

allowing the estimation of acoustic wave focusing along the z axis.

Centre traces

The following discussion includes experimental result of a time-resolved trace captured from the central point of a positive FZP, specifically engineered with a focal length set at 2 μm. This trace is pivotal as it provides insight into the acoustic lens behaviour and efficiency of energy concentration at the designated focal depth, illustrating the ability with which the FZP structure can manipulate phonon fields.

Alongside the data from the positive FZP, a reference trace from a standard flat optoacoustic transducer is provided. This inclusion serves to enhance the comparative analysis, allowing for a more comprehensive understanding of the focusing effects introduced by the Fresnel Zone Plate in relation to the baseline acoustic response of conventional flat transducers.

In the experimental analysis presented in Figure 4.6, time resolved Brillouin scat-

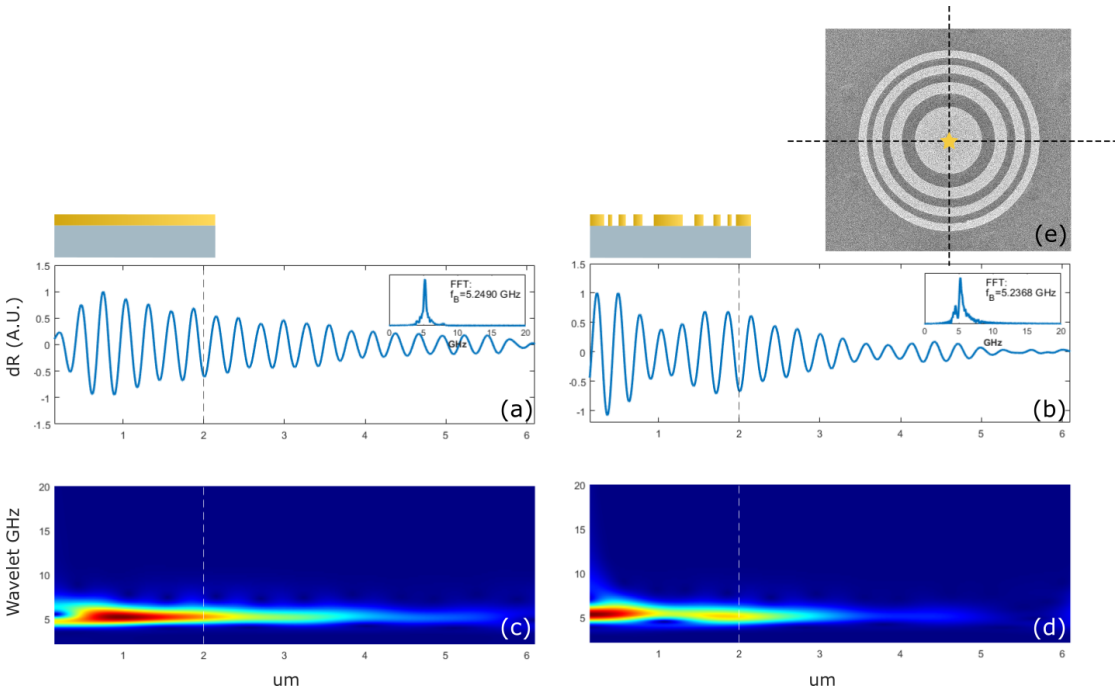

Figure 4.6: Time resolved Brillouin scattering traces and frequency analysis of flat and positive FZP: (a, b) Time-resolved Brillouin scattering traces obtained from a flat gold transducer and the central trace of a $F = 2\,\mu m$ positive Fresnel Zone Plate (FZP) lens, respectively. Insets show the Fast Fourier Transform (FFT) spectrum indicating the Brillouin frequency (f_B) peaks. (c, d) Corresponding wavelet transform visualizations displaying the frequency distribution over time. (e) Scanning Electron Microscope (SEM) image of the Positive FZP lens with the central focus point indicated by the intersection of dashed lines and a yellow star.

tering (TRBS) traces reveal the acoustic response of a flat gold transducer and the focal point of a F = 2 μm positive FZP lens. The traces in (a) and (b) display the TRBS signals, with the central trace of the FZP lens exhibiting a distinct oscillation pattern.The inset windows provide a detailed view of the FFT-derived Brillouin frequency for both traces, with f_B measured at 5.2490 GHz for the flat transducer and a slightly shifted f_B of 5.2368 GHz for the FZP lens. More discussion about the shifting frequency will be included in the experimental results in the concave lens Section 4.2.3: a similar but stronger f_B was observed, along with possible explanations for the shifting. The wavelet transforms in (c) and (d) further illustrate the temporal evolution of these frequencies, offering insights into the focusing effects introduced by the FZP design. The SEM image in (e) shows

the FZP lens for this scan, with the central focal point—a region of heightened acoustic interest—marked by the cross lines and a yellow star. These findings demonstrate the functionality of FZP geometry in modulating and concentrating phonon fields.

Line scans

To thoroughly evaluate the performance of the lens in both axial and lateral dimensions, line scans were conducted along the x and y axes. These line scans are important in analysing the performance of the FZP lens's focusing ability, offering a quantitative measure of the acoustic intensity and resolution in orthogonal directions. From these scans, the consistency of the lens's focus in the axial direction is evident, as is the extent of its resolution within the lateral plane, limited by diffraction (from the optical detection system).

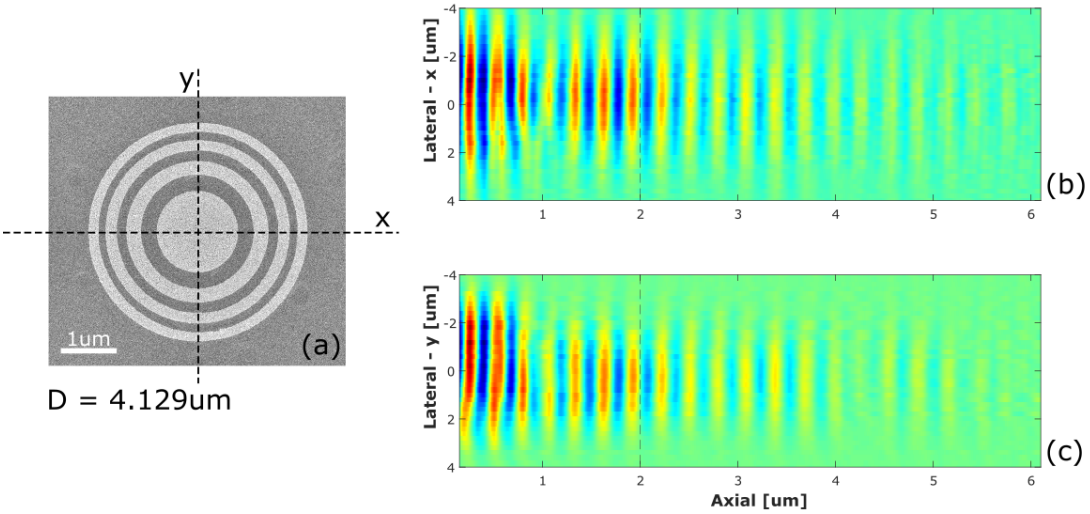

Figure 4.7: Experimental results showcasing the focusing capabilities of a positive FZP lens with a designed focus of 2 μm: (a) SEM image of the FZP with an outer ring diameter of 4.129 μm. (b) Line scan across the axial depth (x-axis) and the lateral scanning position (y-axis) of the probe beam, indicating the acoustic field intensity distribution on the z-axis. (c) A similar line scan revealing the acoustic field's intensity distribution on the y-axis, demonstrating the FZP lens's bidirectional focusing effect.

Figure 4.7 provides experimental insights into the functionality of a FZP lens, as captured by Scanning Electron Microscopy (SEM). Part (a) illustrates the FZP with a precise diameter of 4.129 μm. The FZP's design, which includes multiple concentric rings, is integral to its ability to focus acoustic fields.

The subsequent parts, (b) and (c), detail the line scans along the axial depth and lateral scanning positions of the probe beam. The x-axis denotes the z-axis — essentially, the penetration depth into the sample—while the y-axis marks the lateral position of the probe beam as it moves over the sample's surface(x- and y-axes in part (b) and (c), respectively).

The FZP lens was engineered with an intended focus at a 2 μm axial depth. The results depicted in the line scans indicate a noticeable intensification of the signal at approximately this 2 μm region. This enhancement in signal strength is indicative of the FZP lens's capability to concentrate the acoustic field at the predetermined focal point, thus validating the lens design's precision. The observed focal point concentration demonstrates that the lens design is well-aligned with the objective of focusing coherent phonon fields and thus opens the way to enhancing imaging resolution beyond the diffraction limit.

4.1.3 Discussion

The simulations illustrating the performance of positive, negative, and phase-reversed FZPs, as proposed in Chapter 3, were presented, accompanied by experimental validation of the focusing capabilities of a positive FZP in directing coherent phonon fields.

The simulations and experimental data presented thus far showcase the functioning of a positive FZP, but it's important to note that with the current setup, a true

acoustic field measurement showing the resolution in lateral direction is still challenging. This difficulty arises because the detection probe beam's Point Spread Function (PSF) is larger than the narrow focusing width of the acoustic beam, potentially affecting the accuracy of measurements. A more in-depth discussion regarding the implications of PSFs will be addressed in the preliminary results and perspectives in Section 5.4.

Furthermore, only experimental results from a positive FZP were shown, due to limitations in energy utilization efficiency observed in both positive and negative FZPs. The fundamental issue lies in the fact that only the Au-covered rings in these FZPs are capable of sound generation. Negative FZPs exhibit a more pronounced issue due to their lower percentage of Au coverage, leading to challenges in experimental settings where pump power cannot be increased indefinitely without risking structural damage. Positive FZPs, while somewhat more efficient, still face limitations in this regard, though they were sufficient to obtain experimental traces.

Phase-reversal FZPs theoretically address this energy efficiency problem. However, their fabrication process poses its own set of challenges, often leading to imperfect lens profiles that deviate from the ideal design.

Additionally, there are concerns about the reusability of the effective positive lenses. The Electron Beam Lithography (EBL) fabrication process, while precise, does not lend itself easily to lens cleaning and recycling for multiple experimental iterations. This limitation imposes a constraint on the repeated use of the these lenses, potentially impacting the sustainability and cost-effectiveness of the research process.

Optical and Acoustic PSFs

Though a clear signal increase can be seen at the designed focus from experiments (Fig. 4.7), it still remains challenging to find the real acoustic width of the focused coherent phonon field.

Convolution When using microscopy, the image that is captured is always a diffraction limited representation of the real object that is being studied. This blurring can be explained by the Point spread function (PSF). The PSF describes how a point source or point object looks like in the final image.

The image formation process in a light microscope follows a linear pattern. When two objects A and B are imaged together, the resulting image is the sum of the individual images of the objects. Due to the linearity property, one can calculate the image of an object by breaking it down into smaller parts, imaging each part, and then adding up the results. By dividing the object into smaller and smaller parts, it becomes a collection of small point objects. Every single one of these objects creates a Point Spread Function (PSF) in the image. The PSF is adjusted and resized based on the position and brightness of each individual point. The resulting image is thus a compilation of (frequently overlapping) point spread functions. The process of forming this image can be mathematically described using convolution. It involves convolving the object with the point spread function (PSF) of the imaging setup to obtain the acquired image.

Blurred acoustic field In the pursuit of enhancing imaging resolution beyond the diffraction limit, the acoustic PSF plays a critical role as demonstrated in our recent experimental findings. The data reveal that the acoustic PSF is significantly more confined compared to the probe's optical PSF utilized to gauge the

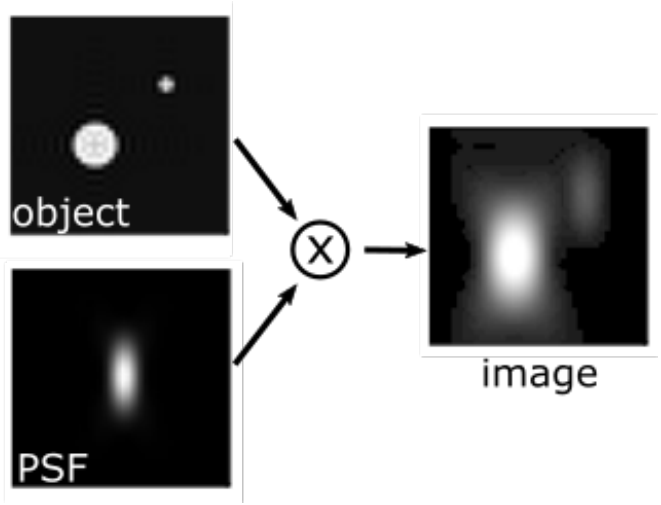

Figure 4.8: Schematic representation of the convolution process in image formation. The original object is depicted in the top left, and its interaction with the PSF, shown in the bottom left, results in the convolved image on the right. The multiplication symbol (×) signifies the convolution operation which combines the object with the PSF to produce the resultant image, illustrating the effect of the imaging system on the appearance of the object.

acoustic field. This discrepancy is pivotal in understanding the limitations of the current experimental apparatus to accurately capture the true acoustic resolution capabilities of the FZP lenses designed for phonon microscopy.

Figure 4.9 presents a comparison of the simulated and experimental results. Figure 4.9 (a) shows the simulated acoustic intensity profile at the focal point, highlighting the intended narrowness of the acoustic field. Conversely, Figure 4.9 (b) illustrates the broader probe intensity profile used in measuring this field, which fails to match the acoustic PSF's narrowness due to the inherent limitations of the measurement system.

The difference between the simulated focused phonon field, as seen in Figure 4.9 (c), and the broader signal obtained from experimental line scans, shown in Figure 4.9 (d), can be primarily attributed to the disparity in the widths of the respective PSFs. The simulated acoustic field exhibits well-defined wave propagation and interference patterns, indicative of a tightly focused phonon field. However,

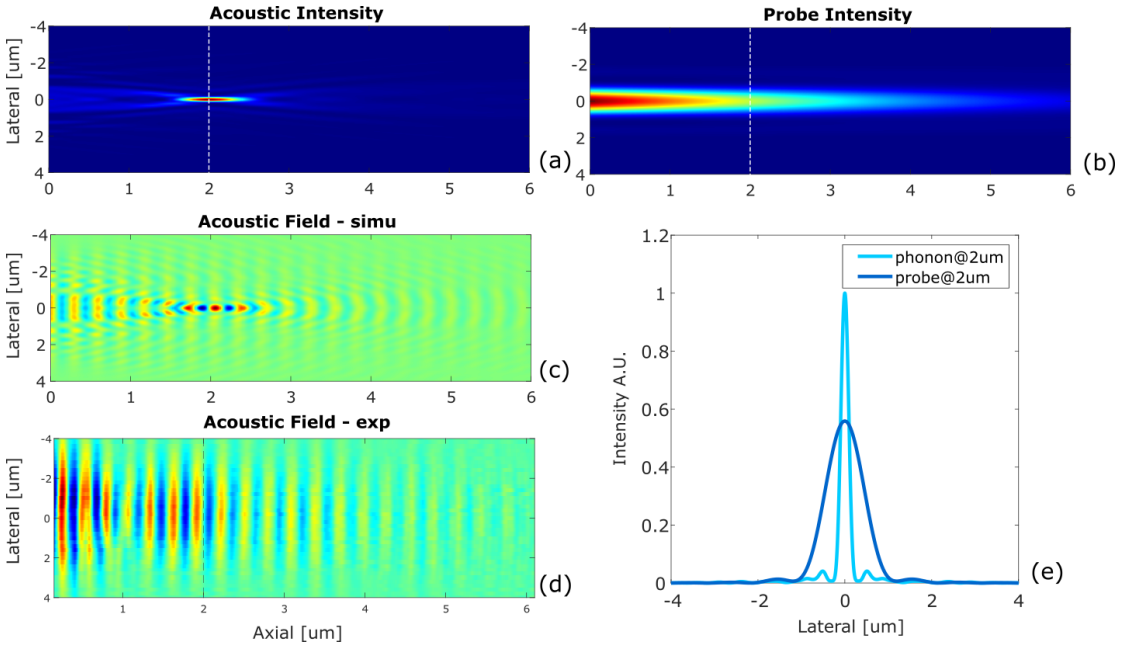

Figure 4.9: Comparative analysis of acoustic intensity and field distribution: (a) Simulated acoustic intensity profile demonstrating the focal point of the acoustic field. (b) Probe intensity profile indicating the measurement sensitivity at the focus. (c) Simulated acoustic field distribution showing wave propagation and interference patterns. (d) Experimental acoustic field distribution confirming the simulation results with visible wave patterns. (e) Overlay of intensity profiles for both the phonon at a 2 μm axial depth and the probe at the same depth, illustrating the concentration and measurement of the acoustic field at the designed focal point.

the experimental acoustic field exhibits a more diffuse pattern, aligning with the broader probe PSF and indicating a limitation in the system's ability to resolve the true extent of the lens's focusing ability.

Figure 4.9 (e) provides an overlay of intensity profiles for both the phonon and the probe at a 2 μm axial depth. The comparison demonstrates the concentration of the acoustic field at the designed focal point, yet also underlines the experimental limitations, as the probe PSF's broader profile results in a diluted representation of the acoustic field's intensity.

These observations underscore the necessity for an advanced measurement system capable of matching the acoustic PSF's precision to fully leverage the super-

resolution potential of the acoustic lenses. Only with such enhancements can the true resolving power of the lenses be realized and applied effectively in high-resolution phonon microscopy.

To mitigate the issue of the larger probe PSF compared to the acoustic PSF, a convolution between the simulated acoustic field and the probe measurement PSF was applied, drawing from established methodologies in conventional microscopy. This process aimed to harmonize the highly precise simulations with the broader, experimentally obtained results.

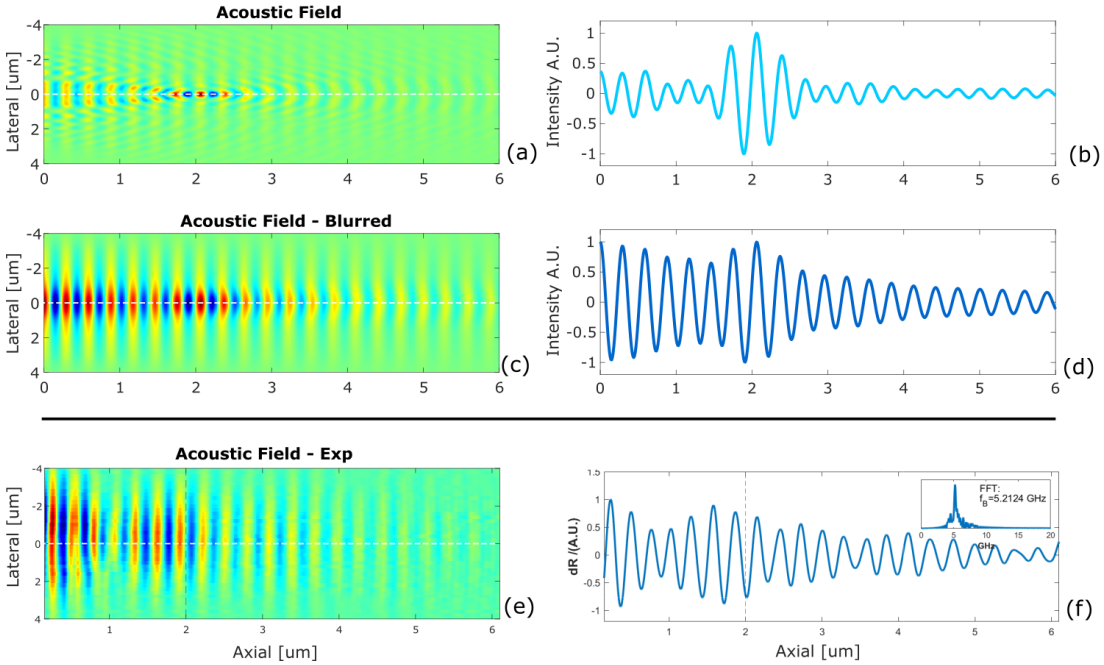

Figure 4.10: Comparisons of simulated and experimental acoustic field distributions and their central axial profiles. (a) delineates the simulated acoustic field, with (b) showing its axial intensity trace along the dashed line. (c) represents the acoustic field simulation convolved with the probe beam's PSF, illustrating the resolution limits of the measurement system, and (d) its axial trace, evidencing signal broadening due to convolution. (e) conveys the experimental acoustic field measurements, and (f) the central axial trace with an FFT inset specifying the Brillouin frequency, revealing the practical constraints when capturing the focused acoustic field.

In Figure 4.10, the original simulated acoustic field (a) and its central axial trace (b) are presented, which starkly contrast with the experimental findings. The

convolution of the simulated acoustic field with the probe PSF, depicted in (c) and (d), mimics the blurring effect inherent in the measurement system, yielding a broadened signal profile that closely resembles the experimental data.

The experimental results are illustrated in (e) with the central axial trace (f), the latter incorporating an inset FFT that confirms the Brillouin frequency. The congruence between the convolved simulation and the experimental results underscores the convolution model's utility in emulating the actual measurements.

By employing this convolution approach, the study effectively narrows the gap between theoretical simulations and experimental limitations. This technique enhances the predictability of experimental outcomes, providing a refined understanding of the resolution capabilities within the current experimental framework and guiding the development of more accurate measurement systems for high-resolution phonon microscopy.

Efficiency of FZPs

In this section, we went deeper into the experimental outcomes obtained from positive FZPs, addressing the inherent limitations in energy utilization that are observed in both positive and negative FZPs. The primary constraint lies in the structural design of these FZPs, where only the rings coated with gold (Au) are active in generating acoustic signals. This design aspect significantly influences the efficiency of energy transfer from the pump laser to the acoustic field.

Negative FZPs as shown in 4.11 (b), in particular, demonstrate a more pronounced inefficiency. This is primarily due to their structural composition, which features a relatively lower percentage of Au-covered areas compared to their positive counterparts. In experimental setups, this leads to a substantial challenge: there is a

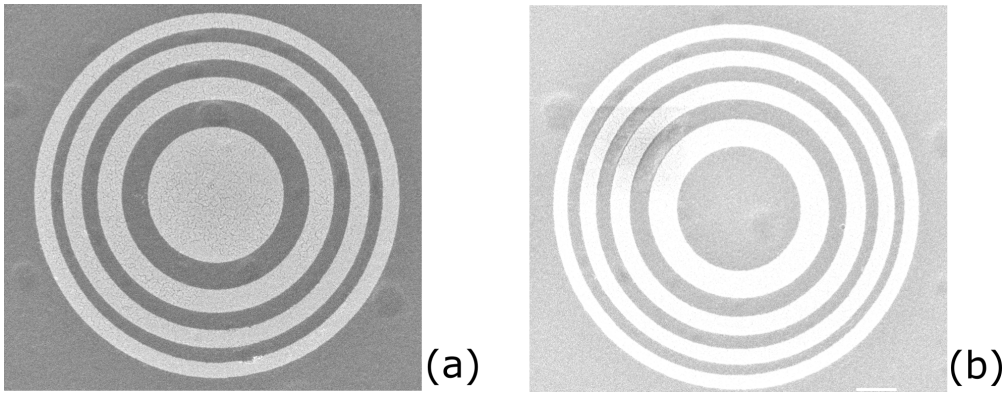

Figure 4.11: SEM pictures of postive and negative FZPs showing the Au covered rings.

finite limit to how much the pump laser power can be increased without causing potential damage to the FZP structure. Consequently, the negative FZPs' ability to focus acoustic energy is hindered, making it difficult to obtain clear and reliable experimental data.

Positive FZPs as shown in 4.11 (a), on the other hand, exhibit a slightly improved efficiency. The greater coverage of Au in their design allows for a more effective conversion of optical energy into acoustic waves. This advantage makes it feasible to conduct experiments within the safe operational limits of the laser, thus enabling the acquisition of experimental traces. However, it's important to note that even positive FZPs are not without their limitations. The efficiency of energy utilization is still not optimal, and there remains room for improvement in harnessing the full potential of the pump laser energy for acoustic signal generation.

Fabrication issues of FR FZPs

The Phase-Reversal FZPs were conceptualized to overcome the limitations posed by positive and negative FZPs in terms of energy efficiency. PR FZPs aim to fully utilize the energy from the pump laser, thus enhancing the sound generation capability without wastage. However, the fabrication of PR FZPs introduces its

own complexities, as precision in the nano-scale manufacturing process is critical to achieve the desired acoustic performance.

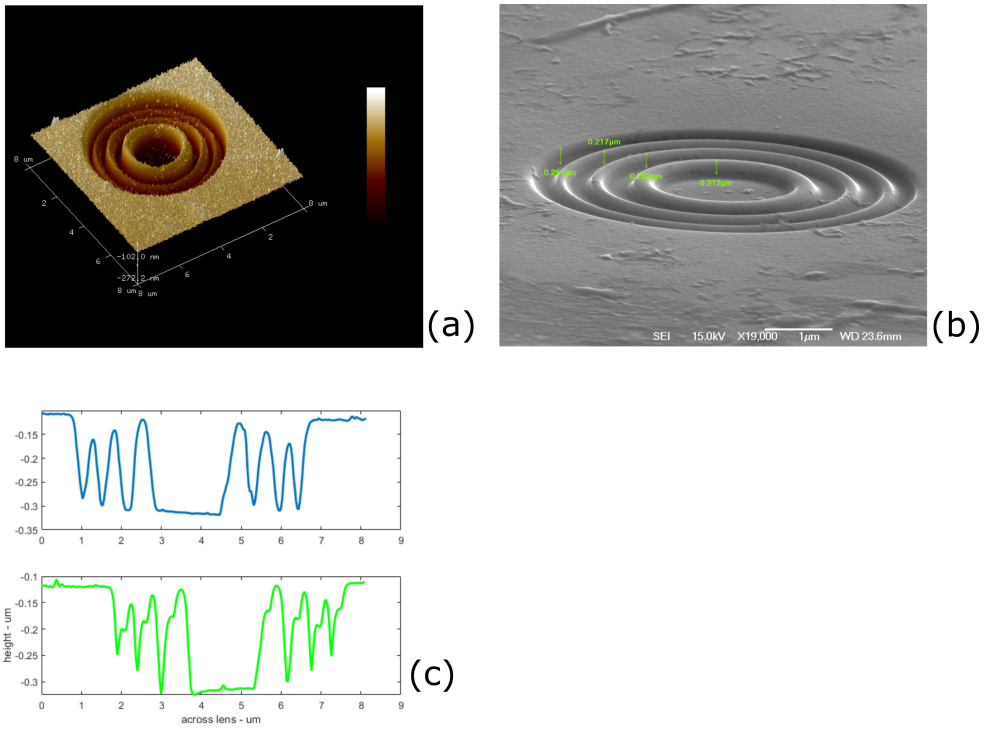

Figure 4.12: Fabrication issues of PR FZP: (a) AFM reconstruct. (b) SEM picture of a PR FZP (c) cross line plots of AFM results.

As depicted in Figure 4.12 (a) and (c), Atomic Force Microscopy (AFM) measurements and (b), SEM picture reveal that the edges of the manufactured lenses are not as sharp as designed, but rather exhibit a rounded profile. This deviation from the intended sharp-edge design can lead to suboptimal sound generation.

To simulate the potential effects of fabrication-induced issues, a simple model was used to examine how a rounded profile could alter the focusing ability. Figure 4.13 shows one example of simulating fabrication-induced issues. A simple model utilising data interpolation is employed to generate a rounded PR-FZP profile. Then feeding this lens profile to the simulation model, a significant decrease can be observed: from the maximum of 28.837 to 10.665 (Arbitrary unit) of acoustic intensity at the focal point.

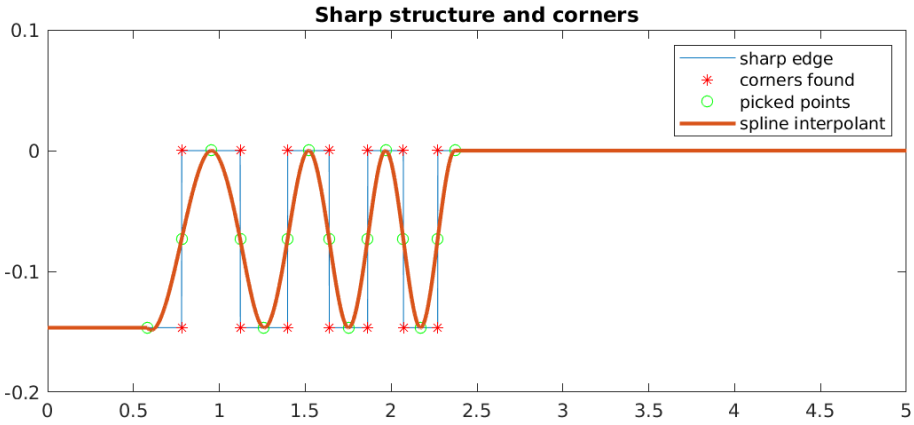

Figure 4.13: Simulated curved lens features using data interpolation. The original PR-FZP profile is plotted with green lines, then centre of each ring is found and labelled with the green dots. Then the thick orange line indicates the interpolation result.

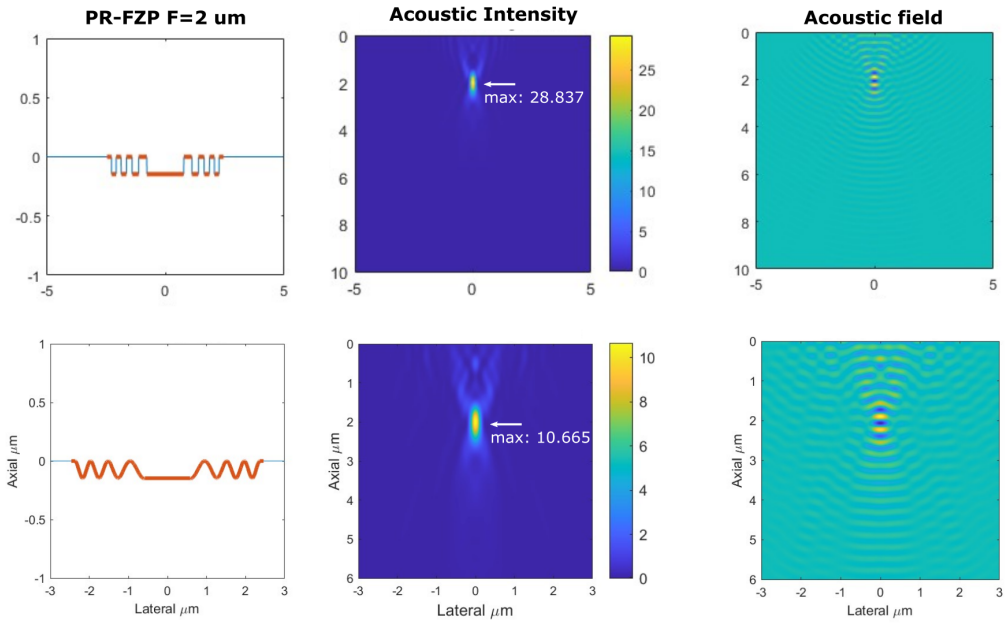

Figure 4.14: Acoustic Intensity, acoustic field and structure of ideal PR-FZP and modified lens profile.

Moreover, the narrow gaps between the concentric rings of the PR-FZP present additional challenges during the gold sputtering process. An uneven deposition of gold can result in a non-uniform acoustic field, potentially leading to the dysfunctionality of the PR-FZP.

Lens reuse and recycle

One of the practical aspects of implementing FZPs in acoustic imaging applications is about the reusability of these lenses, particularly those that have proven effective in focusing the acoustic waves, such as the positive FZPs. Although the EBL fabrication process is renowned for its precision in creating intricate nanostructures, it presents a significant challenge when it comes to cleaning and recycling the lenses for subsequent experimental use.

Because the nano-fabricated lenses are fragile, any cleaning method must be both gentle enough not to damage the structures and strong enough to get rid of all the contaminants effectively. Normal cleaning methods, like acid cleaning or ultrasonic bath cleaning, might not work with nanostructured lenses made with EBL because they could damage the lenses.

Meanwhile, the necessity for a clean lens surface for each experiment is crucial for maintaining consistency and accuracy in the results. For imaging purposes, any leftover contaminants, such as dried bacteria and dirt on the lens surface can cause problems with the acoustic focusing, which in turn could lower the resolution and quality of the imaging.

This limitation of the EBL process, raises worries about the long-term viability and cost concerns of using these lenses in research. Each patch of lenses sitting in one substrate requires a significant investment in terms of time and resources, and the inability to reuse them efficiently may also increase the costs and delay of the research process.

Thus, there is a clear need for developing alternative fabrication or cleaning methods that would enable the repeatable use of lenses without problems in performance. This would not only enhance the sustainability of the research but also

make high-resolution acoustic imaging more accessible and cost-effective.

4.2 Concave lenses

In this section, the focusing properties of concave lenses are thoroughly examined, with a focus on results from simulations as well as experiments. These findings demonstrate how concave lenses have a great deal of promise for achieving true acoustic resolution in phonon microscopy. The section will also discuss their possible contribution to reducing one of the drawbacks of phonon microscopy: the temperature increase at the transducer/cell interface, which is essential to maintaining biocompatibility.

4.2.1 Simulation

Similar to the previous section, numerical simulations have been computed using the single frequency Fourier-Bessel spectrum method (FBASM) presented in Chapter 2 to find the equivalent acoustic field for different concave designs. Table 4.4 lists all the lens designs that are shown in the simulation. Radius R is the sphere's radius to make the lens and r is the radius of the concave lens in the horizontal plane as shown in the following Figure 4.15, which is equals to $D/2$.

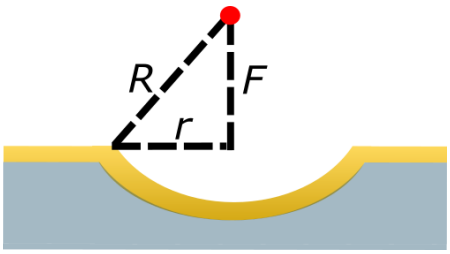

Figure 4.15: Schematic of concave lens design parameters.

Figure 4.16, Figure 4.17 and Figure 4.18 shows the simulated performance of

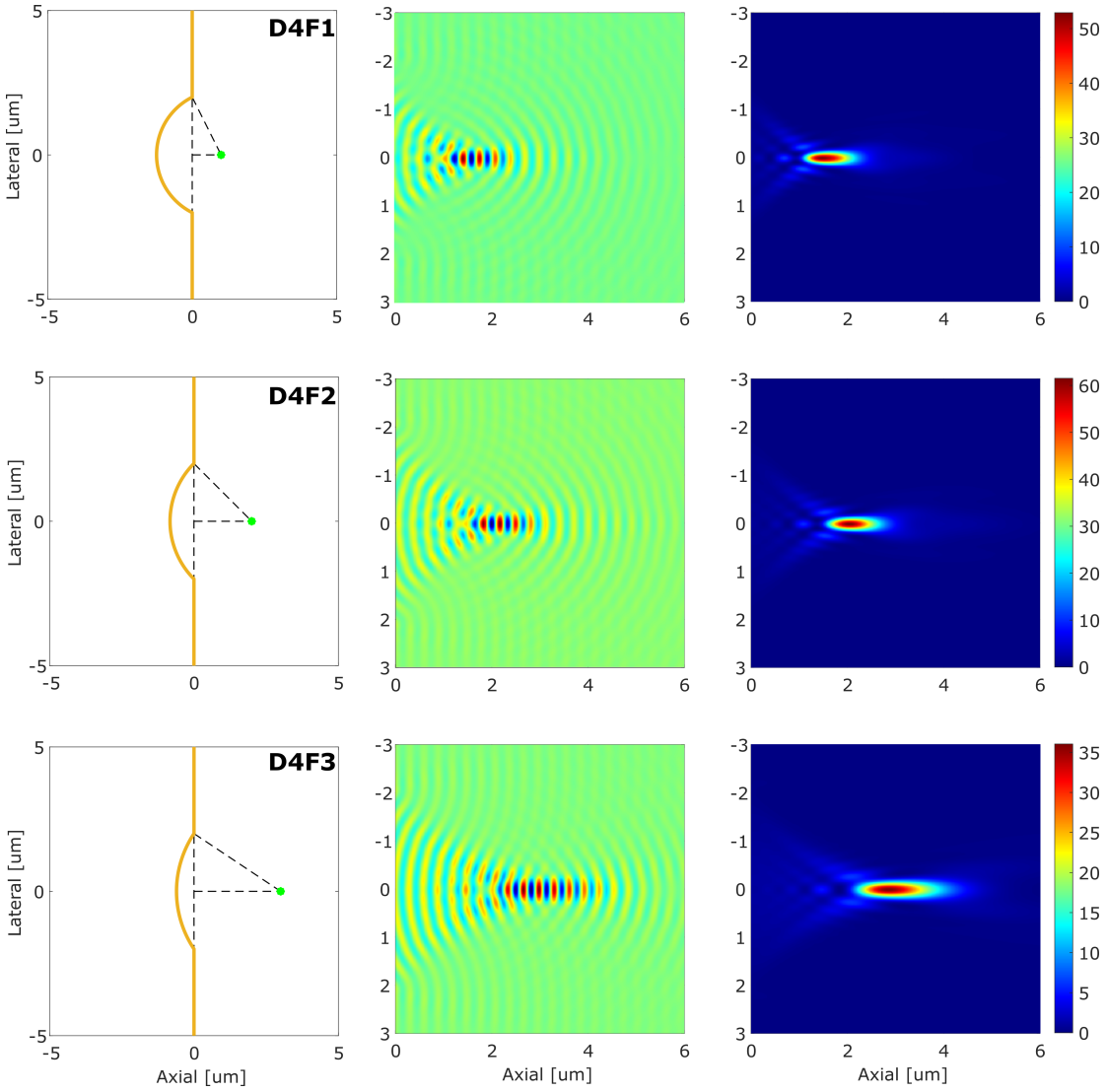

Figure 4.16: Simulated acoustic focusing of concave lenses with varied focal depths: (Left) Cross-sections showing the concave lens profiles designed for 1 μm (D4F1), 2 μm (D4F2), and 3 μm (D4F3) focal depths, each with a lens diameter of 4 μm. (Center) Acoustic field distribution simulations across the lateral plane for each lens. (Right) Corresponding intensity maps illustrate the focused acoustic energy at the respective focal depths.

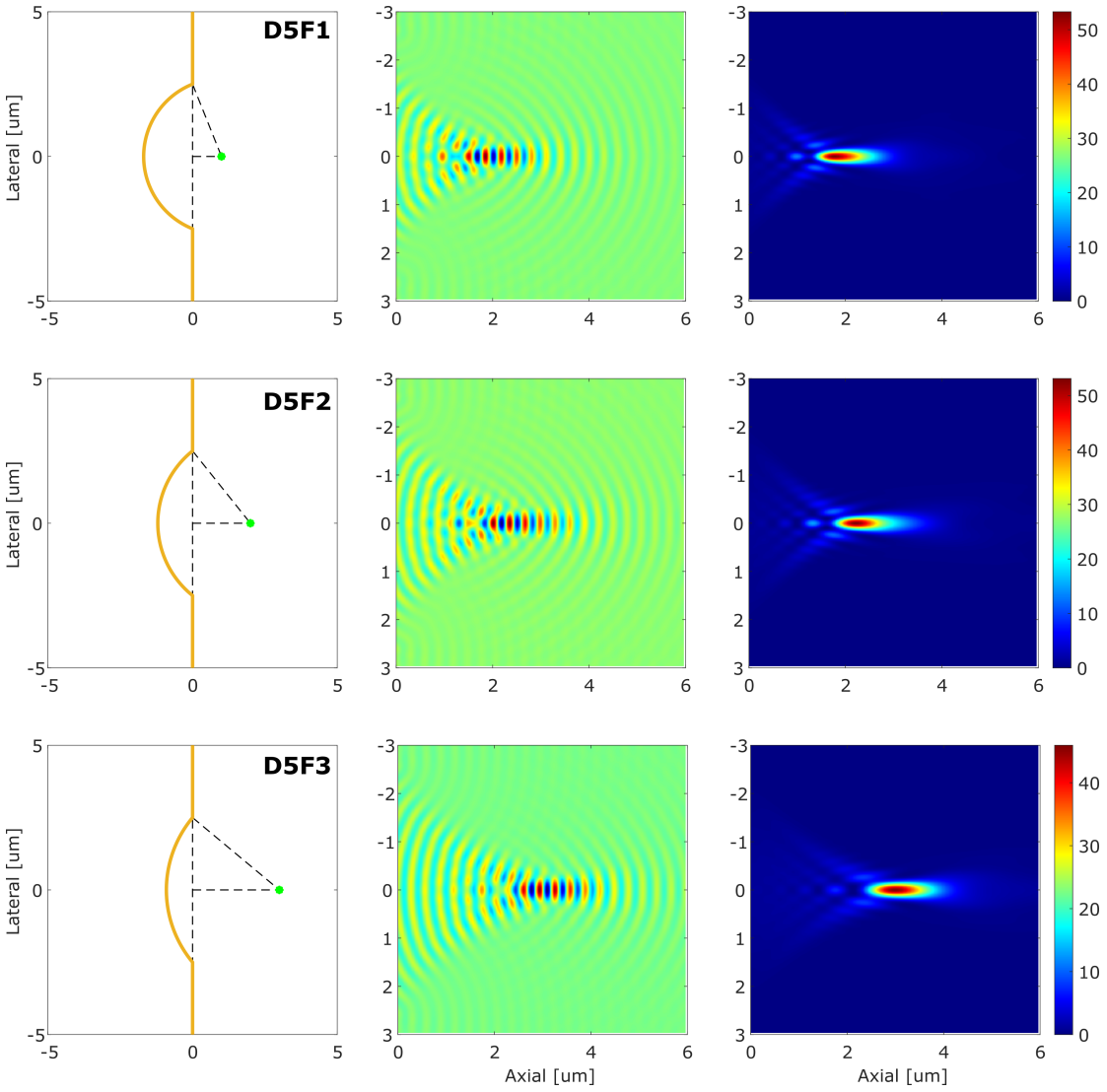

Figure 4.17: Simulated acoustic focusing of concave lenses with varied focal depths: (Left) Cross-sections showing the concave lens profiles designed for 1 μm (D5F1), 2 μm (D5F2), and 3 μm (D5F3) focal depths, each with a lens diameter of 5 μm. (Center) Acoustic field distribution simulations across the lateral plane for each lens. (Right) Corresponding intensity maps illustrate the focused acoustic energy at the respective focal depths.

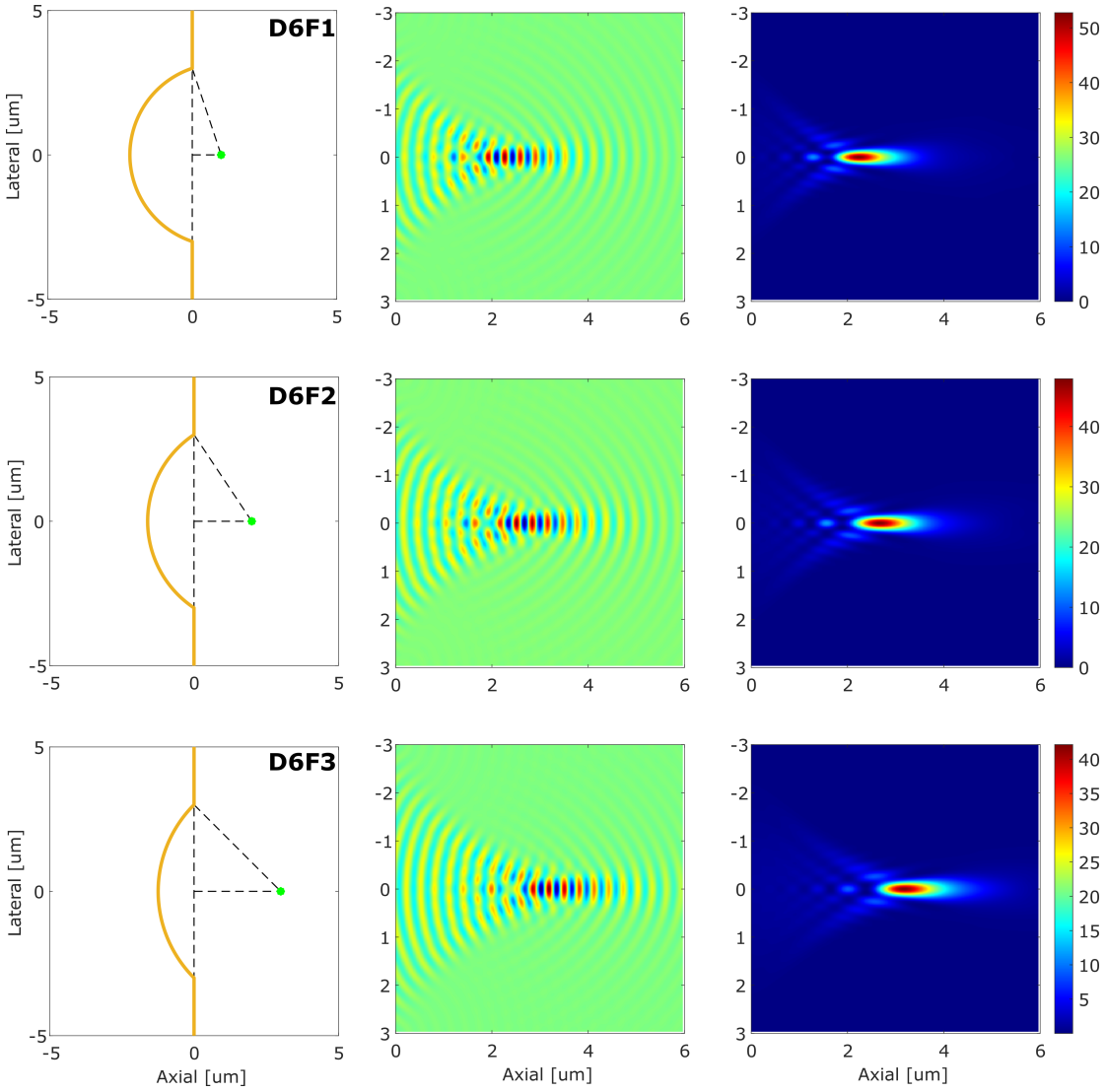

Figure 4.18: Simulated acoustic focusing of concave lenses with varied focal depths: (Left) Cross-sections showing the concave lens profiles designed for 1 μm (D6F1), 2 μm (D6F2), and 3 μm (D6F3) focal depths, each with a lens diameter of 6 μm. (Center) Acoustic field distribution simulations across the lateral plane for each lens. (Right) Corresponding intensity maps illustrate the focused acoustic energy at the respective focal depths.

	$F = 1\,\mu m$	$F = 2\,\mu m$	$F = 3\,\mu m$
$D = 4\,\mu m$	$R = 2.2361\mu m$	$R = 2.8284\mu m$	$R = 3.6056\mu m$
$D = 5\,\mu m$	$R = 2.6929\mu m$	$R = 3.2016\mu m$	$R = 3.9051\mu m$
$D = 6\,\mu m$	$R = 3.1623\mu m$	$R = 3.6056\mu m$	$R = 4.2426\mu m$

Table 4.4: Concave lens design parameters.

multiple concave acoustic lenses, each with a 4 μm, 5 μm and 6 μm diameter, engineered to focus at depths of 1 μm, 2 μm, and 3 μm from top to bottom. The left column displays the lens profiles. The central column shows the acoustic field distribution, revealing the wavefronts' convergence around the focal points. The right column's intensity maps translate these field changes into spatial distributions of acoustic energy, with brighter colours signifying higher intensities at the focus. As the focal depth increases, there is a visible expansion of the focal zone, demonstrating the lenses' capability to precisely direct acoustic waves to specified regions. These simulations are essential for understanding how the lens curvature varies affect the lens' focusing behaviour.

NA	$F = 1\,\mu m$	$F = 2\,\mu m$	$F = 3\,\mu m$
$D = 4\,\mu m$	0.8944	0.7071	0.5547
$D = 5\,\mu m$	0.7428	0.6247	0.5121
$D = 6\,\mu m$	0.6325	0.5547	0.4714

Table 4.5: Numerical aperture (NA) of Concave lenses.

NA of proposed positive concave lenses are shown in Table 4.5, by knowing the focus F and Radius R, NA of the proposed lenses can then be calculated using the acoustic NA equation (3.4).

4.2.2 Experimental results

Experimental measurements of multiple concave lenses are presented, including center traces, line scans, and 2D scans, to demonstrate the enhanced focusing

ability of concave structures in comparison to FZPs.

Centre traces

The following discussion includes experimental results of a time-resolved trace captured from the central point of a concave lens, specifically engineered with a focal point set at 3 μm. This trace provides insight into the acoustic lens behavior and efficiency of energy concentration at the designated focal depth, illustrating the ability with which the concave lens structure can manipulate phonon fields and create strong focus.

Alongside the data from the concave lens, a reference trace from a standard flat optoacoustic transducer is provided. This inclusion allows a more comprehensive understanding of the focusing effects introduced by the concave lens in relation to the baseline acoustic response of conventional flat transducers.

Figure 4.19 presented juxtaposes the time-resolved acoustic traces and wavelet analysis results for a flat optoacoustic transducer and a concave lens with a designed focus of 3 μm. In the left column, Figure 4.19 (a) shows the base signal from the flat transducer exhibiting typical oscillatory behaviour with its corresponding Fast Fourier Transform (FFT) inset depicting the principal frequency component at 5.2490 GHz. Below, Figure 4.19 (c) presents the wavelet analysis of the base signal, displaying a broad distribution of energy across the time-frequency space.

The right column presents the centre focusing trace of the concave lens, as shown the yellow star at the joint of the two dashed lines in x and y axes in Figure 4.19 (e), Figure 4.19 (b) reveals a distinctive trace pattern: an initial low signal intensity followed by a strong signal increase at the designed focal point, which is validated by the FFT inset indicating a dominant frequency of 5.1636 GHz. The wavelet

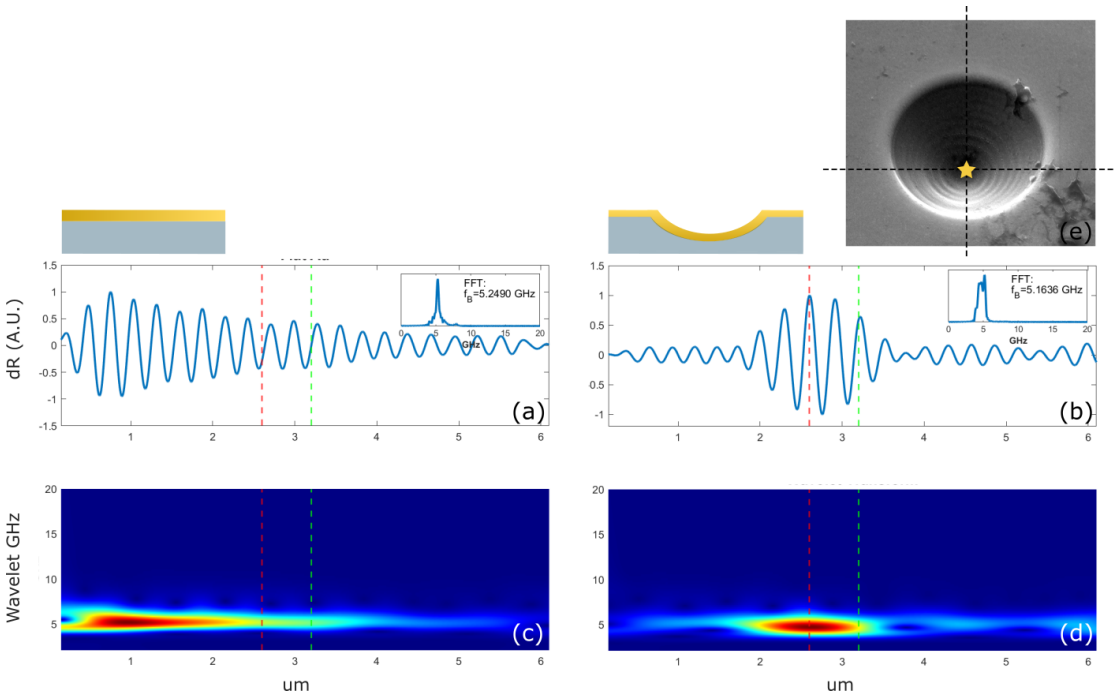

Figure 4.19: Time-Resolved Brillouin Scattering Traces and Frequency Analysis of flat and concave lens: (a, b) Time-resolved Brillouin scattering traces obtained from a flat gold transducer and the central trace of a $F = 3\,\mu m$ concave lens, respectively. Insets show the Fast Fourier Transform (FFT) spectrum indicating the Brillouin frequency (f_B) peaks. (c, d) Corresponding wavelet transform visualizations displaying the frequency distribution over time. (e) Scanning Electron Microscope (SEM) image of the concave lens with the central focus point indicated by the intersection of dashed lines and a yellow star.

transform in panel Figure 4.19 further illustrates the temporal concentration of acoustic energy at the designed focal point, emphasizing the effectiveness of the concave lens in manipulating the phonon field.

This single trace comparison demonstrated a marked deviation from the expected signal decay typically observed in flat transducers, underscoring the unique focusing capabilities imparted by the concave lens structure. The results highlight the contrast between the unfocused and focused acoustic fields.

Following the comparison of flat and concave comparison, more centre traces from a variety of concave lens designs will be presented. These traces will provide deeper insight into the focusing characteristics of each lens configuration, illustrating how

variations in design parameters influence the acoustic field's convergence at the focal point. The comparative analysis of these traces will show the difference of acoustic focusing behaviour inherent to multiple unique concave lens structure.

Here, experimental centre traces obtained from two lenses, each with a diameter of 5 μm and varying designed focal points, 2 μm and 3 μm, are shown below.

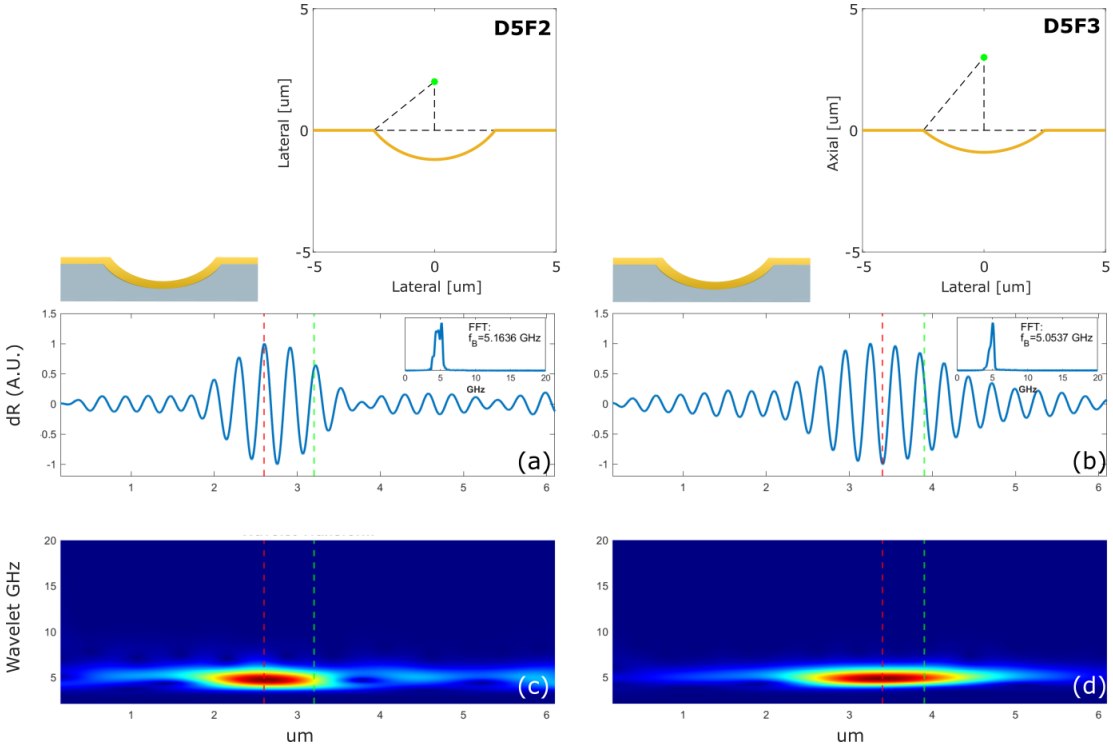

Figure 4.20: Time-Resolved Brillouin Scattering Traces and Frequency Analysis of flat and concave lens: (a, b) Time-resolved Brillouin scattering traces obtained from a flat gold transducer and the central trace of a $F = 2\,\mu m$ concave lens, respectively. Insets show the Fast Fourier Transform (FFT) spectrum indicating the Brillouin frequency (f_B) peaks. (c, d) Corresponding wavelet transform visualizations displaying the frequency distribution over time. (e) Scanning Electron Microscope (SEM) image of the concave lens with the central focus point indicated by the intersection of dashed lines and a yellow star.

Figure 4.20 showcases the impact of structural design variation on the focusing capabilities of concave acoustic lenses. Figure 4.20 (a) and (b) illustrate time-resolved traces taken from the central point of two lenses with identical diameters yet different designed focal distances. The wavelet analysis results in Figure 4.20 (c) and (d) further visualize the frequency components' distribution over time,

highlighting the shift in the concentration of acoustic energy as the design of the concave structure changes. This shift in focus, as engineered by the lens design, underlines the precision with which acoustic fields can be manipulated for targeted applications.

The shift of focusing is noticeable from the variation in the FFT peaks, indicating a change in the f_B corresponding to each lens's focal point. This shift is potentially related to the temperature changing of the water medium in axial direction, following discussion Section 4.2.3 will give more details on this.

Line scans

In order to fully assess the lens's performance in both the axial and lateral directions, line scans were conducted along both the x and y axes. These line scans can provide information for analysing the performance of the concave lens's focusing ability, thus offering a continuous measure of the acoustic intensity from conventional transducer area to the lens area. From these scans, a clear increase in intensity compared to the FZPs is observed experimentally.

Figure 4.21 provides experimental insights into the functionality of a concave lens with a designed focus of 3 μm, as captured by Scanning Electron Microscopy (SEM). Part (a) illustrates the concave lens with a precise diameter of 5.184 μm.

The subsequent parts, (b) and (d), detail the line scans along the axial depth and lateral scanning positions of the probe beam. The x-axis denotes the axial depth—essentially, the penetration depth into the sample—while the y-axis marks the lateral position of the probe beam as it moves over the sample's surface. (c) plots both the edge and centre traces from line scan along x-axis and (e) plots both the edge and centre traces from line scan along y-axis.

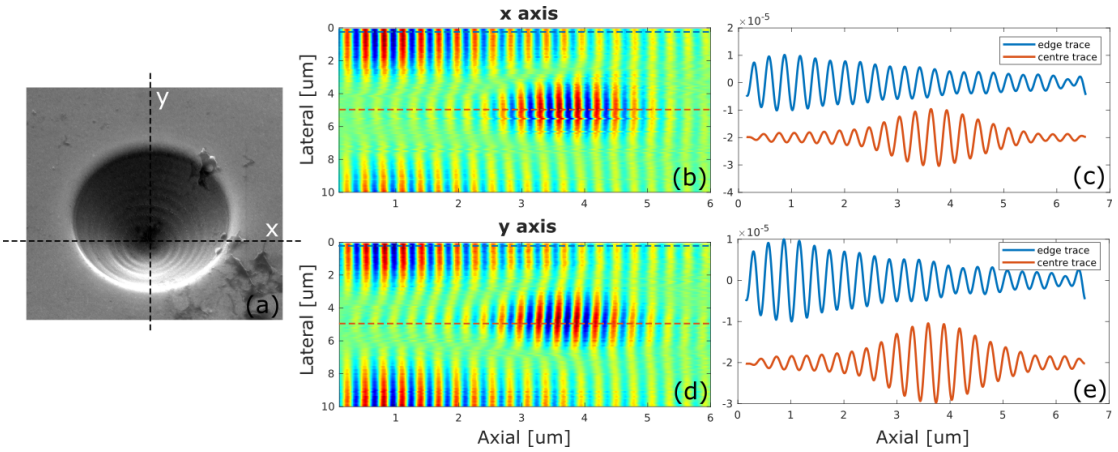

Figure 4.21: line scans across centre of D5F3. (a) SEM image of the concave lens, with dashed lines indicating the scan cross-sections x and y. (b) and (d) are B-scan plots of all the TRBS signals across x and y, respectively. (c) and (e) show TRBS traces at the blue and red dashed lines from (b) and (d), demonstrating the focusing effect at the lens centre.

This concave lens was engineered with an intended focus at a 3 μm axial depth, and has a equivalent radius of 3.9051 μm. The results depicted in the line scans indicate a noticeable intensification of the signal at approximately this 3.9 μm region. This enhancement in signal strength is indicative of the concave lens's capability to concentrate the acoustic field at the predetermined focal point, thus validating the lens design's precision. The observed focal point concentration demonstrates that the lens design is well-aligned with the objective of focusing coherent phonon fields and thus opens the way to enhancing imaging resolution beyond the diffraction limit.

Area 2D scan analysis

In addition to line scans, 2D area scans were conducted to capitalize on the increased energy efficiency of concave lenses as compared to FZPs. These comprehensive scans provide a more detailed understanding of the concave lenses' focusing performance.

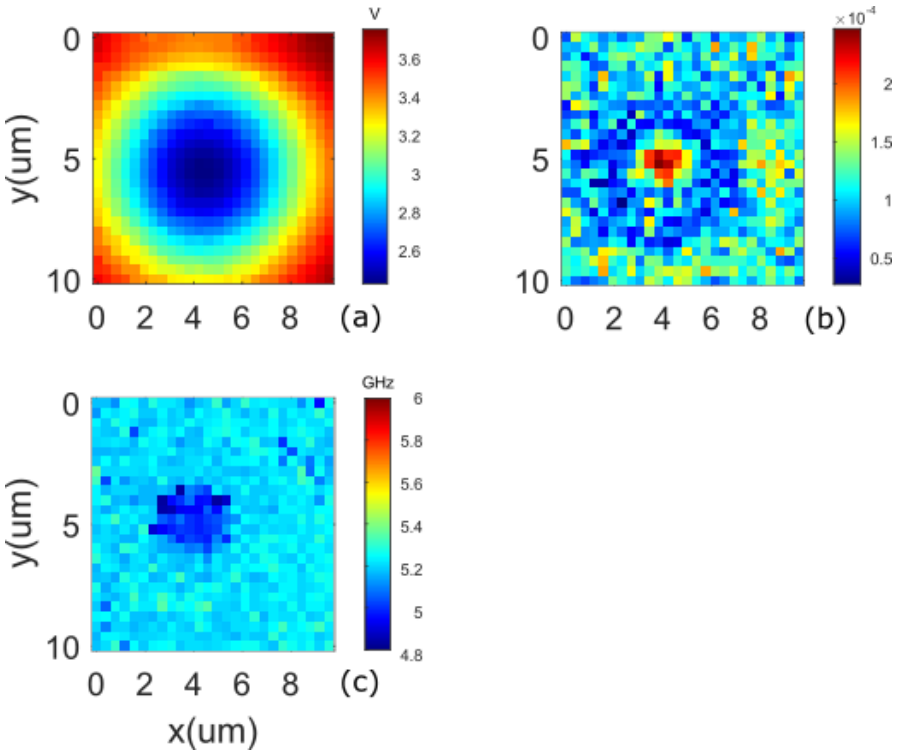

Figure 4.22: 2D scans of a concave lens with a diameter of 5 μm and designed focus of 3 μm, showing enhanced focusing capabilities. (a) DC scan. (b) Brillouin amplitude at the dominant frequency. (c) Brillouin frequency map.

Figure 4.22 are 2D area scan of a concave lens with a diameter of 5 μm, a designed focus of 3 μm and a equivalent radius of lens profile of 3.91 μm. The DC scan (a) sets the stage by visualizing the initial reflected probe light distribution across the lens, which indicates the position of the lens. A very strong and narrow high Brillouin amplitude is observed in map (b), indicative of a significant concentration of acoustic energy at the lens's focal point. This is further corroborated by the Brillouin frequency map (c), where a notable shift in frequency is observed. The lens area has a water Brillouin frequency (f_B) around 5GHz, contrasting with the background region's f_B of approximately 5.2 GHz. This frequency shift suggests a temperature variation between the focal point and the surrounding areas, potentially indicating a cooler focus region which could enhance the biocompatibility of the Phonon Microscopy by reducing thermal effects at the transducer/cell interface. These initial findings suggest an improved ability to focus acoustic energy

without raising temperature, a crucial advantage for biological applications. The implications of these observations and their contribution to the ongoing discourse on biocompatibility will be expounded upon in the subsequent discussion section.

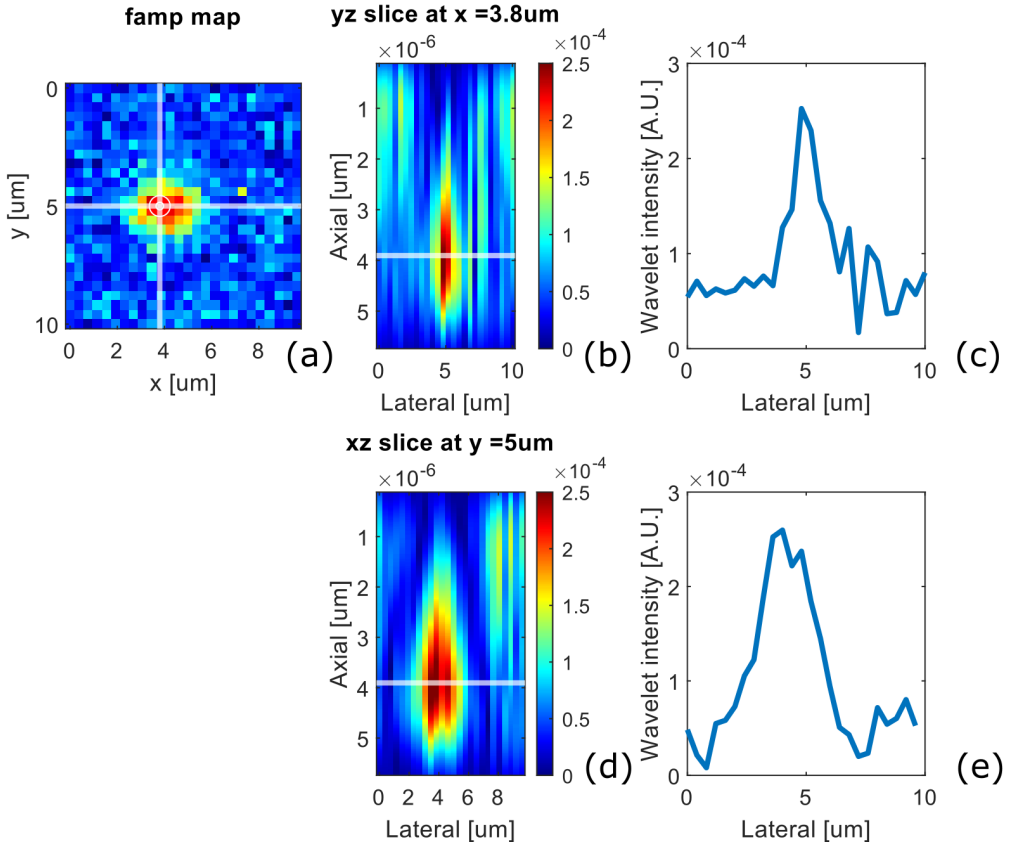

Figure 4.23: Wavelet analysis of a 2d lens scan. (a) Brillouin amplitude at the dominant frequency. (b) Wavelet analysis along the x-axis, showing yz slice information. (c) Signal intensity at designed focus across x axis. (d) Wavelet analysis along the y-axis, showing xz slice information. (e) Signal intensity at designed focus across y axis.

Figure 4.23 presents a detailed wavelet analysis of lines across the centre of the lens, providing valuable insights into the acoustic focusing capabilities of the lens. Figure 4.23 (a) displays the Brillouin amplitude map at the dominant frequency. (b) and (d) offer wavelet analysis along the x and y axes, respectively, presenting yz and xz slice information that further illustrates the precise focal point. The white line marks the designed focal position, where a notable concentration of acoustic energy is observed, as evidenced by the spike in the signal intensity graphs. These

results underscore the potential of the lens in achieving high-resolution acoustic imaging, with a distinct focal region evident at the targeted spot.

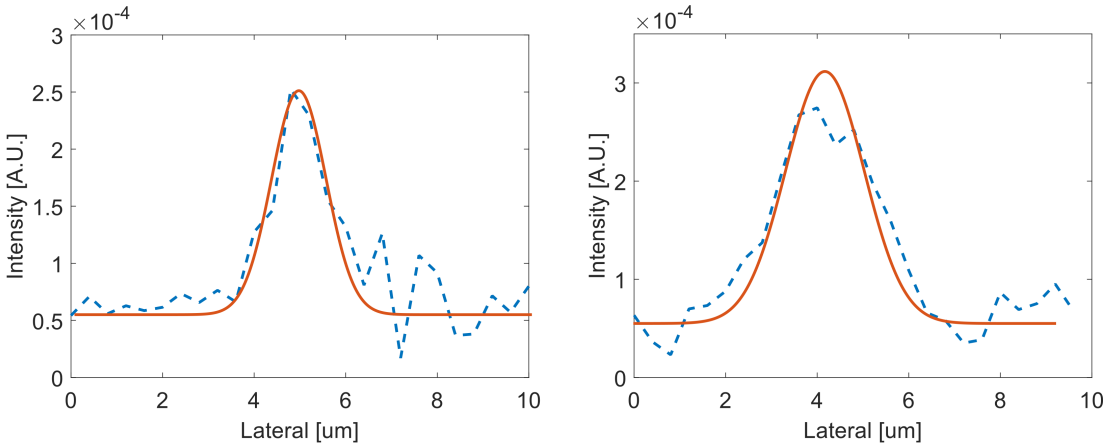

Figure 4.24: Gaussian fits of signal intensity at the designed focus across x and y axes. Left: along x axis, Right: along y axis.

Figure 4.24 presents Gaussian fits of the signal intensity plots from Figure 4.23 (c) and (e), shown as the dashed blue lines, while the solid orange lines represent the Gaussian fitted data. The fitting demonstrates the sharpness and precision of the focusing achieved by the concave lens. The left plot corresponds to the lateral intensity distribution across x axis and the right plot corresponds to the lateral intensity distribution across y axis.

The x profile has a FWHM of 1.87 μm and the y profile has a FWHM of 2.43 μm. The beam shape exhibits variations in different orientation, which can be attributed to multiple factors leading to an uneven distribution. One potential cause is the non-ideal Gaussian shape of either the pump laser beam, resulting in an inconsistent generation of acoustic waves or a non-ideal probe beam. Additionally, the delivery angle of the probe or an inherent imperfection in the probe's Gaussian beam profile could also contribute to this irregularity.

4.2.3 Discussion

Concave acoustic lenses represent a straightforward approach to focusing acoustic waves, leveraging their three-dimensional structures to manipulate the direction and concentration of energy. Unlike the Fresnel Zone Plates discussed earlier, which are planar diffractive structures, concave lenses are inherently three-dimensional and thus present unique challenges in nanofabrication. The complexity of their shape necessitates the use of specialized fabrication techniques such as Focused Ion Beam (FIB) milling, which allows for precise sculpting of the lens profile directly into the substrate material.

Despite the complexities in their fabrication, concave lenses offer significant advantages in terms of energy efficiency. Their curved surfaces are inherently adept at capturing and redirecting the entirety of the incident pump laser energy, ensuring minimal loss and maximum transfer of energy to the focused acoustic field. Meanwhile, thanks to direct milling over the substrate, these lenses are capable of undergoing multiple rounds of sputtering and experiments, which also offer better recycling abilities compared to the EBL-made FZPs.

Lens reuse and recycle

Moreover, the durability and reusability of these concave structures add to their appeal. Fabricated by milling into robust materials like glass substrates, they can withstand repeated use. After conducting experiments, the lenses can be easily regenerated through a process of acid cleaning followed by re-sputtering of the functional layers. This ability to recycle the lenses for multiple tests without degradation in performance is an economical and practical advantage, allowing for extended research use and consistent experimental conditions.

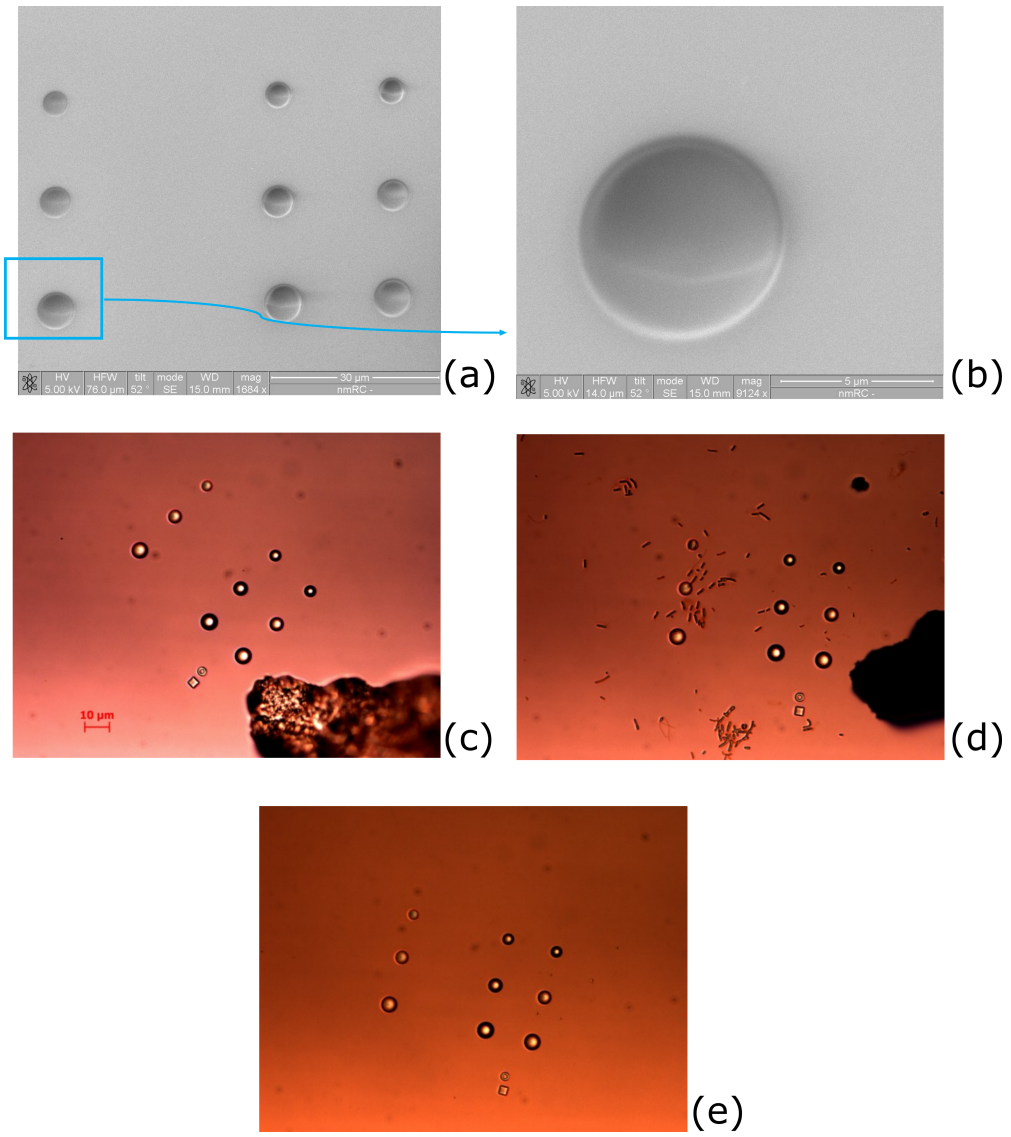

Figure 4.25: SEM images and optical photographs of concave lenses during and after fabrication, experiments and cleaning processes. (a) Overview SEM image showing an array of lenses. (b) A zoomed in SEM image of a single lens. (c) and (d) Post-sputtering optical images depicting contamination from either sputtering residues or an unclean experimental environment, evidenced by the presence of dirt or bacterial accumulation on the lenses. (e) The same group of concave lenses after undergoing an acid cleaning process.

The reusability of the concave lenses is demonstrated in the series of images provided in Figure 4.25. (a) and (b) show the original clean lenses during FIB fabrications. (e) showcases the lenses after undergoing an acid cleaning process. This step is crucial in the maintenance and sustainability of the lenses for repeated use in experiments. The cleaning process effectively removes contaminants such as

residues from sputtering or bacterial from an unclean experimental setup, which are evident in (c) and (d). The restoration of lens clarity observed in image (e) suggests that these lenses have the potential to be recycled, thereby increasing the ability to repeat experiments and the cost-effectiveness of the research process - no need to trough FIB fabrication multiple times.

The performance of the concave lenses after cleaning and reuse remains consistent with the original results, as demonstrated by the repeatability data presented earlier in this chapter. The primary factor influencing the lens performance is the thickness and quality of the sputtered gold layer, which dictates both the optical response and the durability of the lens under laser exposure. In this case, slight adjustments were made to the gold layer thickness to improve tolerance to higher laser power, but these modifications did not affect the overall repeatability of the results. As shown in various datasets presented earlier, the lenses maintained their performance post-cleaning, and no additional data is necessary to further verify repeatability in this context. The stability of the lenses across multiple uses supports their reusability in experimental setups, ensuring consistent results while reducing the need for repeated fabrication processes.

Frequency shift around the focus

The frequency shift at the centre of lens is also of great interest. The focused acoustic energy does not result in a temperature increase, and due to the physical distance between the transducer/medium interface and the designed working region - around the focus, these lenses potentially offers a new solution to address the thermal compatibility issues associated with conventional Phonon Microscopy.

Understand the relationship between the Brillouin frequency f_B and temperature of water can start from exploring the relationship of (a) sound velocity vs temper-

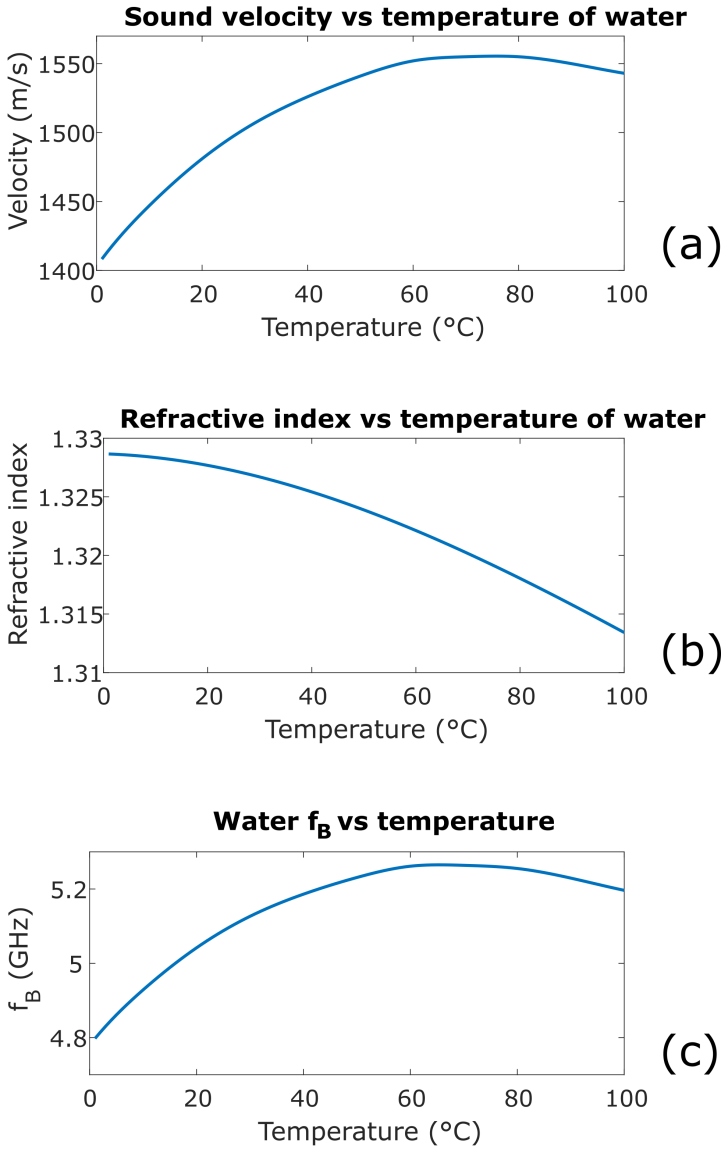

Figure 4.26: Temperature vs Brillouin frequency of water, (a) Velocity vs temperature from literature [178]. (b) Refractive index vs temperature from literature [179], more details will be found in Appendix C. (c) Calculated f_B vs temperature.

ature, and (b) refractive index vs temperature as shown in Fig. 4.26. The sound velocity in water, as depicted in (a), shows an increasing trend with temperature, data sourced from [178]. Similarly, the refractive index (b) exhibits a decrease with rising temperature, with calculation method extracted from [179], more details are discussed in Appendix C. Knowing the equation (4.1): $v = \frac{\lambda_{\text{probe}} f_B}{2n}$, the relationship of f_B vs temperature can be easily found.

In the previous work [180], the authors successfully demonstrated the use of time-resolved Brillouin scattering as a temperature sensor. They measured a temperature increase of up to 55°C on a gold transducer layer situated at the tip of an optical fibre. In order to validate the measurement of the temperature rise in the water, finite element method (FEM) was used to model the steady-state heating by the transducer. Pump and probe powers of approximately 7 and 1 mW, respectively. Using these input powers, the transfer matrix (TMM) optical model was then used to compute total average power absorbed by the transducer: ~ 2 mW. Figure 4.27 presents an axially symmetric map of the temperature rise in the space surrounding the transducer.

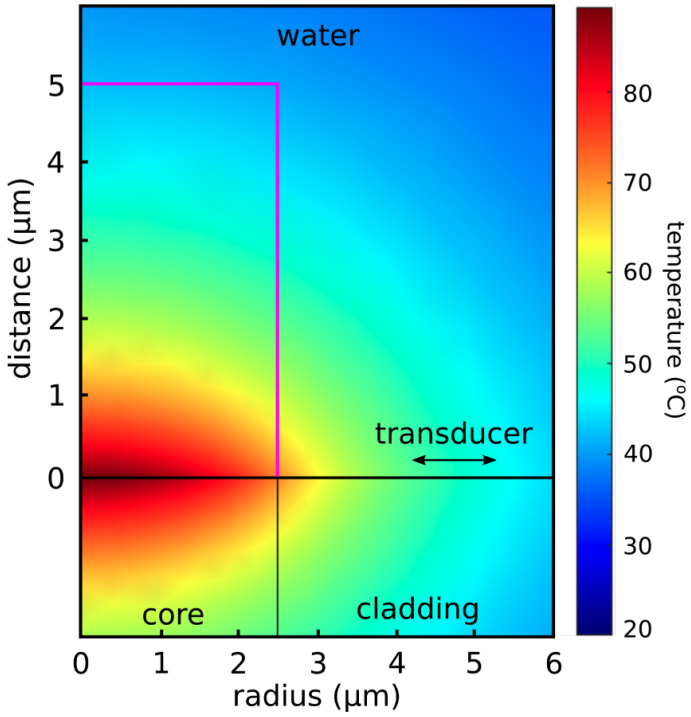

Figure 4.27: The steady-state temperature distribution around the transducer was modelled using the finite element software COMSOL, simulating the axisymmetric temperature rise caused by the transducer's absorption of the pump and probe beams. The model assumed a steady-state heat source, with the absorbed optical power in the 20 nm gold layer directly correlating with the heating rate. For a defined volume of $5 \times 5 \times 5$ μm volume area (highlighted in pink), the average temperature was measured to be approximately 55°C. This data aligns with the thermal response expected from the system. The image was reproduced from a previous study by [180].

Corresponding to the derived f_B versus temperature relationship, the observed leftward shift in f_B may be consistent with the expected trend of decreasing temperature. However, one other cause of the frequency shift is the angle between the coherent phonons and the incident probe beam. To fully understand the factors contributing to the Brillouin frequency shift, a comparative frequency analysis of three structures—conventional transducer, Fresnel Zone Plate (FZP), and concave lenses—has been conducted and plotted together, as shown in Figure 4.28.

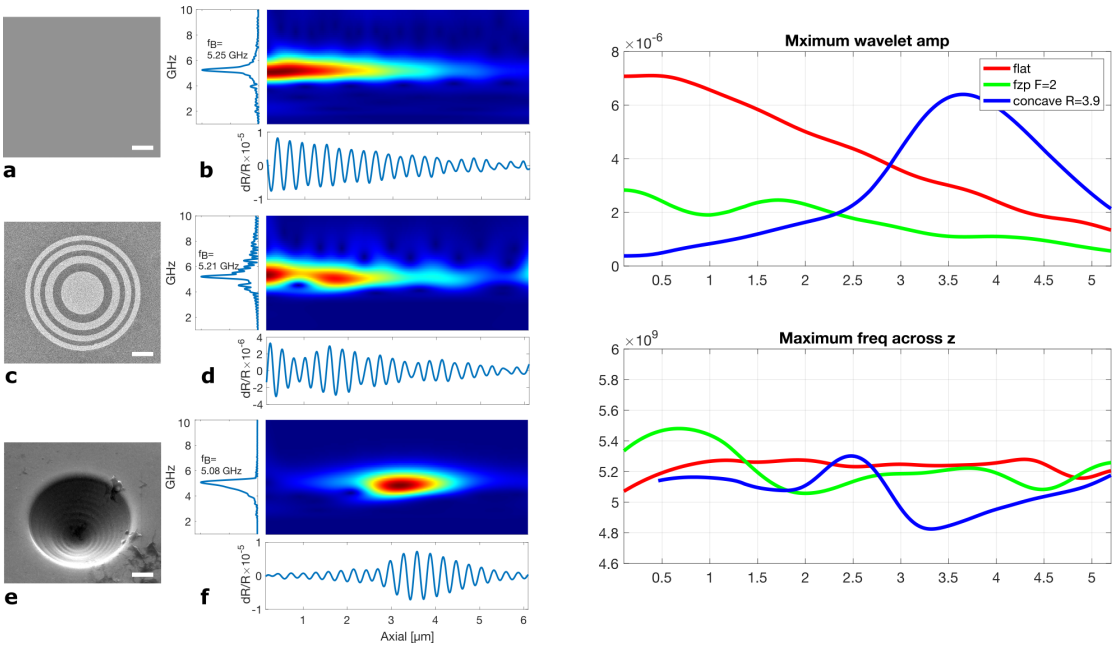

Figure 4.28: Comparison of Brillouin frequency shifts and wavelet amplitude for different lens structures. (a)–(f) represent the center frequency traces of three structures—flat gold surface (a, b), FZP (c, d), and concave lens (e, f)—as discussed earlier, replotted here for easier comparison. (b), (d), and (f) display the frequency spectra and waveforms along the z-axis. The right-hand side shows (top) the maximum wavelet amplitude along the z-axis and (bottom) the corresponding maximum Brillouin frequency f_B. Notably, temperature effects are minimal, as evidenced by the relatively constant frequency in the flat gold surface's bottom plot. The FZP and concave lens exhibit both higher wavelet amplitude and lower frequency shifts around their respective focal points, with the concave lens reaching a minimum f_B of 4.82 GHz, closely matching the predicted f_B shift (∼4.89 GHz) based on acoustic NA and focused pump energy distribution.

Figure 4.28 compares the frequency analysis and wavelet amplitude for three different structures: flat gold, FZP, and concave lens. The left-hand side of the figure

shows the center traces for each structure, similar to earlier plots but rearranged for easier comparison. The right-hand side presents the maximum wavelet amplitude along the z-axis (top) and the corresponding maximum Brillouin frequency.

From these results, the temperature has a negligible effect on the Brillouin frequency shift, as the flat gold surface shows a fairly constant frequency in the lower plot. In contrast, both the FZP and concave lens demonstrate a pronounced increase in wavelet amplitude and a corresponding lower frequency shift near their focal points. For the concave lens, the measured acoustic numerical aperture (NA) predicts a maximum f_B of approximately 4.6 GHz, and considering the energy focusing at the centre, the expected shift to ∼4.89 GHz closely matches the observed minimum frequency of 4.82 GHz, confirming the model's accuracy.

In short, the concave structure causes phonons to propagate at an angle to the vertical probe beam, which is the primary reason for the Brillouin frequency shift, rather than the temperature distribution.

4.3 Summary

This chapter presents a detailed examination of the simulation and experimental results that advance the understanding of optoacoustic transducers, building upon the theoretical foundations and designs discussed previously. It explores a range of optoacoustic lenses, including various Fresnel Zone Plates (Positive, negative, and phase-reversal FZPs were simulated, and in the experimental section, centre point and line scans of a positive FZP with a design focus of $F = 2\,\mu m$, a high NA = 0.7184 were presented) and concave structures (Lenses with diameters varying from 4 μm to 6 μm, and a design focus varying from 1 μm to 3 μm were simulated. In the experimental section, centre point, line scans, and 2D area scans were

presented for multiple concave lenses, which have focuses at $F = 2\,\mu m$ and 3 μm, and a maximum NA=0.6247 were presented), specifically engineered to focus coherent phonon fields.

By employing a strategy that combines the generation of focused coherent acoustic waves across different structures with time-domain resolved Brillouin scattering (TRBS) techniques, this chapter showcases the first ever continuous optical monitoring of focused GHz acoustic fields in water.

Furthermore, the chapter provides a critical evaluation of current system limitations and the challenges encountered, offering insight into preliminary simulation and experimental outcomes. Through this analysis, potential solutions are proposed, paving the way for further advancements in phonon microscopy. This investigation not only identifies avenues for overcoming existing barriers but also sets the stage for future research aimed at achieving true acoustic resolution.

Chapter 5

Preliminary results and perspectives

This chapter on preliminary results and perspectives mainly presents the projects I am currently working on, including theoretical examinations, preliminary experimental implementations, and results related to optoacoustic lenses to varying extents. It also covers some group projects I have been heavily involved in during my PhD and discusses how these contribute to my main project—optoacoustic lenses—past, present, and future.

The optoacoustic lenses presented and demonstrated here have shown their strong focusing ability for GHz picosecond laser-generated coherent phonons. They have the potential to improve the lateral resolution issues caused by optics in PLU-based TRBS imaging techniques. However, improvements in transducer optimization for better SNR are still needed. Also, exploring more lens designs is of great interest, for example, the axicon, because of its capability to create a needle-like long focus beam. Additionally, exploring innovative techniques open the door to novel designs of PR-FZP: utilizing polarized nanorods can introduces structures

that exhibit phase differences within a flat surface, offering a fresh perspective on realising PR-FZP. To characterize the size of the focused acoustic beam, additional experiments, such as edge detection, can be conducted. Last but not least, moving these lenses to a fibre tip may also empower fibre-based phonon probe microscopy, which has the potential for endoscopic development with higher lateral resolution.

5.1 Transducer optimization

In Chapter 3, a single Au layer optoacoustic transducer layer was proposed to achieve proof of concept for the focusing of coherent phonon fields. However, based on the PLU model proposed in Chapter 2, previously research already shown that a Fabry-Perot cavity made up with a structure of Au/ITO/Au provides an opportunity to increase both the absorbance (pump) and transmittance (probe) and thus to improve the SNR [68, 181].

The PLU model presented in Section 2.2 allows simulation of the optical transmission and reflection of both the pump and probe beam, as well as the amplitude of the TRBS signal with different cavity designs. The model can give the transmittance of pump T_{pump}, probe T_{probe}, and amplitude of Brillouin signal (A_{fb} in water medium), then a figure of merit for the OAT performance using NUV (λ_{pump} = 415 nm) and NIR (λ_{probe} = 780 nm) can be produced:

$$OAT \propto \frac{A_{fB^*SNR}}{UV_{\text{dose}}} \tag{5.1}$$

where $\text{SNR} \propto \sqrt{\text{T}_{\text{probe}}}$ and $\text{UV}_{\text{dose}} \propto \text{T}_{\text{pump}}/\text{SNR}^2$ [68]. The result figure of merit (OAT) shown in Figure 5.1 indicates the best performance at approximately thicknesses of 10 nm Au and 150 nm ITO. However, in practice, it is worth con-

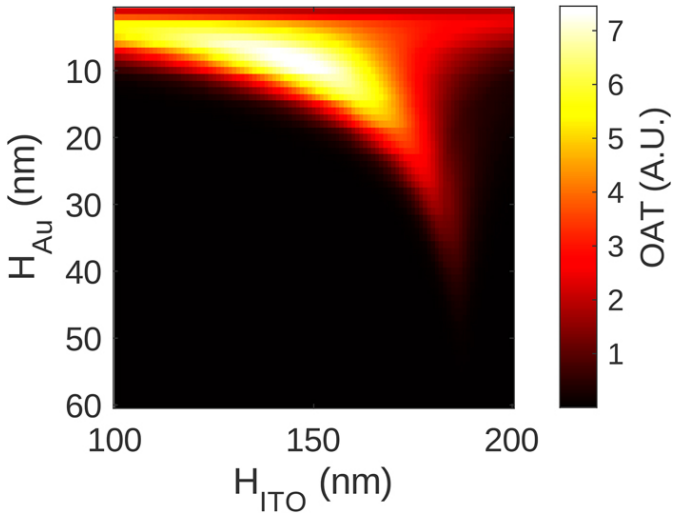

Figure 5.1: Simulation results of the performance for Au/ITO/Au cavity transducers for varying ITO thicknesses by using the PLU model.

sidering to increase the thickness of gold layer to prevent UV leakage. Finally, biocompatibility and fabrication tolerances must also be considered while making design choices.

5.2 Flat Phase-reversed FZP made with nanorods

In addition to simply filling the corresponding rings with gold, i.e. zone plate pattern formed by gold rings as discussed in Section 3.1.2, we can also put some nanorods in these regions, and thus build Phase-Reversal FZPs by generating sound waves with π phase difference in different zones without making curved structures.

When metallic nanorods are thermally excited using short pulsed lasers, they can produce GHz sound waves that become a source of ultrasound[182, 183]. The optical and electronic properties of the nanorods depend heavily on their size and shape. These properties together with the surrounding environment, can determine how the nanorods generate heat and mechanical vibrations. One important

thing using pump-probe setup to detect nanorods is to consider the balance between acoustic resonance and optical resonance, as it closely tied to the design parameters of the nanorods. Acoustic resonance is directly influenced by the absorption coefficient, which varies based on the dimensions of the nanorods (length, width, and thickness). Additionally, the material properties (e.g., Au, Al) play a significant role; however, this discussion is focused solely on Au nanoparticles in this thesis. The acoustic resonance must ideally be as strong as possible to maximize efficiency. In contrast, for the probe, the primary focus is on the sensitivity of the optical resonance, which is also highly dependent on the specific size of the nanorods. The core challenge lies in striking a balance between optimizing the nanorods for robust acoustic resonance while maintaining adequate sensitivity within the optical domain.

There are different ways to model nanorods' behaviour regarding different geometrical properties assumptions for nanorods, such as cylindrical nanorods, cuboid nanorods. In the case of cylindrical nanorods and nanodiscs, two main vibrational frequencies exist, along the length and width, referred to as the extension and breathing modes respectively, both extensional and breathing vibrating frequencies can be calculated analytically [184]. However, in the case of cuboid nanorods, finite element modelling is required to estimate the mechanical vibrations. In addition to the nanorods themselves, it is important to consider their interface with surroundings and how the vibrations will generate sound waves in different media.

In order to realize flat Phase-Reversal FZP made with nanorods, in addition to studying the properties of nanorods, it is necessary to design special excitation pump light sources according to their properties and FZP design theory. Since nanorods have dominant vibration in the direction with a longer dimension, we can place the rods in 90 degrees difference (horizontal and vertical) as shown in Figure 5.2 (a). Then introduce specially polarized pump light with a time delay

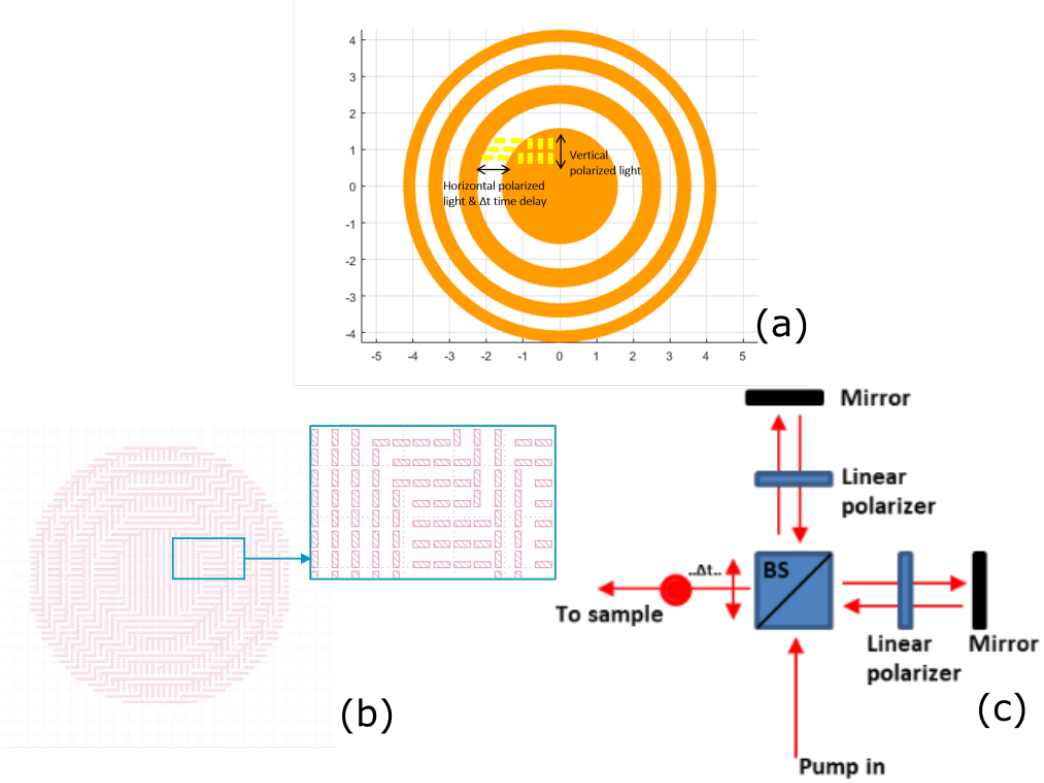

Figure 5.2: Concept of FZ-FZP made with nanorods. (a)Schematic of the acoustic Fresnel Zone Plate lens made of gold nanorods, nanorods in the orange area are excited by vertically polarized light and the nanorods in the opaque area are excited by horizontally polarized light. There is a time delay between these two polarized light pulse to create a phase difference in the ultrasound generated by differently oriented nanorods. (b) Zoom in details. (c) A diagram of the Michelson like optical path design for the pump beam.

in horizontal and vertical linear polarization modes, a phase difference can be created in different zones of the Phase-Reversal FZPs. The alternating zones of 0 and π phase delay can be viewed as the sum of the exciting zones of two normal FZPs. Thus they can take advantage of all the incident energy by adding phase compensation regions instead of only 'on' areas with nanorods. Specially designed polarized pump beam is designed to be adjustable in delay time and orientation, thus we can easily turn on/off different rods regions.

To introduce a phase delay in between horizontal and vertical nanorods located in different zones of the Phase-Reverse FZP, an optical path similar to a Michelson

interferometer was employed for the pump laser. As shown in Figure 5.2(c), a circular pump beam goes into a beam splitter and then it is divided into two paths, each path is composed of a linear polariser and a reflecting mirror, the linear polariser in the two paths are orthogonal. By controlling the length of the two optical paths, the time delay between the vertical and horizontal polarised light pulses can be controlled manually, thus creating a π phase difference acoustic-wise.

5.2.1 Modelling of nanorods

To simulate the working principle of nanorods and find the best size of rods for further experiments, both optical and mechanical behaviours of rods are of great interest.

Optical

This model focuses on how different sizes of nanorods produce optical effects when irradiated at the different pump and probe wavelengths. In our pump-probe system, we want the nanorods to have a higher absorption in the pump wavelength and a higher signal sensitivity in the probe wavelength, where the scattering rate changes the fastest.

Figures 5.3 - 5.5 are some simulation results for the rods sizes included in the first version of the design: The widths are 40, 50 and 60 nm, and the lengths are 130, 145 and 160 nm, respectively.

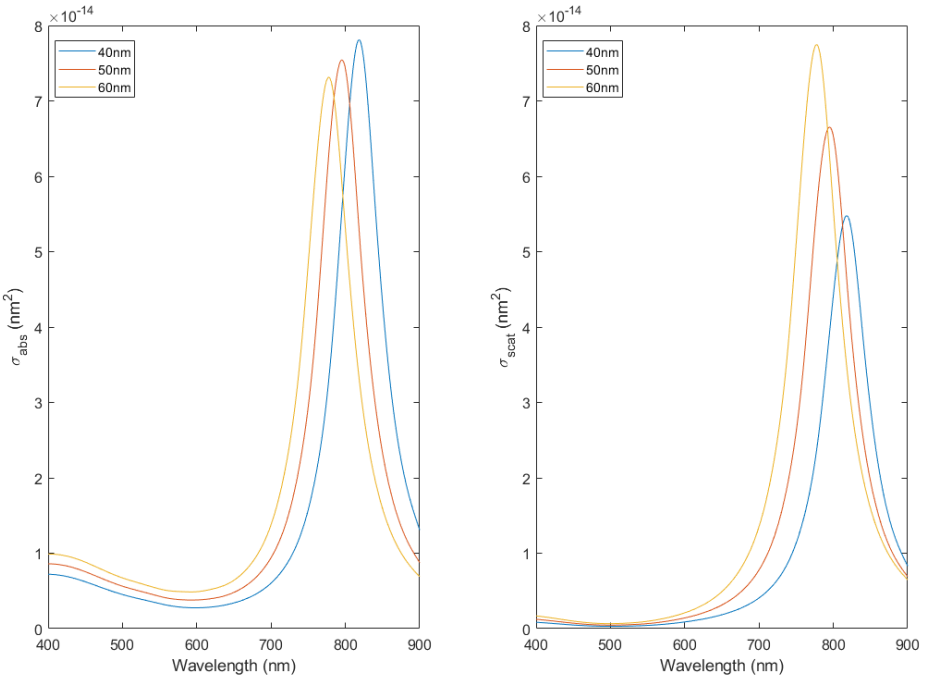

Figure 5.3: Optical response of nanorods with length equals to 130 nm.

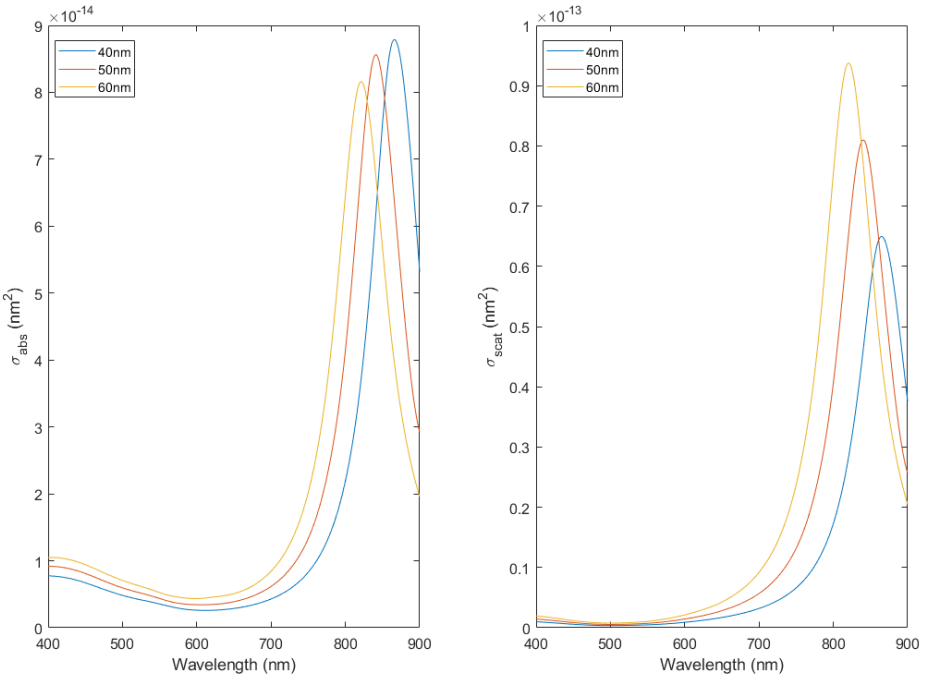

Figure 5.4: Optical response of nanorods with length equals to 145 nm.

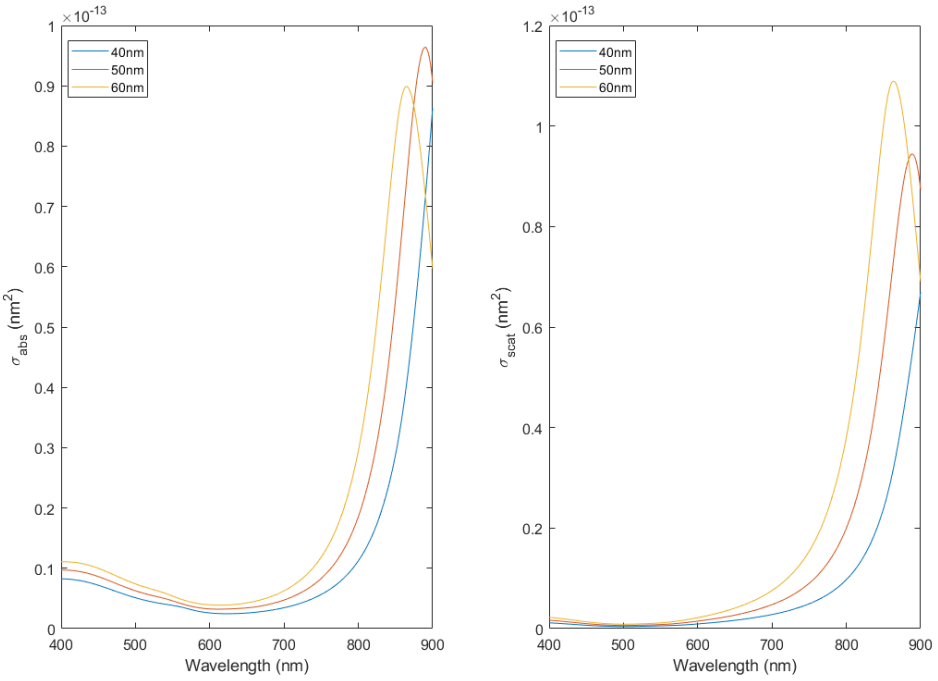

Figure 5.5: Optical response of nanorods with length equals to 160 nm.

Mechanical

As mentioned in the previous section, if the nanorod is modelled as a cylindrical structure, there is an analytical solution to estimate both the extensional and breathing mode. Figure 5.6 shows the extensional and breathing modes of a cylindrical rod, they are vibrations along the length and width, respectively. Equations (5.2) and (5.3) are the formulas to calculate the analytical values [183]:

$$f_{\text{ext}} = \frac{1}{2L}\sqrt{\frac{E}{\rho}} \tag{5.2}$$

$$f_{\text{br}} = \frac{\tau_0}{\pi w}\sqrt{\frac{E(1-\nu)}{\rho(1+\nu)(1-2\nu)}} \tag{5.3}$$

where E is the Young's modulus; ρ is the density; ν Poisson's ratio; and τ_0 is the

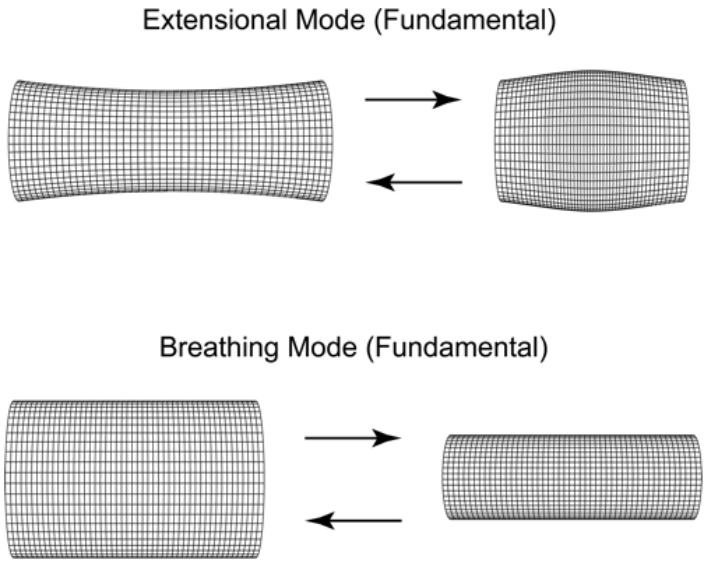

Figure 5.6: A diagram illustrating the extensional and breathing modes of a cylindrical Rod. Figure taken from [185].

first eigenvalue given by:

$$\tau J_0(\tau) = \frac{1-2\nu}{1-\nu} J_1(\tau) \tag{5.4}$$

where J_0 and J_1 are the first two Bessel functions of the first kind.

Take a 40nm×160nm rod for an example, expected values are $f_{ext} = 6.3207$ GHz and $f_{br} = 58.8370$ Ghz.

There is not yet an analytical solution to calculate the vibrations generated, but it is possible to use a finite element model to simulate the vibrations of the nanorods. Figure 5.7 below shows a 3D nanorod simulated in COMSOL, by using the thermoelastic module, adding a heat source to the rod and then calculating the displacements on each surface.

Due to the limitations of EBL production, it is unlikely that the actual edges of the samples are sharp. Figures 5.10 (a) and (b) show two possible actual states of

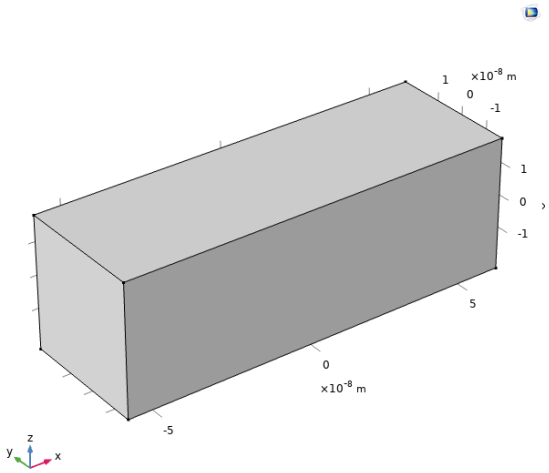

Figure 5.7: 3D cubic nanorod with sharp edges

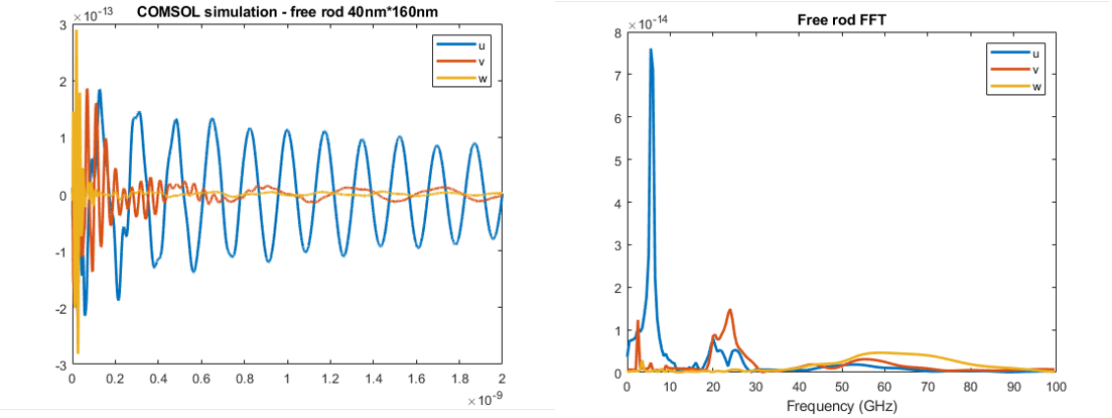

Figure 5.8: Mechanical response in free vibration mod. Left: Time domain simulation results, u, v and w represent the different displacements in three different surfaces, we should mainly look at trace u, since it represents the vibration along the length and has a relative low frequency and longer oscillation time period. Right: FFT results of the time traces in the left.

the rods, both conditions are pending a more optimised analysis in the future. In the meantime, more literature on EBL production needs to be searched to restore the true state of these rods better and thus a more accurate simulation.

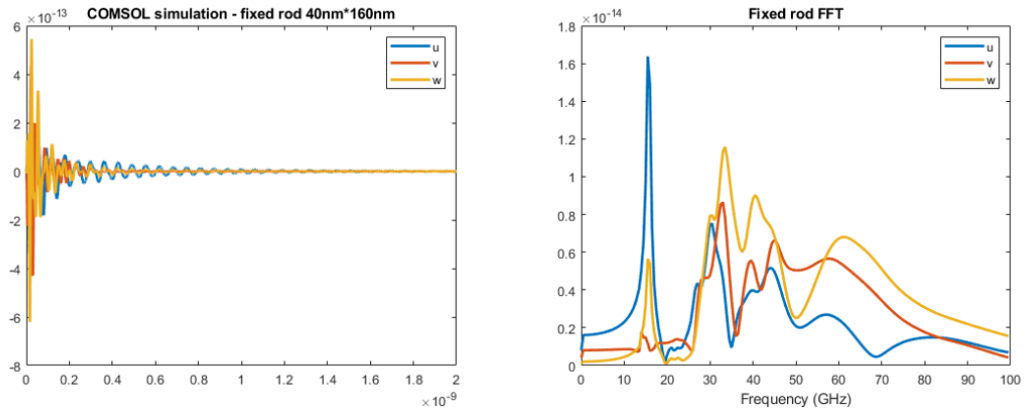

Figure 5.9: Mechanical response in fixed vibration mod. the bottom surface was setted to be fixed and has no vibrations at all. Left: Time domain simulation results, u, v and w represent the different displacements in three different surfaces, same remark as the comment before, since it represents the vibration along the length and has a relative low frequency and longer oscillation time period. Right: FFT results of the time traces in the left.

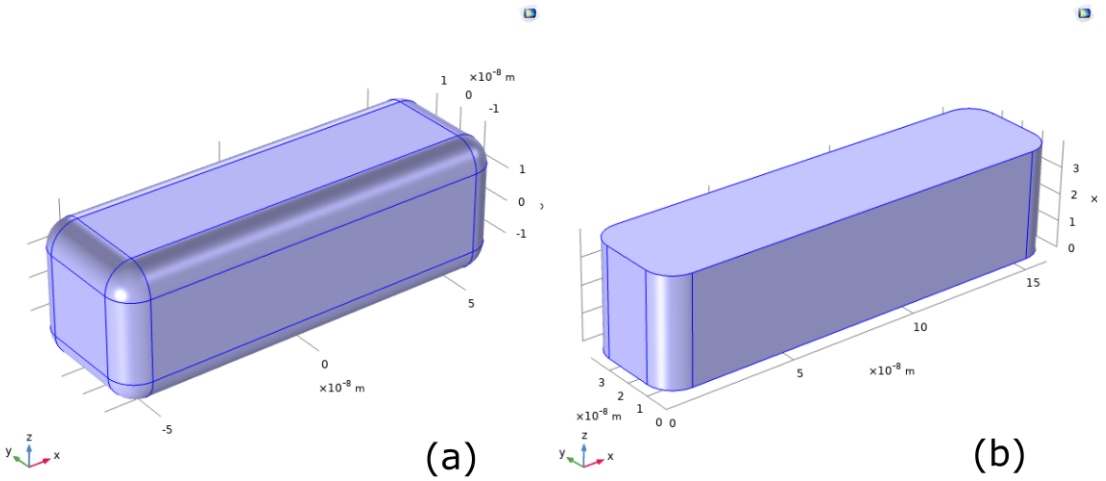

Figure 5.10: COMSOL models of 3D rounded nanorods. (a) 3D cubic nanorods with all rounded edges. (b) 3D cubic nanorods with rounded corners on vertical edges

5.2.2 Nanorods measurements

Some letter patterns made up of nanorods as shown in Figure 5.11 (a) (b) were designed and fabricated to test the nanorods' performance. Electron beam-lithography (EBL) was used for fabrication, all the designs are exported as GDS files using matlab before sending to the EBL machine.

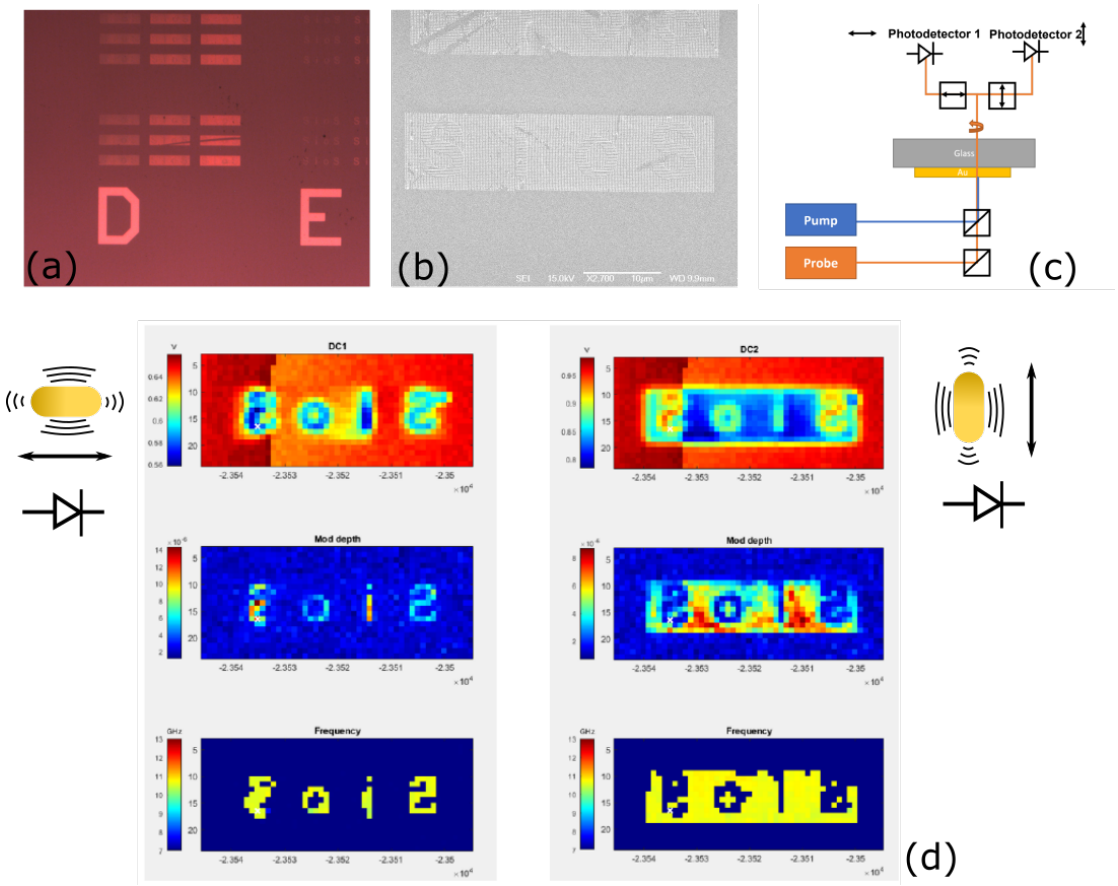

Figure 5.11: Measurements of EBL made nanorods. (a) and (b) Optical and SEM pictures of the letters made with nanorods, (b) is the zoom in view of one block in (a). (c) Diagram of the experimental set up, flipped sample with both pump and probe overlapped underneath. (d) Left: Channel 1 - horizontal polarized light - Detect the sios character; Right: Channel 2 - vertical polarized light - Detect the nanorods in the background.

Using a similar experimental setup discussed in the previous Chapter 3, and introducing linear polarization in horizontal and vertical orientations, along with two detectors as shown in Figure 5.11 (c), we can now conduct a test experiment on letter patterns (see Figure 5.11 (b)) to examine the relationship between the orientation of nanorods and the polarization of light. Figure 5.11 (d) displays the processed results from both detectors: channel 1 presents the horizontal scan results, and channel 2 presents the vertical scan results. For each channel, from top to bottom, the sequence is the DC map, signal amplitude at the selected signal frequency map, and the selected signal frequency map.

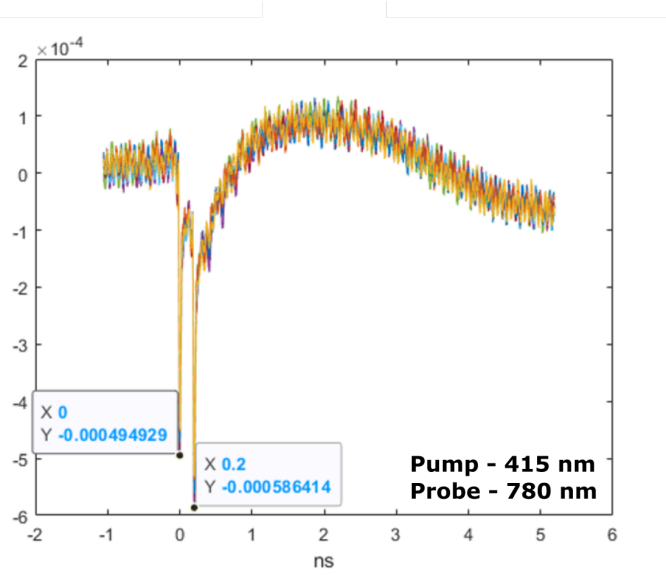

Figure 5.12: Experimental time traces with the Michelson-like dual time delay setup, two copeaks can be observed with a time separation of $\sim$ 0.2 ns, λ_{pump} = 415 nm and λ_{probe} = 780 nm.

Preliminary results demonstrate that with the polarized detection method, horizontal (letter "sios") and vertical nanorods (background of each block) can be differentiated using the amplitude map or the frequency map. A preliminary trace was recorded using the Michelson-like setup described in Figure 5.11 (c). Two copeaks observed in the single trace have a time separation of approximately 0.2 ns ((Fig. 5.12)), thereby enabling the excitation of nanorods (with horizontal and vertical orientations) to create a FR-FZP with a time-delayed pump pulse, and finally achieve the flat PR-FZP with a π phase difference.

Figure 5.13 presents two EBL made FZPs, one positive FZP and a PR-FZP. For both designs, the rods are 160nm×40nm and they are in two orthogonal directions. However, due to laser rig availability, experimental tests on these nanorods made FZPs haven't been performed yet. But all the designs and the premilinary results shown in this section prove that such structures are likely to be realised, making flat PR-FZP made of nanorods possible.

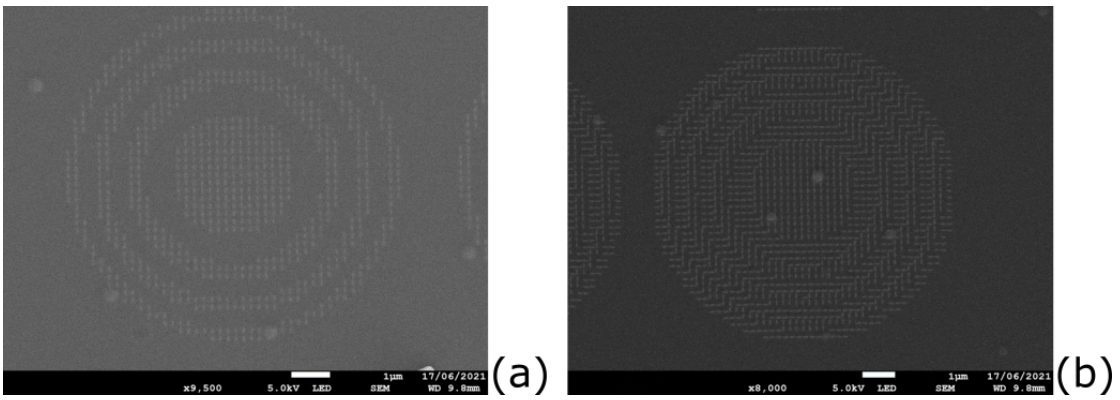

Figure 5.13: SEM pictures of a positive FZP and a PR-FZP made with nanorods. (a) SEM snapshot of a positive FZP lens made with nanorods, in this case, the rods are 160nm×40nm and they are in one direction. (b) SEM snapshot of a PR-FZP lens made with nanorods, in this case, the rods are 160nm×40nm and they are in two orientations.

5.3 Optoacoustic axicon lenses

Because of their peculiar propagation characteristics, Bessel beams—which were first proposed in optics [186, 187]—are now the foundation for many applications [188, 189, 190]. Bessel-like beams in optics are typically created by conical-shaped transparent refractive elements called axicons [191] to focus a Gaussian beam. However, the application on acoustics is not yet broadly applied as in optics, with only few applications reported [192, 193, 194]. However, its needle-like long focusing is also of great interest for TRBS-based imaging techniques, because a long and narrow focus would be ideal for examining in-depth areas of interest within the medium.

Using the similar design idea of acoustic Bessel-like beam formation through flat structures made of rings, introduced in [195] (working in the $10 \sim 20$ kHz range), and the FBSM model from Section 2.2.4, a quick simulation suggests that a GHz Bessel beam can be formed. Compared with the FZPs, a longer depth of focus, but a wider focus, can be achieved.

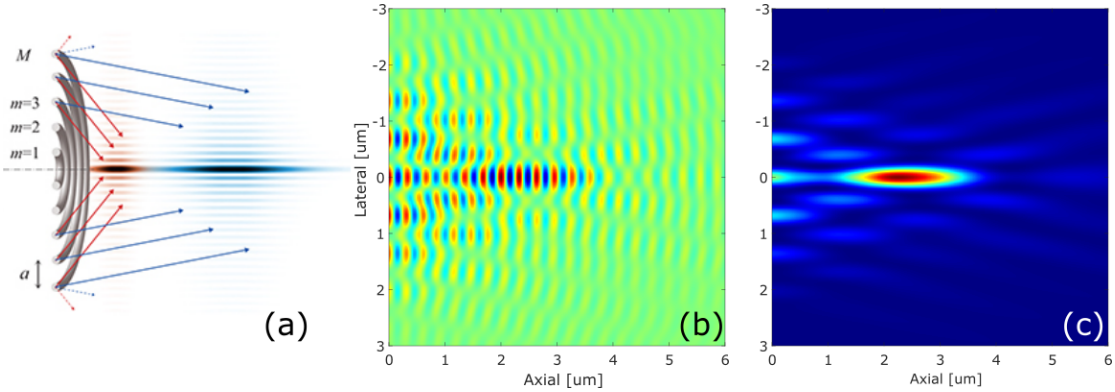

Figure 5.14: Simulated formation of acoustic Bessel-like beams by using concentric rings: (a) Illustration of the formation of Bessel-like beams with multiple concentric rings. Image adapted from [195]. (b) Acoustic field distribution simulations across the lateral plane. (c) Corresponding intensity map illustrating the focused acoustic energy.

Additionally, similar to an axicon that can generate a Bessel beam, the Bessel ultrasonic transducer can produce non-diffracting Bessel ultrasonic beams by making geometrical changes to the optoacoustic structures [194].

The results show that the depth of field of the Bessel optoacoustic transducer is much deeper than the conventional concave structures explored in the Section 4.2.1. And the depth of focus can be adjusted by changing the depth of axicon structure - effectively the cone angle of the conical acoustic lens. The Bessel optoacoustic lenses may help improve both the lateral resolution and also the focusing depth of TRBS based imaging techniques.

5.4 Lens for imaging - Approaching real acoustic resolution

The optoacoustic lenses explored in this thesis present an exciting opportunity to overcome these limitations by leveraging laser-generated coherent phonon fields for TRBS-based imaging techniques, including Phonon Microscopy. However, true

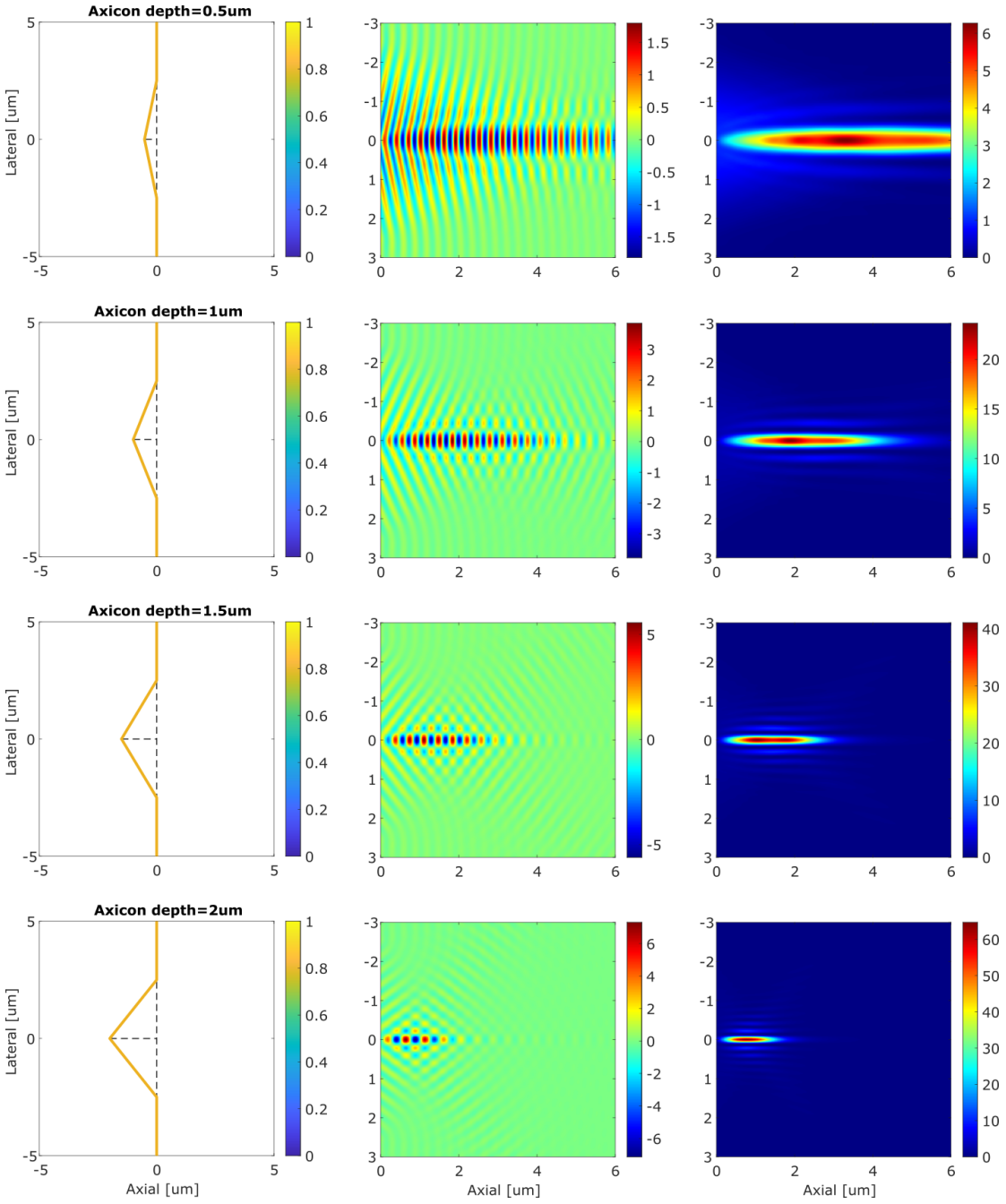

Figure 5.15: Simulated acoustic focusing of axicon lenses with varied design & focal depths: (Left) Cross-sections showing the axicon lens profiles designed for 0.5 μm, 1 μm, 1.5 μm, and 2 μm lens profile depths, each with a lens diameter of 5 μm. (Center) Acoustic field distribution simulations across the lateral plane for each lens. (Right) Corresponding intensity maps illustrate the focused acoustic energy.

sub-optical resolution has not yet been achieved due to the system used to measure the focusing effect - the beam size of the probe (referred to as optical PSF

in the following texts) is limited by diffraction. To achieve the true acoustic PSF (sub-optical, $\sim$ 300 nm), one possible solution is to maintain the current pump-probe setup unchanged or small modification but introduce a resolution target, through either edge detection or grating patterns, to demonstrate the resolution limit these lenses can achieve. A 3D micro-positioner capable of moving in 100 nm steps was built for this proposed idea. Some preliminary results showcasing the moving ability of the 3D micron positioner, along with some edge detection/grating measurements over a conventional transducer, are presented in the following sections.

5.4.1 3D micron positioner

A 3D micron positioner is constructed by stacking three PI-M605 high-precision linear stages and a PI P-721 piezo nano-positioner. Controlling scripts in C++ and MATLAB has been written to enable digital control; this script can integrate with the main pump-probe scanning control software to perform real-time movement and scanning. Each PI-M605 stage has a 50 mm travel range and a 100 nm linear encoder; the PI P-721 piezo has a travel range of 130 μm and a resolution of approximately 5 nm. Though the piezo can provide precise control in the z-axis, its short travel range requires additional practical assistance from the third linear PI-M605 stage. The same positioner is used to pick up the scanning target, with the ise of UV-glue for attachment. Initially, the scanning target is placed on the same substrate as the lens, but to the side - to get the same height while not damaging the lens structures. Then, a small drop of UV-glue is applied to the target. By using the 3D positioner, a needle-like arm is then sent close to the UV-glue drop using the positioner. While monitoring through the camera, once it is observed that the needle arm makes proper contact with the glue drop, a UV

torch is used to cure the glue. The height of the target is recorded and serves as a reference for subsequent approaches when the petri dish is filled with water for later testing.

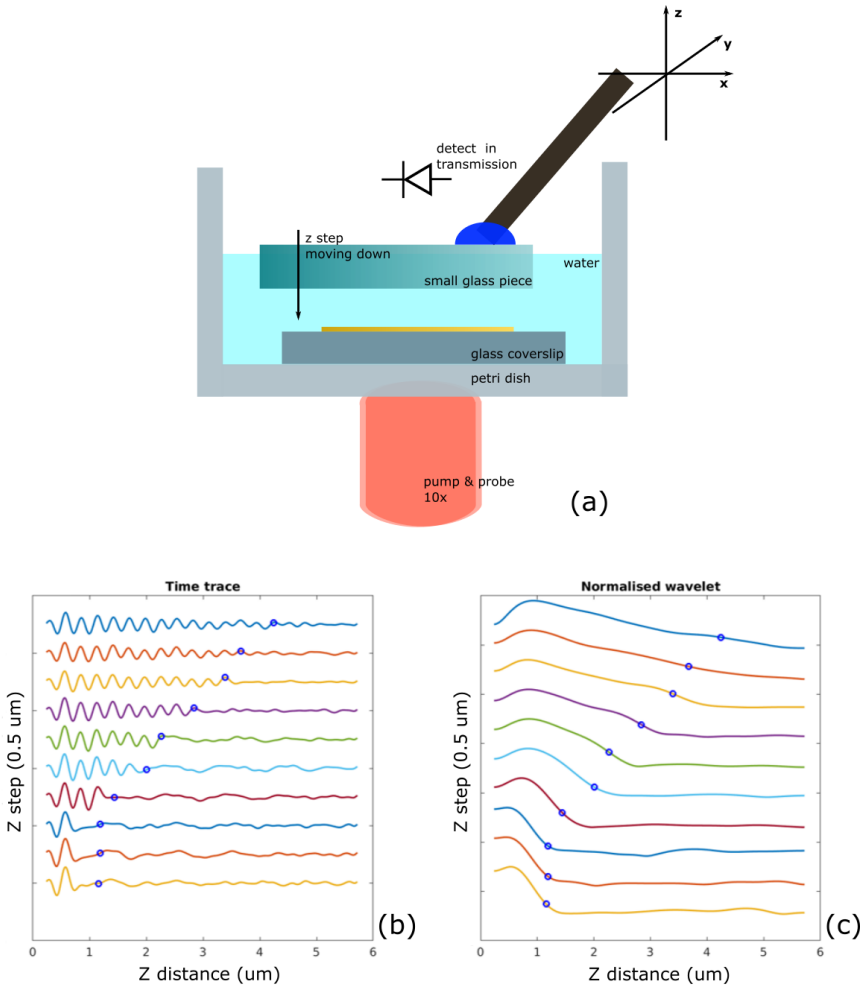

Figure 5.16: Experimental z-approaching results from a conventional Au transducer, NIR-NIR setup with detection in transmission. (a) Diagram showing the experimental setup, where NIR-NIR beams are both delivered from the same 5x objective from the bottom. The scanning target is attached to the 3D positioner, which has the freedom to move and a precision of 100 nm in the x-axis and y-axis, and 5 nm in the z-axis. (b) Time traces showing the approach of the scanning target to the transducer. (c) Wavelet results of the time traces shown in (b).

Figures 5.16 and 5.17 showcase the z-approaching capability of the 3D positioner. Figure 5.16 displays approaching traces taken with the NIR-NIR setup (Figures 3.19 and 3.20), as discussed in Section 3.3.4. The target sample, a small flat glass piece, moves from top to bottom, gradually approaching the bottom substrate on

which the transducer is slitted. Sub-figure (b) presents the filtered time traces during the target's movement from top to bottom, with a step size of 0.5 μm (as labelled on the y-axis), and the x-axis represents the calculated z position using the time series and water velocity. Sub-figure (c) shows the wavelet transform of the detected signal at the f_B of water. From the top blue trace to the 7th dark red trace, the piezo-controlled target moves a total of 6 steps, covering a total travel distance of 3 μm, aligning with the reconstructed z travel range. The acoustic impedance difference between water and glass (the target) impedes the majority of sound energy propagation, leading to the cessation of oscillations observed in (b).

The difference between Figures 5.16 and 5.17 is that in 5.17, the approaching traces are captured with a NUV-NIR setup (Figures 3.21 and 3.22). A series of approaching traces are also achieved in this setup. Although the probe travels through a more complex optical path compared to the previous one, this setup is worth pursuing because it is the same setup used to present all the focusing results in Chapter 4. One thing worth mentioning here is that for both sets of results, when the positioner moves lower to some extent, the TRBS traces stop reflecting the moving distances. One explanation for this is that when the scanning target is attached to the positioner arm, the target is not perfectly horizontally levelled. The slight angle may cause the corner of the target to touch the substrate first, thus introducing distance measurement errors in the z-approaching experiments. With the ability to approach the scanning target to the transducer within a $\sim \mu m$ range, the next step moves to line scanning in the horizontal plane.

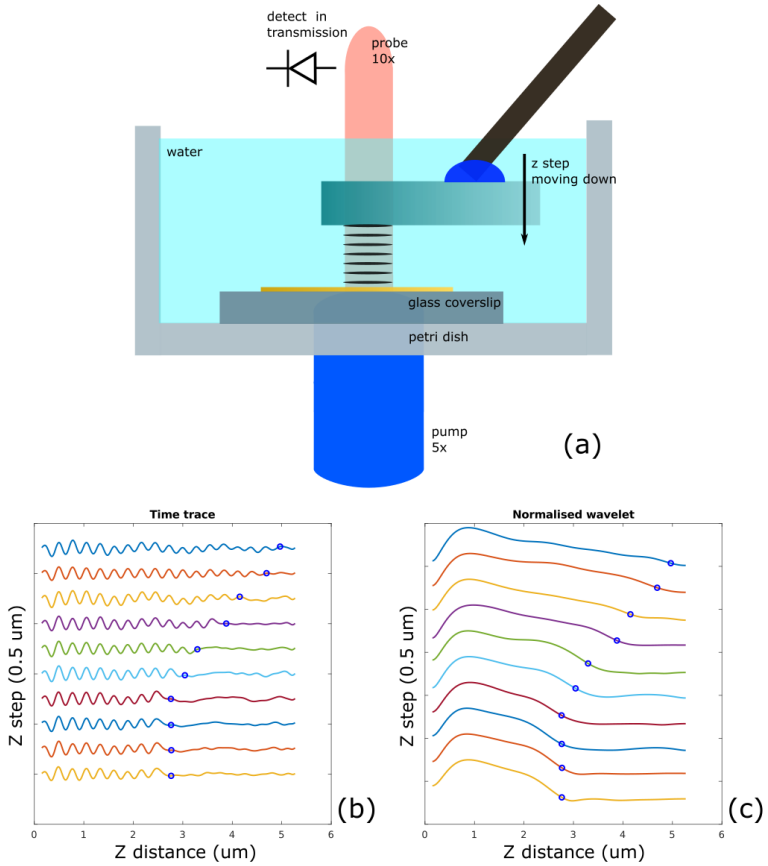

Figure 5.17: Experimental z-approaching results from a conventional Au transducer, NUV-NIR setup with detection in reflection. (a) Diagram showing the experimental setup for the NUV-NIR configuration, with the pump delivered from the bottom 5x objective and the probe from the top 10x objective. The scanning target is attached to the 3D positioner, which has the freedom to move with a precision of 100 nm in the x-axis and y-axis, and 5 nm in the z-axis. (b) Time traces showing the approach of the scanning target to the transducer. (c) Wavelet results of the time traces shown in (b).

5.4.2 Edge detection

Two preliminary results presented here are: glass edge detection and line scanning across a PMMA grating sample. Both are conducted with a NUV-NIR setup, with both pump and probe delivered from the bottom objective (Figure 3.18). Figure 5.18 demonstrates the edge detection from no-glass to glass transition. (a) shows the experimental setup at the top, where the scanning target moves in a horizontal plane, transitioning from no glass in the detection beam to glass

situated in between, as illustrated in the bottom optical pictures. (b) is a B-scan plot of all the filtered traces, where the x-axis represents the TRBS signal in z, and the y-axis represents the positioner's movement in the horizontal plane. When there is no glass on the detection path, TRBS signals continue following natural attenuation. Upon reaching the edge, a no-signal gap is observed, and then as the glass continues moving, the TRBS signal with a sudden stop reappears. However, as the glass continues moving in the same direction, the cessation of the TRBS signal also increases. (c) is plotted using the wavelet method to determine the signal's ending point. This change in TRBS signal can explain the question left from the approaching experiment: there is an angle in the scanning sample.

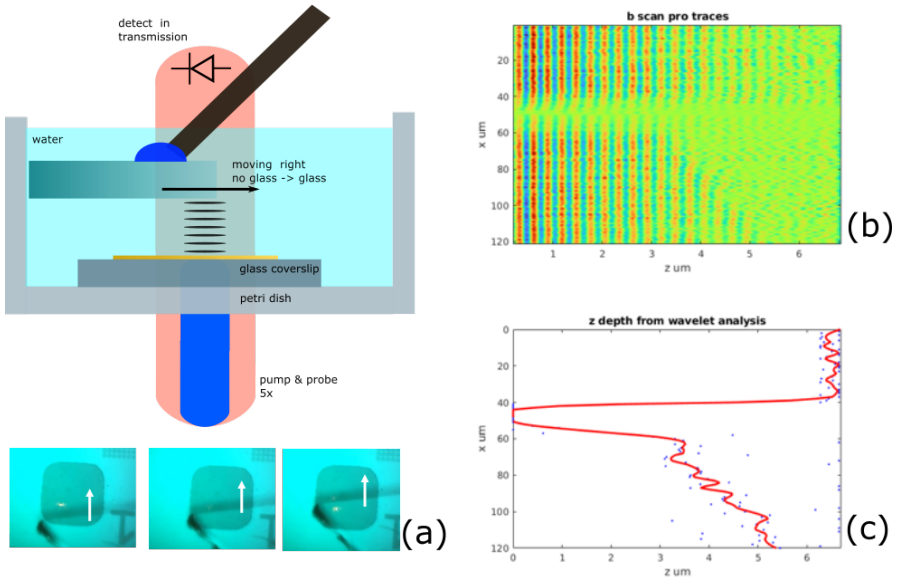

Figure 5.18: Moving the glass horizontally, from no-glass to glass: (a) Diagram showing the experimental setup, where NUV-NIR beams are both delivered from the same 5x objective from the bottom. The scanning target is attached to the 3D positioner and moves in a horizontal plane when a z-depth of approximately μm is achieved. (b) Time traces showing the filtered TRBS signal by scanning the target from no-glass to glass. (c) Wavelet results of the time traces shown in (b).

Figure 5.19 presents some preliminary traces from scanning a PMMA grating pattern with a conventional flat transducer. The gratings, created using a UV mask aligner, have a width of 18 μm and a thickness of approximately 2 μm. The

entire scan covers 100 μm; the top corner, measured as the corner closest to the bottom substrate. The scan commenced from top to bottom as indicated by the yellow line in (a), and in (c), it is from left to right. (b) displays some preliminary traces that align well with expectations; when moving into the PMMA region, shorter TRBS signals are observed. Additionally, the overall trend follows what was also observed in the previous edge detection experiment, indicating an angle in the scanning target.

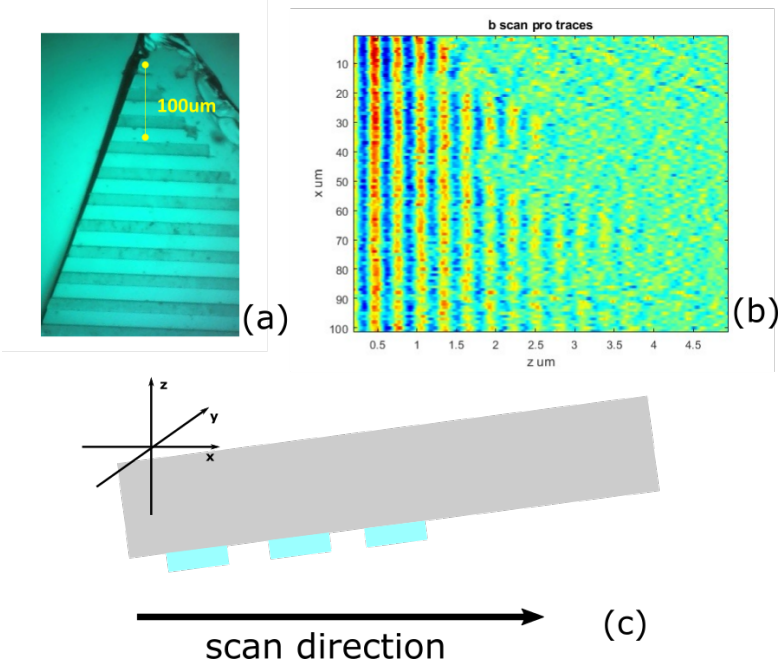

Figure 5.19: Moving the glass horizontally and across grating patterns: (a) The scanning target—a PMMA layer over a glass substrate—is attached to the 3D positioner and moves in a horizontal plane when a z-depth of approximately μm is achieved. (b) Time traces showing the filtered TRBS signal as the scanning target moves from no-glass to glass. (c) The distribution of the PMMA pattern and the proposed target angle.

Given the successful measurements of the z-approaching and edge/grating pattern detection using a conventional transducer. Next steps will be trying to perform edge/grating pattern detection over opto-acoustic lenses.

A question was raised regarding whether deconvolution could be used to determine the acoustic PSF in the viva, particularly in relation to the 'knife edge' experiment.

In the present configuration, both the pump and probe beams move together in a coupled manner, which makes deconvolution ineffective for accurately determining the acoustic PSF. This limitation arises because I am not scanning the sample with a fixed pump while moving the knife edge, which is the typical method for such measurements. Instead, the coupled motion of both beams, along with factors such as water gravity, imposes significant constraints on the implementation of this technique.

To achieve precise PSF measurement via deconvolution, the probe beam would need to be fixed at the top while the sample is moved by adjusting the stage. Additionally, the pump beam would need to be controlled independently, using a fast scanning mirror to achieve the necessary scanning. Under such a setup, deconvolution could indeed provide an accurate determination of the true acoustic PSF size.

5.4.3 Fibre for detection

In addition to this method, another way to reduce the complexity of the experiment is to deliver both the pump and probe from below, then attach a resolution target at the top of the fibre, and also use this fibre directly to collect probe light for detection. Figure 5.20 shows the device concept for this idea.

5.5 Transfer the lens to single mode fibre

Instead of the complex experiments required to find the true acoustic PSF for lenses fabricated on substrates, one solution is to combine the established fibre probe phonon imaging method, as discussed in the background chapter [**?**] (Fig-

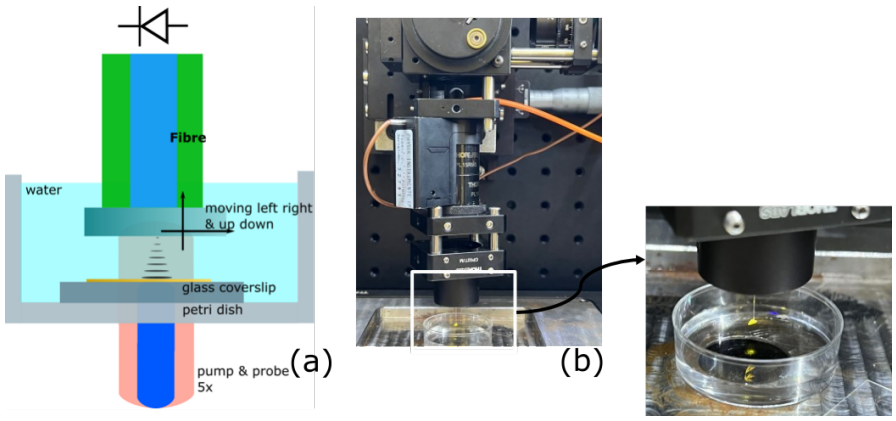

Figure 5.20: Diagram showing the experimental setup for using fibre for collection. An NUV-NIR configuration with both the pump and probe delivered from the bottom objective. The scanning target is attached directly to a multi-mode fibre, which can be held using the same piezo introduced in the previous Section 5.4.1.

ure 2.7), with the optoacoustic lenses developed in this thesis. The key idea is to fabricate optoacoustic lenses directly on the tip of an optical fibre, enabling the generation and detection of focused sub-optical wavelength phonon beams for super-resolution imaging and elasticity characterization of cells, this concept will be refer as phonon probe microscope (PPM) in the following texts.

The proposed fibre-based design involves modifying the end of an optical fibre to serve as both the phonon source and detector as shown in Figure 5.21. This can be achieved by either coating the fibre tip with a metallic thin film and shaping it into a concave surface (acoustic lens) or patterning it into an amplitude zone plate. These structures can generate and detect convergent coherent phonon fields with beam waists smaller than the probing optical wavelength, enabling super-optical resolution imaging.

Two potential configurations are proposed: (a) an all-fibre system compatible with endoscopic applications, and (b) a hybrid fibre/free-space system for improved signal collection efficiency. The all-fibre system couples both the excitation and detection light through the same fibre, making it suitable for in-vivo imaging via endoscopes or biopsy needles. The hybrid configuration separates the excitation

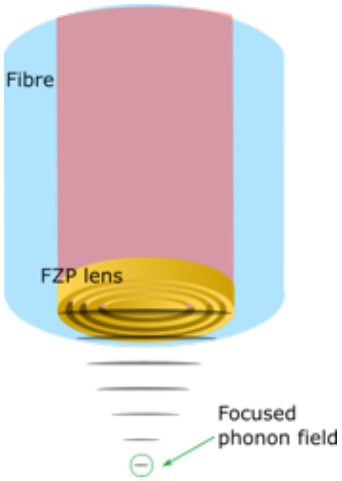

Figure 5.21: Device concept of a sub-optical resolution phonon probe microscope (PPM): Place lenses directly over a single-mode fibre for imaging, which offers great convenience and compatibility compared to previous methods.

and detection paths, allowing more efficient collection of the Brillouin-scattered light using an external objective lens.

5.5.1 Fabrication

Three similar fabrication techniques are presposed for optoacoustic lens creation over fibre tips, which are similar to the lens fabrication procedure over a standard flat substrate: (a) Focused Ion Beam (FIB) milling directly over fibre, (b) Electron Beam Lithography (EBL) with a novel polymer-encapsulated fibre transfer method, and (c) Two Photon Polymerization (TPP).

FIB milling offers a straightforward way to make prototype samples by directly milling the lens profile into a cleaved fibre tip. However, it is limited in lens diameter by the fibre core size. Meanwhile, direct milling using an FIB machine requires a series of tests to find the best stage for sample holding and to solve the charging problem using an FIB-SEM machine. EBL can be used to pattern amplitude zone plates composed of concentric rings, offering an alternative approach that does not require curved surfaces. However, it also necessitates a novel sample

transfer technique to transfer the pattern to a fibre tip. TPP enables the additive fabrication of polymer structures on top of the fibre face, potentially allowing for larger lens diameters and tapered designs to prevent unwanted contact caused by normally cleaved fibre tip.

Figure 5.22 shows an example of EBL made thin Au FZP transferred to a fibre tip using the polymer-encapsulated method. The fabrication process for ultra-thin polymer-encapsulated lenses onto fibre tips involves several steps. Firstly, the encapsulated lenses are separated from the hosting substrate by etching a Cr sacrificial layer and employing tape peeling. Subsequently, using an inverted microscope, the lenses are aligned and adhered onto optical fibre tips. This process involves attaching a glue-dipped fibre to a polymer-embedded lens on adhesive tape. Illumination from an additional light source, such as white light, assists in aligning the lens with the fibre core, followed by UV lamp exposure to cure the optical adhesive. After curing, the encapsulated lens, firmly adhered to the fibre tip, can be removed from the tape. [196].

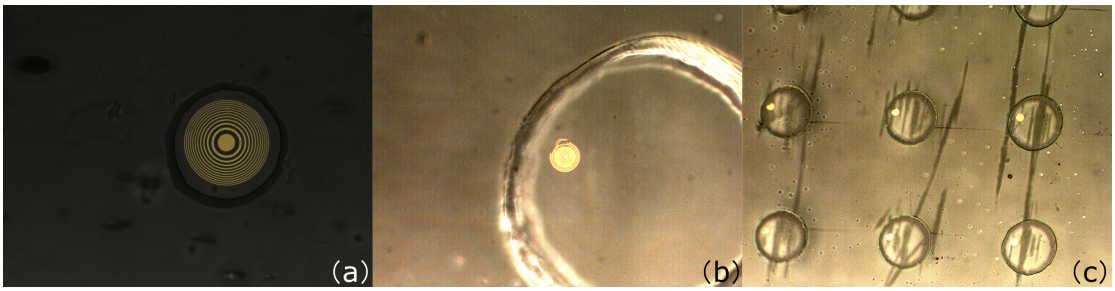

Figure 5.22: EBL-made FZP transferred to a fiber tip using the polymer-encapsulated method. (a) Successful pattern transfer of a larger FZP pattern. (b) Encapsulated optoacoustic FZP pattern.

Figure 5.23 showcases a test run for fabricating lenses directly onto a single-mode fibre.

Fabricating lenses at nano/micron scale on fibre tips presents significant practical challenges. Combining multiple fabrication techniques or exploring alternative

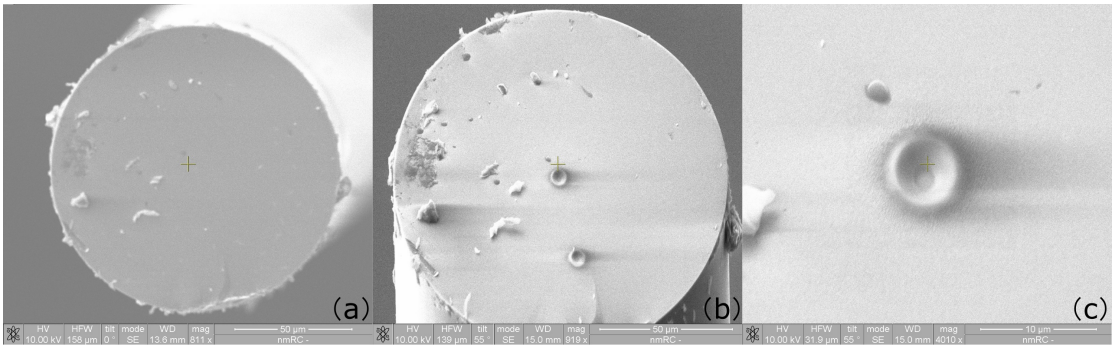

Figure 5.23: Direct FIB milling of a lens over a fibre tip. (a) SEM picture of the cleaved fiber used for direct FIB milling. (b) Dish milled in the centre core of the fibre. (c) Zoom in on the dish.

methods (e.g., nanoimprint lithography) may also be necessary to optimize the lens design and performance in the future.

5.6 Publications and my contributions

During my PhD, I also participated some projects closely related to the lenses, including one perspective paper about picosecond ultrasonics for cell imaging and two research paper: one about improve the scan efficiency by using a multi-core fibre bundle for detection and the other one about quantitative 3D imaging of sub-micrometre biology with label-free Brillouin endo-microscopy.

5.6.1 Picosecond ultrasonics for elasticity-based imaging and characterization of biological cells

This paper focuses on the application of picosecond ultrasonics for elasticity-based imaging and characterization of biological cells. It explores how high-frequency ultrasound waves can be used to generate sub-optical resolution images by detecting Brillouin scattering, enabling the study of the mechanical properties of

cells without the need for physical contact or invasive techniques. The technology shows significant promise in fields such as cell biology, cancer research, and regenerative medicine by offering non-invasive, label-free imaging methods that can provide insight into the elasticity and mechanical behaviour of cells. The paper also addresses challenges, including signal attenuation, biocompatibility, and the need for precise control of signal acquisition, while highlighting the potential of picosecond ultrasonics to revolutionize biological imaging techniques through its high resolution and compatibility with conventional microscopes.

My contribution to this paper centres around the modelling of key aspects related to temperature changes and transducer efficiency. Specifically, I developed models to predict how temperature variations affect the performance of the transducer during the ultrasonic imaging process, which is crucial for maintaining consistent signal quality and ensuring reliable results. Additionally, I worked on optimizing the efficiency of the transducer, which is critical for improving the accuracy and sensitivity of the imaging system. By addressing these factors, my work helps enhance the overall performance of the picosecond ultrasonic system, contributing to the paper's broader goal of advancing non-invasive imaging techniques for biological research.

5.6.2 Parallel imaging with phonon microscopy using a multi-core fibre bundle detection

This paper, "Parallel Imaging with Phonon Microscopy Using a Multi-Core Fibre Bundle Detection," investigates a novel approach to enhance imaging resolution and efficiency by employing a multi-core fibre bundle for parallel detection in phonon microscopy. The research explores how this configuration can simultaneously detect multiple phonon signals, enabling faster and more detailed imaging

of biological and material samples. By integrating a multi-core fibre bundle, the system achieves higher spatial resolution while reducing acquisition time, making it a promising tool for applications such as biological imaging, material characterization, and non-invasive diagnostics. The paper discusses various challenges, including signal processing, fibre alignment, and calibration, and offers solutions to improve overall imaging accuracy through optimized experimental setups and advanced computational reconstruction techniques.

My contribution to this paper includes several key aspects. First, I fabricated the reference target using EBL, ensuring high precision and accuracy necessary for calibrating the system. I was also responsible for calibrating the beam position within the multi-core fibre bundle, which is critical for accurate phonon signal detection and parallel imaging. Additionally, I carried out the experimental measurements, ensuring the proper operation of the setup, and developed the algorithm to reconstruct the map, a computational technique that allows for the visual representation of the detected phonon signals in parallel. These contributions were essential in validating the system's performance and demonstrating the potential of multi-core fibre bundles for faster and more accurate phonon-based imaging.

5.6.3 Label-free Brillouin endo-microscopy for the quantitative 3D imaging of sub-micrometre biology

This paper, "Label-free Brillouin Endo-Microscopy for the Quantitative 3D Imaging of Sub-Micrometre Biology," presents a groundbreaking technique for imaging biological tissues with sub-micrometre resolution using Brillouin microscopy. The research leverages the non-invasive and label-free nature of Brillouin scattering to quantitatively measure mechanical properties of cells and tissues, providing in-

sights into their biomechanical behaviour. The integration of this technology into endoscopic systems allows for in-vivo imaging, offering significant potential for medical diagnostics, particularly in detecting and characterizing diseases where tissue stiffness plays a key role. The paper also emphasizes the ability to generate high-resolution 3D images, making it suitable for complex biological applications without damaging the sample.

In this work, my contributions were focused on two primary areas. First, I was involved in the preparation of the fibre probe, specifically working on the single-mode fibre tip transducer, which is crucial for enabling high-sensitivity Brillouin signal detection in the endoscopic setup. My role also extended to the data processing aspect, where I assisted in analysing the collected data to ensure accurate reconstruction of the 3D images. Furthermore, I contributed to the creation of figures that effectively illustrated the quantitative imaging results, helping to visually represent the key findings of the paper. These contributions were essential to demonstrating the capability of the Brillouin endo-microscopy system in providing detailed mechanical property maps of biological samples with unprecedented precision.

Chapter 6

Future work

This chapter will outline future development plans based on the progress made with optoacoustic lenses and preliminary results. Key areas include optimizing the design of optoacoustic lenses, particularly the transducer cavity, while continuing to develop axicon lenses. Additionally, efforts will focus on advancing phonon-probe microscopy to achieve acoustically-resolved Brillouin spectroscopy, enhancing material characterization techniques. Further exploration of nanorods will also be pursued, along with the development of flat Fresnel-Zone Plate (FR-FZP) lenses utilizing nanorods to improve focusing and imaging capabilities.

6.1 Transducer optimisation

Building upon the discussions in section 5.1, the next step involves the actual fabrication of concave lenses with a three-layer cavity structure. This design is expected to improve the performance of the lenses, and practical tests will be conducted to evaluate the extent of these improvements. The fabrication process will aim to realize the theoretical benefits discussed earlier, providing insights into

how the multi-layer cavity structure influences the acoustic and optical properties of the lenses.

Another key objective is to explore and refine fabrication methods for creating axicon lenses. One of the main challenges in this process is to achieve a smooth, continuous slope, which is critical for the axicon's ability to focus acoustic or optical waves into a sharp point. Overcoming this challenge will involve experimenting with different manufacturing techniques, materials, and surface treatments. Once fabricated, the axicon lenses will undergo rigorous testing to assess their performance and validate their design principles.

6.2 Phonon-probe microscopy

The phonon probe microscope (PPM) is planned to be the first-ever attempt to detect Brillouin scattering (BS) from convergent phonon fields for cell imaging. The fibre-based PPM holds great promise for various applications in cell biology, cancer research, and regenerative medicine: By mapping the mechanical properties of living cells at high resolution, the PPM can provide new insights into the elasticity changes associated with cancer development and metastasis. This could lead to novel biomarkers for early cancer diagnosis and monitoring; The PPM's capability for label-free, non-invasive imaging could be invaluable for monitoring the development of tissue constructs and stem cell differentiation, where traditional fluorescence microscopy techniques are limited by phototoxicity; The endoscopic configuration of the all-fibre PPM system opens up the possibility of in-vivo elasticity characterization and imaging through minimally invasive procedures, potentially enabling early detection of cancers or other pathological conditions.

However, realizing the full potential of fibre based phonon probe microscope

(PPM) still faces several challenges. Firstly, signal attenuation, especially for higher frequency sounds, this can significantly limit the working distance and thus imaging depth. Strategies such as optimizing the lens design, exploring better transducer cavity design and developing better signal processing techniques to improve the SNR are of great importance. Secondly, efficient coupling of excitation light (the pump) into the fibre and the collection of Brillouin-scattered light (the probe) are important to ensure adequate signal are detectable. Addressing this consideration requires careful design of fibre-optic interfaces and lens optimization. Thirdly, fabricating of optoacoustic lenses with fine precision and surface quality at the nano/micron scale poses challenges, especially for fibre-based systems, a combination of multiple fabrication techniques or alternative methods are thus required. Lastly, for in-vivo applications, the biocompatibility of the fibre-based probe also requires consideration in details.

Future research directions could include not only the shared optimising of transducer design and signal processing method. For fibre based technique, we can also explore alternative fibre designs or materials (e.g., photonic crystal fibres, chalcogenide glasses) to improve performance or enable additional functionalities, such as simultaneous optical and acoustic imaging. Also, it worth to investigate integration of the fibre-based PPM with existing endoscopic systems, biopsy needles, or other minimally invasive medical devices for in-vivo applications.

The fibre-based phonon probe microscope (PPM) has the potential to enable sub-optical resolution imaging and elasticity characterization of biological cells in a label-free and non-invasive manner. By focusing laser-generated coherent phonon fields and thus improved Brillouin scattering signal in the focused region, this technique has the potential to revolutionize studies in cell biology, cancer research, regenerative medicine, and healthcare applications.

Realizing the full potential of the PPM will require interdisciplinary collaborations involving knowledge in optics, acoustics, nanotechnology, and life sciences. Overcoming the challenges associated with fabrication, signal attenuation, and biocompatibility is important for enabling new discoveries and translating this technology (a powerful new tool in biological imaging and elasticity characterization) into practical applications.

6.3 More about nanorods

An important focus of future work is to explore nanorods of varying sizes and placed in different media. By investigating how these nanorods respond under different conditions, it will be possible to better understand their optical and acoustic behaviour. This will involve studying the interaction of nanorods with light and sound waves in diverse environments to optimize their use in various applications, such as imaging and sensing.

Another key objective is to investigate both positive and negative Fresnel Zone Plates (FZP) that are constructed using nanorods aligned in a single orientation. The goal here is to understand how the arrangement of nanorods influences the focusing and imaging properties of the FZPs. Testing these lenses will help determine the optimal configurations for specific applications, improving the overall performance of FZP-based devices.

Efforts will also be directed towards refining the Michelson-like optical path design, focusing on achieving precise control over the delivery of double pump pulses. This will require enhancing the synchronization and accuracy of pulse timing, which is critical for improving experimental results. Once this level of precision is achieved, the technique will be applied to a flat Fresnel-Zone Plate (FR-FZP) made with

nanorods oriented in two directions, varying by 90 degrees. This configuration is expected to provide unique optical properties, further advancing the potential applications of nanorod-based FZP lenses.

6.4 Summary

In summary, the future work of this thesis will focus on several key areas to advance the development of optoacoustic technologies. First, the fabrication and testing of concave lenses with a three-layer cavity structure and the creation of axicon lenses will aim to improve their performance through optimized designs and manufacturing techniques. Additionally, further research on the fibre-based phonon-probe microscope (PPM) will seek to enhance its capabilities in non-invasive, high-resolution cell imaging by addressing challenges such as signal attenuation, transducer design, and biocompatibility. Finally, the exploration of nanorods in various sizes and media, as well as the development of flat Fresnel Zone Plate (FR-FZP) lenses with nanorods oriented in two directions, will continue to refine their optical and acoustic properties for imaging and sensing applications.

Chapter 7

Conclusions

In conclusion, this thesis addressed a major problem in the field of time-resolved Brillouin scattering (TRBS) by directly tackling the issues with lateral resolution. Meanwhile, PLU-based TRBS technology enhanced the manipulation of sound fields at higher frequencies (GHz), addressing challenges inherent in the nature of sound for other acoustic microscopy techniques. At the heart of this research lay the design, fabrication, and characterization of optoacoustic lenses, designed to focus coherent phonon fields at GHz frequencies. These lenses, including flat Fresnel zone plates and concave structures, were engineered to go beyond the limits of optical diffraction. They opened the door to a new era of improved lateral resolution in TRBS systems.

The substantial portion of this work was dedicated to the design, nanoscale fabrication, simulation, and characterization of these lenses. The thesis presented proof-of-concept experimental results that not only demonstrated the lenses' focusing ability but also highlighted their importance for future use in high-resolution acoustic/elastic imaging. The road to full-scale image integration is still long, but the early results shown here were not only encouraging; they also showed how

these lenses could change the game by making it possible to achieve unmatched lateral resolution in TRBS.

In addition, the research carefully described in this thesis lays the groundwork for future research that aims to add these optoacoustic lenses to TRBS systems, which would make imaging better in fields like biological cell imaging that need non-invasive, high-precision measuring methods.

7.1 Summary of thesis

Background and Modelling

This chapter started by the discussion of Brillouin scattering, its theory, and application in elasticity imaging - Brillouin Microscopy, and then the integration of detection and measurements using picosecond laser ultrasound, emphasizing improved SNR and resolution in axial in Time Resolved Brillouin Scattering (TRBS) based imaging techniques. A PLU model that explores both the optical and mechanical performance of multilayer thin film structure was introduced to modelling expected time trace signal. After that, this chapter examined wave focusing mechanisms, covering both optical and acoustic focusing via lensing or other systems. It started with an exploration of light and sound focusing through Fresnel zone plates and concave lenses, then progressed to the Fourier-Bessel angular spectrum method (FBASM) for modelling of single frequency wave propagation, since the detection nature of TRBS only select certain sound frequencies match the Brag condition. Additionally, the significance of nano-fabrication techniques, particularly Electron Beam Lithography (EBL) and Focused Ion Beam (FIB), was introduced for their application in creating advanced nano/micron structures.

Methods

This chapter outlined the design and fabrication of optoacoustic lenses, including flat transducers, concave lenses, and Fresnel Zone Plate lenses, using diverse nano/micron fabrication techniques such as sputtering, thermal evaporation, EBL and FIB. A series of GHz optoacoustic Fresnel zone plates, with the highest working frequency ($\sim$ 5 GHz) for acoustic FZPs, were designed, simulated, and tested using picosecond laser ultrasonics-based time-resolved Brillouin scattering techniques. Although concave-shaped acoustic lenses operating in the GHz range have been studied for high-frequency acoustic scanning microscopy, this thesis proposes for the first time the concave shape of the transducer itself, thus maximizing signal efficiency. This chapter further details the experimental setup, especially the use of the Asynchronous Optical Sampling System (ASOPS) for capturing TRBS signals and the modification of optical configurations to meet the requirements of different experiments. Additionally, it delves into the signal processing methods necessary for eliminating thermal background noise, implementing digital filtering, and conducting frequency domain analyses using both FFT and wavelet transforms. These experimental setups and signal processing techniques ultimately enable the reconstruction of GHz phonon wavefronts, thus facilitating the potential for further applications in 3D elasticity imaging.

Results

This chapter presents a thorough analysis of simulation and experimental results, marking the first demonstration of strong, measured focused TRBS traces achieved through the manipulation of femtosecond laser-generated coherent phonons. It explores the performance of various optoacoustic lenses, including multiple types of Fresnel Zone Plates and concave lenses, each designed with different focuses.

Lenses with a diameter smaller than 5 μm and a minimum feature size of a few hundred nm were proven in simulation to be capable of producing a sound focus of approximately 200 nm. A detailed demonstration of focused GHz acoustic fields in water is shown in single-point scans, line scans, and 2D scans. The experimental results align well with the simulated outcomes. FZP with a high acoustic numerical aperture (NA) of 0.72 and concave optoacoustic lens with maximum NA of 0.62 were achieved and presented.

Furthermore, the chapter engaged in a discussion on the current limitations of these measurements: Though a strong focusing was observed, the real acoustic Point Spread Function (PSF) is still unknown due to the diffraction limit caused by the optical measurement system. However, the strong focusing achieved by the proposed optoacoustic lenses suggests potential solutions to the lateral resolution problem faced by all the TRBS based imaging techniques.

Preliminary results, perspectives and future work

This chapter began by discussing improvement plans for the current transducer design and more potential optoacoustic lens structures, including flat PR-FZP made with nanorods and optoacoustic axicon lenses. Then to address the main problem highlighted in the Results chapter, multiple pathways to identify the real acoustic PSF were proposed, with advancements in experiments and some preliminary results presented and discussed. These include the use of a 3D micron positioner, z-approaching in the μm range, and edge detection experiments. Moreover, this chapter also discusses the future of sub-optical fibre-based phonon microscopy, which offers greater accessibility for scanning and even the potential for high-resolution endoscopy applications.

7.2 Closing Remarks

To sum up, this thesis effectively addressed one potential direction to solve the problem of limited lateral resolution in time-resolved Brillouin scattering (TRBS) techniques through the development and characterisation of innovative optoacoustic lenses. By introducing flat Fresnel zone plates and concave structures capable of focusing coherent phonon fields at GHz frequencies, this work stood at the frontier of surpassing the optical diffraction limits in TRBS systems and the high frequency (GHz) sound manipulation area. Together with the promising initial experimental results—the first wavefront reconstruction of a focused GHz acoustic field in water—the thesis highlighted the careful design, nanoscale fabrication, and comprehensive calculations that underscored the great promise these lenses hold for developing high-resolution acoustic/elastic imaging. While full-scale imaging integration was still some way off, the progress made thus far offered a strong basis for future efforts to incorporate these lenses into TRBS-based Phonon Microscopy systems, which might result in a significant improvement in imaging capabilities, particularly for high-precision (substantial improvement in lateral resolution), non-invasive applications such as biological cell imaging. This thesis paved the way for future research to breach existing resolution barriers in TRBS, showcasing the future implications of optoacoustic lenses in the realm of advanced sub-cellular elastic imaging techniques.

Bibliography

[1] Ernst Ruska. The development of the electron microscope and of electron microscopy (nobel lecture). *Angewandte Chemie International Edition in English*, 26(7):595–605, 1987.

[2] J.I. Goldstein, D.E. Newbury, J.R. Michael, N.W.M. Ritchie, J.H.J. Scott, and D.C. Joy. *Scanning Electron Microscopy and X-ray Microanalysis*. Springer New York, 2017.

[3] Gerd Binnig, Heinrich Rohrer, Ch Gerber, and Edmund Weibel. Surface studies by scanning tunneling microscopy. *Physical review letters*, 49(1):57, 1982.

[4] Ke Bian, Christoph Gerber, Andreas J Heinrich, Daniel J Müller, Simon Scheuring, and Ying Jiang. Scanning probe microscopy. *Nature Reviews Methods Primers*, 1(1):36, 2021.

[5] Parker I Bootman MD. Sanderson MJ, Smith I. Fluorescence microscopy. *Cold Spring Harbor protocols*, 2014.

[6] Ram Dixit and Richard Cyr. Cell damage and reactive oxygen species production induced by fluorescence microscopy: effect on mitosis and guidelines for non-invasive fluorescence microscopy. *The Plant Journal*, 36(2):280–290, 2003.

[7] Michael J Rust, Mark Bates, and Xiaowei Zhuang. Sub-diffraction-limit imaging by stochastic optical reconstruction microscopy (storm). *Nature methods*, 3(10):793–796, 2006.

[8] Birka Hein, Katrin I Willig, and Stefan W Hell. Stimulated emission depletion (sted) nanoscopy of a fluorescent protein-labeled organelle inside a living cell. *Proceedings of the National Academy of Sciences*, 105(38):14271–14276, 2008.

[9] Jennifer A. Thorley, Jeremy A. Pike, and Joshua Z. Rappoport. Super-resolution microscopy: A comparison of commercially available options. 2014. Proceeding.

[10] Richard SC Cobbold. *Foundations of biomedical ultrasound*. Oxford university press, 2006.

[11] R Gr Maev. Acoustic microscopy for materials characterization. In *Materials Characterization Using Nondestructive Evaluation (NDE) Methods*, pages 161–175. Elsevier, 2016.

[12] Francesco Bertocci, Andrea Grandoni, and Tatjana Djuric-Rissner. Scanning acoustic microscopy (sam): A robust method for defect detection during the manufacturing process of ultrasound probes for medical imaging. *Sensors*, 19(22):4868, 2019.

[13] Pavlos Anastasiadis and Pavel V Zinin. High-frequency time-resolved scanning acoustic microscopy for biomedical applications. *The Open Neuroimaging Journal*, 12(1), 2018.

[14] Hyunung Yu. Scanning acoustic microscopy for material evaluation. *Applied Microscopy*, 50(1):25, 2020.

[15] Alexander Graham Bell. The photophone. *Science*, os-1(11):130–134, 1880.

[16] T. H. Maiman. Stimulated Optical Radiation in Ruby. *Nature*, 187(4736):493–494, August 1960.

[17] R. M. White. Generation of Elastic Waves by Transient Surface Heating. *Journal of Applied Physics*, 34(12):3559–3567, June 1964.

[18] Photoacoustic microscopy (pam) introduction. BIOPHOTONICS SUMMER SCHOOL Proceedings.

[19] Mingyang Xie, Adnan Shakoor, and Changcheng Wu. Manipulation of biological cells using a robot-aided optical tweezers system. *Micromachines*, 9(5):245, 2018.

[20] Yves F Dufrêne, Toshio Ando, Ricardo Garcia, David Alsteens, David Martinez-Martin, Andreas Engel, Christoph Gerber, and Daniel J Müller. Imaging modes of atomic force microscopy for application in molecular and cell biology. *Nature nanotechnology*, 12(4):295–307, 2017.

[21] Robert Prevedel, Alba Diz-Muñoz, Giancarlo Ruocco, and Giuseppe Antonacci. Brillouin microscopy: an emerging tool for mechanobiology. *Nature methods*, 16(10):969–977, 2019.

[22] Arthur Ashkin, James M Dziedzic, John E Bjorkholm, and Steven Chu. Observation of a single-beam gradient force optical trap for dielectric particles. *Optics letters*, 11(5):288–290, 1986.

[23] René-Jean Essiambre. Arthur ashkin: Father of the optical tweezers. *Proceedings of the National Academy of Sciences*, 118(7):e2026827118, 2021.

[24] Introduction: Optical traps. https://home.uni-leipzig.de/pwm/web/?section=introduction&page=opticaltraps. Accessed: 2024-01-20.

[25] Fernando Perez Cota. *Opto-acoustic thin-fillm transducers for imaging of Brillouin oscillations on living cells", school =*. PhD thesis.

[26] M Lekka, J Lekki, M Marszałek, P Golonka, Z Stachura, B Cleff, and AZ Hrynkiewicz. Local elastic properties of cells studied by sfm. *Applied Surface Science*, 141(3-4):345–349, 1999.

[27] Zhifeng Shao, Jie Yang, and Andrew P Somlyo. Biological atomic force microscopy: from microns to nanometers and beyond. *Annual review of cell and developmental biology*, 11(1):241–265, 1995.

[28] Brillouin, Léon. Diffusion de la lumière et des rayons x par un corps transparent homogène - influence de l'agitation thermique. *App. Phys.*, 9(17):88–122, 1922.

[29] LI Mandelstam. Light scattering by inhomogeneous media. *Zh. Russ. Fiz-Khim. Ova*, 58(381):146, 1926.

[30] T Dehoux and B Audoin. Non-invasive optoacoustic probing of the density and stiffness of single biological cells. *Journal of Applied Physics*, 112(12), 2012.

[31] Thomas Dehoux, M Abi Ghanem, OF Zouani, J-M Rampnoux, Yannick Guillet, Stefan Dilhaire, M-C Durrieu, and Bertrand Audoin. All-optical broadband ultrasonography of single cells. *Scientific reports*, 5(1):8650, 2015.

[32] Sorasak Danworaphong, Motonobu Tomoda, Yuki Matsumoto, Osamu Matsuda, Toshiro Ohashi, Hiromu Watanabe, Masafumi Nagayama, Kazutoshi Gohara, Paul H Otsuka, and Oliver B Wright. Three-dimensional imaging of biological cells with picosecond ultrasonics. *Applied physics letters*, 106(16), 2015.

[33] Vitalyi E Gusev and Pascal Ruello. Advances in applications of time-domain brillouin scattering for nanoscale imaging. *Applied Physics Reviews*, 5(3), 2018.

[34] Alexis Viel, Emmanuel Péronne, Océane Sénépart, Loïc Becerra, Claire Legay, Fannie Semprez, Léa Trichet, Thibaud Coradin, Ahmed Hamraoui, and Laurent Belliard. Picosecond ultrasounds as elasticity probes in neuron-like cells models. *Applied Physics Letters*, 115(21), 2019.

[35] Bertrand Audoin. Principles and advances in ultrafast photoacoustics; applications to imaging cell mechanics and to probing cell nanostructure. *Photoacoustics*, 31:100496, 2023.

[36] Fernando Perez-Cota, Richard J Smith, Emilia Moradi, Leonel Marques, Kevin F Webb, and Matt Clark. Thin-film optoacoustic transducers for subcellular brillouin oscillation imaging of individual biological cells. *Applied optics*, 54(28):8388–8398, 2015.

[37] Fernando Pérez-Cota, Richard J Smith, Emilia Moradi, Leonel Marques, Kevin F Webb, and Matt Clark. High resolution 3d imaging of living cells with sub-optical wavelength phonons. *Scientific Reports*, 6(1):39326, 2016.

[38] Richard J Smith, Fernando Pérez-Cota, Leonel Marques, and Matt Clark. 3d phonon microscopy with sub-micron axial-resolution. *Scientific Reports*, 11(1):3301, 2021.

[39] R.J. Smith, F. Pérez-Cota, L. Marques, and C. Matt. 3d phonon microscopy with sub-micron axial-resolution. *Scientific Reports*, 11(3301), 2021.

[40] Liwang Liu, Laurent Plawinski, Marie-Christine Durrieu, and Bertrand Audoin. Label-free multi-parametric imaging of single cells: dual picosecond optoacoustic microscopy. *Journal of biophotonics*, 12(8):e201900045, 2019.

[41] Jiajun Zhao, Huapeng Ye, Kun Huang, Zhi Ning Chen, Baowen Li, and Cheng-Wei Qiu. Manipulation of acoustic focusing with an active and configurable planar metasurface transducer. *Scientific Reports*, 4(1):6257, 2014.

[42] Armen Sarvazyan, Laurent Fillinger, and Leonid R Gavrilov. Time-reversal acoustic focusing system as a virtual random phased array. *IEEE transactions on ultrasonics, ferroelectrics, and frequency control*, 57(4):812–817, 2010.

[43] C-H Chou, BT Khuri-Yakub, and GS Kino. Lens design for acoustic microscopy. *IEEE transactions on ultrasonics, ferroelectrics, and frequency control*, 35(4):464–469, 1988.

[44] Hongxia Yao. Synthetic aperture methods for medical ultrasonic imaging. Master's thesis, 1997.

[45] Hyoung Won Baac, Jong G Ok, Adam Maxwell, Kyu-Tae Lee, Yu-Chih Chen, A John Hart, Zhen Xu, Euisik Yoon, and L Jay Guo. Carbon-nanotube optoacoustic lens for focused ultrasound generation and high-precision targeted therapy. *Scientific reports*, 2(1):989, 2012.

[46] Taehwa Lee, Jong G Ok, L Jay Guo, and Hyoung Won Baac. Low f-number photoacoustic lens for tight ultrasonic focusing and free-field microcavitation in water. *Applied Physics Letters*, 108(10), 2016.

[47] Jin Di, Jinwook Kim, Quanyin Hu, Xiaoning Jiang, and Zhen Gu. Spatiotemporal drug delivery using laser-generated-focused ultrasound system. *Journal of Controlled Release*, 220:592–599, 2015.

[48] Taehwa Lee, Hyoung Won Baac, Qiaochu Li, and L. Jay Guo. Efficient photoacoustic conversion in optical nanomaterials and composites. *Advanced Optical Materials*, 6(24):1800491, 2018.

[49] Pascal Ruello and Vitalyi E Gusev. Physical mechanisms of coherent acoustic phonons generation by ultrafast laser action. *Ultrasonics*, 56:21–35, 2015.

[50] Irina Kabakova, Jitao Zhang, Yuchen Xiang, Silvia Caponi, Alberto Bilenca, Jochen Guck, and Giuliano Scarcelli. Brillouin microscopy. *Nature Reviews Methods Primers*, 4(1):8, 2024.

[51] Roland Sanctuary, Ravi Bactavatchalou, Ulrich Müller, Wulff Possart, Patrick Alnot, and Jan-Kristian Krüger. Acoustic profilometry within polymers as performed by brillouin microscopy. *Journal of Physics D: Applied Physics*, 36(21):2738, 2003.

[52] Rainer G Ulbrich and Claude Weisbuch. Resonant brillouin scattering of excitonic polaritons in gallium arsenide. *Physical Review Letters*, 38(15):865, 1977.

[53] Masanori Sakamoto, Masahiko Kawabe, Mami Matsukawa, Noriko Koizumi, and Norikazu Ohtori. Measurement of wave velocity in bovine bone tissue by micro-brillouin scattering. *Japanese journal of applied physics*, 47(5S):4205, 2008.

[54] R Harley, D James, A Miller, and JW White. Phonons and the elastic moduli of collagen and muscle. *Nature*, 267(5608):285–287, 1977.

[55] Stephan Reiß, Gerolf Burau, Oliver Stachs, Rudolf Guthoff, and Heinrich Stolz. Spatially resolved brillouin spectroscopy to determine the rheological properties of the eye lens. *Biomedical optics express*, 2(8):2144–2159, 2011.

[56] F Palombo, Marco Madami, N Stone, and Daniele Fioretto. Mechanical mapping with chemical specificity by confocal brillouin and raman microscopy. *Analyst*, 139(4):729–733, 2014.

[57] Giuliano Scarcelli, Pilhan Kim, and Seok Hyun Yun. In vivo measurement of age-related stiffening in the crystalline lens by brillouin optical microscopy. *Biophysical journal*, 101(6):1539–1545, 2011.

[58] C Thomsen, J Strait, Z Vardeny, Humphrey J Maris, J Tauc, and JJ Hauser. Coherent phonon generation and detection by picosecond light pulses. *Physical review letters*, 53(10):989, 1984.

[59] Osamu Matsuda, Maria Cristina Larciprete, Roberto Li Voti, and Oliver B Wright. Fundamentals of picosecond laser ultrasonics. *Ultrasonics*, 56:3–20, 2015.

[60] Thomas Dehoux, Nicolas Tsapis, and Bertrand Audoin. Relaxation dynamics in single polymer microcapsules probed with laser-generated ghz acoustic waves. *Soft Matter*, 8(9):2586–2589, 2012.

[61] Philippe Babilotte, Pascal Ruello, Denis Mounier, Thomas Pezeril, Gwenäelle Vaudel, Mathieu Edely, Jean-Marc Breteau, V Gusev, and Karine Blary. Femtosecond laser generation and detection of high-frequency acoustic phonons in gaas semiconductors. *Physical Review B*, 81(24):245207, 2010.

[62] C Rossignol, Bernard Perrin, S Laborde, L Vandenbulcke, MI De Barros, and P Djemia. Nondestructive evaluation of micrometric diamond films with an interferometric picosecond ultrasonics technique. *Journal of Applied Physics*, 95(8):4157–4162, 2004.

[63] C Rossignol, N Chigarev, M Ducousso, B Audoin, G Forget, F Guillemot, and MC Durrieu. In vitro picosecond ultrasonics in a single cell. *Applied Physics Letters*, 93(12), 2008.

[64] Bertrand Audoin, Clément Rossignol, Nikolay Chigarev, Mathieu Ducousso, Guillaume Forget, Fabien Guillemot, and Marie-Christine Durrieu. Picosecond acoustics in vegetal cells: non invasive in vitro measurements at a subcell scale. *Physics Procedia*, 3(1):323–331, 2010.

[65] O Matsuda and OB Wright. Reflection and transmission of light in multilayers perturbed by picosecond strain pulse propagation. *JOSA B*, 19(12):3028–3041, 2002.

[66] Richard J Smith, Fernando Perez Cota, Leonel Marques, Xuesheng Chen, Ahmet Arca, Kevin Webb, Jonathon Aylott, Micheal G Somekh, and Matt Clark. Optically excited nanoscale ultrasonic transducers. *The Journal of the Acoustical Society of America*, 137(1):219–227, 2015.

[67] Salvatore La Cavera III. *Optical fibre-based time resolved Brillouin scattering*. PhD thesis, University of Nottingham, 2021.

[68] Fernando Pérez-Cota, Rafael Fuentes-Domínguez, Salvatore La Cavera, William Hardiman, Mengting Yao, Kerry Setchfield, Emilia Moradi, Shakila Naznin, Amanda Wright, Kevin F. Webb, Alan Huett, Claire Friel, Virginie Sottile, Hany M. Elsheikha, Richard J. Smith, and Matt Clark. Picosecond ultrasonics for elasticity-based imaging and characterization of biological cells. *Journal of Applied Physics*, 128(16):160902, 2020.

[69] Fernando Pérez-Cota, Richard J Smith, Hany M Elsheikha, and Matt Clark. New insights into the mechanical properties of acanthamoeba castellanii cysts as revealed by phonon microscopy. *Biomedical optics express*, 10(5):2399–2408, 2019.

[70] Omar F Zouani, Thomas Dehoux, Marie-Christine Durrieu, and Bertrand Audoin. Universality of the network-dynamics of the cell nucleus at high frequencies. *Soft Matter*, 10(43):8737–8743, 2014.

[71] Salvatore La Cavera, Fernando Pérez-Cota, Richard J. Smith, and Matt Clark. Phonon imaging in 3D with a fibre probe. *Light: Science & Applications*, 10(1):91, April 2021. Number: 1 Publisher: Nature Publishing Group.

[72] Eugene Hecht. *Optics*. Pearson Education India, 2012.

[73] David Griffiths. *Introduction to elementary particles*. John Wiley & Sons, 2020.

[74] M Claudia Troparevsky, Adrian S Sabau, Andrew R Lupini, and Zhenyu Zhang. Transfer-matrix formalism for the calculation of optical response in multilayer systems: from coherent to incoherent interference. *Optics express*, 18(24):24715–24721, 2010.

[75] C Thomsen, Holger T Grahn, Humphrey J Maris, and Jan Tauc. Surface generation and detection of phonons by picosecond light pulses. *Physical Review B*, 34(6):4129, 1986.

[76] Mami Matsukawa, Pak-Kon Choi, Kentaro Nakamura, Hirotsugu Ogi, and Hideyuki Hasegawa. *Ultrasonics: Physics and applications*. IOP Publishing, 2022.

[77] Philippe Babilotte. A basic complete numerical toolbox for picosecond ultrasonics. In *Acoustics*, volume 1, pages 137–155. MDPI, 2019.

[78] John Frederick Nye. *Physical properties of crystals: their representation by tensors and matrices*. Oxford university press, 1985.

[79] V Gusev, AM Lomonosov, P Ruello, A Ayouch, and G Vaudel. Depth-profiling of elastic and optical inhomogeneities in transparent materials by picosecond ultrasonic interferometry: Theory. *Journal of Applied Physics*, 110(12), 2011.

[80] Sathyan Sandeep, Samuel Raetz, Nikolay Chigarev, Nicolas Pajusco, Théo Thréard, Mathieu Edely, Alain Bulou, Andreas Zerr, and Vitalyi E Gusev. Time-domain brillouin scattering for evaluation of materials interface incli-

nation: Application to photoacoustic imaging of crystal destruction upon non-hydrostatic compression. *Photoacoustics*, 33:100547, 2023.

[81] Vincent Chan and Anahi Perlas. Basics of ultrasound imaging. *Atlas of ultrasound-guided procedures in interventional pain management*, pages 13–19, 2011.

[82] Dong Chen, Sanjay K Sharma, and Ackmez Mudhoo. *Handbook on applications of ultrasound: sonochemistry for sustainability*. CRC press, 2011.

[83] Oleg Minin and Igor Minin. *Ultrasound Imaging: Medical Applications*. BoD–Books on Demand, 2011.

[84] Alexey Sukhovich, Li Jing, and John H Page. Negative refraction and focusing of ultrasound in two-dimensional phononic crystals. *Physical Review B*, 77(1):014301, 2008.

[85] Jakob J Stamnes. *Waves in focal regions: propagation, diffraction and focusing of light, sound and water waves*. Routledge, 2017.

[86] Yong Li, Bin Liang, Xu Tao, Xue-feng Zhu, Xin-ye Zou, and Jian-chun Cheng. Acoustic focusing by coiling up space. *Applied Physics Letters*, 101(23):233508, 2012.

[87] Wenqi Wang, Yangbo Xie, Adam Konneker, Bogdan-Ioan Popa, and Steven A Cummer. Design and demonstration of broadband thin planar diffractive acoustic lenses. *Applied Physics Letters*, 105(10), 2014.

[88] J. Chen, J. Xiao, D. Lisevych, A. Shakouri, and Z. Fan. Deep-subwavelength control of acoustic waves in an ultra-compact metasurface lens. *Nature Communications*, 9(4920), 2018.

[89] Richard V Craster and Sébastien Guenneau. *Acoustic metamaterials: Negative refraction, imaging, lensing and cloaking*, volume 166. Springer Science & Business Media, 2012.

[90] Sergio Jiménez-Gambín, Noé Jiménez, José María Benlloch, and Francisco Camarena. Holograms to focus arbitrary ultrasonic fields through the skull. *Phys. Rev. Applied*, 12:014016, Jul 2019.

[91] Francisco Cervera, L Sanchis, JV Sánchez-Pérez, R Martinez-Sala, C Rubio, F Meseguer, C López, D Caballero, and José Sánchez-Dehesa. Refractive acoustic devices for airborne sound. *Physical review letters*, 88(2):023902, 2001.

[92] RN Johnston, Abdullah Atalar, J Heiserman, V Jipson, and CF Quate. Acoustic microscopy: resolution of subcellular detail. *Proceedings of the National Academy of Sciences*, 76(7):3325–3329, 1979.

[93] D Rugar, J Heiserman, S Minden, and CF Quate. Acoustic microscopy of human metaphase chromosomes. *Journal of microscopy*, 120(2):193–199, 1980.

[94] JA Hildebrand, D Rugar, RN Johnston, and CF Quate. Acoustic microscopy of living cells. *Proceedings of the National Academy of Sciences*, 78(3):1656–1660, 1981.

[95] B Hadimioglu and CF Quate. Water acoustic microscopy at suboptical wavelengths. *Applied physics letters*, 43(11):1006–1007, 1983.

[96] Daniel Rugar, John S Foster, and Joseph Heiserman. Acoustic microscopy at temperatures less than 0.2° k. *Acoustical imaging*, pages 13–25, 1982.

[97] J Heiserman, D Rugar, and CF Quate. Cryogenic acoustic microscopy. *The Journal of the Acoustical Society of America*, 67(5):1629–1637, 1980.

[98] Anette Jakob, Michael Bender, T Knoll, Robert Lemor, T Lehnert, M Koch, M Veith, Q Zhou, BP Zhu, JX Han, et al. Comparison of different piezoelectric materials for ghz acoustic microscopy transducers. In *2009 IEEE International Ultrasonics Symposium*, pages 1722–1725. IEEE, 2009.

[99] Qifa Zhou, Sienting Lau, Dawei Wu, and K Kirk Shung. Piezoelectric films for high frequency ultrasonic transducers in biomedical applications. *Progress in materials science*, 56(2):139–174, 2011.

[100] Minghua Xu and Lihong V Wang. Photoacoustic imaging in biomedicine. *Review of scientific instruments*, 77(4), 2006.

[101] Eric M Strohm, Michael J Moore, and Michael C Kolios. Single cell photoacoustic microscopy: a review. *IEEE Journal of Selected Topics in Quantum Electronics*, 22(3):137–151, 2015.

[102] Eric M Strohm, Elizabeth SL Berndl, and Michael C Kolios. High frequency label-free photoacoustic microscopy of single cells. *Photoacoustics*, 1(3-4):49–53, 2013.

[103] Qiangzhou Rong, Youngseop Lee, et al. High-frequency 3d photoacoustic computed tomography using an optical microring resonator. *BME frontiers*, 2022.

[104] Paul C Beard and TN Mills. Characterization of post mortem arterial tissue using time-resolved photoacoustic spectroscopy at 436, 461 and 532 nm. *Physics in Medicine & Biology*, 42(1):177, 1997.

[105] Min Rui, Sankar Narashimhan, Wolfgang Bost, Frank Stracke, Eike Weiss, Robert Lemor, and Michael C Kolios. Gigahertz optoacoustic imaging for cellular imaging. In *Photons Plus Ultrasound: Imaging and Sensing 2010*, volume 7564, pages 248–253. SPIE, 2010.

[106] Srivalleesha Mallidi, Geoffrey P Luke, and Stanislav Emelianov. Photoacoustic imaging in cancer detection, diagnosis, and treatment guidance. *Trends in biotechnology*, 29(5):213–221, 2011.

[107] Lihong V Wang and Song Hu. Photoacoustic tomography: in vivo imaging from organelles to organs. *science*, 335(6075):1458–1462, 2012.

[108] S. Che, P.R. Guduru, A.V. Nurmikko, and H.J. Maris. A scanning acoustic microscope based on picosecond ultrasonics. *Ultrasonics*, 56:153–159, 2015.

[109] Rita S Rodrigues Ribeiro, Pabitra Dahal, Ariel Guerreiro, Pedro AS Jorge, and Jaime Viegas. Fabrication of fresnel plates on optical fibres by fib milling for optical trapping, manipulation and detection of single cells. *Scientific reports*, 7(1):4485, 2017.

[110] K Jefimovs, O Bunk, F Pfeiffer, D Grolimund, JF van der Veen, and C David. Fabrication of fresnel zone plates for hard x-rays. *Microelectronic Engineering*, 84(5-8):1467–1470, 2007.

[111] Yuxin Wang, Wenbing Yun, and Chris Jacobsen. Achromatic fresnel optics for wideband extreme-ultraviolet and x-ray imaging. *Nature*, 424(6944):50–53, 2003.

[112] Pei Zheng, Bing Hu, Shenheng Xu, and Houjun Sun. A w-band high-aperture-efficiency multipolarized monopulse cassegrain antenna fed by phased microstrip patch quad. *IEEE Antennas and Wireless Propagation Letters*, 16:1609–1613, 2017.

[113] David C Calvo, Abel L Thangawng, Michael Nicholas, and Christopher N Layman. Thin fresnel zone plate lenses for focusing underwater sound. *Applied Physics Letters*, 107(1), 2015.

[114] Gregory T Clement, Hideyuki Nomura, and Tomoo Kamakura. Ultrasound field measurement using a binary lens. *IEEE transactions on ultrasonics, ferroelectrics, and frequency control*, 62(2):350–359, 2015.

[115] Sergio Pérez-López, José Miguel Fuster, Pilar Candelas, Constanza Rubio, and Francisco Belmar. On the use of phase correction rings on fresnel zone plates with ultrasound piston emitters. *Applied Physics Letters*, 112(26), 2018.

[116] Daniel Tarrazó-Serrano, Sergio Pérez-López, Pilar Candelas, Antonio Uris, and Constanza Rubio. Acoustic focusing enhancement in fresnel zone plate lenses. *Scientific reports*, 9(1):1–10, 2019.

[117] Xiangxiang Xia, Yongchuan Li, Feiyan Cai, Hui Zhou, Teng Ma, and Hairong Zheng. Ultrasonic tunable focusing by a stretchable phase-reversal fresnel zone plate. *Applied Physics Letters*, 117(2), 2020.

[118] Ronald G Driggers. *Encyclopedia of Optical Engineering: Las-Pho, pages 1025-2048*, volume 2. CRC press, 2003.

[119] Anders Holmberg. *Nanofabrication of zone plate optics for compact soft x-ray microscopy*. PhD thesis, KTH, 2006.

[120] Lord Rayleigh. Wave theory of light (in encyclopedia britannica). *New York*, 1888.

[121] Robert Williams Wood. Liii. phase-reversal zone-plates, and diffraction-telescopes. *The London, Edinburgh, and Dublin Philosophical Magazine and Journal of Science*, 45(277):511–522, 1898.

[122] Jun Zhang, Yi Chen, and Liuqing Yang. Numerical calculation and measurement for the focus field of concave spherical acoustic lens transducer. In *MATEC Web of Conferences*, volume 283, page 05007. EDP Sciences, 2019.

[123] Dah-Shyang Tsai. Pressure buildup and internal stresses during binder burnout: numerical analysis. *AIChE journal*, 37(4):547–554, 1991.

[124] Yun Jiang. *Fabrication and characterisation of novel ultrasoud transducers*. PhD thesis, University of Birmingham, 2013.

[125] Ke Wang, Qian Ma, Cai-Xin Qu, Hong-Tao Zhou, Miao Cao, and Shu-Dong Wang. Review on 3d fabrication at nanoscale. *AUTEX Research Journal*, 23(3):350–369, 2023.

[126] A Ostendorf and K König. Tutorial: Laser in material nanoprocessing. 2015.

[127] Yu Hong, Ding Zhao, Dongli Liu, Binze Ma, Guangnan Yao, Qiang Li, Anpan Han, and Min Qiu. Three-dimensional in situ electron-beam lithography using water ice. *Nano letters*, 18(8):5036–5041, 2018.

[128] Dong Kyo Oh, Heonyeong Jeong, Joohoon Kim, Yeseul Kim, Inki Kim, Jong G Ok, and Junsuk Rho. Top-down nanofabrication approaches toward single-digit-nanometer scale structures. *Journal of Mechanical Science and Technology*, 35:837–859, 2021.

[129] YuHuang Wang, Chad A Mirkin, and So-Jung Park. Nanofabrication beyond electronics. *ACS nano*, 3(5):1049–1056, 2009.

[130] Robert F Peters, Luis Gutierrez-Rivera, Steven K Dew, and Maria Stepanova. Surface enhanced raman spectroscopy detection of biomolecules using ebl fabricated nanostructured substrates. *JoVE (Journal of Visualized Experiments)*, (97):e52712, 2015.

[131] Charles J Dixon and Ollin W Curtines. *Nanotechnology: nanofabrication, patterning, and self assembly*. Nova Science Publishers, 2010.

[132] Byron D Gates, Qiaobing Xu, J Christopher Love, Daniel B Wolfe, and George M Whitesides. Unconventional nanofabrication. *Annu. Rev. Mater. Res.*, 34:339–372, 2004.

[133] Byron D Gates, Qiaobing Xu, Michael Stewart, Declan Ryan, C Grant Willson, and George M Whitesides. New approaches to nanofabrication: molding, printing, and other techniques. *Chemical reviews*, 105(4):1171–1196, 2005.

[134] Benjamin J Wiley, Dong Qin, and Younan Xia. Nanofabrication at high throughput and low cost. *ACS nano*, 4(7):3554–3559, 2010.

[135] W. Xiong, L.J. Jiang, T. Baldacchini, and Y.F. Lu. 9 - laser additive manufacturing using nanofabrication by integrated two-photon polymerization and multiphoton ablation. In Milan Brandt, editor, *Laser Additive Manufacturing*, Woodhead Publishing Series in Electronic and Optical Materials, pages 237–256. Woodhead Publishing, 2017.

[136] David E. Marschner, Simone Pagliano, Po-Han Huang, and Frank Niklaus. A methodology for two-photon polymerization micro 3d printing of objects with long overhanging structures. *Additive Manufacturing*, 66:103474, 2023.

[137] Madalina Handrea-Dragan and Ioan Botiz. Multifunctional structured platforms: from patterning of polymer-based films to their subsequent filling with various nanomaterials. *Polymers*, 13(3):445, 2021.

[138] P Danilevičius, S Rekštytė, E Balčiūnas, A Kraniauskas, R Širmenis, D Baltriukienė, V Bukelskienė, R Gadonas, V Sirvydis, A Piskarskas, et al. Laser 3d micro/nanofabrication of polymers for tissue engineering applications. *Optics & Laser Technology*, 45:518–524, 2013.

[139] Markus Wimmer and Zoltan Major. Feasibility study of micro-lattice structures by multiphoton lithography. *Acta Polytechnica CTU Proceedings*, 25:83–88, 2019.

[140] Mingjie Li, Yulong Chen, Wenxin Luo, and Xing Cheng. Interfacial interactions during demolding in nanoimprint lithography. *Micromachines*, 12(4):349, 2021.

[141] Nazrin Kooy, Khairudin Mohamed, Lee Tze Pin, and Ooi Su Guan. A review of roll-to-roll nanoimprint lithography. *Nanoscale research letters*, 9:1–13, 2014.

[142] Zhi-Jun Zhao, Junseong Ahn, Soon Hyoung Hwang, Jiwoo Ko, Yongrok Jeong, Moonjeong Bok, Hyeok-Joong Kang, Jungrak Choi, Sohee Jeon, Inkyu Park, et al. Large-area nanogap-controlled 3d nanoarchitectures fabricated via layer-by-layer nanoimprint. *Acs Nano*, 15(1):503–514, 2021.

[143] Stephen Jesse, Albina Y Borisevich, Jason D Fowlkes, Andrew R Lupini, Philip D Rack, Raymond R Unocic, Bobby G Sumpter, Sergei V Kalinin, Alex Belianinov, and Olga S Ovchinnikova. Directing matter: toward atomic-scale 3d nanofabrication. *ACS nano*, 10(6):5600–5618, 2016.

[144] José María De Teresa, Pablo Orús, Rosa Córdoba, and Patrick Philipp. Comparison between focused electron/ion beam-induced deposition at room temperature and under cryogenic conditions. *Micromachines*, 10(12):799, 2019.

[145] Meltem Sezen and M Janecek. Focused ion beams (fib)—novel methodologies and recent applications for multidisciplinary sciences. *Modern Electron Microscopy in Physical and Life Sciences*, pages 121–140, 2016.

[146] Alois Senefelder. *The Invention of Lithography*. Good Press, 2019.

[147] Steven Dew and Maria Stepanova. *Nanofabrication Techniques and Principles*. Springer Vienna, 2012.

[148] Gary Wiederrecht. *Handbook of Nanofabrication*. Academic Press, 2009.

[149] Istvan Mohacsi. *Double-sided Fresnel zone plates as high performance optics in X-ray microscopy*. PhD thesis, University of Basel, 2015.

[150] BW Ward, NP Economou, DC Shaver, J E Ivory, ML Ward, and Stern L A. Microcircuit modification using focused ion beams. In *Electron-Beam, X-Ray, and Ion Beam Technology: Submicrometer Lithographies VII*, volume 923, pages 92–96. SPIE, 1988.

[151] MT Abramo and LL Hahn. The application of advanced techniques for complex focused-ion-beam device modification. In *Proceedings of the 7th European Symposium on Reliability of Electron Devices, Failure Physics and Analysis*, pages 1775–1778. IEEE, 1996.

[152] LR Harriott, A Wagner, and F Fritz. Integrated circuit repair using focused ion beam milling. *Journal of Vacuum Science & Technology B: Microelectronics Processing and Phenomena*, 4(1):181–184, 1986.

[153] Tao Tao, William Wilkinson, and John Melngailis. Focused ion beam induced deposition of platinum for repair processes. *Journal of Vacuum Science & Technology B: Microelectronics and Nanometer Structures Processing, Measurement, and Phenomena*, 9(1):162–164, 1991.

[154] K Nikawa. Applications of focused ion beam technique to failure analysis of very large scale integrations: A review. *Journal of Vacuum Science & Technology B: Microelectronics and Nanometer Structures Processing, Measurement, and Phenomena*, 9(5):2566–2577, 1991.

[155] Alex A Volinsky, Larry Rice, Wentao Qin, and N David Theodore. Fib failure analysis of memory arrays. *Microelectronic Engineering*, 75(1):3–11, 2004.

[156] Naoko I Kato. Reducing focused ion beam damage to transmission electron microscopy samples. *Journal of electron microscopy*, 53(5):451–458, 2004.

[157] Joachim Mayer, Lucille A Giannuzzi, Takeo Kamino, and Joseph Michael. Tem sample preparation and fib-induced damage. *MRS bulletin*, 32(5):400–407, 2007.

[158] Nabil Bassim, Keana Scott, and Lucille A Giannuzzi. Recent advances in focused ion beam technology and applications. *Mrs Bulletin*, 39(4):317–325, 2014.

[159] Ping Li, Siyu Chen, Houfu Dai, Zhengmei Yang, Zhiquan Chen, Yasi Wang, Yiqin Chen, Wenqiang Peng, Wubin Shan, and Huigao Duan. Recent advances in focused ion beam nanofabrication for nanostructures and devices: Fundamentals and applications. *Nanoscale*, 13(3):1529–1565, 2021.

[160] Lucille A Giannuzzi, Brenda I Prenitzer, and Brian W Kempshall. Ion-solid interactions. *Introduction to focused ion beams: Instrumentation, theory, techniques and practice*, pages 13–52, 2005.

[161] Nabil D Bassim, Alexander J Giles, Leonidas E Ocola, and Joshua D Caldwell. Fabrication of phonon-based metamaterial structures using focused ion beam patterning. *Applied Physics Letters*, 112(9), 2018.

[162] Richard J. Smith, Fernando Perez Cota, Leonel Marques, Xuesheng Chen, Ahmet Arca, Kevin Webb, Jonathon Aylott, Micheal G. Somekh, and Matt Clark. Optically excited nanoscale ultrasonic transducers. *The Journal of the Acoustical Society of America*, 137(1):219–227, January 2015.

[163] Fernando Pérez-Cota, Richard J. Smith, Emilia Moradi, Leonel Marques, Kevin F. Webb, and Matt Clark. Thin-film optoacoustic transducers for subcellular brillouin oscillation imaging of individual biological cells. *Appl. Opt.*, 54(28):8388–8398, Oct 2015.

[164] Xiaoyang Chen, Zhuocheng Diao, Siyan He, Guo Zheng, and Qingkang Yu. Amplification characteristics of fresnel zone plate acoustic lens. *STEM Fellowship Journal*, 3(1):15–22, 2017.

[165] Xiangxiang Xia, Yongchuan Li, Feiyan Cai, Hui Zhou, Teng Ma, and Hairong Zheng. Ultrasonic tunable focusing by a stretchable phase-reversal Fresnel zone plate. *Applied Physics Letters*, 117(2):021904, July 2020.

[166] Daniel Tarrazó-Serrano, Sergio Pérez-López, Pilar Candelas, Antonio Uris, and Constanza Rubio. Acoustic Focusing Enhancement In Fresnel Zone Plate Lenses. *Scientific Reports*, 9(1):7067, May 2019.

[167] Enxiao Liu, Yongmeng Liu, Xiaoming Wang, Junjie Zhi, Yuanlin Chen, Chuanzhi Sun, and Jiubin Tan. Design of acoustic fresnel zone plate for contact stress measurement of aero-engine rotor mating surface. *Journal of Sound and Vibration*, 500:116035, 2021.

[168] Rudi Rottenfusser. Proper alignment of the microscope. In *Methods in Cell Biology*, volume 114, pages 43–67. Elsevier, 2013.

[169] Greenfield Sluder and David E Wolf. *Digital microscopy*. Academic Press, 2013.

[170] H Ito, K Ito, M Arai, K Sugimoto, T Matsukura, and R Maeda. Fib etching of glass-like carbon die and mold press of micro glass lens. *Journal of the Japan Society for Precision Engineering*, 72(6):735–739, 2006.

[171] Daniel Tarrazo Serrano. *Design, modelling, characterization and implementation of acoustic lenses for modulation of ultrasound beams.", school =.* PhD thesis.

[172] Karen Sloyan, Henrik Melkonyan, and Marcus S Dahlem. Focused ion beam milling for prototyping 2d and 3d photonic structures. *The International Journal of Advanced Manufacturing Technology*, 107:4469–4480, 2020.

[173] Fernando Pérez-Cota, Shakila Naznin, Rafael Fuentes-Domínguez, Richard J Smith, Matt Clark, et al. Apparent attenuation by opto-acoustic defocus in phonon microscopy. *Photoacoustics*, 19:100180, 2020.

[174] Ronald L Allen and Duncan Mills. *Signal analysis: time, frequency, scale, and structure*. John Wiley & Sons, 2004.

[175] William Hardiman. *Probing single cell biomechanics with optical trapping and phonon microscopy: A correlative study", school =.* PhD thesis.

[176] *Time-Frequency Signal Transforms*, chapter 10, pages 712–801. John Wiley and Sons, Ltd, 2003.

[177] *Wavelet, Subband and Block Transforms in Communications and Multimedia*. Springer, 1999.

[178] Water speed sound vs. temperature. https://www.engineeringtoolbox.com/sound-speed-water-d_598.html.

[179] Alexey N. Bashkatov and Elina A. Genina. Water refractive index in dependence on temperature and wavelength: a simple approximation. In Valery V. Tuchin, editor, *Saratov Fall Meeting 2002: Optical Technologies in Biophysics and Medicine IV*, volume 5068, pages 393 – 395. International Society for Optics and Photonics, SPIE, 2003.

[180] Salvatore La Cavera, Fernando Pérez-Cota, Rafael Fuentes-Domínguez, Richard J. Smith, and Matt Clark. Time resolved brillouin fiber-spectrometer. *Opt. Express*, 27(18):25064–25071, Sep 2019.

[181] Richard J. Smith, Fernando Perez Cota, Leonel Marques, Xuesheng Chen, Ahmet Arca, Kevin Webb, Jonathon Aylott, Micheal G. Somekh, and Matt Clark. Optically excited nanoscale ultrasonic transducers. *The Journal of the Acoustical Society of America*, 137(1):219–227, 2015.

[182] Rafael Fuentes-Domínguez, Fernando Pérez-Cota, Shakila Naznin, Richard J Smith, and Matt Clark. Super-resolution imaging using nano-bells. *Scientific reports*, 8(1):1–9, 2018.

[183] Rafael Fuentes-Domínguez, Shakila Naznin, Leonel Marques, Fernando Pérez-Cota, Richard J. Smith, and Matt Clark. Characterising the size and shape of metallic nano-structures by their acoustic vibrations. *Nanoscale*, 12:14230–14236, 2020.

[184] Min Hu, Xuan Wang, Gregory V Hartland, Paul Mulvaney, Jorge Perez Juste, and John E Sader. Vibrational response of nanorods to ultrafast laser induced heating: theoretical and experimental analysis. *Journal of the American Chemical Society*, 125(48):14925–14933, 2003.

[185] Min Hu, Xuan Wang, Gregory V. Hartland, Paul Mulvaney, Jorge Perez Juste, and John E. Sader. Vibrational response of nanorods to ultrafast laser induced heating - theoretical and experimental analysis, 2003.

[186] JJJA Durnin. Exact solutions for nondiffracting beams. i. the scalar theory. *JOSA A*, 4(4):651–654, 1987.

[187] John Maddox. Making light-spots travel further. *Nature*, 327(6119):183–183, 1987.

[188] X Chu. Analytical study on the self-healing property of bessel beam. *The European Physical Journal D*, 66:1–5, 2012.

[189] Marti Duocastella and Craig B Arnold. Bessel and annular beams for materials processing. *Laser & Photonics Reviews*, 6(5):607–621, 2012.

[190] Pablo Katchadjian, Christina Desimone, and AD Garcia. Application of axicon lenses in ultrasonic techniques. In *AIP Conference Proceedings*, volume 1211, pages 1043–1050. American Institute of Physics, 2010.

[191] John H McLeod. The axicon: a new type of optical element. *JOSA*, 44(8):592–597, 1954.

[192] DK Hsu, FJ Margetan, and DO Thompson. Bessel beam ultrasonic transducer: Fabrication method and experimental results. *Applied physics letters*, 55(20):2066–2068, 1989.

[193] J-Y Lu and James F Greenleaf. Ultrasonic nondiffracting transducer for medical imaging. *IEEE transactions on ultrasonics, ferroelectrics, and frequency control*, 37(5):438–447, 1990.

[194] Xianlin Song, Jianshuang Wei, and Lingfang Song. Bessel ultrasonic probe for large depth of field using conical acoustic lens. In *SPIE Future Sensing Technologies*, volume 11525, pages 466–471. SPIE, 2020.

[195] Noe Jimenez, Vicente Romero-García, R Picó, A Cebrecos, Víctor José Sánchez-Morcillo, LM Garcia-Raffi, Juan Vicente Sánchez-Pérez, and K Staliunas. Acoustic bessel-like beam formation by an axisymmetric grating. *Europhysics Letters*, 106(2):24005, 2014.

[196] Fei He, Rafael Fuentes-Dominguez, Richard Cousins, Christopher J Mellor, Jennifer K Barton, and George SD Gordon. Single-and multi-layer micro-

scale diffractive lens fabrication for fiber imaging probes with versatile depth-of-field. *arXiv preprint arXiv:2401.14551*, 2024.

[197] Gdsii toolbox. [online] https://sites.google.com/site/ulfgri/numerical/gdsii-toolbox.

[198] Raith gdsii. [online] https://github.com/ahryciw/Raith_GDSII.

[199] Klayout 0.28.17 documentation. [online] https://www.klayout.de/doc.html.

Appendices

Appendix A

White light spectroscopy

A white light spectrometer, a convenient post-fabrication layer thickness assessment tool, was used as discussed in Section 3.2.1. The wavelength of light, the material's optical characteristics, the qualities of the materials nearby, and the thickness of the desired material are the only factors that can be specifically linked to the optical resonances of a film or cavity. Light that is reflected or transmitted through the material can be recorded and spectrally examined using a VISNIR spectrometer (Ocean Optics USB2000+) when a broadband VIS light source is shone onto the film as shown in Figure A.1. Then, by comparing the optical resonances recorded by the spectrometer software with theoretical calculations, an equivalent film thickness can be determined.

The comparison of the expected and the detected traces is done in MATLAB as explained in Figure A.2 (a). Theoretical calculation of the Au transmittance $T(\lambda)_{model}$ were calculated and plotted (blue lines in the top of Figure A.2 (b)), then the script loads the measured trace $T(\lambda)_{exp}$ (red in the top of Figure A.2 (b)), after that, fitting a curve (Bottom figure of Figure A.2 (b)) to compare the experimental result with all the theoretical curves. A fitting score range from 0

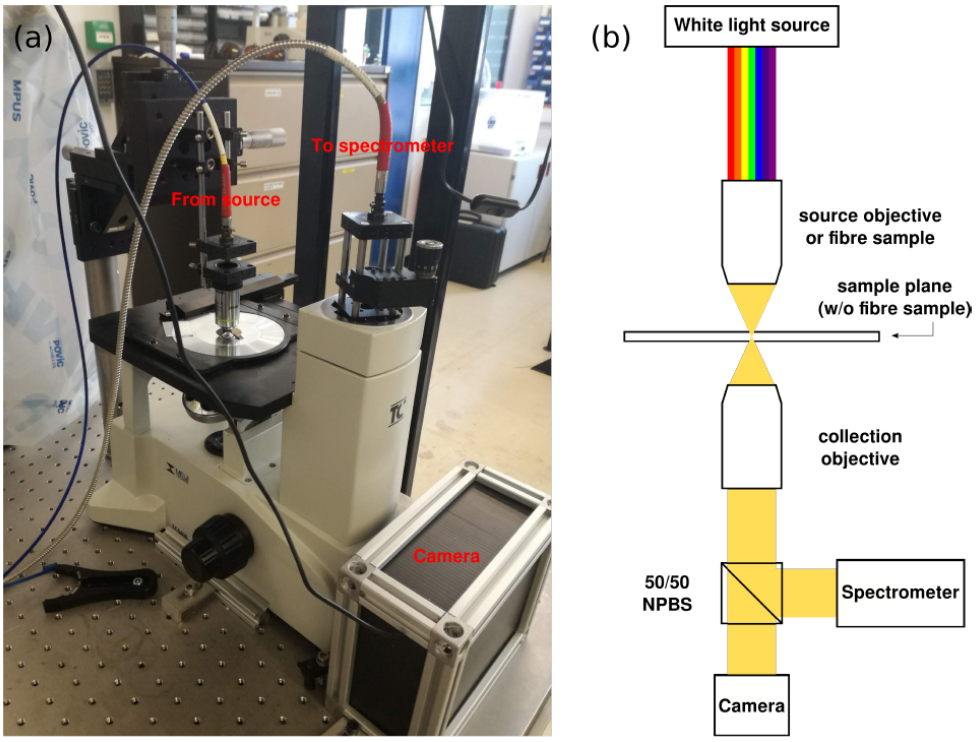

Figure A.1: White light spectroscopy design. (a) Picture of the spectrometer that was built to measure reflection and transmission spectra of either planar or optical fibre samples. White light is delivered to and from the microscope body via optical fibre patch cables. (b) Schematic of the spectrometer optical design. Source light is brought to the sample plane either by objective lens or optical fibre, and is collected with an objective lens that relays the light for spectroscopy or imaging. Image reproduced from [67].

to 1 is calculated and given for each theoretical trace according to its similarity with the experimental trace ($fittingscore = 1 - |T(\lambda)_{\text{model}} - T(\lambda)_{\text{exp}}|$). The maximum value of that fitting curve is labelled as the fitting result for the layer thickness. This spectroscopy also allows measurements of the thickness of ITO for an Au/ITO/Au cavity structure, provided the thickness of the Au mirror is known. This can be achieved by separate sputtering of a cavity from one run to multiple runs, adding a measurement step after the first deposition of the Au layer.

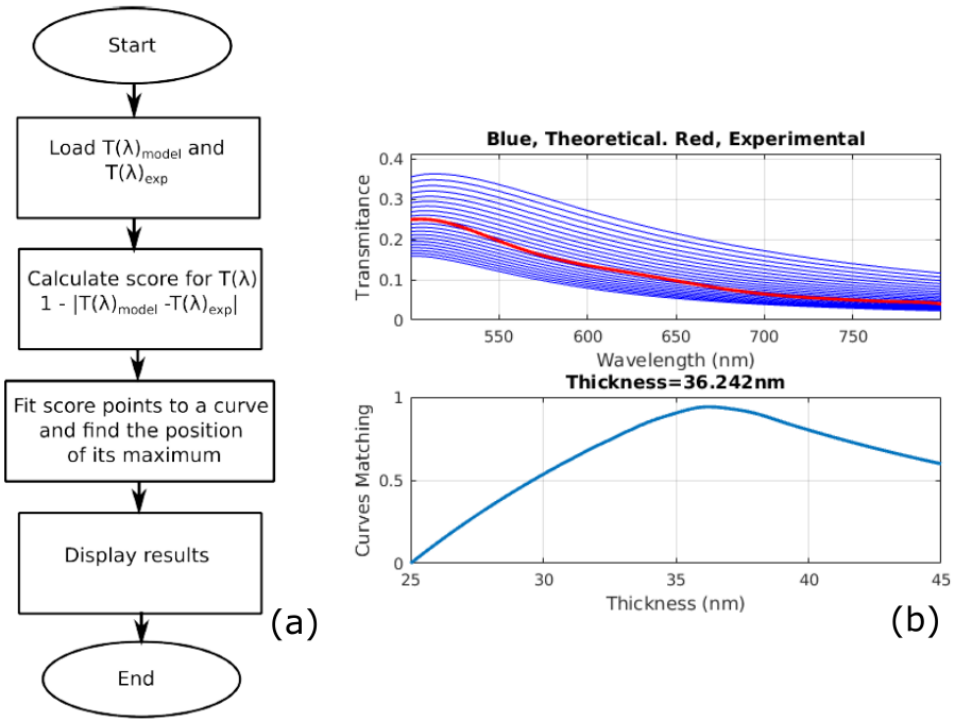

Figure A.2: White light spectroscopy algorithm diagram and example fitting result. (a) Flow chart of the steps to calculate Au thickness H_{Au} based on the proposed fitting method. (b) Example of the output measurement of an Au layer thicknesses (blue lines). The closest match between experimental and theoretical spectra (the bottom figure, the maximum matching number) is considered to be the measures film thickness.

Appendix B

GDSII design

GDSII library files are used to specify the layout of integrated circuits, MEMS devices, nanostructured optics, etc. They are also the standard file format for lithography designs. One of the initial steps in the fabrication process is the design and creation of a GDSII pattern file for direct exposure via electron-beam lithography. To make a GDSII file, two GDSII layout software options are explored for this project: a script-based approach (Octave & MATLAB toolbox and Raith-GDSII MATLAB toolbox) and a graphical CAD tool (KLayout).

The Octave & MATLAB toolbox and the Raith-GDSII toolbox are used to generate all the EBL-readable design files in this thesis. These toolboxes provide a simple, versatile, and scriptable means of generating patterns for both focused ion beam (FIB) and electron beam lithography (EBL) tools using MATLAB. They are particularly useful when a layout results from design through numerical modelling, e.g., for the nanorods, FZP pattern presented in this thesis. Both toolboxes are open source and can be downloaded from GitHub [197, 198]. Layouts produced can then be inspected with an open-source layout viewer KLayout, which offers more freedom for minor error correction and pattern reconstruction for the final

design file.

KLayout is an open-source GDSII viewer and editor and available for free downloading from the internet. It can be easily downloaded and installed from [199]. In this project, KLayout was mainly used for both its viewing and editing functions, thanks to its highlights in:

- Capabilities for overlays: several layouts can be loaded into a single window.
- Advanced layer display features include the ability to name layers, apply additional transformations, choose specific hierarchy levels, and choose shapes based on specific properties.
- Explore the hierarchy by showcasing a cell within its larger context.
- Support for external libraries is available. Bound to a layout in a dynamic manner, making it particularly useful for libraries generated by MATLAB.

Appendix C

Water refractive index

Taking into account both the wavelength and temperature dependence of water refractive index is very important for understanding the relationship between Brillouin frequency shift and environmental temperature. According to literature [179], the following Cauchy formula with temperature-dependent coefficients (C.1) and approximated Cauchy coefficients (C.2) are used to calculate the refractive index vs temperature data.

$$n(\lambda, T) = A(T) + \frac{B(T)}{\lambda^2} + \frac{C(T)}{\lambda^4} + \frac{D(T)}{\lambda^6} \tag{C.1}$$

where λ, is the wavelength in nm; and $A(T), B(T), C(T), D(T)$ are the Cauchy coefficients presented as a function of the temperature; T is temperature, °C.

$$
\begin{aligned}
A(t) &= 1.3208 - 1.2325 \cdot 10^{-5}t - 1.8674 \cdot 10^{-6}t^2 + 5.0233 \cdot 10^{-9}t^3 \\
B(t) &= 5208.2413 - 0.5179t - 2.284 \cdot 10^{-2}t^2 + 6.9608 \cdot 10^{-5}t^3 \\
C(t) &= -2.5551 \cdot 10^{8} - 18341.336t - 917.2319t^2 + 2.7729t^3 \\
D(t) &= 9.3495 + 1.7855 \cdot 10^{-3}t + 3.6733 \cdot 10^{-5}t^2 - 1.2932 \cdot 10^{-7}t^3
\end{aligned}
\tag{C.2}
$$

Appendix D

Transforms

D.1 Fourier transform

The Fourier transform for time t and frequency ω is:

$$F(\omega) = \int_{-\infty}^{\infty} f(t) e^{-j\omega t} dt \tag{D.1}$$

and the reverse transform is:

$$f(t) = \frac{1}{2\pi} \int_{-\infty}^{\infty} F(\omega) e^{j\omega t} d\omega \tag{D.2}$$

which are continuous valued and vary from $-\infty$ to ∞.

Fast Fourier transform (FFT)

The numerical grid for real space and frequency space for a FFT is defined as:

FFT is used for signal that is finite in duration & discrete in time, $f[0], f[1], \ldots, f[N-1], f[N]$. The DFT $F[0], F[1], \ldots, F[N-1], F[N]$ is also finite in duration & discrete in time. The forward transform is define as:

$$F[k] = \sum_{n=0}^{N} f[n] e^{-jk\omega_0 n} \quad k = 0, 1, \ldots, N-1 \tag{D.3}$$

and the inverse transform is:

$$f[n] = \frac{1}{N} \sum_{k=0}^{N} F[k] e^{jk\omega_0 n} \quad n = 0, 1, \ldots, N-1 \tag{D.4}$$

where

$$\omega_0 = \frac{2\pi}{N} \tag{D.5}$$

Note that to prevent aliasing in the sampled function, the function must be sampled above the Shanon-Nyquist limit.

2D Fourier transform

The 2D Fourier transform between the functions $f(x, y)$ and $F(k_x, k_y)$ is given by:

$$F(k_x, k_y) = \int_{-\infty}^{\infty} \int_{-\infty}^{\infty} f(x, y) \exp[-ik_x x - ik_y y] \, dxdy \tag{D.6}$$

The FFT algorithm can be used to numerically evaluate this by running it first along the elements in one dimension and then along the elements in the other one.

D.2 Hankel Transform

The Hankel transform is a radial equivalent of the Fourier transform that can be applied to any function: $F(r,\theta) = A(r)B(\theta)$. This is useful for optical systems as it enables us to simulate beams that exhibit either radial symmetry or a consistent azimuthal phase: $U(r,\theta) = A(r)\exp(in\theta)$.

Hankel Transform demotivated from Fourier transform

The Hankel transform may be derived directly from the two dimensional Fourier transform (D.6). By assuming radial co-ordinates r and θ in real space and k_r and ϕ in frequency space. These are related to the Cartesian co-ordinates as:

$$\begin{aligned} x &= r\cos\theta \quad k_x = k_r\cos\phi \\ y &= r\sin\theta \quad k_y = k_r\sin\phi \end{aligned} \tag{D.7}$$

where $r \in [0, \text{inf}]$ and $\theta \in [0, 2\pi]$. Equation (D.6) may then be re-written as:

$$\int_0^\infty \int_0^{2\pi} \exp\left[-irk_r(\cos\theta\cos\phi + \sin\theta\sin\phi)\right] r dr d\theta \tag{D.8}$$

$$\int_0^\infty \int_0^{2\pi} \exp\left[-irk_\tau\cos(\theta-\phi)\right] r dr d\theta \tag{D.9}$$

One can derive the Hankel transform directly from the Fourier transform by considering functions that have radial symmetry:

$$A(r,\theta) = f(r)\exp(in\theta) \tag{D.10}$$

The Hankel transform pair now can be written as:

$$\mathcal{H}\{f(r)\} = F\left(k_\tau\right) = \int_0^\infty f(r) r J_n\left(r.k_\tau\right) dr \tag{D.11}$$

and

$$\mathcal{H}\left\{F\left(k_r\right)\right\} = f(r) = \int_0^\infty F\left(k_r\right) r J_n\left(k_r \cdot r\right) dk_r \tag{D.12}$$

where J_n is the n^{th} Bessel function. Note that, the Hankel transform and Inverse Hankel transform are identical, unlike the Fourier transform.